Dissertation

submitted to the

Combined Faculties of the Natural Sciences and for Mathematics

of the Ruperto-Carola University of Heidelberg, Germany

for the degree of

Doctor of Natural Sciences

presented by
Diplom Physicist: Michael Speidel
born in: Essen

Oral examination: 16^{th} of November 2005

Atmospheric Aerosol Particle Formation: Aircraft-Based Mass Spectrometric Measurements of Gaseous and Ionic Aerosol Precursors.

Referees: **Prof. Dr. Frank Arnold**

Prof. Dr. Kurt Roth

Dedicated to my parents.

Bildung Atmosphärischer Aerosolpartikel: Flugzeuggetragene Massenspektrometrische Messungen Gasförmiger und Ionischer Aerosolvorläufer.

Kondensationswachstum von Aerosolpartikeln, sowie die Neubildung von Nanopartikeln, hängen in erster Linie vom Vorhandensein von Schwefelsäure ab. Durch kosmische Strahlung gebildete atmosphärische Ionen können die Bildung von Cluster-Ionen auslösen, welche dann durch gegenseitiges Anlagern sowie durch Kondensation von Schwefelsäure wachsen. Ein chemisches Ionisations Ionenfallen-Massenspektrometer (IT-CIMS) sowie ein Quadrupol Massenspektrometer (QMS) dienten in der vorliegenden Arbeit zur quantitativen Bestimmung des Vorläufergases der Schwefelsäure, SO_2, sowie zur Messung atmosphärischer Cluster-Ionen. Die zum Nachweis von SO_2 verwendete Ionenmolekülreaktion wurde isotopisch kalibriert. Aus Wandverlusten und Ionenhydratisierung resultierende Messunsicherheiten werden dadurch elegant umgangen. Das modifizierte IT-CIMS konnte im Rahmen der Flugzeugkampagne ITOP (International Transport of Ozone and Precursors) an Bord des deutschen Forschungsflugzeuges Falcon erfolgreich eingesetzt werden. In einer weiteren Flugzeugkampange, CONTRACE (Convective Transport of Trace Gases), diente das QMS an Bord der Falcon zur Messung atmosphärischer Cluster-Ionen. Signifikante Korrelationen zwischen gemessenen kleinen Partikeln und Cluster-Ionen wurden festgestellt. Im Rahmen von ITOP stieß man auf eine mit SO_2 stark verschmutzte Luftmasse, im Bereich der unteren Stratosphäre, welche aus überschießender Konvektion in Nordamerika stammte. Modellsimulationen auf Basis der SO_2 Daten deuten an, dass die gemessenen Partikel allein aus binärer Nukleation und anschließendem Wachstum (Kondensation und Anlagerung) von H_2SO_4 und H_2O erklärt werden können.

Atmospheric Aerosol Particle Formation: Aircraft-Based Mass Spectrometric Measurements of Gaseous and Ionic Aerosol Precursors.

The condensational growth of aerosol particles and the formation of fresh, nanometer-sized particles depend primarily upon the presence of H_2SO_4. Atmospheric ions produced by cosmic rays can initialize the formation of cluster ions, which subsequently may grow by mutual coagulation and condensation of H_2SO_4 and H_2O. In the present work, measurements of the H_2SO_4 precursor SO_2 and atmospheric cluster ions were performed using an ion trap chemical ionisation mass spectrometer (IT-CIMS) and a quadrupole mass spectrometer (QMS). The ion molecule reaction to determine atmospheric SO_2 was calibrated isotopically. So problems arising from wall losses and ion hydration are circumvented in an elegant manner. The modified IT-CIMS was integrated into the German research aircraft Falcon and successfully employed during the international aircraft campaign ITOP (International Transport of Ozone and Precursors). During another aircraft campaign, CONTRACE (Convective Transport of Trace Gases), the QMS aboard the Falcon detected atmospheric cluster ions. Significant correlations between detected small particles and cluster ions were found. During ITOP a plume of strongly enhanced SO_2 concentrations in the lowermost stratosphere was observed, that originated from North America by overshooting deep convection. Model simulations based on the SO_2 data indicate that the measured particles can be explained by binary nucleation and growth (condensation and coagulation) of H_2SO_4 and H_2O.

Contents

Chapter 1

INTRODUCTION

1.1 Thesis Objectives

Presented here is a detailed account of the development, testing, and application of an instrumental apparatus called Ion Trap Chemical Ionisation Mass Spectrometer (ITCIMS) to determine atmospheric mole fractions of SO_2 from aircraft platforms. A precise characterization of a quadrupole mass spectrometer setup to determine cumulative abundances of natural ambient cluster ions in the atmosphere and its application during an aircraft campaign followed by a detailed data analysis comprises a second major topic of this thesis. The objectives of this work were the following:

1. Design and construction of an ITCIMS setup which can be deployed on aircraft platforms for in situ atmospheric studies.

2. Development of methods yielding high ITCIMS sensitivity and accuracy for SO_2 under ambient conditions, including moist air environments such as the marine boundary layer and altitudes from ground to 12 km.

3. Determine the vertical SO_2 distributions above central Europe.

4. Analyse influences of sulfur dioxide related long-range transport phenomena from northern America to Europe.

5. Validate the deposition of sulfur dioxide into the marine boundary layer by seagoing ships.

6. Characterize the occurrence of large natural ion clusters in terms of particle nucleation in the ambient atmosphere.

The chapters in this thesis are logically divided into laboratory development and airborne field deployments of the ITCIMS and QMS instruments. From a thematic point of view, the thesis is divided into SO_2 chemistry and its atmospheric occurrence on the one hand and the potential impact of SO_2 onto particle nucleation by conversion to sulfuric acid on the other hand. The ITCIMS instrument served to determine ambient sulfur dioxide mole fractions, whereas the QMS instrument was used to obtain the abundance of charged clusters, predominantly formed by condensable gases like sulfuric acid.

Chapter 1 provides background information on nucleation theory and results on earlier performed charged-cluster measurements. An overview about the atmospheric sulfur cycle, SO_2 sources and sinks is presented. Other airborne sulfur dioxide detection methods are listed.

Chapter 2 presents a detailed account of the instrumentation and components used to create an isotopically calibrated ITCIMS for the the measurement of SO_2 in the atmosphere on aircraft platforms. In great detail the airborne QMS apparatus is characterized.

Chapter 3 delivers results of the airborne deployment in continental air of the QMS instrument in June 2003. Data analysis and results of the field campaign are discussed.

Chapter 4 shows the determined vertical SO_2 profile. In particular two flights are described. The intersection with an urban pollution plume and the crossing through very clean Atlantic air masses nicely illustrates the good performance, accuracy and dynamic range of the ITCIMS instrument.

Chapter 5 discusses the detection of a highly polluted SO_2 air parcel in the lowermost stratosphere during the flight campaign in July 2004. The resulting potential of particle nucleation in the lowermost stratosphere (LS) as well as transport mechanisms capable to efficiently uplift polluted air from the planetary boundary layer (PBL) to the LS are elucidated.

1.2 Research Significance

1.2.1 Health Impacts of SO_2

Considerable attention has been given in recent years to epidemiological studies and research into the health effects of ambient air pollution [Schlatter, 1994]. Studies have covered different acute and chronic health effects which occur as a result of SO_2 pollution and its potential to induce nanometer-sized particles [Imai et al., 1986], [Stjernberg

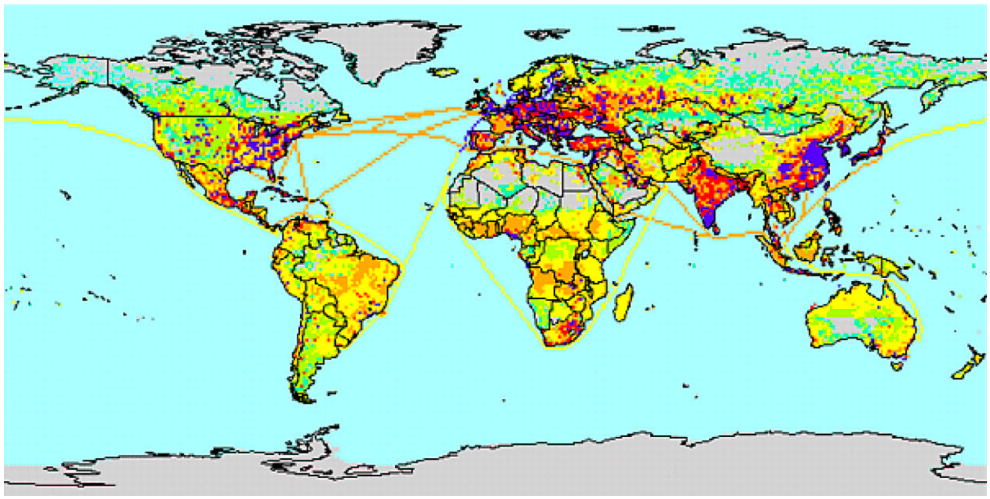

Figure 1.1: shows global SO_2 from anthropogenic sources in 2000. The blue pixels correspond to the highest whereas grey pixels correspond to the lowest pollution by SO_2. Picture was taken from the EDGAR database.

et al., 1985]. The latter probably holds the higher risk, since SO_2 gas would earlier stick to the mucous membranes whereas ultrafine particles formed by SO_2-induced sulfuric acid nucleation, penetrate deeper into the respiratory system.

Linking pollution and health, it has been confirmed that in a number of cases the prevalence of persistent coughing and phlegm is significantly related to air pollution including that arising from SO_2 and NO_x. Various statistical observations exist on the relationship between the prevalence of chronic bronchitis and SO_2, NO_x air concentrations, respectively. In polluted areas the prevalence of persistent coughing and phlegm is 2-3 times higher than in areas where pollution is less extensive. Such a relationship is also derived for areas where mortality results from lung cancer.

1.2.2 Sulfur Emission Rates

Figure 1.1 shows the global anthropogenic sulfur dioxide sources as they are given by the EDGAR database (Emission Database for Global Atmospheric Research). Color coding refers to the source strength of sulfur dioxide with blue being the highest emission and grey the lowest. Clearly Europe, the Eastern United States, India and China appear as major source contributors. The lines represent high-traffic intercontinental ship routes.

Most of the SO_2 and particulate emission reductions which have taken place in Western Europe since the 1980s were due to a switch from coal to oil and gas, the

increased use of nuclear energy, and technological improvements in sulfur and dust removal installations.

Political conventions taking care of local air quality in Central and Eastern Europe are the so-called "Sofia Initiatives", adopted by the Third "Environment for Europe" ministerial conference in Sofia, Bulgaria in October 1995. The aim of these initiatives is to accelerate the implementation of the Environmental Action Programme (EAP) for Central and Eastern Europe, through policy, regulation and investment measures. Concerning SO_2 the significant reduction of sulfur and particulate emissions was set as a target.

Concerning fuel standards, the EU Directive 93/12/EEC from March 23, 1993 for the sulfur content of certain liquid fuels was taken as a reference point. The fuel sulfur content of diesel fuel must be less than 0.05% on weight basis, and the gasoline sulfur content must be $< 0.2\%$. Fuels with a higher sulfur content cannot be traded within the EU.

However 2005 the EU launched the emission trading scheme, a market where local emission allowances are traded. An "emission consumer" who owns more certificates than needed to cover his emission rate, may sell his certificates to someone who is in the opposite position. The U.S. existing environmental financial markets for sulfur dioxide are the most developed. Also China participates in emission trading. To what extend emission trading turns out to effectively reduce the environmental burden remains arguable.

1.2.3 Conclusions

Finally, it should be mentioned that aside from the health risks associated with the inhalation of gases and particles, there are also significant economic consequences arising from SO_2 and particulate pollution. These include deforestation, acidification of water and soil, and the accelerated deterioration of building materials, including historical monuments.

It is thus important to permanently control ambient sulfur dioxide concentrations in order to ascertain the completion of climate protocols as well as to further understand its transport and influence beyond national borders.

1.3 Background

1.3.1 SO_2 Sources and Sinks in the Atmosphere

Sulfur is present in the *Earth's* crust at a mixing ratio less than 500 ppm and in the *Earth's* atmosphere at a total mixing ratio less than 1 ppm [Seinfeld and Pandis, 1998]. It is an essential element to live. In the oxic environment bacteria reduce sulfate to sulfide in order to form amino acids and proteins. Disulfide bridges serve to control the functional structure of proteins beside hydrogen bridges. The sulfur cycle is conceptually shown in **figure 1.2**.

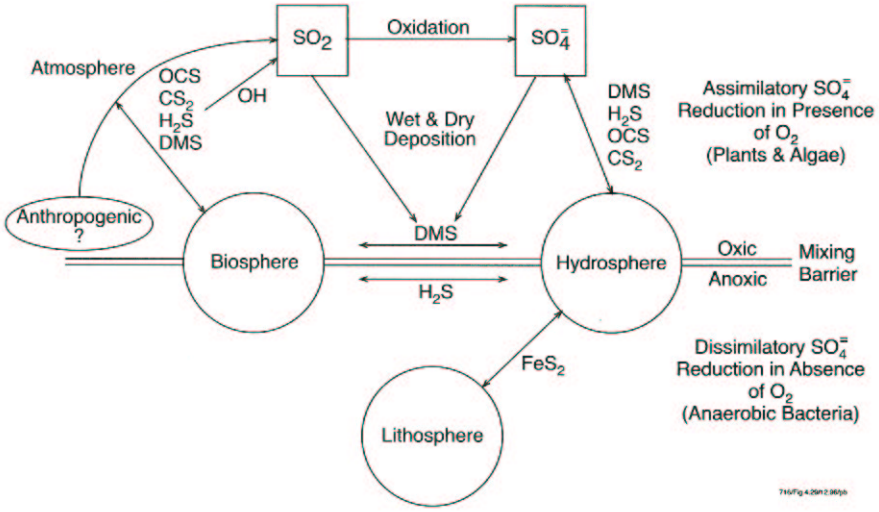

Figure 1.2: Exchanges of sulfur in the global environment (figure taken from [Brasseur et al., 1999]).

The production of sulfur compounds is split into two major compartments depending on whether the compound is produced in the absence or presence of oxygen. The metabolism of anaerobic bacteria uses sulfate (SO_4^{2-}) for respiration. This primarily leads to the production of H_2S in the biosphere and hydrosphere.

The lithosphere takes up certain amounts of the produced H_2S due to the chemical reaction of sulfide with metal ions like iron, some of which is eventually released into the atmosphere by weathering. H_2S is thus one of the primary species emitted by soils and vegetation but contributions from volcanoes also play a role. Dimethylsulfide (DMS) is formed in the ocean by some marine plankton to control their internal osmotic pressure. Trees and plants act as source and as sink of carbonyl-sulfide (OCS). The dominating process depends on the composition of ambient air, as well as on light intensity and soil

moisture. Sulfur dioxide emerges mainly from volcanoes and biomass burning. These sources account for 10% and 2%, respectively, of the global SO_2 flux. However, the main sulfur source is affiliated with human activities and comprises about 75% of the total sulfur emissions with 90% occurring in the Northern Hemisphere. **Figure 1.3** shows the contributions of fossil fuel combustion and natural sources of the Northern Hemisphere, where coal and oil combustion contribute to 53% and 28%, respectively. The increase in energy consumption of Asian countries increases the sulfur emissions significantly beside contributions from Europe and the northeastern United States.

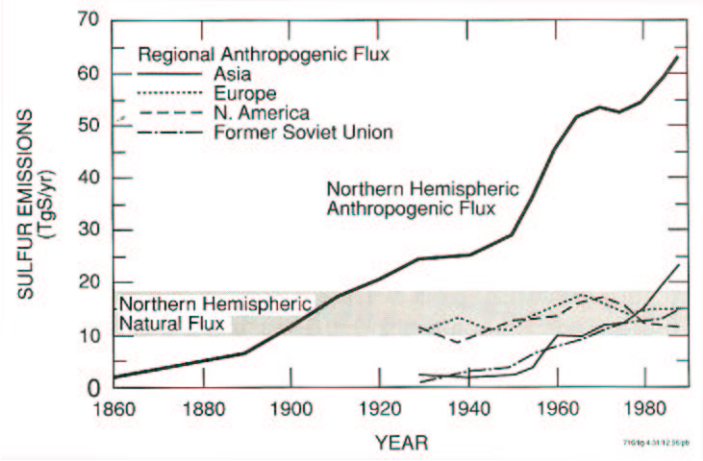

Figure 1.3: Natural and fossil fuel emissions of SO_2 in the Northern Hemisphere from 1860 to 1990 (IPCC,1996), fig. from [Brasseur et al., 1999]

.

The marine atmosphere is additionally polluted by the increasing ship traffic [Lawrence and P.J.Crutzen, 1999]. Measurements of marine boundary layer air in an area of heavy ship traffic and the related plume chemistry are part of this thesis and given in B.2.4. Another anthropogenic sulfur source which gained importance during the last two decades is the increasing air traffic. Air traffic reflects the only significant man-made source of pollutants in the upper troposphere, lowermost stratosphere. Due to the low natural background concentrations of sulfur compounds in these altitudes the deposition of only small amounts may influence already the chemical balance. Another reason is the long lifetime due to little mixing of lower stratospheric and upper tropospheric air masses via the tropopause [Hoinka et al., 1993], [Forster et al., 2003]. The most important natural source of stratospheric SO_2 is believed to refer to OCS which due to its little reactivity with OH radicals, its low water solubility and reactivity with other trace gases becomes transported to high altitudes. It is responsible for the formation

Average SO_2 mole fractions at different observation sites	**pptv**
Marine surface layer	20 pptv
Free troposphere (> 5km)	50 pptv
North American clean continental site	160 pptv
Coastal Europe	260 pptv
Polluted continental air	1500 pptv
Global sulfur emission estimates	**Tg(S)/year**
Fossil fuel combustion	70
Biomass burning	2.8
Volcanoes	7-8

Table 1.1: Sulfur dioxide emission rates and corresponding contributions from biomass burning, fossil fuel combustion and volcanic activity; from [Seinfeld and Pandis, 1998].

of stratospheric sulfuric acid and related to the appearance of aerosol particles which form the Junge layer [Logan et al., 1979], [P.J.Crutzen, 1976].

The major sink of SO_2 in the atmosphere is the wash out by clouds. Absorption of SO_2 in water results in HSO_3^-. H_2O_2 is one of the most effective oxidants of S^{IV} in clouds and fogs and leads to the formation of SO_2OOH^- and via further reaction with H_2O molecules to sulfuric acid. Beside nitrogen oxide, sulfur dioxide emissions are thus responsible for acid precipitation. An overview about the sulfur dioxide emission fractions which arise at different observation sites is given in **table 1.1**. Also shown are the global sulfur emission rates contributing to the SO_2 flux.

1.3.2 SO_2 Distribution in the Atmosphere

Sulfur dioxide is one of the dominant pollutants in the lower and middle troposphere. Therefore most investigations have dealt with the temporal and spatial distribution of this atmospheric trace gas near ground and to altitudes up to 12 km [Thornton et al., 1993] and [Thornton et al., 1997]. Little is still known about the vertical transport of sulfur dioxide and its mixing ratio near the tropopause. Nevertheless SO_2 penetrating the stratosphere is of great importance in terms of stratospheric sulfur chemistry, particularly for the formation and persistence of the stratospheric aerosol layer [Junge, 1974]. It is worthwhile mentioning that the Junge aerosol layer is sustained during non-volcanic periods. Beside volcanic activity and quiet volcanic gasing transport mechanisms which also lead to a deposition of sulfur dioxide in the lowermost stratosphere were observed by [Poulida and R.R.Dickerson, 1996] and [Thornton

et al., 1997]. [Georgii and Meixner, 1980], and [Möhler and F.Arnold, 1992] measured vertical sulfur dioxide profiles at altitudes from mid troposphere up to the lower stratosphere. SO_2 abundances varied between 10 and 400 pptv from -6 and 2.4 km relative to the local tropopause height. Derived sulfuric acid mixing ratios scattered between about 0.01 and 0.06 pptv. The H_2SO_4 data slightly decreased with height above the tropopause level. [Laaksonen et al., 2000] investigated the potential of upper tropospheric cloud formation from sulfur dioxide. Due to the absence of a large aerosol surface in the stratosphere, the formation of sulfuric acid by photolytic conversion of SO_2 is very effectively contributing to the nucleation of new particles. These particles if grown above a critical size which stabilizes them against evaporation, will sediment by gravitational forces, with a velocity proportional to $\sqrt{d}$, where d denotes the particle diameter. However, once these ultrafine aerosol particles reach the troposphere the increase in water vapor may lead to further condensational growth and eventually may lead to contributions of cloud condensation nuclei.

Sulfur dioxide measurements in the free troposphere revealed a median concentration of 0.065 ppbv over the marine remote atmosphere compared with a value of 1.02 ppbv in the boundary layer [Thornton et al., 1987]. The SO_2 background over the oceans can be explained by long-range transport from the continents but also by oxidation of CS_2 and COS initiated by OH radicals [Brasseur et al., 1999].

The major sulfur dioxide measurements are centered around highly polluted regions of Europe and North America, where the anthropogenic emissions are high. Enhanced fossil fuel burning during wintertime is generally associated with increased levels of SO_2 in urban air masses.

A sharp decrease in the SO_2 mixing ratio from the ground to about 5 km in continental air masses is a well known phenomenon for lower layers of the troposphere. Concentrations in the ppbv range are expected in the boundary layer over major anthropogenic source regions of Europe and the United States. Above 5 km a relatively constant value is generally observed. An SO_2 mixing ratio between 0.1 and 0.01 ppbv seems to be typically for layers above 6 km and can be considered as background value for the higher troposphere [Georgii and Meixner, 1980]. Enhanced washout by clouds in lower tropospheric layers is a reason for the sulfur dioxide decrease.

1.3.3 Airborne SO_2 Measurement Techniques

Several different techniques exist to detect sulfur dioxide online in the ambient atmosphere from an airborne platform [Gregory et al., 1993]. Detection limit and sampling frequency are related to the values given in [Gregory et al., 1993]. The following tech-

niques are currently used for SO_2 detection on airborne platforms: (1) Gas chromatography flame photometry, (2) gas chromatography mass spectrometry, (3) chemiluminescence, (4) airborne multi-axis DOAS and (5) chemical ionization mass spectrometry. In (1) the sulfur-containing gas in the incoming air stream is pre-concentrated in a Teflon trap cooled with liquid argon. After pre-concentration for several minutes (typically 3 min), the trap contents are volatilized (via heating) into a carrier gas (air). The sulfur gas in the carrier gas is separated by gas chromatography and then analyzed flame-photometrically. The sample frequency comprises about 10 to 12 min. In-flight calibration can be performed on a frequent interval by use of standard addition of SO_2 near the sample inlet. The detection limit of this method is given to be at 20 pptv.

Method (2) also works by pre-concentrating the incoming air stream in a Teflon trap cooled with liquid argon for several minutes. The trap contents are then volatilized into helium which serves as a carrier gas. Separation of the sulfur gas occurs via gas-chromatography and the separated sulfur dioxide vapor is then analyzed via a mass spectrometer. An isotopically labeled variant of sulfur dioxide is constantly added near the sample inlet and used for calibration. Thus sample losses that may occur in the inlet of the instrument are accounted for, as any variation in the sensitivity of the spectrometer. Typically 3-4 min are required per analysis sequence. A detection limit of 10 pptv is given in the above cited literature.

The chemiluminescence technique in (3) detects SO_2 traces in a solution. Two methods exist, one relies upon separating ambient SO_2 in a filter, the other on a continuous chemical reaction.

For the technique, filter material is impregnated with sodiumtetrachloromercurate ($Na_2(HgCl_4)$) that forms a very stable complex with sulfur dioxide, disulfitomercurate. Analysis of the formed SO_2 complex relies upon oxidation with $KMnO_4$ to SO_4^{2-} that is accompanied by chemiluminescence ($\lambda < 500$ nm). The light yield is proportional to the amount of SO_2 in the complex. The detection limit is given with 26 pptv with a sampling frequency of 5 to 20 min. A description of this method can be found in [Georgii and Meixner, 1980] and [Jaeschke, 1978].

The continuous chemiluminescence method uses about the same detection principle. The main sulfur dioxide-carrying gas stream is flushed through a sodium hydroxide solution, where the SO_2 becomes chemically converted to sulfite. It then reacts in the same manner as mentioned above with $KMnO_4$ and the emitted light signal is detected via a photomultiplier. Here the detection limit is at about 30 pptv with a measurement point every 3 min.

It was recently reported by [Wang et al., 2005] about SO_2 detection with an airborne multi-axis DOAS (Differential Optical Absorption Spectroscopy) (4). The DOAS in-

strument consists of two grating spectrometers. One spectrometer operates in the UV between 300–440 nm, the other covers the visible part of the spectrum (400– 550 nm). The scattered sunlight, collected by the two spectrometers which are mounted outside the aircraft is collected by optical fibers. For the sulfur dioxide detection it absorption at 316.5–325.5 nm is used. The reader is referred to [Platt, 1994] for further details of the DOAS system.

(5) The chemical ionization mass spectrometry method is object of the current thesis and described in great detail in the following chapters.

1.3.4 Nucleation in the Atmosphere

As a fact water nucleates on foreign particles much more readily than it does on its own. This is the reason why droplets in the ambient atmosphere are formed at relative humidities slightly above 100%. Once the initial nucleation step has occurred, the nuclei of the new phase tend to grow rather rapidly. Nucleation theory attempts to describe the rate at which the first step in the phase transformation process occurs, the rate at which the initial very small nuclei appear.
The present work focuses on the binary system of sulfuric acid and water since it is of high relevance in the atmosphere.
New particle formation is correlated with enhanced levels of gas-phase sulfuric acid [Weber et al., 1995], [Eisele and Hansen, 2000] and low aerosol surface area[1]. Water is also involved in the formation of new particles because it is abundant and it significantly suppresses the vapor pressure of sulfuric acid. In the middle and lower troposphere, nucleation frequently occurs where classical binary H_2SO_4/H_2O nucleation theory does not predict new particle formation. This led to considerations whether other species (e.g. organic species, NH_3) are involved [Coffman and Hegg, 1995], [Kulmala et al., 2000] in the nucleation process or that an ion-induced mechanism is important [Arnold, 1981], [Arnold, 1982], [Keesee and A.W.Castleman, 1985], [Fangqun and Turco, 2001], [Eichkorn et al., 2002], [Lovejoy et al., 2004].
Ion-induced nucleation may also explain a possible link between the galactic cosmic ray flux, which mainly determines the ion concentration in the background atmosphere, and global cloudiness [Fangqun, 2002], [Nigel and Svensmark, 2000]. A plot showing the ion concentration throughout the atmosphere is given in **figure 1.4**. The maximum ion density appears to be at an altitude of 10 km. Total ion density varies between 1000 - 6000 cm^{-3}.
Wilson´s early smog chamber experiments (1911) evidently showed that ions can act

[1]The aerosol surface area serves as dominant sulfuric acid sink.

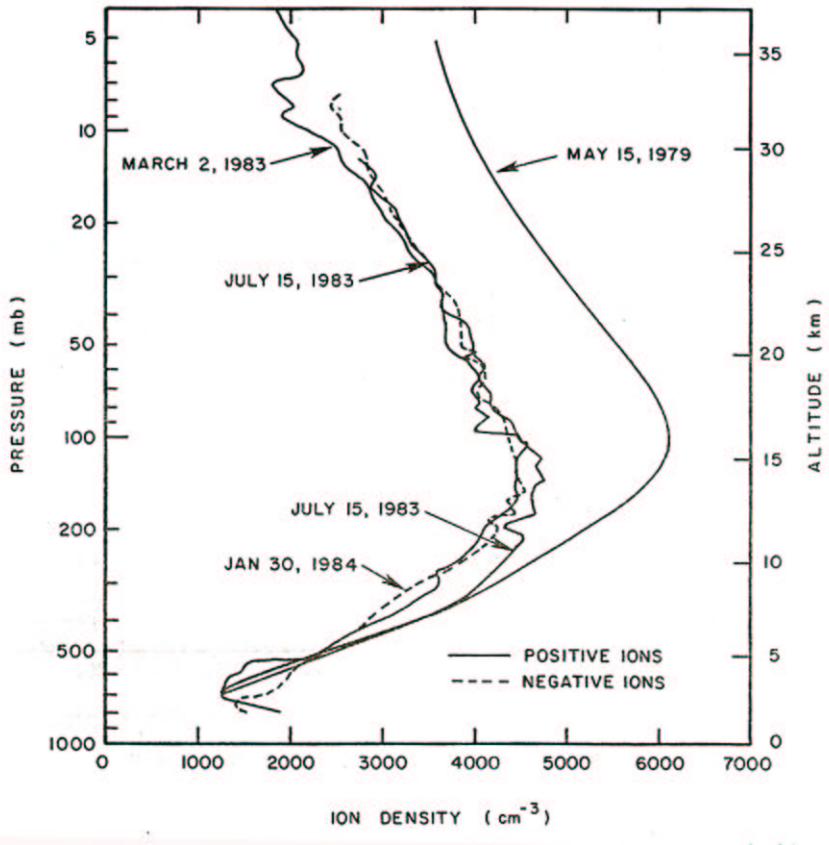

Figure 1.4: Comparison of several ion density profiles made by Rosen et.al.: [Rosen et al., 1985]

as nucleating species.

Due to the induced electrostatic interactions with polar ligands, ions are capable to form stable clusters, to reduce the number of molecules in a critical cluster and consequently to decrease the critical size [Nadykto and F.Yu, 2003]. The reactive ions (e.g. N_2^+, O_2^+, N^+ and O^+) and electrons produced by the initial ionization of air[2] are converted rapidly to cluster ions of protonated bases (e.g. $H_3O^+(H_2O)_m$, $NH_4^+(H_2O)_n$) and of the conjugate bases of strong acids (e.g. $NO_3^-(HNO_3)_x(H_2O)_y$). In the presence of gaseous sulfuric acid, $NO_3^-(HNO_3)_x(H_2O)_y$ cluster ions are converted to cluster ions of $HSO_4^-(H_2SO_4)_x(H_2O)_y$. Charged clusters grow by agglomeration of acid and / or water molecules but also by coagulation to aerosol and recombination with ions of opposite polarity. The relative importance of various kinetic processes involving the species

[2]The galactic cosmic rays form ion pairs $cm^{-3}s^{-1}$ at a rate of 1-30 with a maximum at about 10km altitude [Rosen et al., 1985].

of interest can be estimated by considering an upper-limit neutral-neutral collision coefficient of $2 \cdot 10^{-10}\ cm^{-3}s^{-1}$, an ion-neutral reaction coefficient of $2 \cdot 10^{-9}\ cm^{-3}s^{-1}$ and an ion-ion recombination coefficient of $2 \cdot 10^{-6}\ cm^{-3}s^{-1}$ [Fangqun and Turco, 2001]. Taking a sulfuric acid concentration of $10^6\ cm^3$ into account, the average ion recombination lifetime results in $t_{ir} = 0.5$ s, the ion-neutral collision lifetime to $t_{in} = 500$ s and the neutral-neutral molecular collision with an H_2SO_4 molecule to $t_{ic} = 5000$ s. Hence ions predominately neutralize by recombination to larger clusters and thus may kinetically grow to stable neutral clusters, larger than a critical size. This is an elegant mechanism to bypass the energetic barrier to form a stable cluster. The rate-limiting process concerning ion-induced nucleation results from the ionization rate Q which is determined by the cosmic ray flux and the solar activity. Q is about 30 cm^3 at 8 km altitude whereas at 5 km it is only about 5 cm^3 [Reiter, 1992]. Due to the high energy of the cosmic ray, the ionization probability is almost the same for each type of molecule. Thus the ion pair production rate increases nearly proportional to the neutral gas density which reaches its maximum at about 13-15 km altitude. In the following the fundamental principle which underlies the formation of a cluster out of vapor molecules will be discussed. This process is currently referred to as homogenous nucleation. Afterwards cluster formation in the presence of ions will be elucidated (ion-induced nucleation) and compared to homogenous nucleation. Finally the interplay of both mechanisms in the atmosphere is illustrated.

Since in the atmosphere pressure P, temperature T and particle number N vary, it is sensible to relate the thermodynamic potential to those three variables. The Gibbs energy delivers the wished dependence G = G(T,P,N) = -SdT + VdP + μdN. The chemical potential μ(T,P) of an ideal gas is defined by: μ(p,T) = μ°(T,1 atm) + RT ln(p), where μ° is the standard chemical potential defined at a pressure of 1 atm and therefore is a function of temperature only. Due to the second law of thermodynamics (dQ = 0) a system will try to increase its Gibbs free energy, dG $\leq$ 0. Considering the change of Gibbs free energy accompanying the formation of a single drop of pure A of radius R_p containing n molecules of the substance: $\Delta G = G_{droplet}$ - G_{vapor}. If g_v and g_l are the free energies of a molecule in the vapor and liquid phase, respectively, ΔG can be written as:

$$\Delta G = n(g_v - g_l) + 4\pi R_p^2 \sigma \tag{1.1}$$

where the surface tension σ is considered. The molecules in the drop occupy a spherical volume with v_l being the volume of a single molecule in the liquid phase. Combination of the expressions so far leads to:

$$\Delta G = \frac{4\pi R_p^3}{3v_l}(g_l - g_v) + 4\pi R_p^2 \sigma \tag{1.2}$$

Using the fact that dg = v dp at constant temperature and assuming that the molecular volume in the liquid v_l is much smaller than the molecular volume in the vapor phase v_v, the difference in the Gibbs energies g_l - g_v can be expressed by:

$$g_l - g_v = -kTln\frac{p_A}{p_A^\circ} \tag{1.3}$$

after integration over p/dp ranging from p_A° to p_A. P_A is the actual equilibrium partial pressure and p_A° the saturation vapor pressure of species A over a liquid surface. This finally leads to an expression which can be interpreted physically:

$$\Delta G = -\frac{4}{3}\pi R_p^3 \frac{kT}{v_l} ln\frac{p_A}{p_A^\circ} \; + \; 4\pi R_p^2 \sigma \tag{1.4}$$

Two terms contribute to the change in ΔG when a droplet is formed from vapor: One can be related to the volume term which depends on the radius of curvature R_p of the formed droplet, the other is given by the surface tension, the amount of work necessary to extract a molecule out of the bulk liquid. **Figure 1.5** shows the derived expression of ΔG for subsaturation and supersaturation. S equals the ratio p_A/p_A°.
Considering the maximum in ΔG one obtains the so-called critical radius $R_p^\star$. Until $R_p < R_p^\star$ holds, non-equilibrium conditions will lead to the evaporation of the droplet.

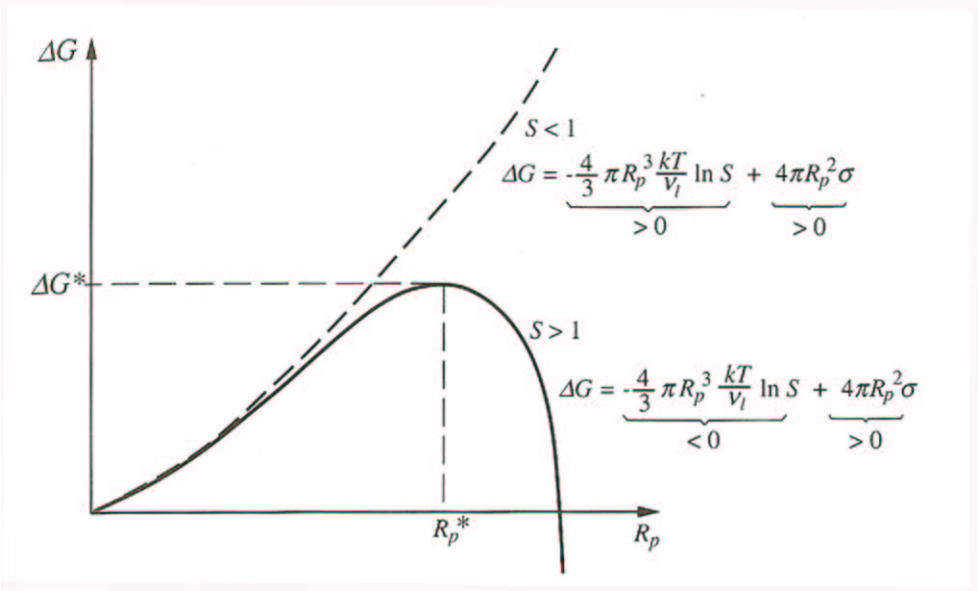

Figure 1.5: Gibbs free energy change for homogenous nucleation of a droplet of radius R_p at the saturation ratio S. Picture from [Seinfeld and Pandis, 1998].

Once this energetic barrier is overcome the droplet grows until the surrounding supersaturation is used. In other words, the critical size of a cluster is that for which the evaporation rate of single vapor molecules is equal to their arrival rate. Thus a continuous nucleation net flux J exists. Some modification of the last equation leads to the so-called Kelvin equation:

$$p_A = p_A^{\circ} exp(\frac{2\sigma\ v_l}{\mathrm{kTR_p}}) \tag{1.5}$$

The Kelvin equation basically tells that the vapor pressure over a curved interface always exceeds that of the same substance over a flat surface. This becomes more clear if one considers the amount of adjacent molecules in a curved and a flat surface. The forces exerted upon each molecule are smaller in case of a curved surface, than for a flat one due to less neighbouring molecules. Thus the vapor pressure increases.
A major simplification in homogenous nucleation emanates from the fact that the surface tension is taken as that of the bulk liquid monomer; thus it is assumed that a cluster of a small number of molecules exhibits the same surface tension as the bulk liquid. This assumption is termed capillarity approximation. Since the aim of nucleation theory is to obtain an expression $N_i(t)$ which describes the number of clusters formed by i monomers, the following differential equation is proposed:

$$\frac{dN_i}{dt} = \beta_{i-1}N_{i-1}(t)\ -\ \gamma_i N_i(t)\ +\ \gamma_{i+1}N_{i+1}(t) \tag{1.6}$$

with γ being the reverse and β the forward rate constant, in terms of detachment and attachment of a monomer onto the i_{th} cluster. A nucleation rate J can be derived from the above expression. In case of attachment of monomers under supersaturated conditions (S > 1) a net flux of J leads to a continuous production of clusters. In order to calculate J, a constrained equilibrium conditions is introduced, by setting J = 0 at S > 1. This constrained equilibrium condition only holds for cluster radii smaller than the critical size and this is due to the earlier stated capillarity approximation which in principle is the biggest limitation in classical nucleation theory.
If binary homogenous nucleation is considered, the basic principles of homogenous nucleation remain the same. The significant difference is that when two or more vapor species are present, neither of which is supersaturated, nucleation can still take place as long as the participating vapor species are supersaturated with respect to a liquid solution droplet. Thus heteromolecular nucleation can occur when a mixture of vapors is subsaturated with respect to the pure substances as long as there is supersaturation with respect to a solution of these substances. An important example of binary nucleation is the atmospheric production of sulfuric acid droplets in the presence of water

vapor. This is basically due to the low vapor pressure of sulfuric acid.
Finally the mechanism of ion-induced nucleation and its relevance in atmospheric nucleation will be discussed.

Introducing an ion in the process of cluster formation will create a central force field that makes it more difficult for a polar molecule to evaporate. The effect of the ion embedded in the cluster on the arrival rate of vapor molecules is considerably weaker than that on the evaporation rate. Thus the Gibbs energy will be expanded by the potential electrical energy:

$$\Delta G = \Delta G_{hom} \; + \; \frac{q^2 e_0^2}{8\pi\varepsilon_0}(\frac{1}{\varepsilon_g} - \frac{1}{\varepsilon_r})(\frac{1}{r} - \frac{1}{r_0}) \tag{1.7}$$

where q denotes the charge of the ion[3], ε_0 is the influence constant, ε the dielectrical constant of the nucleating vapor molecules, r_0 the radius of the core ion and r the cluster radius [Nadykto and F.Yu, 2003]. In the case of homogenous nucleation, the evaporation rate decreases monotonically with increasing number of monomers in the cluster (i), approaching the bulk liquid value equal to the condensation rate at saturation (S = 1). When S > 1, there is only one cluster size ($i^\star$) at which the rate of evaporation and that of condensation balance to yield a critical nucleus at unstable equilibrium with the vapor phase. If an ion is introduced molecules are attracted leading to a decreasing rate of evaporation. This should be most significant for small clusters (small i) and becomes negligible when i approaches infinity due to screening of the ion by the surrounding molecules. When the ion-molecule interaction energy is sufficiently large, the condensation rate balances the evaporation rate even if S $\leq$ 1. This implies that the evaporation rate first increases with i, achieves a maximum at a certain value of i, and then decreases approaching the bulk value. Thus for S > 1, there are two values of i at which the evaporation rate and the condensation rate balance, the smaller is a stable subcritical cluster and the larger is the unstable critical nucleus. **Figure 1.6** reflects the explained context for the homogenous versus the ion-induced case.
In the atmosphere generally one cannot distinguish between one type of nucleation and the others. Also the measured nucleation rates often cannot be simply explained by the binary system of sulfuric acid and water, particularly those in the marine boundary layer. Hence the ternary system which comprises sulfuric acid, ammonia and water is considered [Kulmala et al., 2000]. **Figure 1.7** shows a simplified scheme of the interplay of the three discussed nucleation mechanisms. Homogenous nucleation of a binary and a ternary system, as well as ion-induced nucleation. By recombination and

[3]in this work only singly charged ions are treated.

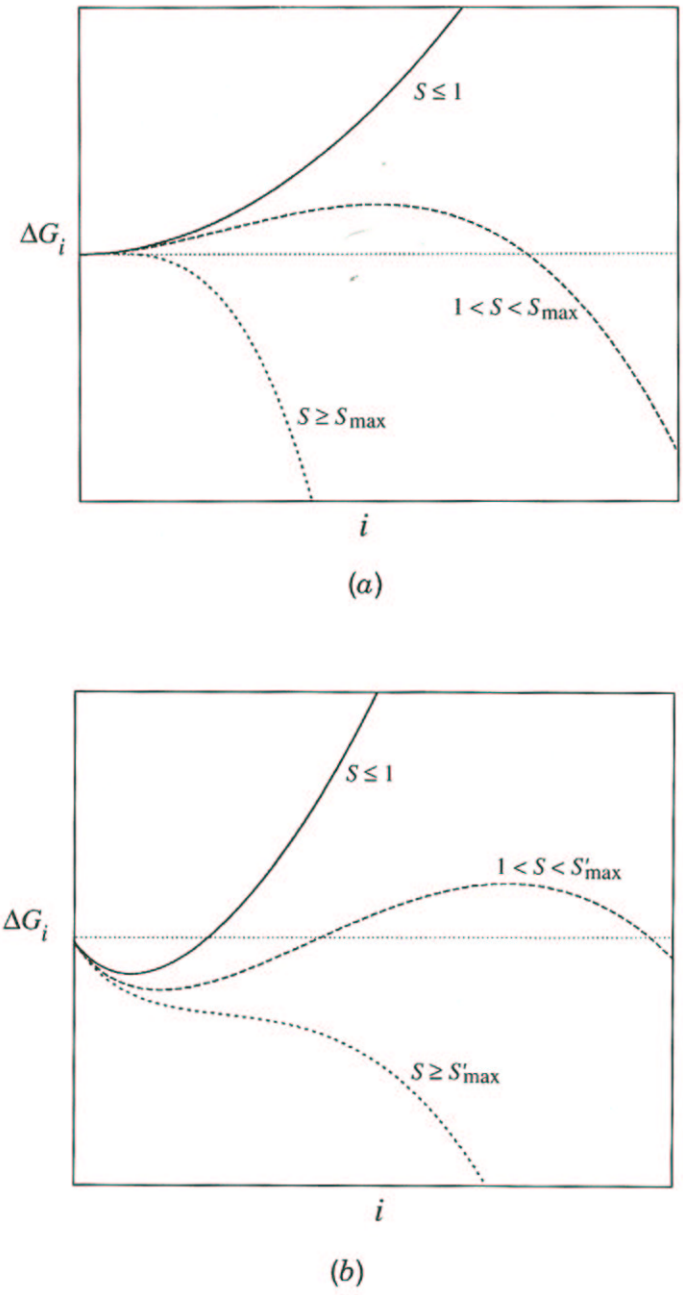

Figure 1.6: Ion-induced nucleation.(a) Free energy of cluster formation in homogenous nucleation. (b) Free energy of cluster formation in ion-induced nucleation. S_{max} and S'_{max} are the maximum values of the saturation ratio for which no barrier exists in homogenous and ion-induced nucleation, respectively. Picture and figure caption taken from [Seinfeld and Pandis, 1998].

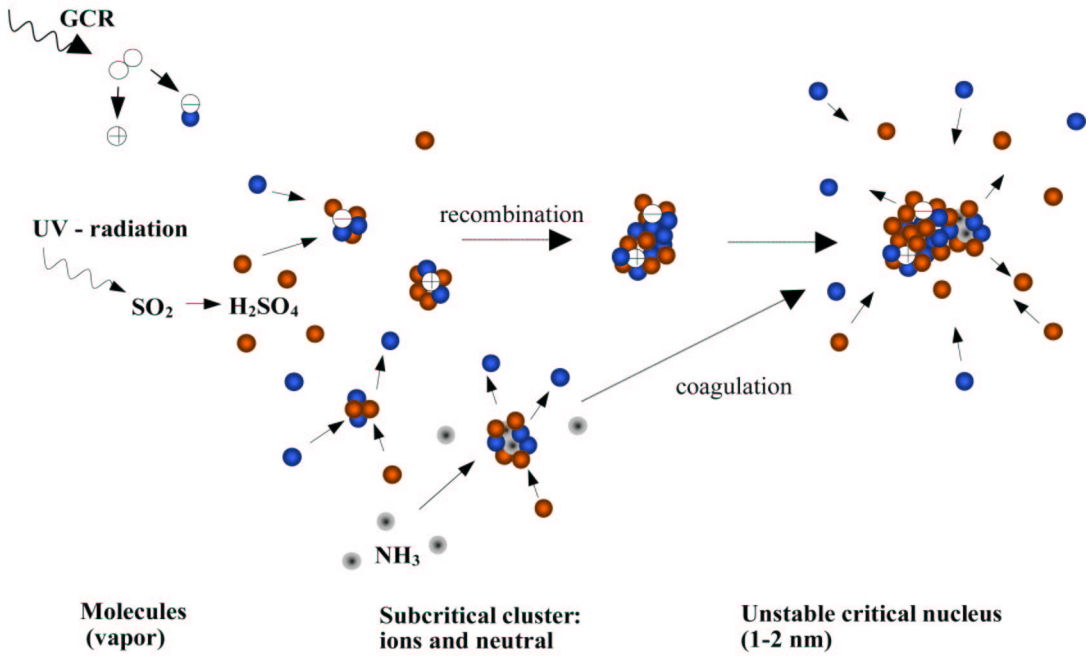

Figure 1.7: Nucleation scheme which consideres binary homogenous nucleation of water and sulfuric acid, ion-induced nucleation and ternary homogenous nucleation of ammonia, sulfuric acid and water.

coagulation of oppositely charged clusters, the unstable critical nucleus is formed. Further condensation of vapor will eventually lead to sizes above the critical radius and may even bring the initial cluster to form a cloud condensation nucleus ($\sim$ 100nm). However, attachment onto the surface of preexisting aerosol particles is more likely. This in turn can lead to changes of the hygroscopicity of the existing aerosol particles. However, a comparison of homogeneous model calculations and experimentally derived ion-induced nucleation rates show up to a sulfuric acid concentration of 3.5 $\cdot$ 10^6 cm^3 always higher rates of ion-induced nucleation than binary homogenous nucleation [Wilhelm, 2003], considering a temperature range of 223-227 K and a water vapor concentration of $2 \cdot 10^{15}$ cm^3. Thus it was found that in the free troposphere the ion-induced nucleation rate is likely to exceed the binary homogenous nucleation rate, that is in the absence of a large aerosol surface which acts as sink for sulfuric acid. Homogenous nucleation is controlled mainly by coagulation on preexisting particles whereas the limiting factor controlling ion-induced nucleation is given by the ionization rate Q. Thus the production rate of ultrafine ($<$ 3nm) particles is most sensitive

to the sulfuric acid and ion concentration. Sulfuric acid controls the growth rate of ion clusters, while the ion concentration determines the lifetime of the charged clusters [Fangqun, 2002]. [Nigel and Svensmark, 2000] pointed out that the influence of solar variability, which in turm modulates the ionization rate, is strongest in low clouds ($<$ 3km), which points towards a microphysical mechanism involving aerosol formation that is enhanced by ionization due to cosmic rays. If such a mechanism would change cloud properties the Earth′s radiation budget will be altered. The radiative properties of clouds result from their ability to cool the surface by reflecting the incoming radiation but also by trapping outgoing long-wave radiation. The net radiative impact of a particular cloud is mainly dependent upon its height above the surface and its optical thickness. High optically thin clouds tend to heat, while low optically thick clouds tend to cool [Hartmann, 1993].

[Svensmark and Christensen, 1996] retrieved the low cloud cover data from the ISCCP (International Satellite Cloud Climate Project) which comprises an archive of data over the globe from geostationary and polar orbiting satellites for the period July 1983 to December 1990. Cloud detection is based on visible (daytime only) and infrared threshold techniques. From the observation it was found that during the period of minimum solar activity in 1986 total cloudiness was 3-4% higher than near solar maximum in 1990. The correlation appeared to hold when three further satellite data sets were used to extend the period of analysis to 1996 although there may be problems of inter- calibration. However, whether a galactic cosmic ray mediated climate effect concerning low cloud occurrence exists is still under debate [Kernthaler et al., 1999], [Wagner et al., 1999].

1.3.5 Previous Airborne Measurements of Charged Molecular Cluster

First atmospheric mass spectrometric ion-cluster measurements were performed by [Arnold et al., 1977], [Arnold and Henschen, 1978]. The spectra with a total mass range of 0 - 612 amu were recorded throughout the stratosphere by use of meteorologic balloons. Experiments with a similar mass spectrometer implemented into the German research aircraft Falcon, operated by DLR, were performed by [Heitmann and Arnold, 1983]. The instrument was set to detect negative ion compositions. The measurements in the upper troposphere revealed the presence of two major ion families, $NO_3^-(HNO_3)_n$ and $HSO_4^-(HNO_3)$. The inferred HNO_3 abundances supported the view that an upper tropospheric HNO_3 source exists. As far as nucleation is concerned they suggest that H_2SO_4 may be strongly supersaturated in the upper troposphere and thus

thermodynamic requirements for nucleation are easily met. The detection of negative and positive gaseous natural ion-cluster in parallel and on board of FALCON was first performed by [Eichkorn et al., 2002] and [Wilhelm, 2003]. These experiments gave direct examples for ion mediated nucleation. It was also shown that in the background atmosphere ion-induced nucleation seems to exceed homogenous binary nucleation of sulfuric acid and water. Also clusters with $500 < m < 800$ amu were highly enhanced in polluted tropospheric air parcels. In the framework of this work the natural ambient ion-cluster measurements on board of the FALCON were repeated and the covered altitude range was extended further down to ambient pressures of about 900 mbar.

Chapter 2

METHOD AND LABORATORY EXPERIMENTS

The following chapter will give an overview about two different instruments used in this thesis. A quadrupole mass spectrometer built by MPI-K Heidelberg and a commercially ion-trap mass spectrometer modified by the MPI-K. Schematics of both instruments and characteristic parameters will be derived and explained. The used method of chemical ionisation to detect trace gases in the pptv (parts per trillion volume) range is introduced and major ion-molecule reactions are discussed.

2.1 Quadrupole Mass Spectrometer (QMS)

2.1.1 Instrumental Schematics and Layout

Figure 2.1 shows the setup scheme of the airborne quadrupole mass spectrometer. Between the interior (A) and the analyzer region (B) a pressure gradient of typically about 6 orders in magnitude exists. A small fraction of the ambient air gas jet enters the analyzer by passing through a critical orifice and expands into the cavity.
The cavity is cryogenically[1] pumped with liquid neon (cryo pump, 1-3 l/min) backed by a turbo-molecular pump (Balzers company). The turbo-molecular pump is necessary to pump in the air contained He since its freezing point is below that of liquid neon. The pressure inside the cavity (B) depends on the pressure in the first compartment

[1] Atmospheric gases freeze out at the 27 K cold, inner wall of the cryo pump and form a N_2,O_2 condensation matrix. The hereby possible background pressure is given by the saturation partial pressure of the main gas constituents above the solid phase at the boiling point of the used cooling agent.

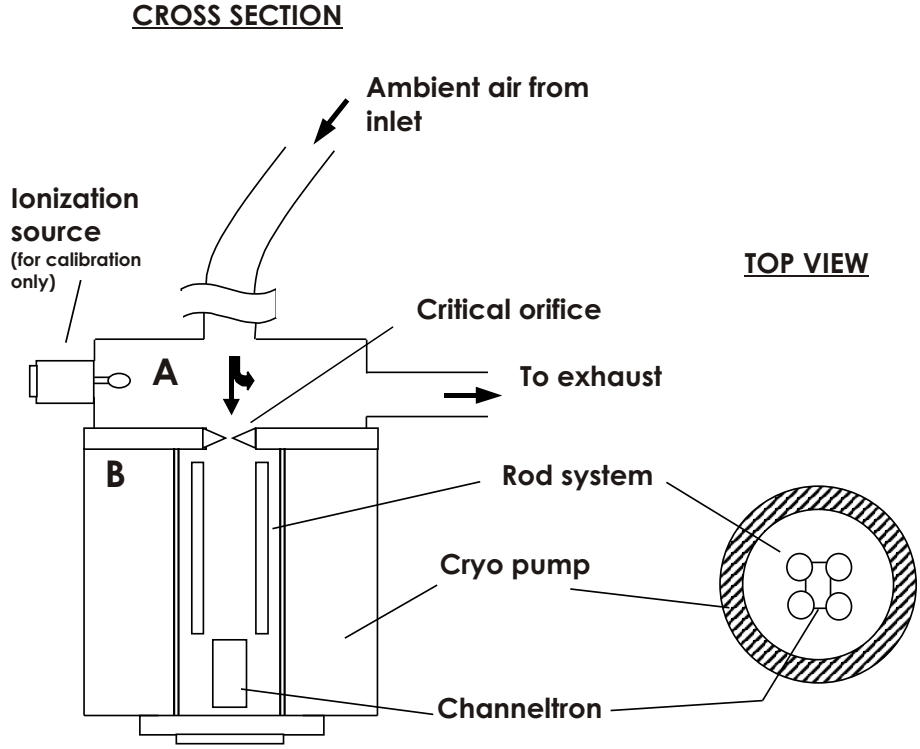

Figure 2.1: Setup scheme of the cryogenically pumped quadrupole instrument.

(A) and on the diameter of the critical orifice (diameter 0.15 mm). During experiments, the pressure in A varies depending on flight level from about 200 mbar up to 600 mbar maximum. In B the pressure stays at about 10^{-4}mbar. A higher pressure in A (up to 900 mbar) is possible but leads to a reduced transmission because scattering on He molecules will become a more dominant process [2]. The resulting reduced transmission will decrease the count rate and thus worsen the signal to noise ratio.
The main flow through A and the exhaust is maintained by the impact pressure of ambient air which hits the air inlet mounted outside the aircraft. The inlet is facing towards flight direction. The exhaust pipe extends until it reaches the bottom of the aircraft body where it stretches outside trough the aircraft body. Inlet and exhaust pipes are 40 mm in diameter and made of stainless steel (KF 40). The rod system of the quadrupole mass spectrometer consists of four, axially symmetric molybdenum rods, each with a diameter of 4.8 mm. The oscillator frequency amounts to 1.4 MHz with a ramp voltage varying between 0 and 2.5 kV. The total length of each rod is about 15

[2] In order to accommodate for that, the diameter of the orifice should be variable.

cm. That results in a theoretical total mass range of 1681 amu[3]. The exhaust pipe of the setup carries an anemometer, a temperature and a pressure sensor. The instrument has to be newly implemented before each flight. This is because the cryo pump can only be filled with liquid neon outside the aircraft. Additionally the cylindrical cryo pump cage has to be heated in between each flight. Accumulated water vapor at the inner walls of the cryo pump from several flights will otherwise lead to an insulation layer (ice surface) which reduces heat transport and thus decreases the cryo pump efficiency. A detailed description of the cryo pump technology in our group is given by [Krieger, 1988].

2.1.2 Ion Optics

The ion optics of the used quadrupole instrument is rather simple as one can see already from the schematics. The molecules, neutral and charged, enter the quadrupole by passing through a pinhole (critical orifice). The pinhole is grounded relative to the quadrupole rods which are set to a potential of a few hundred millivolts. Due to the large pressure gradient between the two compartments (A, B in **figure 2.1**), molecules passing through the pinhole will frequently collide[4] with each other. In the early section of the hereby formed molecular beam, random thermal motion is converted into translational motion. As the gas moves out from the pinhole, it expands and as it does so it cools. The expansion is adiabatic thus no energy is lost and also the number of collisions will reduce. The average velocity remains the same. However, the distribution of velocities is narrowed because temperature has fallen which corresponds to random motion [Pilling and P.W.Seakins, 1995]. The charged molecules will experience now the electric field which is applied between the pinhole and the quadrupole rods. They will be focused towards the quadrupole acceptance field if mass to charge ratio and field acceleration suit transmission confinements. Otherwise, if the acceleration by the applied electric field results in a too strong velocity component the molecules will end up hitting the quadrupole rods. Thus applying the proper field voltage between pinhole and quadrupole is important for optimizing transmission (sensitivity). This problem will be discussed in great detail in **chapter 2.1.5** where both expressions will be defined and derived for the used QMS.

[3]The obtainable maximum mass range can be calculated from:

$$q_{max} = \frac{e}{m} \frac{2V}{r_0^2 2\pi\nu^2} \tag{2.1}$$

with $q_{max} = 0.908$, $\nu = 1.4$ MHz and $V_{max} = 2.5$ kV [Paul et al., 1985], [March, 1997].

[4]This process is responsible for the so-called collision-induced dissociation.

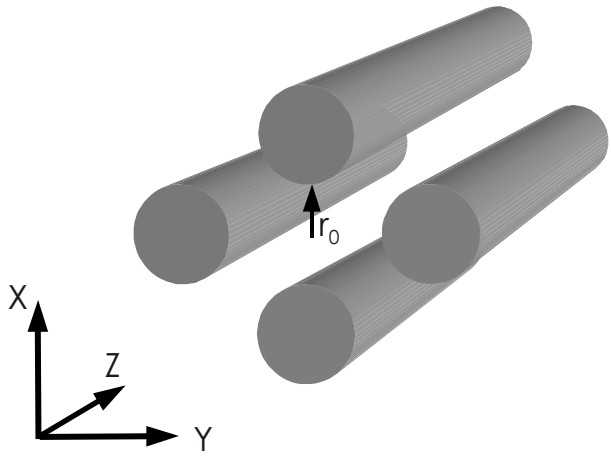

Figure 2.2: Scheme of a quadrupole rod system.

The following section will briefly explain the quadrupole field properties mentioned at the beginning of this chapter in a mathematical way. For a detailed derivation of the given expression the reader is referred to [Ghosh, 1995].
In a quadrupole field the potential Φ in three-dimensional space is given by:

$$\Phi \;=\; \frac{\Phi_0}{2r_0^2}\,(\lambda x^2 \;+\; \sigma y^2 \;+\; \gamma z^2) \tag{2.2}$$

where Φ is an externally applied electric potential; λ, σ, and γ are multiplicative constants depending on the nature of the field. Further only a certain two- dimensional case will be considered, with $\lambda = -\sigma = 1$[5]. With the z-axis being the axis of symmetry, the equation above simplifies to:

$$\Phi(x,y) \;=\; \Phi_0\,\frac{x^2 \;-\; y^2}{2r_0^2} \tag{2.3}$$

This can be realized by a four rod structure with the simplification of round instead of hyperbolically shaped rods (**figure 2.2**).
r_0 denotes the minimal distance of the rod surface to the symmetry axis with a ratio of 1.148 of rod radius r to r_0. The shown rod system can be used as a mass filter, if Φ_0 will be chosen as superposition of an AC and a DC voltage:

$$\Phi_0 \;=\; (U \;+\; V\;cos\omega t) \tag{2.4}$$

The equations of motion can be then written as:

$$\overrightarrow{F} \;+\; \overrightarrow{\nabla}\Phi \;=\; 0 \tag{2.5}$$

[5]In three dimensions (i.e. an ion trap field) the formulas are the same.

$$m\ddot{x} + 2e(U + V cos\omega t)\frac{x}{r_0^2} = 0 \tag{2.6}$$

$$m\ddot{y} - 2e(U + V cos\omega t)\frac{y}{r_0^2} = 0 \tag{2.7}$$

$$m\ddot{z} = 0 \tag{2.8}$$

These are uncoupled differential equations which describe independently the motion of an ion with a periodic force acting onto it. By introducing the following substitution:

$$\omega t =: 2\xi \quad \frac{8eU}{Mr_0^2\omega^2} =: a \quad \frac{4eV}{Mr_0^2\omega^2} =: q \tag{2.9}$$

one obtains (with the consideration that $\dot{z} = v_z = 0$) the so called **Matthieu equation** ($u = u(x, y)$):

$$\frac{d^2u}{d\xi^2} + (a_u - 2q_u cos2\xi)u = 0) \tag{2.10}$$

All solutions of the Matthieu equation can be written in general as:

$$u(\xi) = \alpha_1 e^{\mu\xi} \sum_{n=-\infty}^{n=\infty} C_{2n} e^{2in\xi} + \alpha_2 e^{-\mu\xi} \sum_{n=-\infty}^{n=\infty} C_{2n} e^{-2in\xi} \tag{2.11}$$

Here $\mu = \alpha \pm i\beta$. α_1 and α_2 are integration constants whose values depend on the initial conditions of the ions. The constants C_{2n} depend on the values of the parameters a and q. Ion trajectories depend crucially on the operating parameters a and q. However, solutions are not stable for all values of β. The constraints for β are: $\mu = \pm i\beta$ with β being not an integer. If otherwise β is an integer the solutions are periodic but unstable. For example in the a-q diagram shown in **figure 2.3** the lowest region of stability lies between $\beta = 0$ and $\beta = 1$. In the region enclosed by the solid lines the ion trajectories are stable in both the x- and y-directions. If the quadrupole is operated with the parameters a, q chosen for that region, the ions traverse through the electrode structure without being lost.

If operated at other a, q values the ions will be lost and therefore the device acts as a mass filter. In practice one keeps the U/V ratio constant and scans both U and V. A fixed a/q ratio implies a straight line in the stability diagram (operating line). This range of ions which lies in between the intersection of the operating line with the stability region will be passing through. If on the other hand, the slope will be zero by setting U = 0, all ions with q < 0.908 are stable. This is the so called RF-only-mode ($\Phi_0 = V cos\omega t$). The QMS spectrometer described here was always run in this mode. By scanning the RF-amplitude from 0 up to V_{max} ions with increasing mass

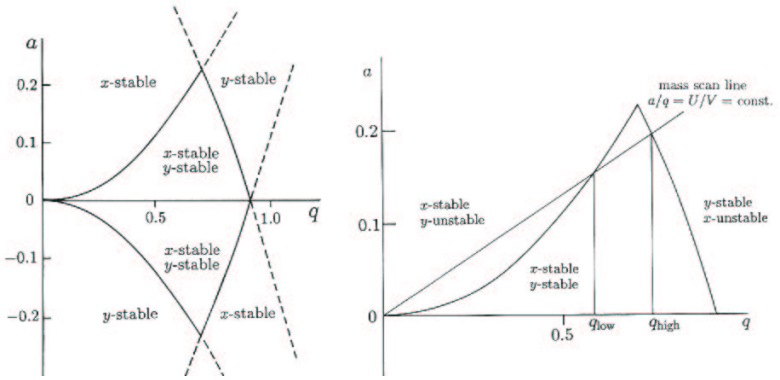

Figure 2.3: The lowest stability region (left) and in more detail with a mass scan line for the ratio U/V = const. (right).

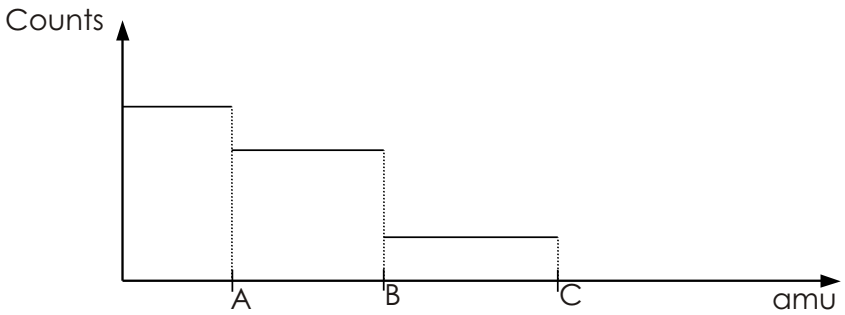

Figure 2.4: Hypothetic high pass mode spectra (RF-only-mode) of an increasing ion mass distribution with only three different groups of masses A,B and C.

will be detected. Thus if one considers a given ion distribution with a certain amount of ions contained in several distinct mass bins, a RF-only-mode spectra would look like a step function (**figure 2.4**). The common line mode spectra can be obtained by differentiating the RF-only-mode spectra.

2.1.3 Ion Detection

After having reached the quadrupole rod system, the ions travel with constant speed ($\overrightarrow{F} = 0$) and will pass mass-selectively the quadrupole field until they exit the rod system. An attractive potential of about 3.5 kV (positive ions), 2.5 kV (negative ions) respectively, then guides the passed ions into a channeltron (Galileo Electro-Optics Corp.). A channeltron is an electron multiplier and is operated in pulse mode for the present setup. Once an ion hits the interior surface layer of the channeltron, electrons

of that layer are released by the impact and become accelerated in a high-voltage field. They in turn produce secondary electrons by impact as well. A cascade of up to 10^8 electrons evolves which at the end of the channeltron will generate a voltage pulse. This voltage is read by a pulse-counting electronics [Gollinger, 1993]. The following two **figures 2.5** and **2.6** illustrate the described context.

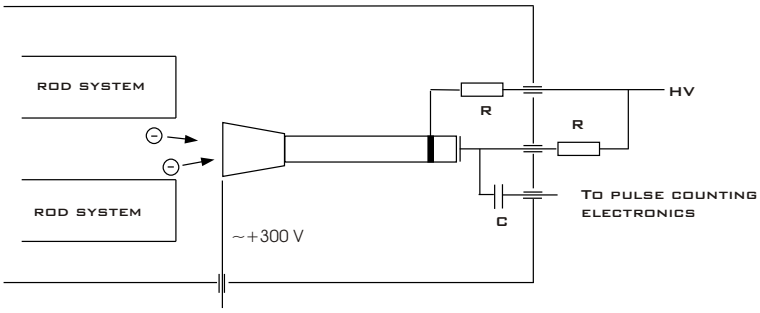

Figure 2.5: In-axis mounted channeltron as it is used in the quadrupole mass spectrometer.

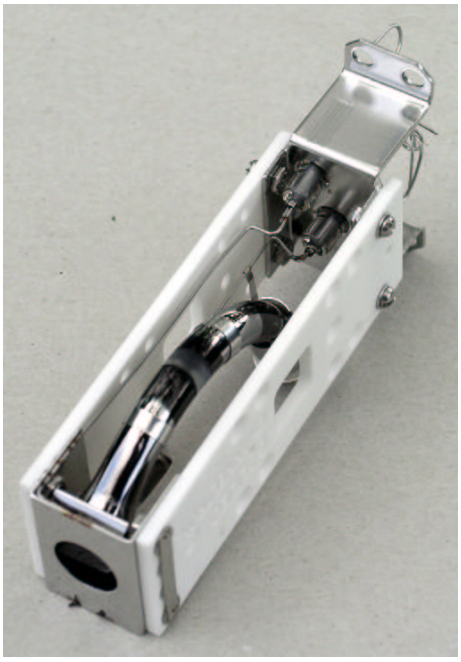

Figure 2.6: Photography of a channeltron as it is used in the QMS instrument.

2.1.4 Calibration

The theoretical mass range of the QMS instrument was calculated to 1681 amu. Thus for proper calibration molecules of high molecular weight are necessary. The previously used [Wilhelm, 2003] mass calibration with Kr (83 amu) and Xe (131 amu) was applied and improved such that Kr and Xe gas were injected in parallel into compartment A of the instrument (**figure 2.1**). Xe and Kr become ionized by electron impact. The necessary fast electrons are produced by the source mounted sideways of compartment A. The obtained high pass mode spectra are shown in **figure 2.7**, with and without a gas flow of Kr and Xe. Also the via differentiation gained line mode spectra are shown. Kr and Xe peaks are detected at channel 227 ± 40 and 341 ± 40, respectively. The peak position was calculated by Gauss fitting the peaks of the line mode spectra.

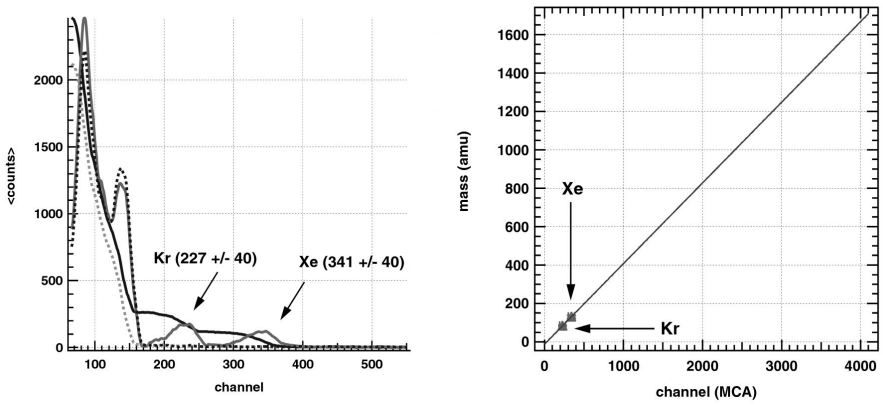

Figure 2.7: Experimental mass calibration with Xe and Kr as standard gas. High pass mode spectra and line mode spectra (differentiated high pass spectra) with and without the two standards. Calibration was derived by Gauss fitting the Xe and Kr peak.

Since 4096 channels are available (multi channel analyzer card)[6] one obtains a calibration factor of 0.42 *amu/channel* with an offset of -13 amu. The shown two-point calibration line illustrates that the calibration is very sensitive to errors in the Kr, Xe channel positions. Considering the error in the channel positions of Kr, Xe, respectively, the slope of the calibration curve varies by ± 0.05 amu/channel, that in turm causes a constant relative mass inaccuracy of $\Delta m/m = 0.1$. It is important to mention that this inaccuracy is different from a mass resolution derived by the gaussian shape

[6]In case analysis is performed with a PCM (pulse code modulation) decoding system, 5200 channels are available. For further detail concerning the PCM system see [Aufmhoff, 2004].

of a single peak. It arises from the calibration with only two species of a known mass, Kr and Xe. The derived inaccuracy will be later used as parameter b to fit the recorded cumulative distributions.
An option to a more precise calibration tool would be the use of an electrospray ionization source, similar to the one used to calibrate the IT-CIMS instrument (**chapter 2.2.4**). The method offers a vast variety of different molecules with high molecular weight.

2.1.5 Ion Transmission and Ion Sensitivity

The sensitivity S of a quadrupole mass spectrometer can be defined as the ratio of the ion count rate at the channeltron (cps = counts per second) to the atmospheric ion density n_i before the spectrometer interior, separated by a critical orifice (compartement A, figure 2.1).

$$S \;=\; \frac{cps}{n_i} \tag{2.12}$$

Total transmission T of the QMS instrument equals the ratio of detected ions to those passing the critical orifice.

$$T \;=\; \frac{cps}{\Phi_i} \tag{2.13}$$

The ion flow into the spectrometer depends on the conductance L of the orifice and can be written as:

$$\Phi_i \;=\; L\; n_i \;\sim\; d^2\; n_i \tag{2.14}$$

The total transmission also critically depends on mechanical and electronic uncertainties as well as on the decoupling of the ions out of the gas jet which in turn depends on the applied axial voltage between orifice and rod system. This optimum voltage will be experimentally derived in the following. Therefore the sensitivity will be plotted as a function of outer pressure p_0, varied between 200 to 900 mbar and axial voltage V_{axis}. Later the gas jet density behind the orifice will be calculated and used to derive the gas kinetic transmission.
To that purpose the ion density n_{i0} was experimentally defined first. The spectrometer was used with sampling line and exhaust tube as implemented into the research aircraft (inlet and exhaust tubing made out of KF 40 pieces) and additionally a radioactive ^{210}Po source served to produce a certain amount of ions (**chapter 2.3.3**). The activity of the compound was calculated to be 22 MBq (A_0 = 92.9 MBq Dec 2002, t_H = 138.4 days, personal communication Dr. G. Heusser). The energy per α quantum amounts to 5.4 MeV and thus, with an average ionization energy in air of 35 eV, about $1.5 \cdot 10^5$ ions will be produced per α particle. 22 M decays/second lead to a total production

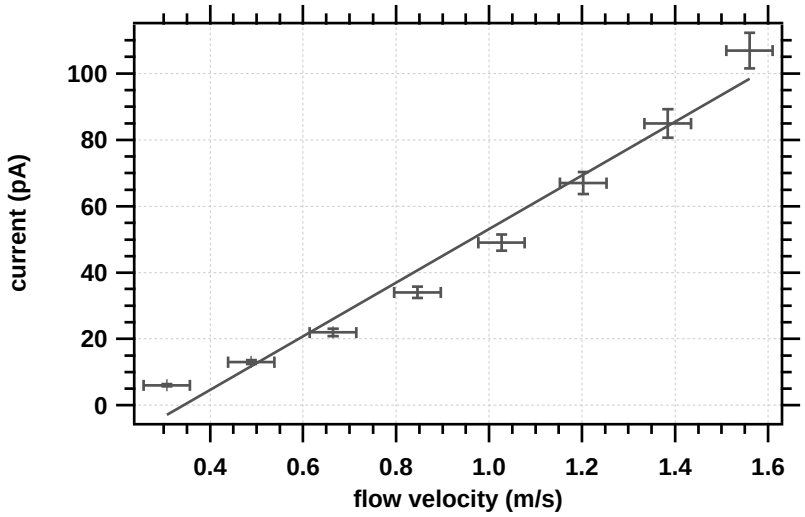

Figure 2.8: Electrostatic probe current as function of flow velocity. The theoretical predicted linearity does not hold mainly due to ion recombination.

rate of $3.3 \cdot 10^{12}$ ions per second.
Two types of experiments were performed. During the first experiment a Gerdien probe (also called electrostatic probe) [7] measured the ion current at about 200 cm away from the radioactive source. A voltage of 250 V was applied to the capacitor. Pressure p_0 was kept constant at 550 mbar whereas gas velocity changed from 0.3 - 1.6 m/s [8]. **Figure 2.8** shows measured current versus flow velocity. The slope of the curve gives the ion density n_i. Theory predicts a linear relation between current I and the velocity $\overrightarrow{v}$ of a moving area A, which carries a certain charge density n_i e:

$$< I > = < v > \; n_i \; A \; e \tag{2.15}$$

The recombination of ions is so far not considered and is the main reason why linearity is not conserved. During the second type of experiment, the pressure p_0 changed between 200 and 900 mbar while the velocity remained constant at 1 m/s. Thus the Gerdien current was measured at two different distances of 25 cm and 200 cm from the radioactive source. The time for ions to recombine changed in both experiments. In the first experiment as function of gas velocity, in the second experiment as function

[7] A Gerdien probe is a radially symmetric cylinder capacitor (r_a = 20 mm, r_i = 3 mm). Charged air molecules sucked into the cylinder are guided by an electric field to the central electrode and thus cause a small ion current, normally in the range of pA. A relation exists between charge, mobility and mass [Tammet., 1995].

[8] The applied voltage is high enough to detect all ions at 1.6 m/s with a Gerdien length of 25 cm.

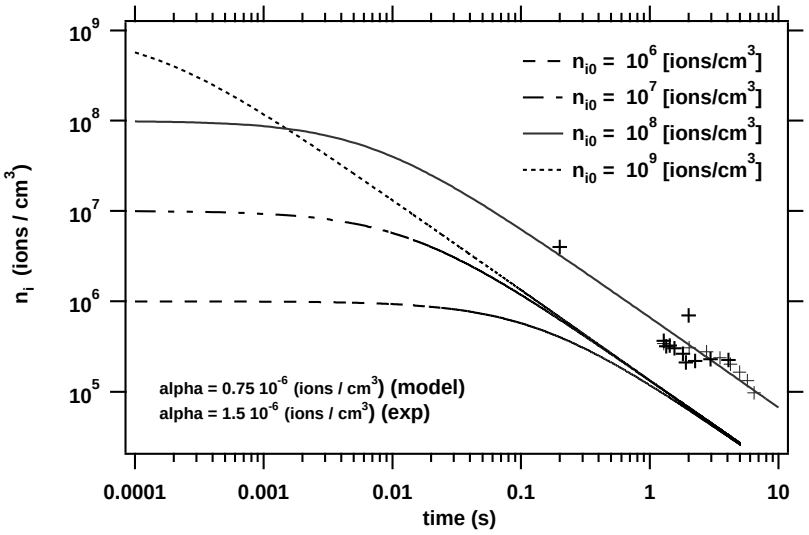

Figure 2.9: Ion density n_i experimentally derived and validated with an ion recombination model. From fitting the model to the experimentally obtained data points n_i resulted to 10^8 ions / cm^3 and the ion recombination coefficient α to 1.5 10^6 cm^3 s^{-1}.

of distance to the ion source. To better evaluate the data a basic ion recombination model was taken into account. It is based on the following reaction:

$$A^+ + B^- + M \rightarrow AB + M \tag{2.16}$$

With the assumption that $[A^+] = [B^-]$ (which is experimentally approved) an equation for n_i can be derived:

$$n_i(t) = \frac{1}{\alpha\, t + \frac{1}{n_{i0}}} \tag{2.17}$$

With four different initial ion densities n_{i0} and an ion recombination coefficient of $\alpha = 0.75 \cdot 10^{-6}$ cm^3 s^{-1} **equation 2.17** is fit to the experimental data set. The fit converged for $\alpha = 1.5 \cdot 10^{-6}$ cm^3 s^{-1} and $n_{i0} = 10^8$ ions/cm^3. This value for n_{i0} is four orders in magnitude smaller than the initial value calculated from the radioactive compound (10^{12} ions / cm^3). The reason might be that the range of α particles in air at 1000 mbar is about 3.9 cm (R = 0.3 $E^{3/2}$). Since α particles release the most energy at the end (Bethe-Bloch-Formula) and the source is centered within a tube of 40 mm in diameter a certain fraction of α particles will simply hit the wall. **Figure 2.9** shows the derived ion densities $n_i(t)$ obtained for two different positions of the capacitor relative to the radioactive source. Further the sensitivity was calculated as function of pressure p_0 and axial voltage V_{axis} that is the voltage between rods and orifice. In another set of experiments V_{axis} was varied in steps of 0.2 V from -10 to 1.4 V for negative, -5 to 2.0

V for positive ions, respectively. More positive (negative) voltages in each case did not change the count rates significantly. Pressure p_0 was varied between 200 to 900 mbar. For analysis the count rates were converted to cps (counts per second) by dividing them by dwell time (780 μs) times 4096 channels and the number of sweeps (10). With the above destined ion density $n_{i0} = 10^8$ ions/cm^3 and the recombination coefficient $\alpha = 10^{-6}$ cm^3 s^{-1}, $n_{i(t)}$ was calculated for the used experimental setup. It resulted in $n_i = 10^6$ ions/cm^3 considering a distance between radioactive compound and orifice of 62 cm. This value was then taken to calculate the sensitivity S. The **figures 2.10, 2.11, 2.12** and **2.13** and show S(V_{axis}, p_0). The sensitivity for negative ions increases up to 0.18 (cps/(cm^{-3}) at $p_0 \sim 400$ mbar and $V_{axis} = 0.4$ V. The maximum in S is not very pronounced within the 400 mbar region as long as V_{axis} stays below +0.5 V. At -10 V (not shown in the graphs) S reaches values of about 0.05. To more positive voltages (above 0.5 V) S steeply reduces to about 0.04. Pressure dependency nearly vanishes within +0.6 to +1 V. In order to achieve highest sensitivity (transmission) with simultaneously low pressure dependency the axial voltage was set to +0.6 V. Then sensitivity remains constant at about 0.1 (cps/(cm^{-3})). In total between ± 1 V and p_0 = constant, S changes by up to a factor of 2. For V_{axis} smaller than 0.5 V and p_0 changing between 200 and 900 mbar S varies by up to a factor of 3.
Sensitivity for positive ions increases up to 0.32 (cps/(cm^{-3})) at p_0 = 300 mbar and V_{axis} = -1.0 V. The maximum in S is pronounced around that voltage with p_0 varying between 200 and 400 mbar. The pressure dependency in S is minimal only in the small voltage range between -0.7 to -1.0 . Thus V_{axis} is set to -1.2 V. To more negative axial voltages the sensitivity decreases and the same happens as axial voltage increases above -0.5 V. Keeping p_0 constant S varies by a factor of 2 as it does in equal measure with V_{axis} constant and p_0 varying.
Thus sensitivity shows for positive and negative ions a diverse strong coupling on alternating axial voltages or pressure. The overall discrepancy in S for negative and positive ions by about a factor of 5 is caused by the channeltron voltages[9] which simply lead to a higher sensitivity for negative ions. The total range of S is much smaller as it is in pressure regimes where the ions would earlier decouple (below p_0 = 100 mbar, $\lambda > 1$) but was not of interest for the present instrument, since measurements below 12 km should be performed.

[9]The channeltron is relativ to ground at a positive potential of about 300 V.

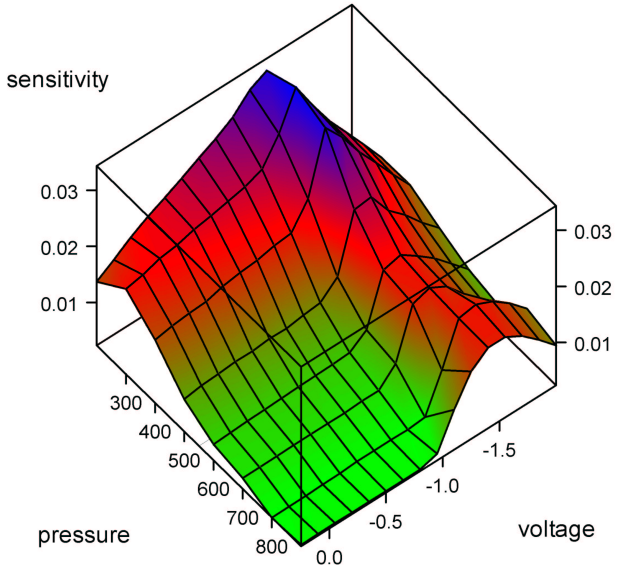

Figure 2.10: Sensitivity S (cps / cm^3) of the QMS instrument for positive ions as function of pressure and axial voltage.

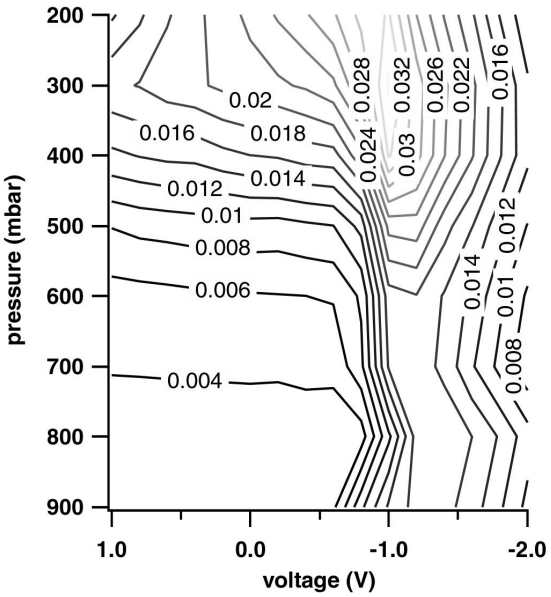

Figure 2.11: Contour plot of the derived sensitivity for positive ions. For further details see text.

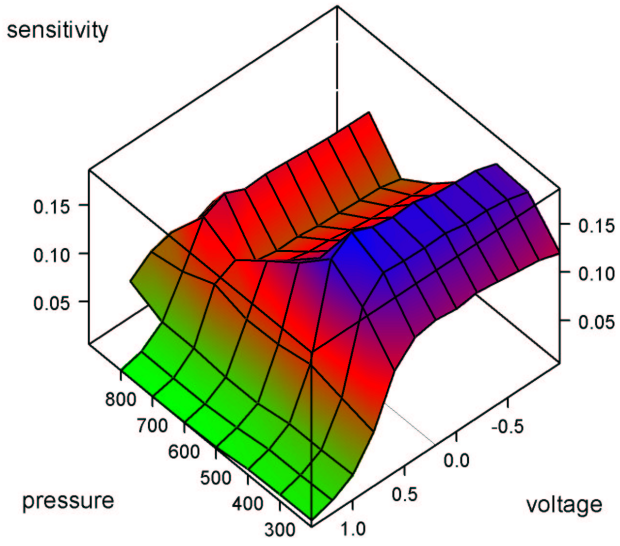

Figure 2.12: Sensitivity S (cps / (ions/cm^3)) of the QMS instrument for negative ions as function of pressure and axial voltage.

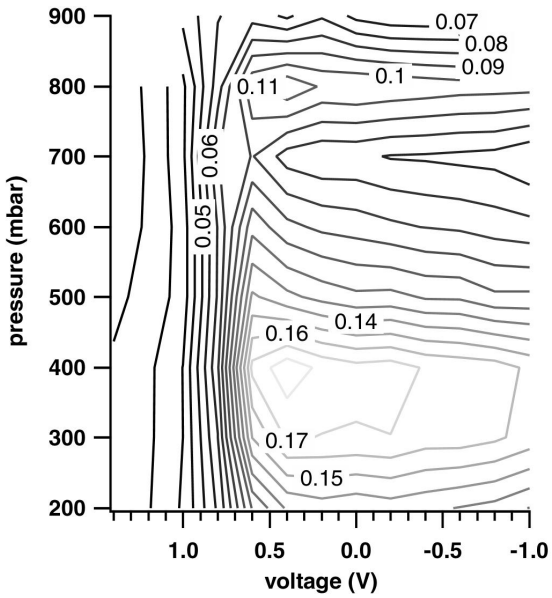

Figure 2.13: Contour plot of the derived sensitivity for negative ions. For further details see text.

To gain a better understanding of how sensitivity (transmission) is influenced by the high pressure p_0 in front of the critical orifice, the gas jet density ρ and the mean free path λ as a function of the axial distance z are calculated. Finally transmission is shown as the function of p_0 with V_{axis} as parameter. The plots will only be shown for negative ions. This is no limitation since both ion types obey the same physical laws. Ions will become decoupled from the gas jet by the axial field voltage V_{axis}. Decoupling occurs already briefly behind the inlet orifice, when the ion drift velocity due to the applied electric field becomes larger than the ion initial velocity. They will gain kinetic energy which may lead to dissociation of ion clusters when colliding with neutral gas molecules. The pressure inside the spectrometer can be written as

$$p \;=\; p_0 \; 0.0343 \; (d/z)^{2.8} \;+\; p_{qms} \tag{2.18}$$

[Ashkenas and F.Sherman, 1966] where d = critical orifice diameter, z = axial distance away from the orifice and p_{qms} = pressure inside the spectrometer. This formula takes the high jet pressure directly behind the orifice into account which rapidly decreases to a background of p_{qms}[10]. Collision frequency and mean free path depend on the density distribution within the gas jet ρ = p/(kT). Therefore also the energy exchanged by collision of ion clusters with neutral gas molecules depends on ρ. **Figure 2.14** shows the measured pressure inside the spectrometer as function of p_0. The calculated mean free path λ and ρ are plotted in **figures 2.15** and **2.16**.

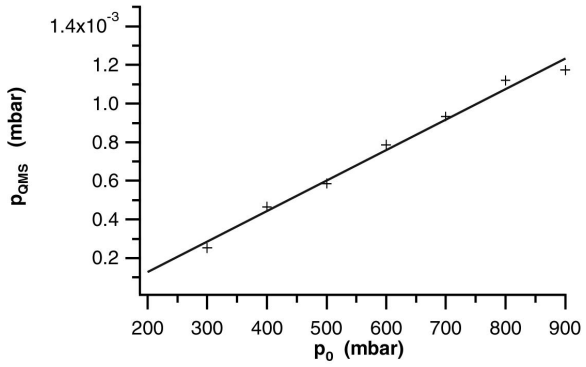

Figure 2.14: Pressure measured inside the QMS instrument by use of a getter pump as function of pressure in front of the entrance orifice.

[10]This background gas pressure is mainly caused by helium molecules since the cryo pump does not pump helium.

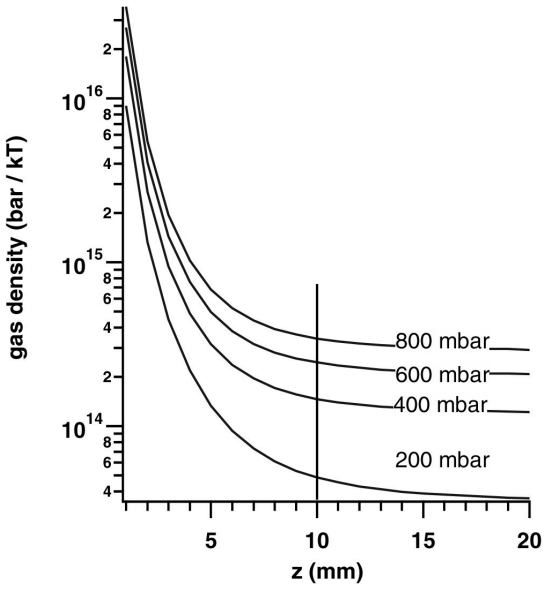

Figure 2.15: Density distribution of molecules in the QMS instrument as function of the axial distance from the critical orifice.

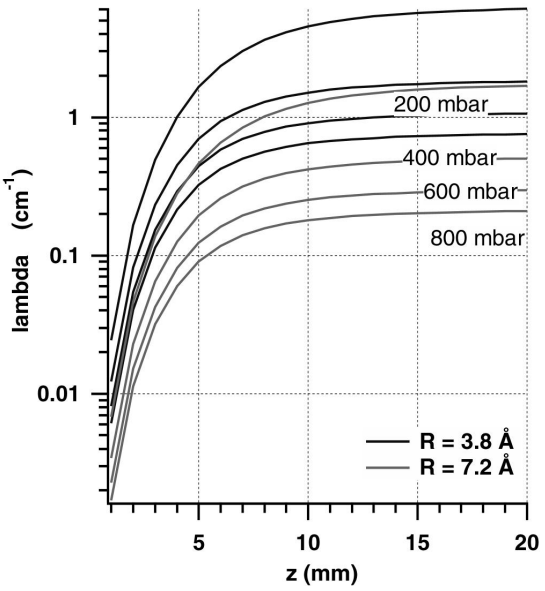

Figure 2.16: Derived molecular mean free path λ from the measured pressure inside the spectrometer and the calculated density distribution. For further details see text.

From **figure 2.14** a linear relation appears between spectrometer pressure p_{QMS} and p_0. The pressure sensor, a so-called Getter pump, actually measures a current and is thus proportional to the gas density. Since the sensor is mounted behind the channeltron, only a background pressure and no pressure gradient is detected. The calculated density ρ as function of axial distance z is plotted for three different values of p_0 (**figure 2.15**). Apparently the density varies by two orders of magnitude behind the orifice and already reaches the background of p_0 for z > 10 mm. The vertical line denotes the position of the rod system. The derived mean free path λ in **figure 2.16** refers to a decoupling of the neutral gas molecules. λ is calculated for two different molecule diameters (R = 3.8 and 7.2 $\mathring{A}$ [11]) and for a p_0 of 200, 400, 600 and 800 mbar. It appears that for 200 amu and z > 10 mm λ is around 1. In other words one collision occurs within the mean free path. By assuming that the ions during at least half λ move collision free, the kinetic energy can be estimated to:

$$E_{kin} \;=\; e\,E\,\frac{\lambda}{2}\frac{m_2}{m_1+m_2} \tag{2.19}$$

Figure 2.17 shows the kinetic energy for a single collision of small ions (200 amu) with air molecules (m = 30 amu) at p_0 = 200 mbar.

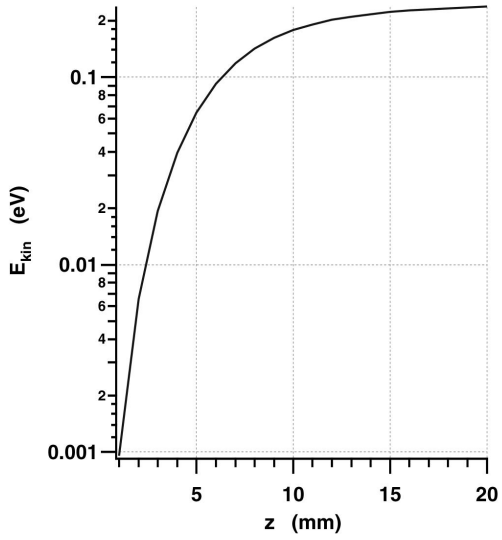

Figure 2.17: Kinetic energy of a charged cluster (200 amu) with an air molecule (30 amu) at 200 mbar in front of the spectrometer

.

[11]This corresponds to 200 and 1300 amu taking a $H_2SO_4(H_2O)$ cluster with a 60%" fraction of H_2SO_4 molecules into account and thus a mass density of 1.4 10^3 kg/m^3.

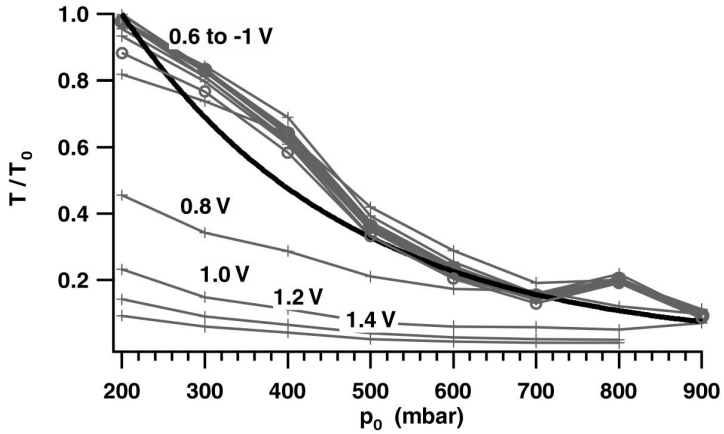

Figure 2.18: Normalized transmission T/T_0 of the QMS instrument as function of pressure. Parameterized by the axial voltage. Black line results from theory.

Typical binding energies of cluster ions are ~ 0.5 eV [Glebe, 1994]. Thus no dissociation should occur before the ions will enter the quadrupole.
Finally, transmission is related to σ and ρ by

$$T/T_0 \;=\; exp(-\sigma\ L\ \rho_{QMS}) \tag{2.20}$$

where σ = scattering cross section, L = spectrometer length (L = 10 cm) and n_{QMS} the already calculated number density. For σ[12] the geometric cross-section πr^2 is chosen. **Figure 2.18** shows the normalized transmission parameterized by the axial voltage used in the experiment, calculated from the above equation with molecular radius of = 5 Å. **Equation 2.20** actually differs from the earlier defined transmission where T = cps/Φ_i. The first formula considers the transmission of charged clusters in terms of a "netto" equation (amount of detected to introduced ions). The second formula refers to a gas kinetic approach, where transmission is basically determined by collisions between the molecules. Experimental data suggest in accordance to theory an increasing transmission of the QMS instrument with decreasing pressure. The proposed exponential increase from the theoretical curve in T/T_0 for p_0 being below 400 mbar is not reflected in the experimentally derived transmission. Moreover is the observed pressure dependence diverse and also voltage dependent. Good accordance can be seen for p_0

[12] σ is given explicitly by

$$\sigma = \pi r^2 |1 \;-\; \frac{V_p(r)}{\mu v^2/2}| \tag{2.21}$$

with the polarization potential $V_p = -e^2\alpha\ /\ 2r^4$.

being larger than 500 mbar.
Axial voltages oppositely charged to the charge of the ions systematically shift the transmission to lower values, as expected. Theory fits best to axial voltages ranging from 0.6 to -1 V for negative ions. Voltages between 0.8 to 1.4 V show an increase in transmission with increasing pressure but not as strong as proposed by theory. Voltages ranging from 0.6 to -1 V in show a lower, non-exponential behavior as if converging against a certain T/T_0 ratio.
The diverse dependence probably results from a stronger decoupling tendency of the ions when experiencing a higher field force by a more attractive axial potential. On the other hand in case of lower field forces decoupling is less effective and interacting collisions reduce the probability for the ions to enter the quadrupole acceptance field. This effect of course depends on the ion mass and therefore is much more pronounced in case of clusters of low molecular weight.
Additionally it is important to mention though, that the derived experimental transmission is based on a total count rate over all masses. Since the theoretically derived transmission only considers an average mass of 450 the experimentally derived transmission must deviate. This apparently does not reflect a mass dependence of the observed transmission but leads to the deviations in the low pressure regime.

2.2 Ion Trap Mass Spectrometer (ITMS)

2.2.1 Instrumental Schematics and Layout

Figure 2.19 shows the setup of the Ion Trap Mass Spectrometer (ITMS) used in the present work. The instrument was commercially purchased with an electrospray unit (Finnigan LCQ, Finnigan Company, USA). The electrospray unit was removed and substituted by a stainless steel adapter to fit a tubing 40 mm in diameter. The originally mounted skimmer in front of the first octapole was substituted by a sampling electrode with an inlet hole 0.015 cm in diameter (**figure 2.20**).
Ions from the flow reactor are guided onto the sampling electrode through the pre-chamber ($p = 70$ mbar) via a cone shaped tubing with an opening of about 10 mm in front of the sampling electrode (**figure 2.20**). The main buffer gas stream leaves the pre-chamber via the exhaust tube (**appendix C.1**), where temperature is determined and buffer gas humidity is measured with a capacity sensor. The flow reactor consists of stainless steel tubes, 40 mm in diameter (KF 40). The distance from the ion source (DIC) to the sampling electrode is about 30 cm. Ions travel with approximately 1.7 m/s and thus reach the sampling electrode after a reaction time of 0.16 s. This time is

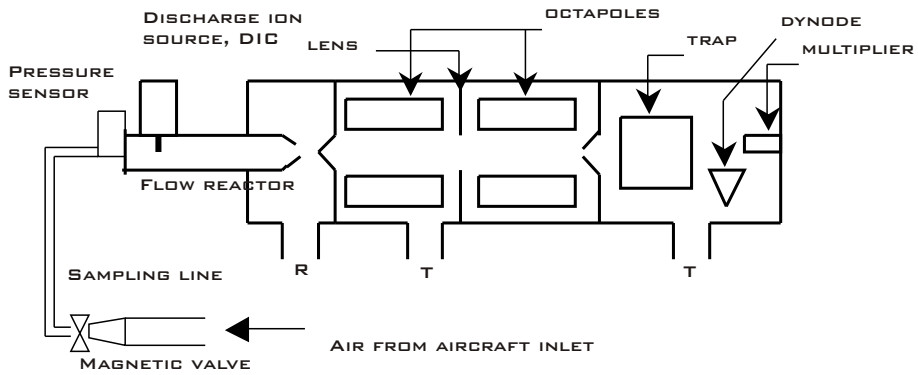

Figure 2.19: Instrumental setup of the IT-CIMS as it is used on board of the research aircraft FALCON (DLR).

kept constant by a pressure sensor at the entrance of the flow reactor (Flow controller M4203692A, serial EL-Press, Bronkhorst company, Netherlands) and a critical orifice ($\emptyset = 4mm$) before the rotary pump (R, **figure 2.19**, rotary pump 28 V DC, 25 m^3/h end pressure $5 \cdot 10^{-3}$ mbar). The total flow is experimentally derived to be 8.75 slpm $\pm$ 1.8 %, assuming a temperature of 30 °C. The oxygen flow is 0.37 slpm controlled by a 1 liter mass flow controller (MFC) (Bronkhorst, Netherlands). The isotopic flow of $^{34}SO_2$ is 8.48 smlpm $\pm$ 1.2 %, controlled by a 20 smlpm MFC (Bronkhorst, Netherlands).
The manifod of the IT-CIMS comprises the ion optics, the ion trap and the detection unit and is illustrated in **figure 2.20.** It comprises two pumping stages. In the first pumping stage which is the first octapole region, the pressure is about 10^{-3} Torr (pumping rate 125 l/sec). The analyzer region is evacuated down to $2 \cdot 10^{-5}$ Torr at a rate of 200 l/sec. The analyzer region comprises the second octapole, the ion trap, the conversion dynode and the multiplier . A split flow turbo-molecular pump (Balzers Pfeiffer TMH 260/130) provides the vacuum for both compartments. The turbo-molecular pump is backed by a dry membrane pump (MZ D4 Vacuum Brand, modified to 28 V).
Ambient air enters the aircraft through an inlet which points along the airstream outside of the aircraft **(see appendix C.1)**. The pressure controlled magnetic valve shown in **figure 2.21** follows. It is the main component which controls the total gas stream entering the measurement unit and keeps the pressure inside the flow reactor at constant 70 mbar, while outside pressure changes with altitude. To this purpose a pressure sensor feedback operates onto the magnetic valve. Isotopic sulfur dioxide is released by a small pipe right in front of the valve. A steady flow of the isotopic gas mixes with the ambient air stream which is sucked through the valve. One has to

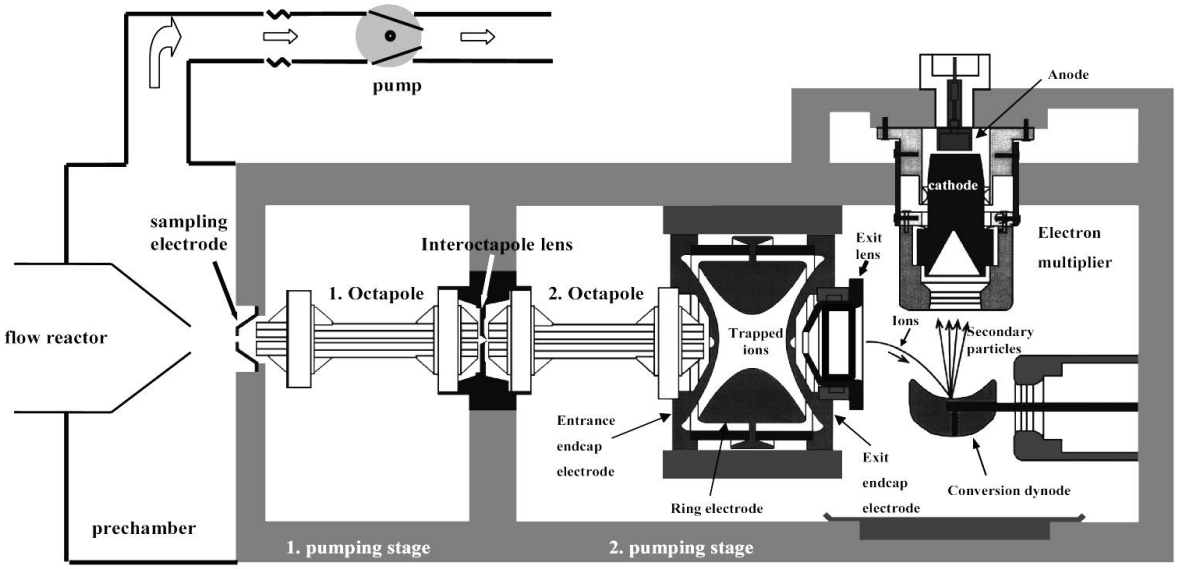

Figure 2.20: Cross section of the ion trap mass spectrometer. The manifold (gray) comprises the ion optics, the ion trap and the detection unit (conversion dynode plus multiplier). It is separated into two pumping stages.

assume that all $^{34}SO_2$ molecules emitted by a the MFC become transported into the tubing. This assumption is necessary, since pressure before the valve is not constant. However the number of isotope molecules remain constant due to the properties of the MFC. Thus, if all molecules pass through the valve, the calibration gas mixing ratio in the flow reactor remains constant no matter how pressure in front of the valve changes with altitude.

Atmospheric and isotopically marked SO_2 concentrations experience the same wall losses at the sampling line, the same temperature gradient, velocity and water vapor mixing. Thus the chemical reactions with the educt ions take place under the same conditions.

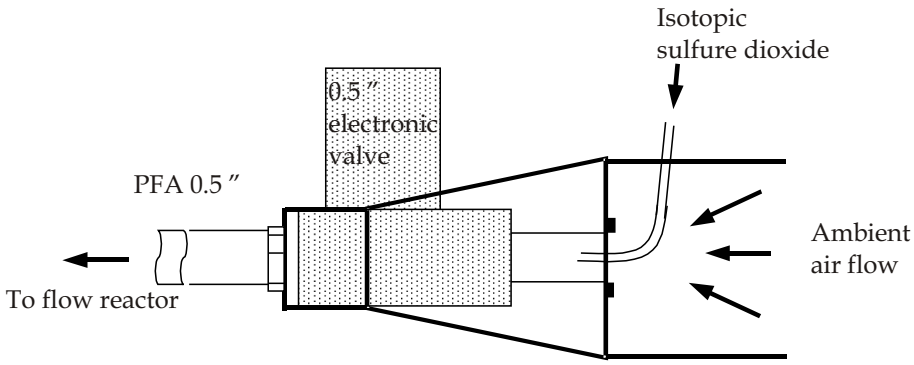

Figure 2.21: Magnetic valve which is controlled by the pressure sensor of the flow reactor to keep $p_{reactor}$ at 70 mbar. The isotopic standard is released directly in front of the electronic valve. The valve is embedded into an aluminium housing, which funnel-like reduces its diameter from KF 40 mm to 0.5″.

The whole setup is especially designed for aircraft use. Thus weight and required space are as minimized as possible.

2.2.2 Ion Storage and Detection in a Trap

The advantage to use an ion trap compared to a normal quadrupole rod system rises amongst others from the possibility to perform fragmentation studies of cluster ions [Kiendler, 1999]. Detection limits (between 15-4000 amu) are larger in comparison to a quadrupole spectrometer, including high-resolution (no mass discrimination) mass spectra. A detailed description of the ion trap technology is given in [March, 1997] and more briefly in [Aufmhoff, 2004]. Here only a short introduction will be given necessary for better understanding the present work.
The principle difference underlying the use of a rod system or an ion trap is the three-dimensional quadrupole field instead of a two dimensional as it is used by the rod array. The trap consists of two radially symmetric end caps facing against each other and a ring electrode which is mounted perpendicularly to the symmetry axis of the two end cap electrodes (**figure 2.22**). The inner surfaces of the electrodes are hyperbolic. The inner radius of the ring electrode is $r_0 = 0.707$ cm and the separation of the two end cap electrodes measured along the axis of the ion trap is $2 \cdot z_0 = 1.57$ cm. Both end cap electrodes have a small hole in their centers to allow ions to penetrate into and out of the mass analyzer cavity. The ions are injected by a voltage pulse into the trap, by an electronic gate which will be only open during a short period of time, the so called injection time. The gating procedure is performed by applying a short voltage

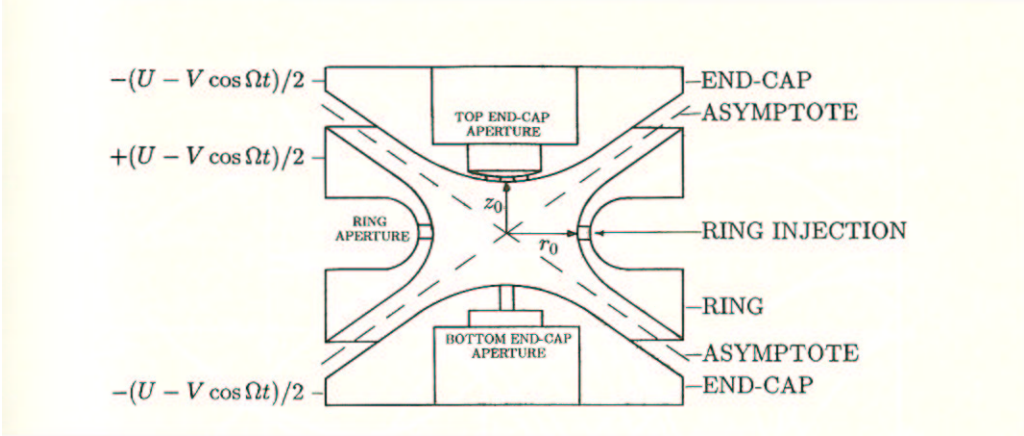

Figure 2.22: Schematic drawing of the Paul Ion Trap as it is used in the mass spectrometer. The trap comprises two end-cap electrodes facing against each other separated by a ring electrode. Applied voltages and polarities are indicated

.

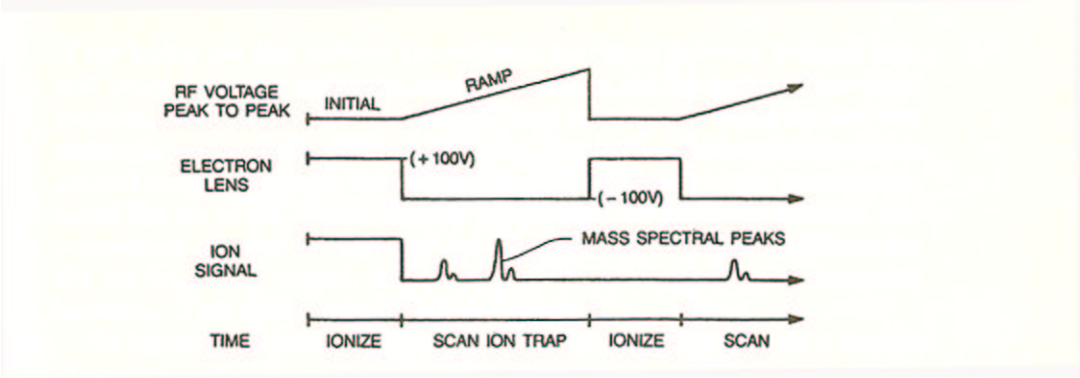

Figure 2.23: Timing diagram for obtaining mass spectra trough mass selective instabilities. (picture taken from Ghosh [1995])

pulse of ±10 V onto the interoctapole lens (see next chapter). The instrument can be run in an automatic gain-control mode. This offers the possibility to always fill the trap with the same amount of ions by automatically adjusting the injection time. To define the necessary injection time, the instrument will perform a pre-scan by which the time to achieve the desired count rate is estimated from the actual ion count rate. In the present work, the instrument was always run in the automatic gain control mode. **Figure (2.23)** shows schematically the applied voltage algorithm to detect ions. The algorithm comprises injection and read out of ions. Upon injection trapped

ions are collisionally cooled by He atoms confining them closer to the trap center and thus increasing the efficiency of trapping. He damping gas enters the mass analyser cavity at a continuous flow of about 1 ml/min trough a nipple on the exit end-cap electrode. The partial pressure of helium in the mass analyzer cavity is maintained at approximately 10^{-3} torr. The cooling of the trapped species by He atoms also leads to collision induced dissociation of trapped ion molecules. This is an important effect and used for fragmentation studies. The kinetic energy of stored ions of a selected mass is increased by resonant excitation via an additional RF voltage applied to the end cap electrodes. This excitation induces energetic collisions of parent ions with He atoms and will lead to internal ion-excitation. Eventually the parent ions will dissociate into fragments. Even without the additional RF voltage at the end caps, dissociation will occur by ion resonance excitation. This phenomena is observed for associated water clusters for instance and will be discussed later in detail. It is thus that hydrated ions are difficult, if possible at all, to measure with the ion trap. As already mentioned the trap generates a quadrupole field which in turn will produce an ideal trapping potential well for the confinement of the ions. The potential well is created by applying an (RF) potential to the ring electrode and grounding the two end-cap electrodes. The RF (radio frequency) voltage of the ring electrode is an AC voltage of constant frequency (0.76 MHz) and of variable amplitude (0 to 8500 V). This voltage produces the three dimensional, rotationally symmetric quadrupole field which drives ionic motion in both axial and radial directions on stable trajectories confined with the mass analyzer. Ions of the selected m/e (mass to charge) ratio can be stored in that field. Scanning is accomplished by changing the RF voltage. This change moves the ions in the stability region to a position where they become unstable in the z-direction and leave the trapping field for detection. The ion detection system comprises a conversion dynode and an electron channel multiplier. The conversion dynode is located off-axis at a right angle to the ion beam. A potential of + 15 kV is applied to the conversion dynode for negative ion detection.

2.2.3 Ion Optics

Behind the sampling electrode in **figure 2.20** the ions are focussed and transmitted by the ion optics. The optics consists of two octapoles separated by an interoctapole lens. The octapoles are an array of cylindrical rods used without any ramp voltage in the so called RF-only-mode (**chapter 2.1.2**). In this case, the octapole acts not as mass filter but as focussing device. The applied RF voltage amounts to 2.45 MHz with 400 V peak to peak. Additionally a DC offset voltage is applied (typically -10 to +

10 V). The sign of the offset voltage switches depending on the charge of the ions to detect. It is positive for negative ions and vice versa. The interoctapole lens assists in the focusing and gating of ions. During ion transmission, i.e. during the ion injection and storage step of mass analysis, a positive potential (max. 10 V) is applied to the interoctapole lens for negative ions. That is to drag the ions into the second octapole by adding a forward directed momentum and to push them towards the mass analyzer region. During gating, the applied potential at the interoctapole lens is set to -300 V. Thus all ions are repelled and prevented from entering the second octapole region.

2.2.4 Calibration

The ion trap instrument is mass calibrated with a solution of caffein (300μ l, 195 amu), a peptide out of 4 different aminoacids (MRFA, 5μl, 524 amu) and Ultramark (2.5 ml, 922 amu) which is a special substance delivered from Finnigan Company. An electrospray ionization unit (Finnigan) serves to inject the liquid into the spectrometer. Parameters are automatically changed during calibration to fit the mass peaks of the injected species.

2.2.5 ITMS Tuning

The instrument can be automatically tuned to a certain mass peak, in order to achieve the highest possible count rates for that very mass. After tuning count rates for the specified mass normally increase by a factor of 10. For the sulfur dioxide measurements discussed later on in this work the instrument was tuned to mass 112 amu which corresponds to the SO_5^- ion.

2.3 Chemical Ionisation Mass Spectrometry (CIMS)

The following chapter will give insight into gas phase kinetics. This chapter is supposed to motivate the method of chemical ionization mass spectroscopy (CIMS). The equilibrium constant for basic association reactions will be derived thermodynamically. The derived expression will later be used to characterize the effective collisional dissociation of water clusters provoked by an ion trap.

2.3.1 Reaction Kinetics

Chemical Ionisation Mass Spectrometry is a technique to efficiently detect trace gases, which are of low concentration in the ambient air. The technique is based upon the reaction of the analyte molecules with artificially produced reactant ions to form a new molecule of known mass and charge. By their charge these molecules are than detected with a mass spectrometer. The process is described by the following equation:

$$A^{\pm} + X \rightarrow B^{\pm} + Y \tag{2.22}$$

The analyte X (trace gas) reacts with an educt ion $A^{\pm}$ carrying either a positive or negative charge to form a product ion $B^{\pm}$ and some neutral molecule Y. The probability of the ion-molecule reaction to take place depends in a simple picture upon the geometrical cross section of the interacting molecules and is practically given by the molecular diameter. Considering a two-body collision, one obtains the following rate coefficient[13]

$$k = \pi d^2 \sqrt{\frac{8 k_B T}{\pi \mu}} e^{-\frac{E_0}{k_B T}} \tag{2.23}$$

where d = sum of molecular radii ($r_A + r_B$), T = Temperature, E_0 = energy barrier and μ = reduced mass. The formula comprises two components. The first is given by the so-called collision frequency factor with which the reactants collide. This factor refers to the Maxwell velocity distribution of the colliding molecules. The second component comprises an expression which determines the fraction of collisions which have enough energy to overcome the barrier to reaction. The energy barrier arises from the rearrangement of valence electrons. Collision theory considers the molecules as hard spheres, structureless and without any interaction until they come in contact. It is also possible to derive a temperature dependence of the rate coefficient. Also theory does not consider shielding effects of the reaction sites by neighbored molecules. A more detailed but complex description is obtained by the transition state theory (TST). Here the transition state is the highest energy point and the reactants at this configuration are known as an activated complex. For an atom and a diatomic molecule the reaction would look like the following:

$$A + BC \rightarrow X^{\ddagger} \rightarrow AB + C \tag{2.24}$$

[13] the rate coefficient can be seen as $k = \rho / \mathcal{N}_{\mathcal{A}} \mathcal{N}_{\mathcal{B}}$, where ρ = number of collisions and $\mathcal{N}_{\mathcal{A}}$, $\mathcal{N}_{\mathcal{B}}$ = number of colliding molecules of type A, B respectively. The maximum possible value of the rate coefficient of a bimolecular reaction is achieved if every molecular collision between molecules of A and B results in reaction. This is called the gas kinetic collision rate which at room temperature is about $2 \cdot 10^{-10}$ cm^3 s^{-1}.

where $H^{\ddagger}$ labels the activated complex. TST examines a reaction from an equilibrium, or really a statistical aspect, in contrast to the dynamic, collision-oriented point of view given before. In the present work molecular processes are sufficiently described by the more illustrative collisional theory and thus TST will not be further discussed. Further information on TST can be found in [Pilling and Seakins, 1995]. More important is the derivation of a formula to calculate the ambient trace gas concentration. From the simple bimolecular reaction, a reaction rate R(t) can be derived. It is defined as the number of molecules or ions which react per unit time.[14]

$$R(t) = -\frac{d[A^{\pm}](t)}{dt} = \frac{d[B^{\pm}](t)}{dt} = -k[X][A^{\pm}] \tag{2.25}$$

R(t) is directly proportional to the concentration of the neutral reactant X and of the ion $A^{\pm}$. The proportionality factor is the rate coefficient k of the bimolecular reaction. Generally k is temperature and pressure dependent. Using the reaction above to derive k, it is assumed that no side reactions occur and that $B^{\pm}$ is the only product ion. Also no backward reaction is considered. The following expression for the concentration of k, X can then be obtained:

$$k = \frac{1}{t_r[X]}\ ln\ \frac{[A^{\pm}]_{t=0}}{[A^{\pm}]_{t=t_r}} \tag{2.26}$$

It follows the time constant τ after which the initial ion concentration decreased by 1/e:

$$\tau = \frac{1}{k[X]} \tag{2.27}$$

The reciprocal of τ is called reaction frequency and a measure of the velocity of the reaction. From **2.26** the trace gas concentration [X] can be derived. Under the assumption that no further loss processes appear,

$$[A^{\pm}]_0 = [A^{\pm}] + [B^{\pm}] = const. \tag{2.28}$$

the trace concentration [X] calculates to:

$$[X] = \frac{1}{kt_r} ln(1 + \frac{[B^{\pm}]_{t_r}}{[A^{\pm}]_{t_r}}) \tag{2.29}$$

assuming that the primary ion $A^{\pm}$ only reacts with the trace gas species X, which is generally not the case. Reactions in parallel can be neglected if the ratio $[B^{\pm}]_{t_r}/[A^{\pm}]_{t_r}$

[14] Ion and molecule concentrations will be in the following denoted by brackets which refers to molecules per cm^3.

is small. Otherwise the following expression for the reaction of the primary ion $A^{\pm}$ with several trace gases $[X]_i$ has to be taken into account:

$$[X]_i = \frac{1}{k_i t_r} \frac{[B_i^{\pm}]}{\Sigma_{j=1}^{n}[B_j^{\pm}]} \; ln \; (1 + \frac{\Sigma_{j=1}^{n}[B_j^{\pm}]}{[A^{\pm}]}) \tag{2.30}$$

This is the so-called **Parallel-ACIMS Formula**, where n refers to the number of different product ions originating from the same reagent ions $A^{\pm}$. The rate coefficient in the formula does differ for any species. A detailed deduction of the above equation is given in [Wollny, 1998].

2.3.2 Association Reactions

Cluster ions are normally formed by a sequence of association reactions of the following form:

$$A^{\pm}X_{n-1} \; + \; X \; + \; M \; \rightleftharpoons \; A^{\pm}X_n \; + \; M \tag{2.31}$$

where $A^{\pm}$ denotes a positive or negative ion which binds a neutral molecule X, called ligand. M plays the role of only a collision partner which stabilizes the formed complex. Energetically gas phase reactions are described by the Gibbs energy G and the enthalpy H:

$$G \; = \; H \; - \; TS \tag{2.32}$$

$$H \; = \; U \; + \; pV \tag{2.33}$$

In the case of an ideal gas H and U (from the ideal gas law) are only a function of temperature T and do not depend on pressure p or volume V, and it follows [Becker, 1975] [15]:

$$G(p) \; - \; G^0 \; = \; RT \; ln \; \frac{p}{p^0} \tag{2.34}$$

The change $\triangle G_{n-1,n}$ of the Gibbs energy is thus given by:

$$\triangle G_{n-1,n} \; = \; \triangle G^0_{n-1,n} \; + \; RT \; ln \; \frac{p_A^{\pm} X_n}{p_A^{\pm} X_{n-1} \; p_x} \tag{2.35}$$

The index n indicates the association of the n^{th} ligand. Since the ions are assumed to be ideal gas particles, the partial pressures p_A can be substituted by concentrations. If **reaction 2.31** is in equilibrium $\triangle G_{n-1,n} \; = \; 0$ and thus:

$$-\frac{\triangle \; G^0_{n-1,n}}{RT} \; = \; ln \; \frac{[A^{\pm}X_n]}{[A^{\pm}X_{n-1}] \; p_x} \; = \; ln \; K_{n-1,n} \tag{2.36}$$

[15] the index G^0 denotes the Bibbs energy at standard pressure and standard temperature

where $K_{n-1,n}$ is the equilibrium constant of **reaction 2.31**. Later on in this chapter the derived expression will be used to thermodynamically calculate the degree of hydration as function of water vapor concentration. The calculated degree of hydration will then be compared to the experimentally obtained hydration as it is obtained when sampling humidified air with an ion trap.

2.3.3 Ion Source

Various possibilities exist to ionize molecules of a certain type of gas. The ion source should produce selectively and with sufficient flux the wished primary ions which than further react to the source ions. The two methods described here were both used in the present work. The ionized gas was oxygen (purity 5.0) during all experiments. One method is to use a radioactive substance for ionization. In the present work an α emitter, ^{210}Po, was deployed. The second method is to use a high- frequency glow discharge source.

Figure 2.24 shows a schematic drawing of the high-frequency glow discharge ion source, in the following abbreviated DIC (20 kHz, maximum amplitude 15 kV).

The glow discharge zone is separated from the main gas flow by a capillary tube,

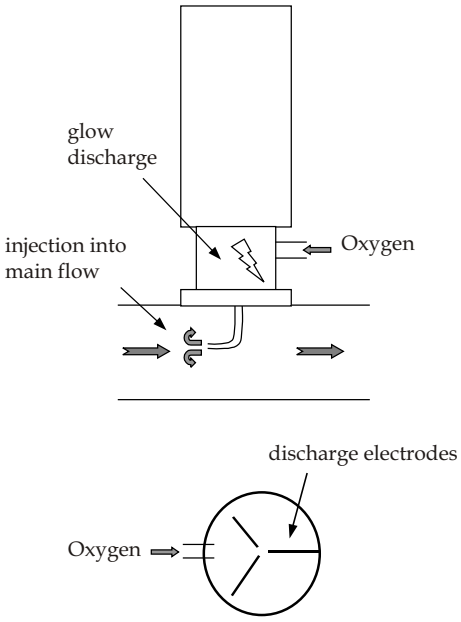

Figure 2.24: Capillary high frequency glow discharge ion source. The glow discharge zone is separated from the main gas flow by a capillary tube, flushed by a continuous flow of oxygen.

which is flushed by a continuous flow of oxygen. The ions are carried by the oxygen gas flow into the main flow reactor [Möhler and Arnold, 1991][Reiner and Arnold, 1994]. This leads to the production of O_2^-, O_3^- primary ions by electron association. By electron impact dissociation of O_2 also O^- is formed as well as neutral oxygen atoms in the ground or first excited state (O, O^1D). As soon as these ions leave the glow discharge zone they will interact with H_2O, CO_2, NO_2 and SO_2 which are present in the buffer gas. Since these trace gases have different electron affinities ($H_2O : 0.9eV, CO_2 : 0.6eV, SO_2 : 1.1eV, NO_2 : 2.3eV$) the source ions will preferentially react with NO_2. But since CO_2 is the most abundant trace gas, the formation of CO_3^- will be predominate:

$$CO_2 + O_2^- \rightarrow CO_2^- + O_2 \tag{2.37}$$

$$CO_2^- + O_2 \rightarrow CO_3^- + O \tag{2.38}$$

or directly by:

$$CO_2 + O_3^- \rightarrow CO_3^- + O_2 \tag{2.39}$$

The reactions with SO_2 and NO_2 proceed similarly but are more efficient since in both cases the rate coefficient is close to the collisional coefficient.
Reactions with water vapor are of importance since they lead to the formation of radicals.

$$O^1D + H_2O \rightarrow 2\,OH \tag{2.40}$$

$$OH + OH \rightarrow HO_2 + H \tag{2.41}$$

Since the electron affinity of O_x^- is smaller than that of the OH radical electron transfer will occur:

$$O_x^- + OH \rightarrow O_x + OH^- \tag{2.42}$$

Another reaction pathway which leads to the production of ions is given by:

$$O^- + 2H_2O \rightarrow 2OH^- + H_2O \tag{2.43}$$

$$O_3^- + H_2O \rightarrow HO_2^- + OH + O \tag{2.44}$$

It is worth mentioning that O_3^- reacts with a rate coefficient close to the collisional rate with SO_2 and terminates with the SO_2^- ion. Primarily O_3^- forms the CO_3^- educt ion by reaction with CO_2.
HO_2^- reacts further with CO_2 to form HCO_4^- which together with SO_2 also forms HSO_4^- very efficiently. Both ions HSO_4^- and HCO_4^- are observed in the mass spectrum. However, these ions do not interfere the SO_2 measurement, since they originate from

different educt ions then the used CO_3^-. This changes in case of the SO_4^- ion. It can be formed by reaction of $O_2^-(H_2O)_n$ with SO_2. SO_4^- may react with SO_2 to SO_3^- and SO_3 [Reiner, 1992]. SO_3^- would again form SO_5^- by reaction with O_2 and therefore could influence the SO_5^- concentration which results by reaction of the CO_3^- ion. Anyway, under atmospheric conditions the ion was not abundant.
The HCO_4^- ion can be used to derive the amount of water vapor in the flow reactor. It offers a new method to detect water vapor very precise. The method is explained in detail in **appendix A.1.2** and also mentioned by [Jost et al., 2003].
The production of charged and neutral radicals is different when a radioactive compound is used for ionization. A ^{210}Po α emitter (65 MBq, 5.4 Me, half-time 138.4 days, range of α particles 3.78 cm in air and at 1 bar pressure) also served as ionization source. The preparation consists of polonium chromate pressed on a copper backing, covered with a thin layer of palladium (Amersham Buchler Company). The experimental setup for the polonium source is shown in **figure 2.25**. The source is embedded in a cylindrical aluminium container, a detailed description can be found in [Hanke, 1999]. Between the open side of the polonium source and the bottom of the container, ionization takes place. During the experiments to determine the transmission and sensitivity of the quadrupole instrument the ^{210}Po radioactive source was directly mounted into the tube of the main gas flow without the container shown in **figure 2.25**.

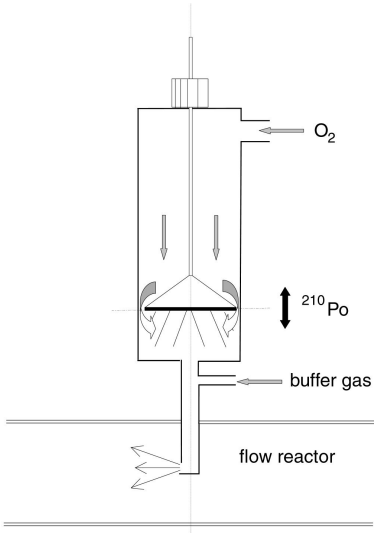

Figure 2.25: Container carrying the radioactive ion source (^{210}Po).

2.3.4 SO_2 Detection with an Ion Trap

To detect SO_2, the formation of SO_5^- by gas phase ion-molecule reactions was used [Möhler and Arnold, 1992],[Seeley et al., 1997]. The following reaction scheme was first suggested and investigated by laboratory experiments in our group [Reiner, 1992]:

$$CO_3^-(H_2O)_m \; + \; SO_2 \longrightarrow SO_3^-(H_2O)_n \; + \; (m-n)(H_2O) \; + \; CO_2 \tag{2.45}$$

$$SO_3^-(H_2O)_n \; + \; O_2 \longrightarrow SO_5^-(H_2O)_m \; + \; (n-m)H_2O \tag{2.46}$$

Latter reaction occurs instantaneously in the presence of enough O_2. The rate coefficient of **reaction 2.45** depends upon hydration of the educt-ion. In order to be able to calculate the analyte mole fraction the water vapor mixing ratio in the flow reactor must be known. An effective rate coefficient k_{eff} weighted by the contributions of the individual coefficients k_n for different water vapor concentrations is given by:

$$k_{eff} = \sum_{n=0}^{3} k_n \, \frac{[CO_3^-(H_2O)_n]}{[CO_3^-]_{tot}} \tag{2.47}$$

The above expression was derived from **equation 2.36** of the previous chapter. Due to collisions between the He atoms of the ion trap and the hydrated educt ions the degree of hydration of these ions will be effectively reduced. The initial hydration in the flow reactor is thus not directly accessible and can only be derived indirectly via the measured water vapor content in the flow reactor. To measure the water vapor content on board of an aircraft precisely and fast is difficult. Thus isotopically labelled $^{34}SO_2$ was used to permanently calibrate the reaction. This will be topic of the next chapter.
The buffer gas contains CO_2. By the following reaction it forms the negatively charged educt ion which participates in **reaction 2.45:**

$$CO_2 \; + \; O_x^- \; + \; mH_2O \longrightarrow CO_3^-(H_2O)_n \; + \; O_{x-1}^- \; + \; (m-n)H_2O \tag{2.48}$$

Since CO_2 is about three to six orders of magnitude more abundant than SO_2 in the atmosphere, the rate-limiting parameter for the reaction to produce sufficient educt ions is the oxygen flow through the ion source. The total count rate and hereby also the SO_5^- count rate increase with oxygen flow[16].

[16]Since the experiment is used on board of an aircraft, space limitations only allow one $2L$ gas bottle to be used during the flights. This basically confines the used oxygen flow.

2.3.5 Online Isotopic Calibration

Isotopically labelled $^{34}S^{16}O_2$ was passed into the sampling line directly behind the aircraft inlet. Wall losses, mixing and instrument sensitivity were thus almost the same as for atmospheric sulfur dioxide. A mass spectrum with a calibration peak of 711 pptv by use of ultradry air (synthetic air, Westfalen Gase, Germany) and a continuous flow of 8.48 sccm $^{34}S^{16}O_2$ is shown in **figure 2.26**. From the corresponding count rates at mass 112 and 114 amu respectively, ambient sulfur dioxide mole fractions were computed with a precision of ±16%. The delivered isotopic $^{34}S^{16}O_2$ (Westfalen Gase, Germany) was factory-certified to 650 ±10 ppbv. Re-calibration in our lab resulted in a mixing ratio of 740 ± 6 ppbv [Nau, 2004]. Computation of the ambient SO_2 mixing ratios was done by taking into account the isotopic purity of the standard as well as the natural isotopic ratio of air. **Equation 2.49** gives the relation between isotopic purity, chemical purity of the standard and derived atmospheric SO_2 mole fractions [Bandy et al., 1993]:

$$C_a = C_s \frac{K_{ss}R - K_{as}}{K_{aa} - K_{sa}R} \tag{2.49}$$

C_a is the ambient concentration, C_s is the concentration of the standard after injection into the flow reactor, R is the ratio of ambient analyte signal counts to isotopic standard signal counts. The K_{ij} values refer to percentage contributions of the i^{th} species in the j^{th} species and are listed in **table 2.1**.

species ($^{34}S^{16}O_2$, $^{32}S^{16}O_2$)	chemical purity (ppbv)	K_{aa}	K_{ss}	K_{as}	K_{sa}
Standard	650		0.934	0.035	
Ambient		0.9457			0.0457

Table 2.1: Isotopic purity in percentage contribution (K_{ij}) of the i^{th} compound in the j^{th} species, as well as the chemical purity of the standard.

Information about the presence of other species interfering at mass 112 amu and/or 114 amu by observing the ratio 112/114 without isotopic calibration gas. Taking into account the terrestrial abundances of ^{32}S,^{34}S,^{16}O and ^{18}O in nature , one expects the ambient 112/114 ratio to be 18.34[17]. The experimentally derived ambient abundance ratio 112/114 is shown in **figure 2.27**. The calculated slope agrees well with the expected ratio.

[17]The ratio is obtained by the following calculation: $^{34}S^{18}O^{16}O_4 + {}^{32}S^{16}O_5 = 0.051$ with $^{32}S^{16}O_5 = 0.9389$. Additionally the number of permutations (5) of the ^{18}O atom has to be considered.

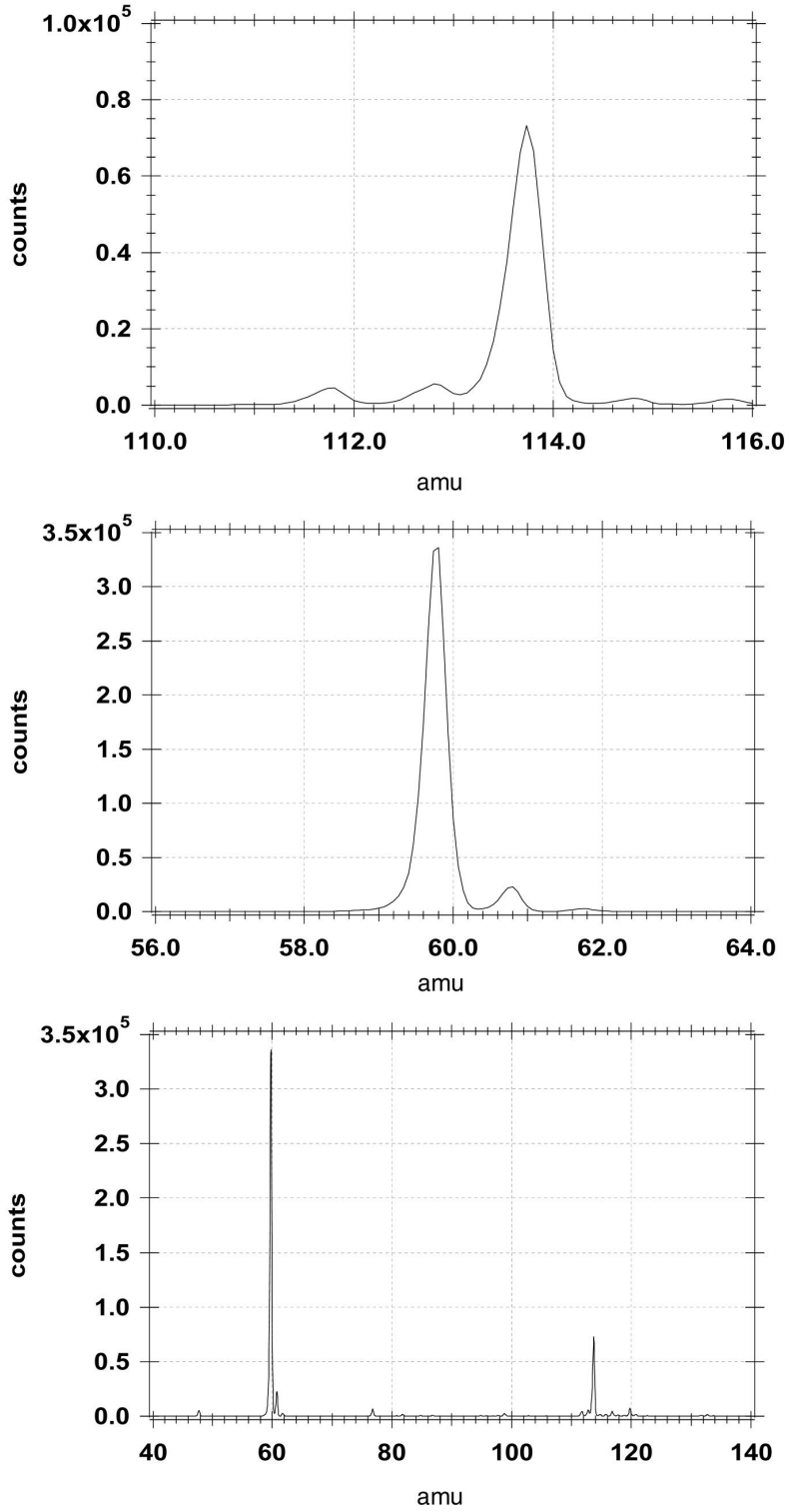

Figure 2.26: Mass spectra obtained by a $^{34}SO_2$ calibration signal of 711 pptv. A zoomed view and a total view are given. Upper graph shows $^{32}SO_2$ and $^{34}SO_2$ counts. Middle graph shows the CO_3^- counts and the lower graph illustrates all together. For a detailed description see text

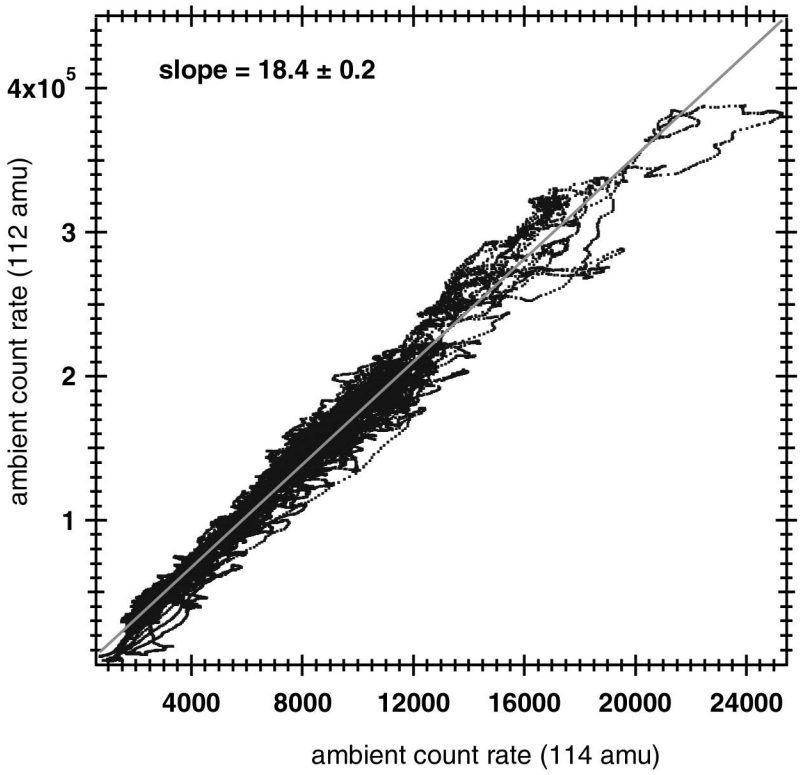

Figure 2.27: Natural isotopic ratio of $\frac{^{32}SO_2}{^{34}SO_2}$ taking into account ^{16}O and ^{18}O.

2.3.6 Water Vapor and Trapping Efficiency

By use of an ion trap instead of a quadrupole to detect charged molecules, hydration of the educt-ions cannot be directly considered as dissociation of the hydrates occurs within the trap. It is necessary to measure the water vapor concentration in the flow reactor where the association reactions take place, and thermodynamically derive the expected degree of hydration. **Expression 2.36** gives the relation between the thermodynamic quantities and the ion count rates. The rate coefficient for each hydration stage can be derived experimentally (assuming $\triangle H^0$ and $\triangle S^0$ are known). Since an online calibration method is used to derive the analyte concentration, it is not necessary to consider the effects of hydration. Analyte and calibration gas experience the same water association and subsequently also the same dehydration within the detection process. The advantage of having an online calibration gas can be used to define the collision induced dissociation provoked by the ion trap and the critical entrance orifice.

Different hydration stages of an ion are described schematically by the following reac-

n ($\sharp\ H_2O$)	1	2
$-\Delta H^0$ (kcalmol^{-1})	14.1	13.6
$-\Delta S^0$ (calK^{-1}mol^{-1})	25.2	29.6

Table 2.2: Thermodynamic parameters for $CO_3^-(H_2O)_{n-1} + (H_2O) \rightarrow CO_3^-(H_2O)_n$. [Keesee and Castleman, 1986]

tion.

$$A^- + H_2O + M \rightleftharpoons A^-(H_2O) + M \rightleftharpoons A^-(H_2O)_2 + M \rightleftharpoons A^-(H_2O)_3 + M \quad (2.50)$$

The corresponding ion ratios $\Gamma_n := \frac{CO_3^-(H_2O)_n}{(CO_3^-(H_2O)_{n-1}}$ can be calculated from

$$\Gamma_n := \frac{p_w}{p_0}\ e^{-\frac{\Delta G^0_{n-1,n}}{RT}} \quad (2.51)$$

By comparing the theoretical Γ_{theo} with the experimentally obtained Γ_{exp}, a dissociation factor is obtained. **Table 2.2** shows the used values for ΔH^0, ΔS^0 with T at 298 K. The calculated values for Γ_{theo} and p_w/p_0 are listed in **table 2.3**

dew point [°C]	p_w/p_0	Γ_1 (exp)
-60	1.66810$^-$6	0.12
-30	3.91910$^-$5	2.81
-20	9.66510$^-$5	6.93
-10	2.20110$^-$4	15.79
-5	3.23810$^-$4	23.23
0	4.16610$^-$4	29.89
8	7.33110$^-$4	52.6

Table 2.3: Calculated Thermodynamic parameters for $CO_3^-(H_2O)_{n-1} + (H_2O) \rightarrow CO_3^-(H_2O)_n$.

Water vapor partial pressure inside the flow reactor was calculated using the equation:

$$p_w = e_{sat(H_2O)}(T_0)\ e^{\frac{A_w(T-T_0)}{T-B_w}} \quad (2.52)$$

with $B_w = 38.25$, $A_w = 17.15$, $T_0 = 273$ K and $e_{sat(H_2O)} = 6.107$ hPa [Pruppacher and J.P.Klett, 1996]. **Figure 2.28** shows Γ_{exp} and Γ_{theo}. Γ_{exp} is about three orders of magnitude smaller than the theoretically expected value. Thus on can conclude,

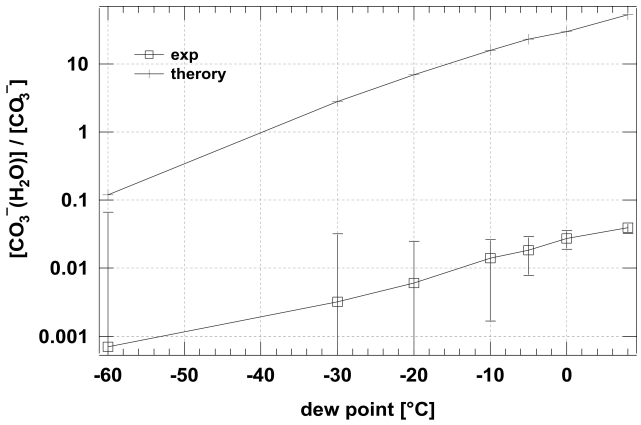

Figure 2.28: Theoretical and experimentally obtained hydration ratios of the $CO_3^-(H_2O)$ association reaction.

that the system (entrance orifice and trap) is rather efficiently removing the hydrates. Also only the first hydrated stage can be observed. That appears in **figure 2.29** where count rates of CO_3^-, $CO_3^-(H_2O)$ and $CO_3^-(H_2O)_2$ are plotted against the dew point temperature. The second hydrate appears at much smaller count rate than the first hydrate. Since the slope of the count rate of the second hydrate is strongly decreased in comparison to the first hydrate, Γ_2 would show the opposite behavior to what is expected from theory. Instead of the observed increase of the first hydrate with dew point, the second hydrate would show a decrease. The reason for the converse behavior probably results from bad statistics due to the small count rate of this ion.

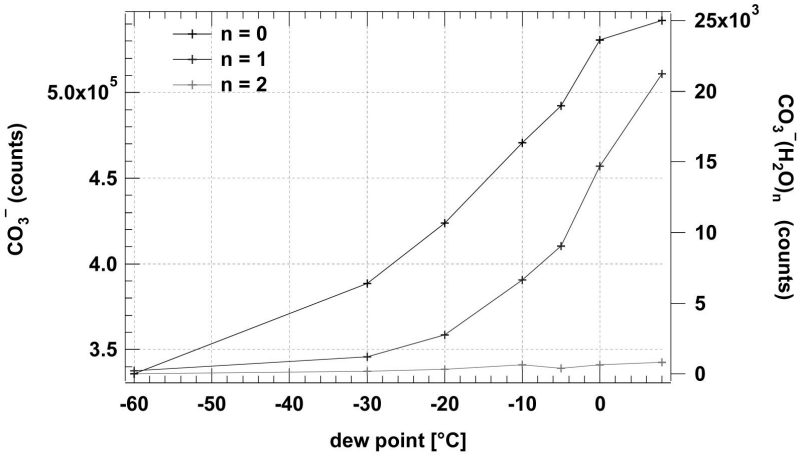

Figure 2.29: Count rates of the observed hydration stages. The second hydration can be barely observed.

2.3.7 Instrumental Background and Sensitivity

Several sources are contributing to a background signal. When using an online isotopic calibration standard (see **chapter 2.3.5**) one has to distinguish between background contributions related to the isotopic purity of the calibration standard and those related to impurities caused by contamination of sampling line and instrument. Also included can be electronic noise of the detection unit. In the following the sum of each of the mentioned background contributions will be referred to as total background.
An ambient sulfur dioxide molecule is converted to an SO_5^- ion by reaction with a CO_3^- ion and an oxygen molecule. The natural isotopic distribution leads to two distinct mass peaks at 112 amu and 114 amu corresponding to:
112 amu: $^{32}S^{16}O_5^-$
114 amu: $^{34}S^{16}O_5^-$ or $^{32}S^{16}O_4^{18}O^-$
Contributions to these mass lines from other ambient isotopes like ^{33}S (0.75 %), ^{36}S (0.75 %) or ^{17}O (0.048 %) are neglected due to their little relative abundances. The calibration gas standard is of a certain isotopic purity with relativ abundances of ^{32}S (3.5%) , ^{33}S (3.1%) and ^{34}S (93.4%). For online calibration some fraction of this isotopic standard is added to the sampled ambient air right after the main inlet (**appendix C.1**). Due to the isotopic composition of the standard the mass peaks at 112, 114 amu respectively will increase. The increase certainly depends on the adjusted isotopic gas flow. In order to extract the standard contribution from the ambient signal at 112 amu, and vice versa the ambient contribution from the standard signal at 114 amu, **equation 2.49** is used. The calculated ambient concentration still contains the background related to instrument contamination and electronic noise. If known, this background has to be subtracted from the count rates at mass 112, 114 amu respectively before the ambient gas concentration is calculated. The following experiments were performed in order to define this background count rate.
Figure 2.30 shows the setup which was used to detect the background signal. Each tubing consists of stainless steel with 40 mm inner diameter (KF 40) and 15 cm in length.

The background was measured under two different conditions. First only dry air (dew point below -60 °C) was used as buffer gas. The pressure p_0 measured with the sensor as shown in **figure 2.30** was varied between 200 and 900 mbar. Since 200 mbar correspond to about 12.5 km altitude, changes in background with different flight levels could be simulated. Second the pressure p_0 was kept constant at 900 mbar but the water vapor concentration was changed. 5 minutes were passed before taking spectra at each set dew point. That was for the humidity sensor (capacity sensor, Panametrics

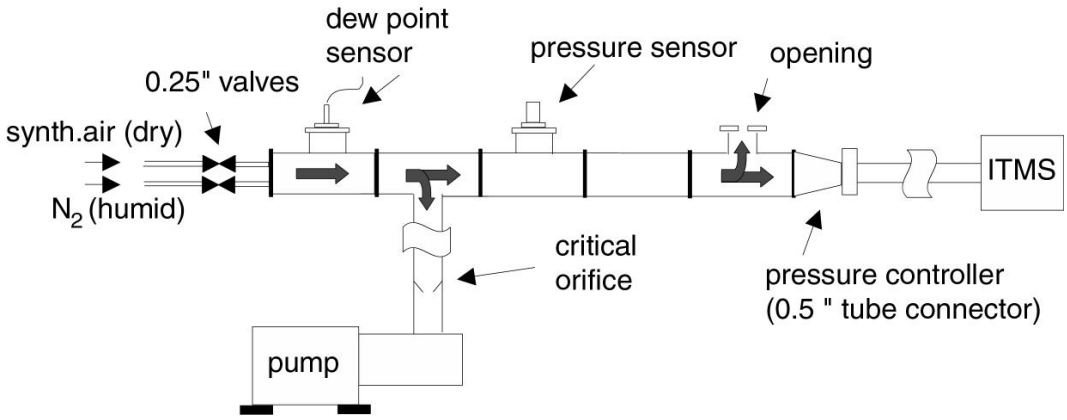

Figure 2.30: Setup for background detection. For further details see text.

company) to adjust to the changed water vapor conditions.
Synthetic air (Westfalen Gase, Germany) served as dry buffer gas for the first background experiment. The N_2-valve and the opening (**figure 2.30**) were closed such that the pressure p_0 was regulated by controlling pumping power and buffer gas flow. Starting from 200 mbar, 200 spectra for each adjusted pressure were taken. First the spectra were recorded without any isotopic standard, then an isotopically marked SO_2 flow of 8.48 sccm (20 sccm MFC) was added to the buffer gas such that a mixing ratio of 711 pptv was reached inside the flow reactor (the same ratio as used during the aircraft campaigns). Again 200 spectra were recorded. Before the pressure was set to another value, the isotope flow was stopped and wait until the count rate at 114 amu reached its initial background value without isotope. The two gained sets of mass spectra, with and without added isotopic gas standard, were then evaluated by use of **equation 2.49**, when calibration gas was added and by use of the **parallel ACIMS formula (2.30)** in the absence of the calibration gas.
Calculated background ratios in pptv are shown in **figure 2.31**. Each data point represents an average over the 200 single spectra, with 5 scans per spectrum and an injection time of 250 ms. The error bars refer to the standard deviation obtained by averaging over the recorded 200 data points per each pressure value. A background average mixing ratio of 10 ± 1 pptv at mass 112 amu (3 ± 0.5 pptv at mass 114 amu, not shown in the plot) was obtained for a dry buffer gas. Within accuracy a pressure dependence of the background was not found.

In the next experiment the water vapor dependence of the background was examined. Hence water vapor was introduced into the sampling line by passing a certain

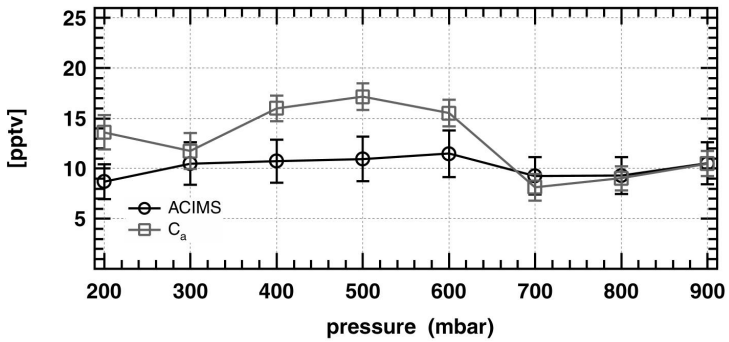

Figure 2.31: Background SO_2 mixing ratio at mass 112 amu as function of pressure p_0 (dew point below -60^0C)

.

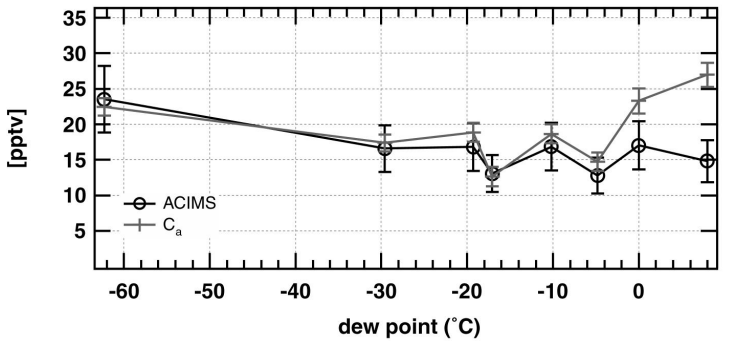

Figure 2.32: Background SO_2 mixing ratio at mass 112 as function of dew point (at $p_0 = 900mbar$)

.

N_2 flow (N_2 5.0, from Westfalen Gase, Germany) through a glass bottle filled with distilled water. Humidity was controlled by changing the amount of mixing between dry synthetic air and the water-enriched N_2 flow. Dew point varied between ultradry air ((-60 ± 2)°C, zero N_2 flow) and 8 °C. A certain air stream effused through the opening to ensure no mixing of ambient air with the buffer gas (**figure 2.30**). 200 spectra at each dew point were recorded and isotopic SO_2 was temporarily added as described above for the first experiment. The calculated background ratios are shown in **figure 2.32**. Each data point represents an average over the 200 spectra, with 5 scans per spectrum and an injection time of 250 ms. Background mixing ratios were then calculated with the ACIMS formula and compared with the result obtained by **equation 2.49**. C_s was set to 711 pptv.

In case humidity was added, the background mixing ratio results to an average of 19 ± 1 pptv at mass 112 amu. Within the measurement error, a humidity dependence can be neglected. The error was determined by Gauss fitting the deviation from the mean, when plotted into a histogram. Due to the 200 sampled data points per dew point temperature the mean value becomes very precise. The standard deviation of the background (mean value) was determined to 20 pptv and equals the 1 - σ level. Thus the probability for a measured concentration to fall within the 1 - σ range of the background results in 68.3%. Therefore a detection limit of 20 pptv is given.
The background values calculated with the ACIMS formula and derived from isotopic online calibration, agree well within the measurement error, defined in the way described above. The deviation increases with increasing dew point. This exactly reflects the water dependency of the rate coefficient used for the calculations made by the ACIMS formula and does not surprise. The calculations were performed using a constant value of $1.0 \cdot 10^{-9}$ (cm^3). However, there exists a deviation of several pptv between the background examined with a dry and a humidified buffer gas. This difference cannot be reasonably well explained but is likely to occur due to a lower isotopic gas concentration in the flow reactor than the actual value of 711 pptv used for the calculation. Instead using the ACIMS formula a mole fraction of about 650 pptv of isotopic gas in the flow reactor can be calculated when dry buffer gas and the isotope standard are present. Thus probably the mass flow controller used for the calibration gas did not function properly in that case.
The question rises to what extent the measured background of 10, 19 pptv respectively results from contamination of the vacuum system or from electronic noise ? Considering synthetic air being produced by directly compressing ambient air at ground level with a chemical purity of $N_2 = 5.0$ and an original SO_2 fraction of say 10 ppbv, a mole fraction of 0.1 pptv will remain in the used dry buffer gas. The background signal at mass 112 amu and 114 amu in the absence of the calibration gas, does appear gaussian-shaped with a somewhat shifting center peak around 112 amu and not as statistically fluctuating spikes. Thereby electronic noise from the electron multiplier is excluded as a dominant source. We assume that the actual background is caused by contamination of the instrument, tubing and the ionization source. Contributions resulting from SO_2 in the used buffer gas are apparently small. No filter material was found, capable of reliably removing low SO_2 contaminations. [Parrish et al., 1991] report on a method of zero air generation with respect to SO_2. Ambient air was passed through a glass filter material impregnated with potassium hydroxide. In a time of the order of hours the potassium hydroxide was converted to potassium carbonate by absorption of atmospheric carbon dioxide. Both of these compounds effectively absorb SO_2.

Due to the good agreement of the calculated (ACIMS) and the result obtained from isotopic calibration, a humid background of 19 pptv was considered for data analysis of the ITOP campaign data. This value was then subtracted from the ambient concentration obtained by **equation 2.49**. No count rate was subtracted from the original count rate at mass 112 and 114 amu, since it remains unclear how large this statistical contribution really is. In the following the error will be discussed present in the ACIMS calculation and the isotopic calibration.
The error in ACIMS is dominated by the uncertainty of the rate coefficient (±20%) mainly. The relative error in C_a equals 12% for mole fractions exceeding 100 pptv and is dominated by the uncertainty in C_s. In the following the error calculation for C_a is derived:
The count rate of a single data point is software averaged over 5 mass scans. Additionally the count rate per mass scan given by the multiplier (**chapter 2.2.1**) is amplified by a factor of 1000 (personal communication: Thermo Finigan Company), leading to a count rate per data point of $n = N/200$, where N denotes the sum over 5 scans and excluding the amplification factor. Count rates at mass 112 amu ($^{32}SO_2$) varied between N = $5 \cdot 10^4$ and N = $5 \cdot 10^5$. Thus when calculating the error of a data point (5 mass scans), the statistical contribution from $(\sqrt{n}/n)$ only contributes with a percentage < 5% to the total error and only at low SO_2 concentrations. A single mass scan instead contains larger statistical amounts. Further error calculations only refer to 5 mass scans. Several contributions have to be considered. ΔR, the ratio of analyte and standard count rate, is as mentioned above of statistical nature and proportional to $\sqrt{N_{a,s}}$ where the index a,b denotes ambient and analyte counts. The absolute error ΔC_s, is calculated by the ratio of the injected $^{34}SO_2$ flow to total flow, times initial mixing ratio of the standard (734 ppb ± 6%). The total flow through a critical orifice is given by:

$$\Phi_{total} \;=\; 0.93 \; s \; d^{\,2} \; p_0 \; \sqrt{\frac{T}{293}} \tag{2.53}$$

where s is a correction factor (s = 0.86) and d = 0.39 cm the critical orifice diameter. During flight, the temperature in the flow reactor is measured with a precision of Δ T = 1 K and the flow reactor pressure varies by about 2 mbar. The oxygen mass flow controller is considered with a 1% inaccuracy. The error of the isotope mass flow controller also contributes with a 1% inaccuracy. The error in the isotope gas mole fraction contributes with $\Delta C_s/C_s = 6\%$ the largest contribution to the total error. **Figure 2.33** illustrates the calculated relative error as function of the ambient sulfur dioxide fraction. Abundances larger than 50 pptv are afflicted with an error between 12 to 16 %. For low values of SO_2 the error increases to above 40%.

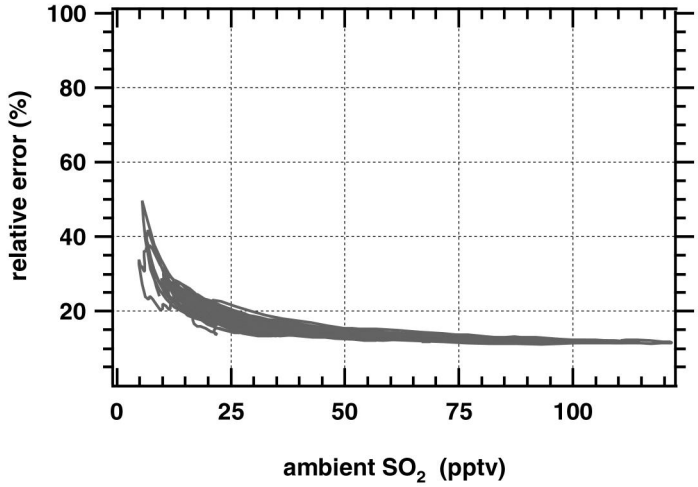

Figure 2.33: Relative error per measured SO_2 data point (5 mass scans) as function of ambient sulfur dioxide concentration.

Additionally to the ascertainable error, inaccuracies appear which are not accessible. Ambient SO_2 molecules first have to pass the inlet which is bend 90° against flight direction and permanently heated at 20 °C to avoid icing. Right before the main magnetic valve which controls the flow into the sampling line, the isotopic standard is added (refer chapter **2.2.1**). Some fraction of the ambient sulfur dioxide might become surface adsorbed onto the stainless steel wall of the inlet. Due to heating of the inlet no water film should form on the inner side of the inlet which would increase surface adsorption. When passing through clouds this might lead to an underestimation of abundant SO_2 mixing ratios. All further effects of wall losses are considered, since the isotopic standard is admixed.

2.3.8 Conclusions

The QMS instrument has been characterized in great detail. Operating parameters such as the axial voltage were optimized. The operating principle of the ion trap spectrometer was optimized to detect gaseous atmospheric SO_2 with an isotopic online calibration for the first time in our group. The sampling line and flow reactor were built more compact with a concurrently much better pressure sensing by use of a feedback-controlled magnetic valve. Both instruments were implemented during campaigns into the research aircraft FALCON. The detected ambient SO_2 mole fractions serve as upper limits due to the not specifiable adsorption effect of the aircraft inlet to sulfur

dioxide. A background of 19 pptv was determined by use of humidified buffer gas. The major contribution of this background is likely to result from SO_2 which is due to contamination of instrument, tubing and ionization source. A negligible amount is due to electronic noise of the detection unit. The following chapters will report on data collected during the CONTRACE and ITOP flight campaigns.

Chapter 3

ATMOSPHERIC CLUSTER ION MEASUREMENTS

3.1 Introduction

The main objective of the CONTRACE project was to investigate the upward transport of polluted airmasses from the boundary layer to the mid (MT) and upper troposphere (UT), and to study their impact on the trace gas budget over Europe. Both the rapid convective transport in thunderstorms as well as the more slow and widespread uplift in warm conveyor belts (WCBs) ahead of cold fronts were studied. The long-range pollution transport from North America to Europe and its impact on European trace gas composition was a major aim [Huntrieser et al., 2003]. Therefore the research aircraft Falcon was equipped with instrumentation of several research groups (Institute for Atmospheric Physics, DLR, IMK-IFU Garmisch and MPI-K Heidelberg) to detect many atmospheric trace gases: CO, CO_2, O_3, NO, NO_y, CN, H_2O_2, CH_2O, VOCs, atmospheric ions, $(CH_3)_2CO$, CH_3OH and SO_2. Additionally the flight planning was supported by newly developed chemical tracer forecasts provided by TUM Freising (Lagrangian particle dispersion model FLEXPART) and MPI-C Mainz (global chemistry transport model MATCH-MPIC).
The present thesis only deals with the last part III of the CONTRACE project, which took place in 2003 and during which the MPI-K focused on the investigation of atmospheric ion-induced nucleation. The measurements were performed with the cryogenically pumped quadrupole mass spectrometer described in **chapter 2**. The recorded spectra are cumulative ion distributions. The instrument when operated in this mode, is of increased sensitivity compared to the usually used common line mode spectra.

Only the flight of the 16^{th} of July will exemplarily be shown here. That is because the aircraft cruised exclusively between 7 to 9 km altitude in the absence of large water clouds and because several periods of significant small-particle growth (N > 5 nm) were observed.

3.2 Analysis of High Pass Mode Mass Spectra

For simplification in the following only mass spectra for negative ions will be considered, although during the CONTRACE campaign both positive and negative ions were measured. All observations hold likewise for both types of ions. However, it is worthwhile to mention that in some cases, the nucleation rate of negative ions has been observed to be up to 100 times higher than that of positive ions. The difference in nucleation rates is assumed to be a result of the effect of different dipole moments [Kusaka et al., 1995].
The recorded high pass mode mass spectra were processed in several steps. It appeared that all spectra showed a strong rejection in count rate within the first 80 amu mass range. As discussed in **chapter 2** the mass cumulative spectra should show initially the highest count rates due to their integral property . The observed initial rejection was always present and might be caused by a trigger mismatch between ramp voltage and detection unit. The multi-channel analyzer may have started to read data before the ramp voltage was properly applied. Thus data in the mass range between 0 to 80 amu was excluded. **Figure 3.1** shows the observed feature exemplarily for 10 spectra added and smoothed over 52 mass channels. The mass range above 800 amu was truncated due to little signal such that the total mass range for the analysis

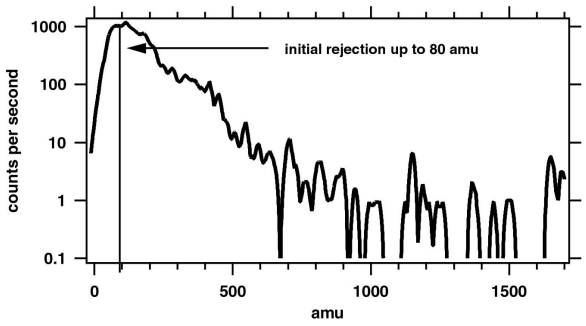

Figure 3.1: Initial rejection of mass counts up to about 80 amu present in a high-pass-mode spectra. Due to the strong rejection the count rate up to 80 amu was excluded from analysis.

comprised 80 to 800 amu. The individual spectra showed several peaks overlaid the cumulative distribution. In laboratory experiments using the aircraft setup (cryogenic pumping), the appearing peaks could be related to different axial voltages as shown in **figure 3.2**. Because sensitivity changes with axial voltage and pressure, the applied 0.6 V derived in **chapter 2** were chosen, in order to operate the instrument close to the regime where only a weak pressure dependence exists at comparatively high sensitivity. Unfortunately the overlaid peaks occurred at this axial voltage. This fact was first observed after the campaign when looking in more detail into the data. However, it remains unclear why the observed mass peaks actually appear in the spectra. The increased sensitivity apparently led to changes in the response function of the system. In the next step of analysis a defined number of mass spectra was added in order to achieve better statistics. The number of summed spectra was related to the convergence of a fit function onto the measured cumulative distribution. It turned out that adding 10 spectra led to a convergence of the fit function at every spectrum recorded. In the following the used fit function will be derived. The concept is related to that of particle measurements.
Since a cumulative distribution is recorded, the corresponding abundance of ions with a certain mass is not directly accessible. Moreover the following relation exists:

$$F_N(M_i^\star) \;=\; -\int_0^{M_i^\star} n_N(M_i)\, dM_i \tag{3.1}$$

where $n(M_i)$ equals the searched ion mass abundance. The negative sign is due to a descending ($m_i > m_i^\star$) distribution. We assume that in the atmosphere different cluster ion families of the following form exist: $(\mathrm{NO_3^-}, \mathrm{HSO_4^-})(\mathrm{HNO_3}, \mathrm{H_2SO_4})_\mathrm{x}(\mathrm{H_2O})_\mathrm{y}$. The term "core ion" will later in this chapter always refer to the actual ions (NO_3^-, HSO_4^-) plus the number of acid ligands expressed by "x". The ions within a family then only distinguish by the degree of hydration, denoted by "y". Hydration will lead to a mass distribution of each ion family. If the core ion remains the most abundant, a log-normal distribution would describe the degree of hydration. Higher degrees of hydration are less likely and depend their occurrence depends on the relative humidity. The problem is that the instrumental resolution is not good enough to resolve the different stages of hydration. Rather a Gauss shaped peak appears in the spectrum. Thus instead of the log-normal distribution, a Gauss distribution was chosen. Then $n(M_i)$ can be taken as the sum of several gauss curves corresponding to several different core ions, ion-families

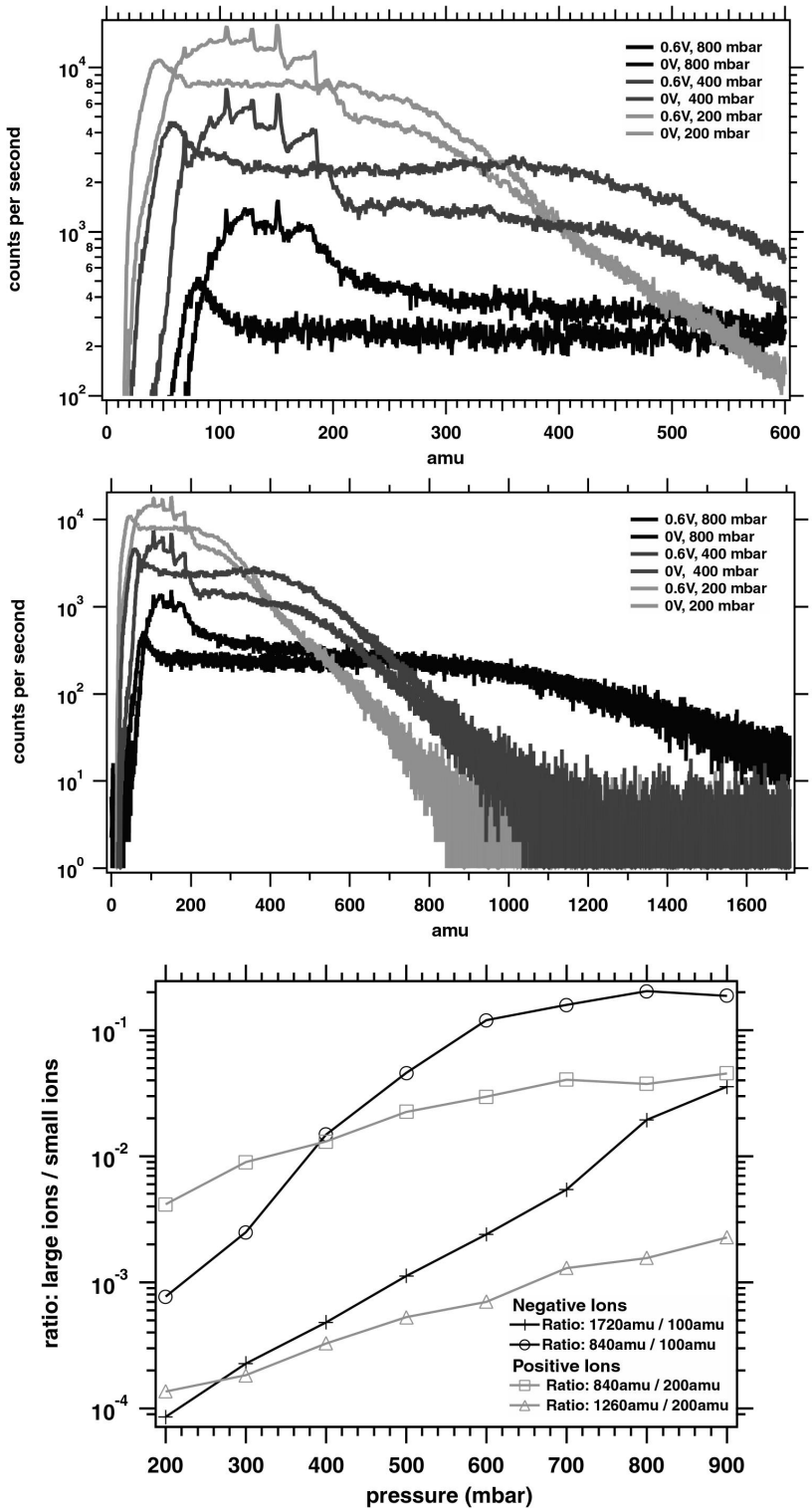

Figure 3.2: High-Pass-Mode mass spectra parameterized by pressure and axial voltage. The bottom graph shows the derived large to small ion count ratios as function of pressure. Important are the overlaid peaks at 0.6 V axial voltage (zoom view) which significantly change the shape of the spectrum.

respectively and the described context is reflected by **equation 3.2**:

$$F_N(M_i^\star) \;=\; -\sum_{l\,=\,1}^{k}\int_0^{M_i^\star} e^{-\frac{(M_i-M_{il})^2}{\tau_i}}\; dM_i \tag{3.2}$$

with M_{il} being the mass of the l^{th} core ion. The parameter k defines the amount of core ions that exist and is in principle a huge number. The integral in **equation 3.2** is the so-called error function. It is further assumed that the core ions with a varying number of ligands deliver the major contributions to the measured spectrum. Then their masses can serve as base points to describe a fit function.
The count rates of the recorded spectra tend to rapidly decrease with increasing ion mass such that the main contribution of relevant ions is below about 500 amu. Sulfate clusters with x = 3 and y = 2 already equal a mass of 427 amu. If only the core ions (y=0) are considered in a fit function, a combination of 12 different cluster ions would result. Since the $HSO_4^-(HNO_3)$, $NO_3^-(H_2SO_4)$ cluster respectively equal in mass, k is reduced to 11. **Equation 3.2** was parameterized in the following way:

$$F_N(M_i) \;=\; y_0 \;+\; A_{il}\; erfc\,(b_{il}(M_i - M_{il})) \tag{3.3}$$

The ion masses M_{il} considered in the fit are shown in **table 3.1**. 10 different cluster ions were taken into account. The fit properly converged onto each spectrum with b kept constant at 0.1 and 0.01 for the hydrated sulfate cluster. A_{il} was constrained to values $0 < A_{il} < 150$. The fit convergence improved for large masses when the hydrated sulfate cluster with $HSO_4^-(H_2SO_4)_3(H_2O)_2$ was considered. The two clusters $HSO_4^-(HNO_3)_2$ (223 amu) and $HSO_4^-(HNO_3)_3$ (286 amu) reduced the fit convergence and were thus not considered.

cluster ion	mass (amu)
$NO_3^-(HNO_3)$	125
$NO_3^-(HNO_3)_2$	188
$NO_3^-(HNO_3)_3$	251
$NO_3^-(H_2SO_4)$	160
$NO_3^-(H_2SO_4)_2$	258
$NO_3^-(H_2SO_4)_3$	356
$HSO_4^-(H_2SO_4)$	195
$HSO_4^-(H_2SO_4)_2$	293
$HSO_4^-(H_2SO_4)_3$	391
$HSO_4^-(H_2SO_4)_3(H_2O)_2$	427

Table 3.1: Cluster ions considered in the fit function to derive the recorded cumulative ion distribution.

Figure 3.3 shows the derived abundances (cm^{-3}) of the considered atmospheric cluster ions as function of time during the CONTRACE flight of the 16^{th} of July 2003.

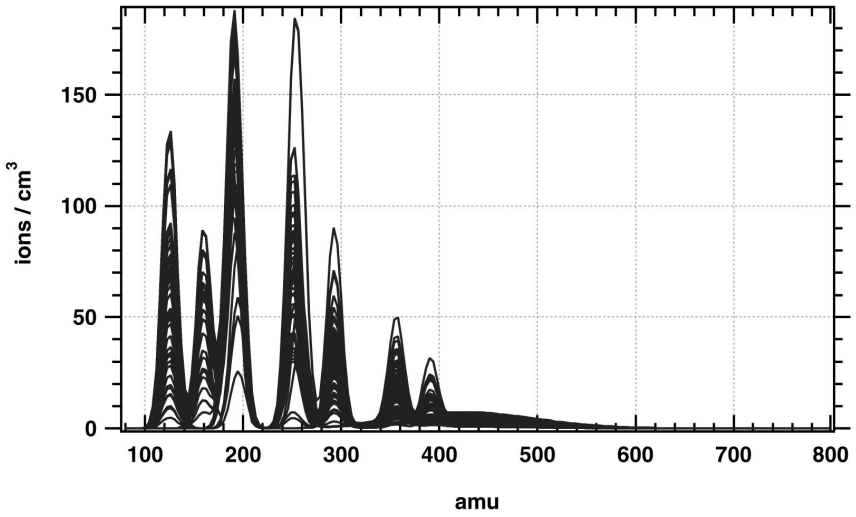

Figure 3.3: Atmospheric cluster ion abundance (cm^{-3}) derived with a fit function. The measurements were performed during the CONTRACE flight of the 16^{th} of July 2003.

The conversion of count rate to concentration was obtained from the sensitivity derived in **chapter 2** and equals S = 0.12 s^{-1} cm^3. The total ion concentration varied between 1000 and 10000 cm^{-3}, in agreement to literature [Viggiano, 1995]. The peaks

correspond to the mass of the implemented core ions. The most abundant clusters are those of mass 188, 195 and 251 amu, that is the nitrate $NO_3^-(HNO_3)_{2,3}$ and the sulfate cluster $HSO_4^-(H_2SO_4)$. Mass 251 appears 90% more often than mass 258 which in term shows once the highest concentration of 180 ions cm^{-3}. At mass 160 two types of ions coincide, $NO_3^-(H_2SO_4)$ and $HSO_4^-(HNO_3)$. The width of all peaks is constant due to the fixed value of fit parameter b. When b was not preset but constrained, fitting time drastically increased and convergence was not always guaranteed. To fix b at a value of 0.1 also means that hydration is not explicitly considered. The Gauss width rather corresponds to a $\Delta M/M$ inaccuracy of the instrument as it is derived in **chapter 2.1.4**. The fact that hydration is not explicitly considered clearly limits the proposed analysis method. On the other hand, if the atmospheric cluster ion distribution would look significantly different, the fit function would not have converged with the chosen parameterization. The preset parameter values were defined by trial and error until a configuration was found which converged to all spectra. Surely another configuration exists which also leads to a result. To obtain the best configuration, the implemented algorithm needs to be further improved. Therefore the resolution of the instrument needs to be increased in such a way that single hydrations stages can be observed. The Gauss fit could be substituted by a log-normal fit. Parameter b could be fitted onto each single core ion mass previously to the fit onto the whole spectrum . Thereby individual hydration stages are considered. Thus the following results are more of a preliminary character although the overall picture should not significantly change.

3.2.1 Derived Condensable Gas Concentration

In this section a method is described to experimentally derive the concentration of condensable gases from cumulative ion mass distributions. Condensable gases are species of low vapor pressure such as HNO_3 or H_2SO_4. The vapours responsible for the condensational growth are not necessarily the same that caused the particle formation. Sulfuric acid, ammonia and water vapours are the most likely candidates for initial particle formation. However, the possible importance of organic vapours is still under investigation.

The approach used is independent of the type of condensable gas but here for simplification only applied to gaseous sulfuric acid. A detailed description is given in [Wilhelm, 2003], [Eichkorn et al., 2002]. This leads to a system where particle formation occurs only due to nucleation and condensation. Evaporation as well as coagulation are neglected. The approach is purely kinetic. The term "condensation" might be used in

a somewhat sloppy manner. Condensation appears when a certain energetic barrier has been exceeded and vapor physically condenses onto a preexisting surface. Before, heterogenous (presence of preexisting aerosols), homogenous or ion-induced nucleation control the growth (heterogenous) and the new formation (homogenous, ion-induced) of particles (**chapter 1**).

The number of sulfuric acid molecules attached to a charged molecule increases with increasing number concentration of sulfuric acid molecules in the gas phase. The probability of a collision between a sulfuric acid molecule and an ion is given by the following expression:

$$P(m) = exp(-(\frac{t_{CA}}{t_{ir}})m) \tag{3.4}$$

where t_{ir} defines the time for ion-ion recombination processes. Thus $t_{ir} = (\alpha n_i)^{-1}$ $= (\alpha(\frac{Q}{\alpha})^{0.5})^{-1}$. Q stands for the atmospheric ionization rate which is caused by the galactic cosmic rays and is intensity-modulated via the solar activity. It thus can be seen as an important climate parameter. A value of Q $\approx 30\ cm^{-3}s{-}1$ is considered in the performed calculations. The ion number concentration n_i of both polarities[1] equals $\sqrt{\frac{Q}{\alpha}}$. t_{CA} stands for the time passed until an acid molecule collides with an ion. Or expressed by the rate coefficient for the attachment of a sulfuric acid molecule onto an ion $t_{CA} = (k_{CA}\mathrm{H_2SO_4})^{-1}$. With increasing cluster diameter, k_{CA} increases and α will be reduced because the charge of the core ion becomes more and more screened. By this process the probability P grows. For a small ion $k_{CA} \approx 3 \cdot 10^9$ and $\alpha \approx 1.3 \cdot 10^6$ [Su and W.J.Chesnawitch, 1985]. With the given values of k_{CA}, α, Q and by using the gaseous sulfuric acid concentration as fitting parameter, its abundance can be derived from fitting P(m) onto each cumulative spectrum. **Figure 3.4** shows the condensable gas concentrations calculated for the flight which took place the 16^{th} of July 2003.

[1]It is assumed that by the cosmic ray flux positive and negative charges are produced in equal amounts.

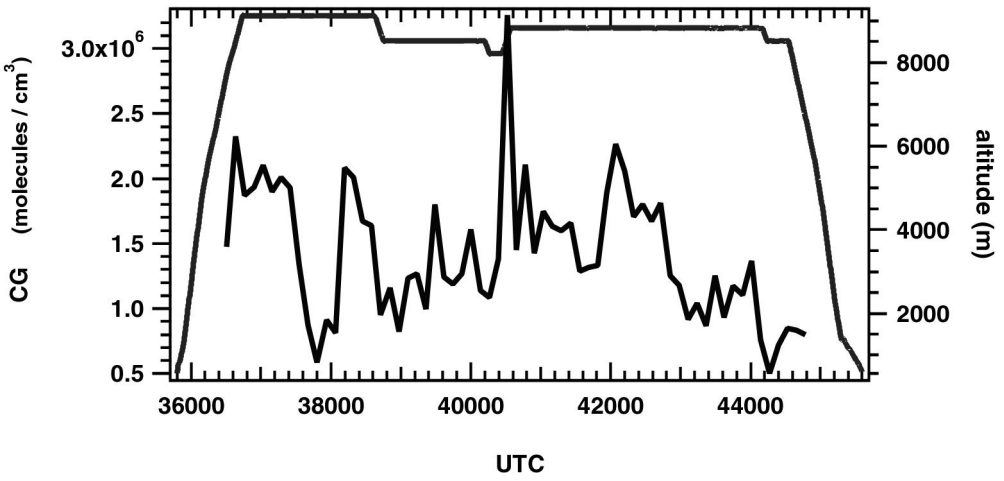

Figure 3.4: Calculated condensable gas concentration for the flight of the 16^{th} of July 2003.

3.3 Measurements during the CONTRACE Campaign 2003

3.3.1 Charged Cluster Measurements

With the analysis method derived in the previous chapter, certain cluster ion concentrations in the atmosphere were computed, from measured spectra as a function of time. **Figure 3.5** shows the temporal evolution of the derived condensable gas concentration, the concentration of two cluster ions ($HSO_4^-(H_2SO_4)_3(H_2O)_x$) with x = 0 and x = 2, as well as the particle concentration of N > 5 nm. The concentration of cluster ions with x = 0 is higher by about a factor of 5 than that of clusters with x = 2. Concentrations of up to 30 molecules cm^{-3} of the hydrated form occur. In comparison the sulfuric acid concentration varies between (0.5 - 3)$\cdot$ 10^6 cm^{-3}. Since sulfuric acid was derived with respect to the collision rate of the acid molecules, a positive correlation between cluster ion and sulfuric acid abundance is expected. Also both quantities might be correlated to the particle concentration. A particle, cluster correlation is not implicitly, since the particle detection limit is at about 5 nm. If a sulfuric acid cluster density of ρ = 1543 kg m^{-3},[2] is assumed a sulfuric acid cluster diameter of 0.47 nm results. In **figure 3.6** the scatter plots of particles, condensable gas and cluster ions

[2]The density was estimated for the x = 2, y = 3 sulfate cluster. Hereby the approximation density formula given by [Kulmala et al., 1998] is used with a sulfuric acid mass fraction of 0.7.

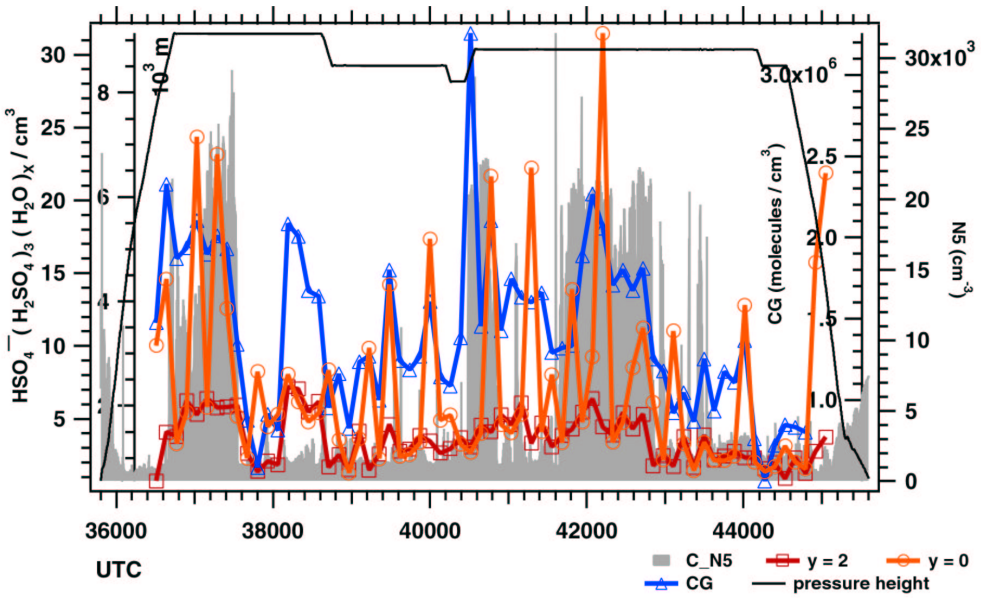

Figure 3.5: Temporal changes of small particles (N > 5 nm), condensable gas and cluster ion concentrations.

are given. The bottom graph shows all considered clusters of x = 1,2,3 and y = 0,2 plotted versus the particle concentration. The top graph plots cluster concentrations versus sulfuric acid concentration. The lines correspond to a linear regression to define the degree of correlation between each quantity.
To evaluate the scatter plots, the correlation coefficient R was determined by means of a linear regression. R basically measures the linearity between two variables X and Y. Additionally R^2 is given in %. A value of R = 0.8 for instance means that 64% of the variance in Y is explained or predicted by X. Still the correlation could be by chance. Thus the confidence limits at a 95% confidence level were calculated which is the likely range of the true value. Depending on the sample size, which comprises 67 data points in all cases here, a conclusion can be drawn whether the correlation is by chance or significant. The result is shown in **table 3.2**.
First the correlation between cluster ions and the derived condensable gas is significant except for x = 2, y = 0. Here the found correlation is by chance. Second the cluster ions also show a significant correlation to the small particle concentration (N5) beside the cluster of 293 amu (x = 2, y = 0) which is not significantly correlated. The correlation of the double-hydrated sulfate cluster with the particle concentration N5 is R = 0.69 and the likely range is 0.54 - 0.80. Interestingly the ions can be separated into two groups by their correlation coefficient.

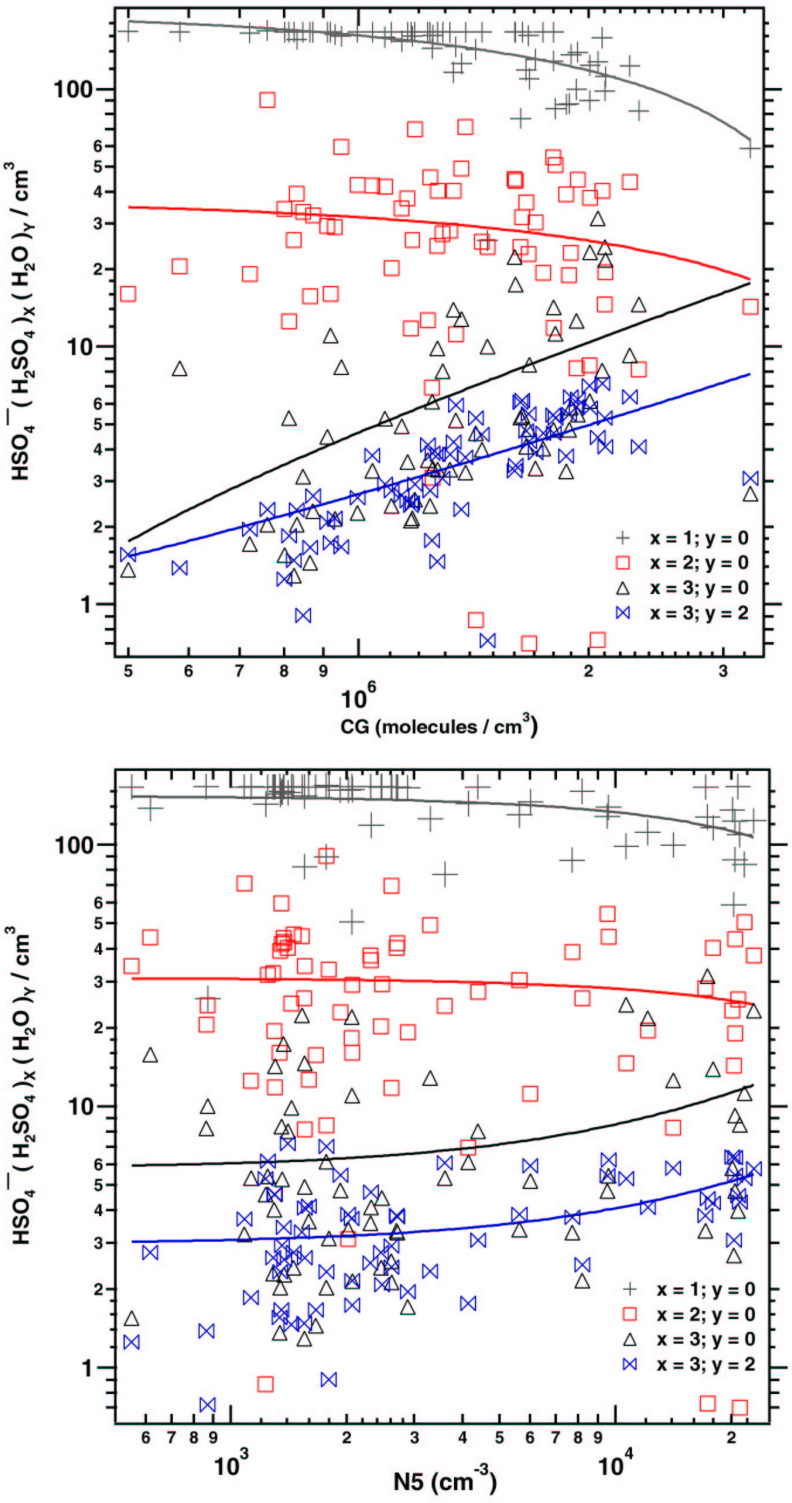

Figure 3.6: Scatter plots of particles (> 5nm) condensable gas and cluster ions.

[cluster ion]/[particle]	R	R^2 (%)	UCL	LCL	RESULT
x=1 y = 0	-0.41	17	-0.59	-0.19	SIG
x=2 y = 0	-0.11	1	-0.34	0.13	–
x=3 y = 0	0.29	8	0.05	0.5	SIG
x=3 y = 2	0.46	21	0.25	0.63	SIG
[cluster ion]/[CG]	R	R^2 (%)	UCL	LCL	RESULT
x=1 y = 0	-0.66	44	-0.78	-0.5	SIG
x=2 y = 0	-0.17	3	-0.39	0.07	–
x=3 y = 0	0.46	21	0.25	0.63	SIG
x=3 y = 2	0.69	48	0.54	0.80	SIG

Table 3.2: Correlation coefficients of particles (< 5nm), gaseous sulfuric acid and sulfuric acid clusters. UCL and LCL refer to the upper, lower limit of a 95% confidence interval respectively. Whether a correlation is significant or not is shown in the last column. Dashed lines refer to a correlation by chance.

X = 1, 2 results in a negative value of R, x = 3 and y = 0, 2 in a positive. That observation holds for the correlation of the charged clusters with the N5 particles as well as for the correlation with the condensable gas. It suggests the growth of smaller clusters to bigger ones by attachment of sulfuric acid and water molecules. For atmospheric conditions (ion production rate = 1-30 cm^{-3} s^{-1}, $H_2SO_4 < 5 \cdot 10^7$ cm^{-3}), cluster ions accumulate less than 100 sulfuric acid molecules before they are lost due to recombination [Lovejoy et al., 2004]. Therefore the pathway for ion-induced nucleation involves ion cluster growth followed by recombination producing a stable neutral cluster, larger than the critical cluster that continues to grow [Arnold, 1980]. This is an effective mechanism to bypass the thermodynamically given barrier of critical cluster formation and might reflect the reason of the observed positive correlation between measured small particle and sulfuric acid cluster concentrations.
To gain more insight into the ion cluster evolution and chemistry the NO_3^- clusters which grow by condensation of nitric acid were plotted against NO_y, NO_x and NO_2 mixing ratios measured during the flight. NO_y includes NO_x, that is NO + NO_2 but also HNO_3 and PAN (peroxyacetyl nitrate). The scatter plots are shown in **figure 3.7** and the correlation coefficients are listed in **table 3.3**. The three different cluster families are always negatively correlated to each trace gas. From **figure 3.3** it emanates that the three nitrate clusters of mass 125, 188 and 251 amu were the most abundant ions during the flight. Since the peak at mass 188 is actually centered between 195 and 188 amu no answer can be given to what extend the sulfate cluster at 195 amu

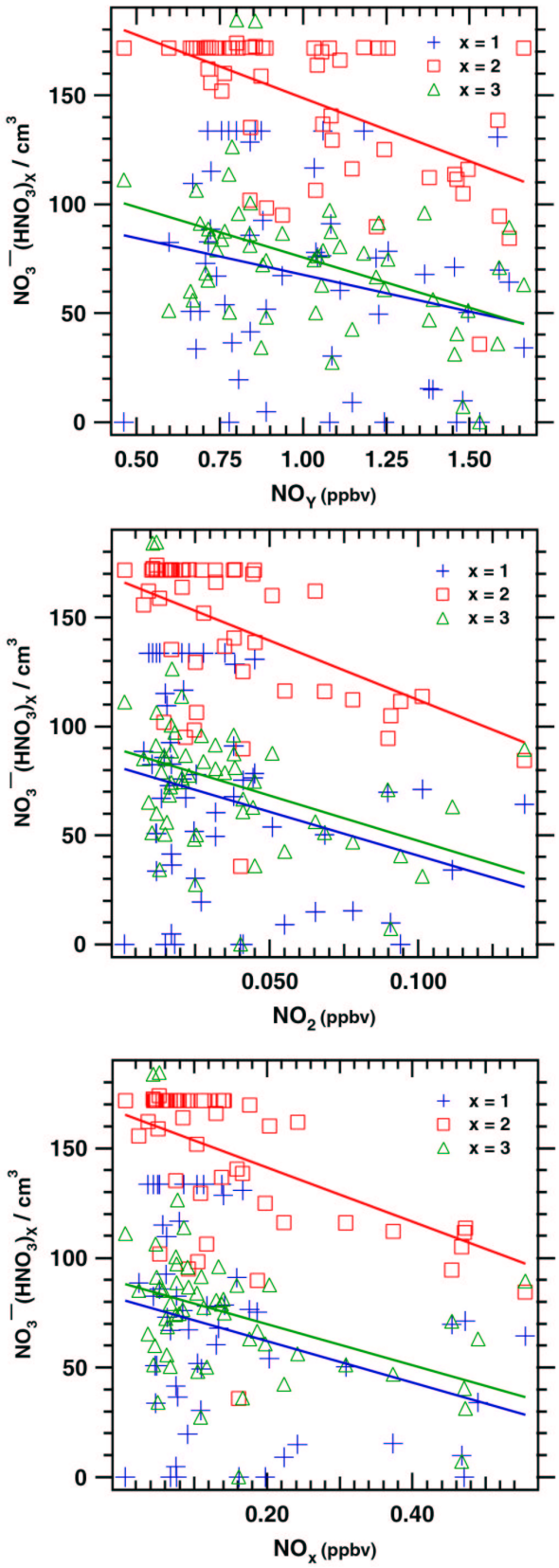

Figure 3.7: Correlation of nitrate cluster $NO_3^-(HNO_3)_x$ with NO_y, NO_x and NO_2.

contributes. However, the tendency towards a negative correlation coefficient should remain. The NO_y concentration increases during flight temporarily by a factor of two. Since hereby also the HNO_3 concentrations elevates, the cluster will grow. Apparently the masses favoured by the growth are higher than the one of the x = 3 nitrate such that no accumulation in this mode appears. This would explain the negative correlation to NO_y. Since HNO_3 partly emerges photochemically from NO_x, a reduction in NO_x lowers the forward reaction with the nitrate clusters and thus increases their population. The same argument holds for the ascertained negative NO_2 correlation.
The nitrate clusters (x = 1, 2, 3) also show a negative correlation with the calculated condensable gas concentration (R = -0.29 x = 1, R = -0.69 x = 2, R = -0.74 x = 3). This might be explained by the formation of mixed HNO_3, H_2SO_4 cluster.
Elevated atmospheric CO mole fractions indicate a polluted air mass. Polluted air masses should show enhanced condensable gas concentrations. If so, sulfate cluster ions are of higher occurrence in a polluted air parcel and the derived CG concentration should reflect this elevation. **Figure 3.8** shows the correlation between the condensable gas and the CO mole fraction.

[cluster ion]/[NO_y]	R	R^2 (%)	UCL	LCL	RESULT
x=1	-0.24	5.8	-0.45	0.00	–
x=2	-0.55	30	-0.70	-0.36	SIG
x=3	-0.43	18	-0.61	-0.21	SIG
[cluster ion]/[NO_x]	R	R^2 (%)	UCL	LCL	RESULT
x=1	-0.3	9	-0.50	-0.06	SIG
x=2	-0.52	27	-0.68	-0.32	SIG
x=3	-0.39	15	-0.58	-0.17	SIG
[cluster ion]/[NO_2]	R	R^2 (%)	UCL	LCL	RESULT
x=1	-0.27	7	-0.48	-0.03	–
x=2	-0.49	24	-0.65	-0.28	SIG
x=3	-0.36	13	-0.55	-0.13	SIG

Table 3.3: Correlation coefficients of nitrate ion cluster with different trace gases (NO_y, NO_x and NO_2). UCL and LCL refer to the upper, lower limit of a 95% confidence interval respectively. Whether a correlation is significant or not is shown in the last column. Dashed lines refer to a correlation by chance.

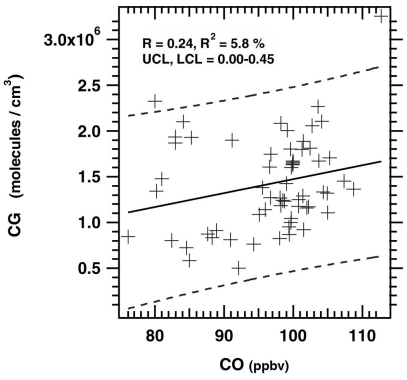

Figure 3.8: Scatter plot of the CO mole fraction (ppbv) versus condensable gas concentration. Dashed lines refer to the prediction band considering a 95% confidence level. UCL, LCL denote the upper, lower limit of the confidence interval respectively.

Also shown in the graph is the prediction band taking into account a confidence level of 95%. The prediction band is that area where 95% of all measured values should fall in. The correlation is just about significance.
Panel 3.9 shows the temporal abundance of several trace gases during the flight of the 16^{th} of July. Starting with the top plot, relative humidity and CG concentration, it appears that with respect to ice, saturation is reached. It is therefore likely that the aircraft crossed several Cirrus clouds at altitudes of about 9 km. These periods coincide with those of elevated NO_y and NO_x mole fractions. Ozone varies between 80 to 120 ppbv which does not indicate a lower stratospheric entrusion. CO varies between 80 to 150 ppbv and indicates weak polluted air masses. The correlation between CG concentration and CO mole fraction as well as the strong correlation of nitrate and sulfate clusters with the CG concentration implies enhanced growth of these clusters within polluted air masses. In earlier studies during the CONTRACE project [Wilhelm, 2003] this finding was also observed. Interestingly the bottom plot in **figure 3.9** indicates enhancements of the NO_x/NO_y ratio also when the CG concentration is increased. The NO_x/NO_y ratio can serve as indicator whether an air mass is at the early stage of its chemical evolution or already aged. It seems here that the observed air masses were quite recently deposited at this altitude.

Finally the goal of atmospheric ion-cluster measurements is to estimate the rate of ion-cluster formation. Since theory is rather complex and the effect of the dipole-charge interaction is not well characterized, the explicit calculation of ion-induced nucleation rates was refrained. Also the extraordinary dependence of the more simple homogenous, binary $H_2SO_4 - H_2O$ nucleation rate on temperature, relative humidity and

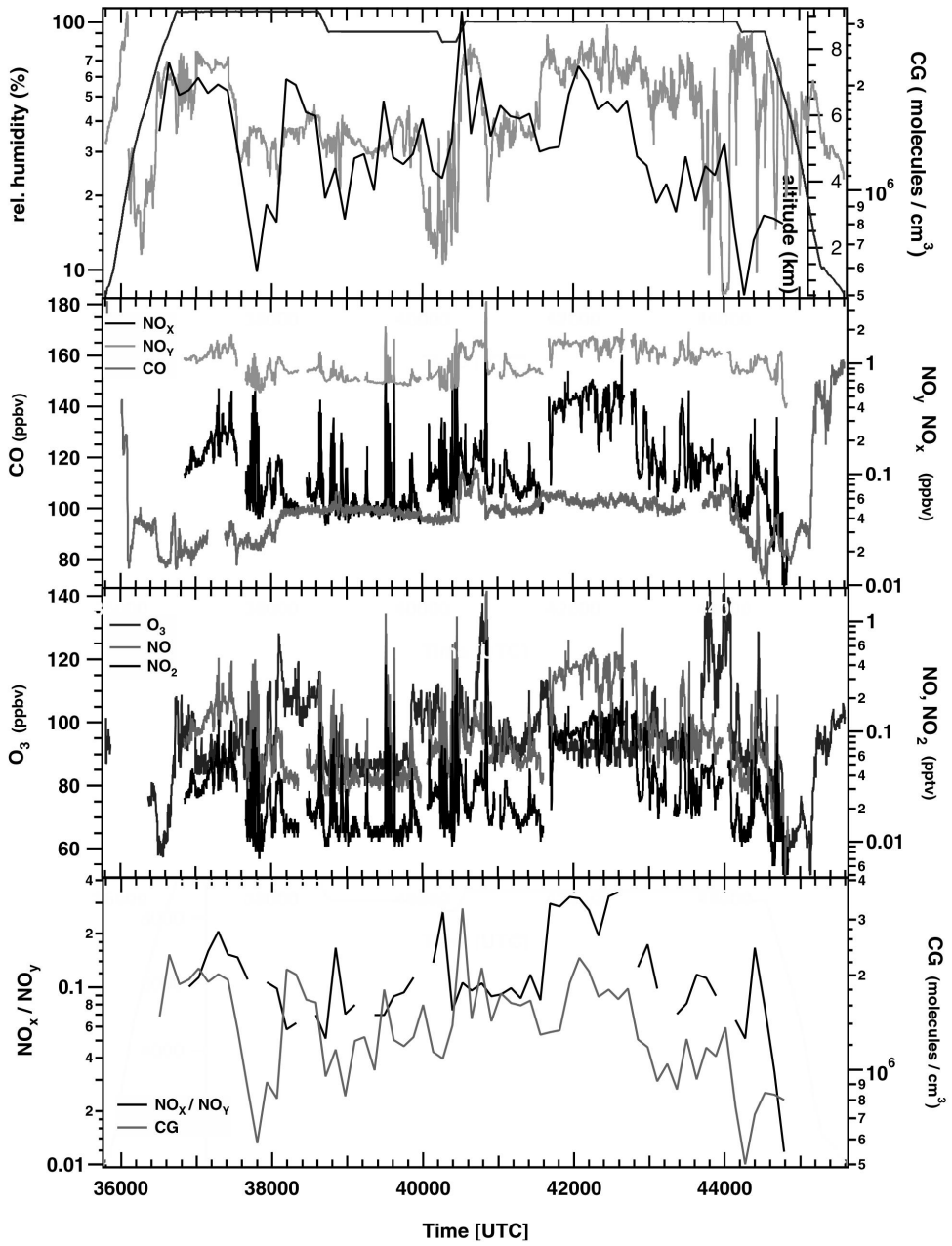

Figure 3.9: Measured trace gas mole fractions during the CONTRACE campaign flight 16^{th} of July, 2003.

H_2SO_4 concentration means, that the inevitable uncertainties in atmospheric measurements produce as much uncertainty in nucleation rate predictions as do the potential uncertainties in theory. This steep variation, although a liability for predicting the nu-

cleation rate, is an asset for estimating atmospheric conditions when nucleation is likely to occur. Using J = 1 cm$_{-3}$s^{-1} as the critical rate above which nucleation is significant, the critical gas-phase sulfuric acid concentration that produces such a rate can be evaluated from the following empirical fit to nucleation rate calculations [Jaecker-Voirol and Mirabel, 1989], [Kerminen and Wexler, 1994]:

$$C_{crit} = 0.16exp(0.1T - 3.5RH - 27.7) \tag{3.5}$$

where T denotes the temperature in Kelvin, RH the relative humidity on a scale of 0 to 1 and C_{crit} is in μgm^{-3}. Thus when the gas phase sulfuric acid concentration exceeds C_{crit}, one can assume that $H_2SO_4 - H_2O$ nucleation commences. **Figure 3.10** shows the measured CG concentration together with C_{crit} and the particle concentration N5.

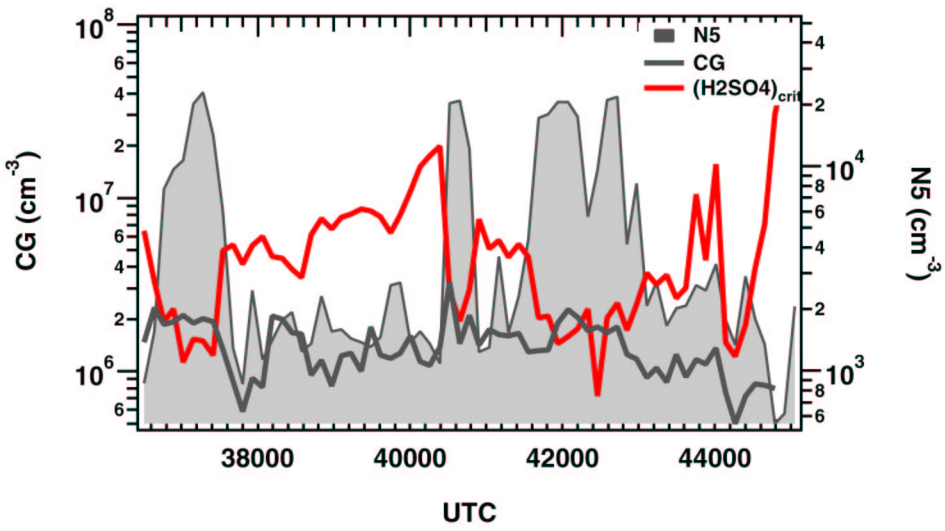

Figure 3.10: Condensable gas-, critical sulfuric acid- and particle concentration.

It appears that in the time intervals UTC 36638-37415 (A), 40520-4077 (B) and 41814-42848 (C) where C_{crit} is below or similar to the CG concentration, also the N5 particle concentration is enhanced. In comparison **figure 3.11** shows the corresponding concentration of the $HSO_4^-(H_2SO_4)_3(H_2O)_2$ cluster. Here increases in cluster concentration are not reflected by the CG values which successively exceed the C_{krit} values. If one assumes that the sulfate clusters of 427 amu did not preexist but grew due to an increase in CG, the observed difference in N5 and N(427 amu) denotes a more efficient ion-induced nucleation rate in the background atmosphere than the one obtained by binary homogenous nucleation of sulfuric acid and water. The three periods of time

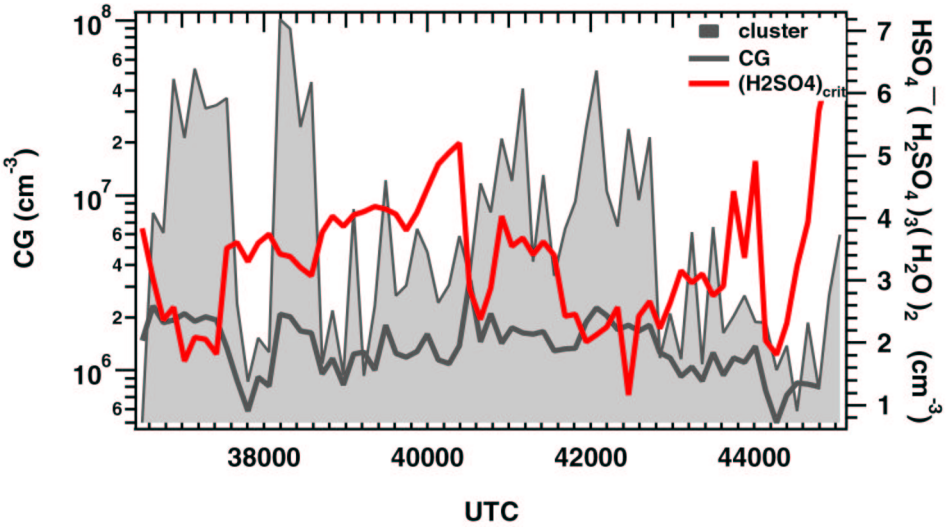

Figure 3.11: Condensable gas-, critical sulfuric acid- and sulfate ion cluster concentration.

A,B and C when CG $\geq C_{crit}$ also coincide with elevated CO, NO_x and NO_y mole fractions. The ratio of NO_x/NO_y identified the air masses during the periods A,B and C to be of recent origin. Thus one might conclude that small particles, more than 5 nm in diameter, were of enhanced abundance in the polluted air masses A,B and C. The increased small particle production coincides with a condensable gas concentration equal to or higher than an empirically estimated lower limit of sulfuric acid necessary to allow binary nucleation with water. In contrast the $HSO_4^-(H_2SO_4)_3(H_2O)_2$ cluster concentration showed enhancements also where CG $\leq C_{crit}$, indicating that ion-induced nucleation seems to be a more effective mechanism in the background atmosphere than in polluted air parcels.

3.3.2 Conclusions

The during the CONTRACE campaign 2003 gained cumulative mass spectra were evaluated. A condensable gas (CG) concentration was calculated from the mass spectra. The knowledge of a CG concentration is important for estimating nucleation rates. The measured particle concentrations N5 (> 5nm in diameter) by the DLR yiel a correlation coefficient of R = 0.55 when related to the CG abundance. A new approach was tested to derive ion cluster abundances from the cumulative mass spectra. The method is based on the assumption that major contributions to the spectra result from

nitrate and sulfate clusters and their hydrates. The different cluster count rates were calibrated to ion concentrations. Total ion concentrations varied between 1000 and 10000 cm^{-3}. Nitrate and sulfate cluster abundances were related to different trace gases such as CO, NO, NO_x, NO_y. Specifically the $HSO_4^-(H_2SO_4)_3(H_2O)_2$ cluster was observed in terms of ion-induced nucleation. It was found that ion-induced nucleation seems to be of more importance in the background atmosphere, whereas homogenous nucleation of the binary system sulfuric acid and water is more efficient in polluted air masses. The result is in accordance with previous observations [Wilhelm, 2003].

Chapter 4

ATMOSPHERIC SULFUR DIOXIDE MEASUREMENTS

4.1 Introduction

The following chapter shows SO_2 data gained during the international campaign ITOP (Intercontinental Transport of Ozone and Precursors), which took place summer 2004. The campaign demonstrates the reliable performance of the IT-CIMS apparatus developed in the framework of this thesis, used on board of the research aircraft FALCON. Two flights out of seven will be discussed in more detail, comprising the detection of an urban pollution plume which contained large amounts of SO_2 relative to background and the sampling of a subtropical air mass low in SO_2 pollution. Data of the ITOP campaign were corrected by subtracting a background of 19 pptv of every single data point.

4.2 Analysis and Evaluation of ITOP SO_2 time series

4.2.1 ITOP Objectives

ITOP is an international project involving teams from Germany, France, the UK and the USA. Its aim is to study intercontinental transport of air pollutants by means of coordinated flights over three geographic regions, (namely the East Coast of North America, Azores and the West Coast of Europe). ITOP is a component of the broader international programme ICARTT (International Consortium for Atmospheric Research

FL ♯	DATE	UT	ALTITUDE (km)	AREA
13	13.07.04	8:04-10:22	0.44 - 11.4	Po Valley
19	19.07.04	9:45-10:41	1.4 - 11.4	Munich to Creil
22	22.07.04	9:41-13:39	0.2 - 11.1	Creil - Spanish west coast (Santiago)
25a	25.07.04	13:41-16:34	0.3 - 10.1	Creil - Irish coast (Shannon)
25b	25.07.04	17:40-19:38	0.8 - 10.5	Irish coast (Shannon) - Creil
26	26.07.04	15:08-18:46	0.6 - 7.2	English Channel
31	31.07.04	12:09-13:45	0.4 - 10.2	Northern France
03	03.08.04	14:25-17:18	0.2 - 6.7	Northern France

Table 4.1: Summary of the 8(9) ITOP flights 2004.

on Transport and Transformation), which coordinates the efforts of various American and European groups who had developed plans for field campaigns in summer 2004, with the aim of improving our understanding of the factors determining air quality over the two continents and over remote regions of the North Atlantic. For this reason the German research aircraft FALCON was based during three weeks in summer 2004 at Creil, France as an operating aircraft platform. During that period of time, the newly developed IT-CIMS set up was used to measure atmospheric SO_2 abundances.

4.2.2 Overview of the ITOP SO_2 Measurements

The present data were obtained during 8 aircraft flights performed above central Europe and the North Atlantic. **Table 4.1** shows date, time, altitude range in which measurements were performed and target area of each individual flight, sorted by flight number. SO_2 time-series of each flight are given in **appendix B.1**. Individual flight tracks of the ITOP campaign projected onto a map, are presented in **figure 4.1**. The following **figure 4.2** shows the median SO_2 mixing ratio throughout the atmosphere, indicated by the black line. The median is calculated with a vertical resolution of 250 m. The area between the two red lines comprises 80% of the determined SO_2 values. The flight of the 13^{th} of July is neglected in the figure. Two maxima appear at 1.8 km and 2.2 km altitude. Above 2.5 km the median profile decreases steadily to values between 30 pptv and 40 pptv until it reaches 7 km. Above 7 km no significant changes appear in the profile.

The median SO_2 concentration below about 3 km can be used to characterize the planetary boundary layer (PBL) pollution. 80% of the values scatter between 100 pptv and 250 pptv which is considerably lower than expected. Continental values reach

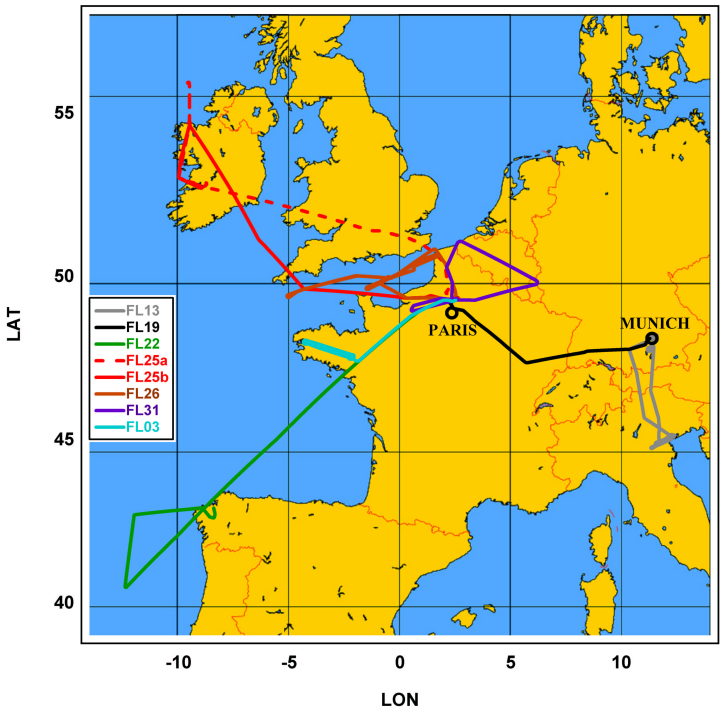

Figure 4.1: Map showing the individual flight tracks of the ITOP campaign 2004.

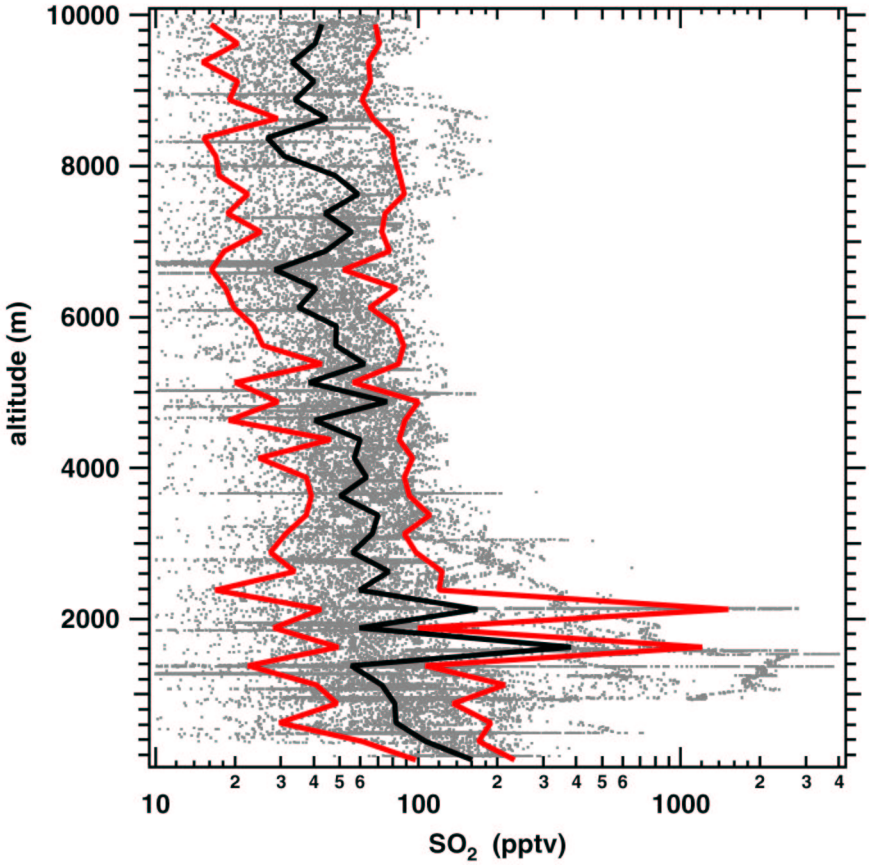

Figure 4.2: Median (black line) and area where 80% of the determined vertical SO_2 values fall in, indicated by the two, red lines. FL13 is not considered.

up to 1500 pptv and 20 - 90 pptv in case of the marine surface layer [Seinfeld and Pandis, 1998]. The problem arises from the way the data is presented here. Marine, continental and urban PBLs are considered equally. Additionally the median distorts the picture and in fact the average would result in larger values. To better characterize the degree of SO_2 pollution in the PBL, air masses which got intercepted above Paris during the ascent and descent of the aircraft are looked at in detail. Also included is the boundary data of the two flights of 23_d and 30_{st} of July, which belong to the campaign SHIPS. The Paris PBL is illustrated in **figure 4.3**. The black curve represents the median (50% percentile) whereas the two red lines define the area where 80% of the data points fall in, corresponding to the 10%, 90% percentile respectively. A vertical resolution of 250 m was chosen.

Below an altitude of 875 m above Paris, data presented in the figure only refers to the flight of 26_{th}, 31_{st} and 23_d of July. We assume that the PBL at this altitude is not fully characterized by the three flights, due to the small amount of data points. Between 875 m and 1.7 km altitude the median varies between 200 - 400 pptv. 80% of the SO_2 values lie within 80 pptv and 2500 pptv. At an altitude of about 1.7 km the median mole fractions decrease sharply and adopt mixing ratios below 100 pptv above 2 km. The profile for the Paris area is in accordance to the expectations. The high variability of SO_2 concentrations in the PBL can result of changes in relative humidity, the presence of clouds, the OH-production rate and the amount of aerosol. Scatter plots of SO_2 with NO_y, CO and relative humidity are given in **appendix B.1**. Some of the measured low SO_2 mole fractions correspond to enhanced relative humidity and indicate wash out processes. The main sources of urban SO_2 which has to be considered here, are coal-fired power plants and car traffic.

Figure 4.4 shows vertical SO_2 abundances of all ITOP-campaign flights, covering an altitude range from 0.2 to 11.5 km. The values scatter between the detection limit of 20 pptv and 4000 pptv. The variability is largest up to an altitude of 4 km. The steep SO_2 decrease above 1 km altitude up to 4 km altitude reflects efficient SO_2 loss preferably by cloud-processes. Again one has to consider that the vertical profile of **figure 4.4** reflects contributions of urban, continental and marine boundary layer air.

Above 4 km altitude the atmospheric SO_2 mole fraction decreases only slowly with altitude. Average abundances are at about 50 to 60 pptv, which is in accordance to previous measurements [Georgii and Meixner, 1980], [Bandy et al., 1993]. At about 8 km the decrease becomes steeper until at 10.5 km a background value of about 30 pptv is reached. The latter described vertical profiling of sulfur dioxide holds for 4 flights out of 8 performed during the campaign and the observed decrease in SO_2 abundances in large altitudes has been observed earlier by [Möhler and F.Arnold, 1992]. In con-

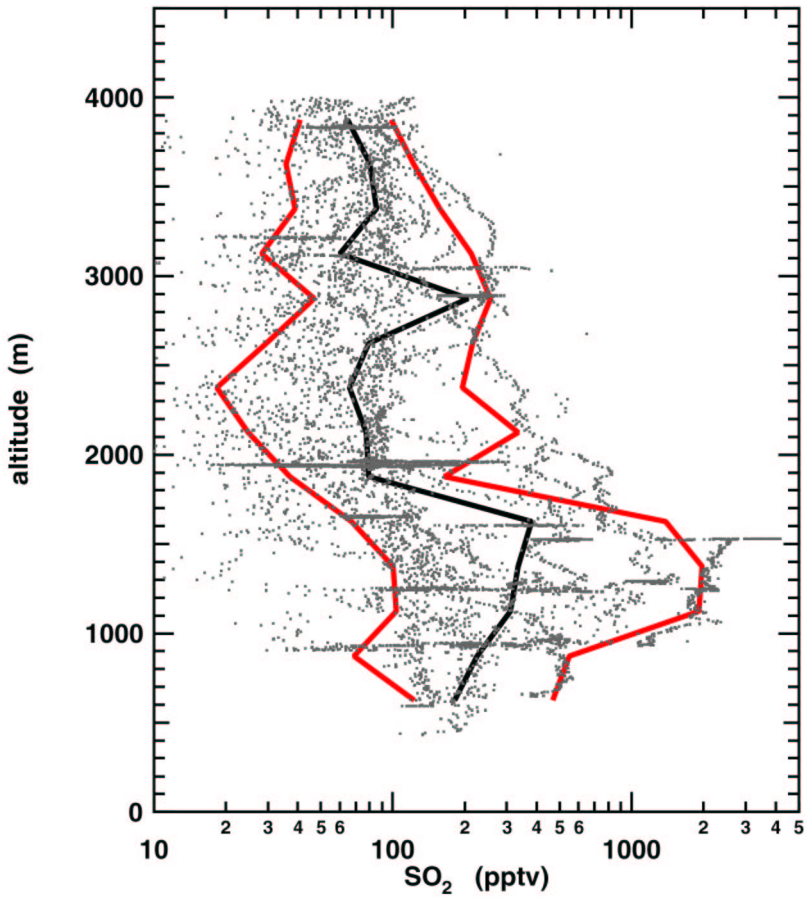

Figure 4.3: Boundary layer SO_2 pollution above the Paris area. 80% of the measured SO_2 mole fractions fall within the two red lines (10% and 90% percentile), whereas the black line represents the median.

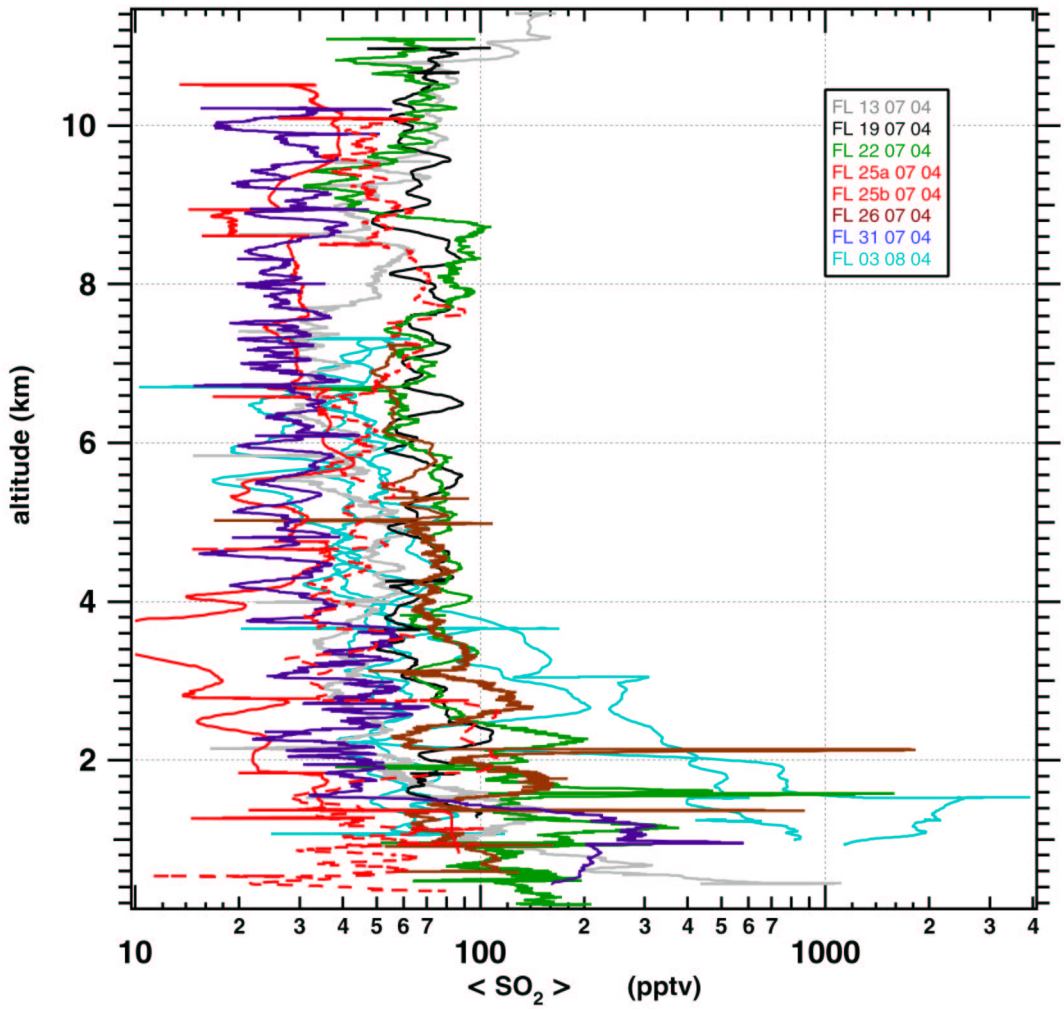

Figure 4.4: Average vertical SO_2 mole fractions measured during ITOP. Remarkably high SO_2 abundances are seen during FL13 at large altitudes. Also FL19 and FL22 show enhancements of SO_2 with altitude in compare to the other shown average profiles.

Approximate TP level (km)	Flight number	Max. altitude (km)
10	13	11.3
11	19	11
12	22	10.7
10	25a	9.7
10	25b	10
11	26	7
10.5	31	9.8

Table 4.2: Thermally derived tropopause heights for the ITOP flights.

trast the vertical profiles of FL13, FL19 and FL22 show with altitude increasing SO_2 mixing ratios above 9 km. An average over these three flights leads to a mole fraction of 140 pptv at 11.5 km altitude. One would expect further decreasing mixing ratios at altitudes above the tropopause, since SO_2 effectively becomes photo-oxidized to sulfuric acid. In other words the observed increased SO_2 values cannot be related to aged air masses. They rather represented air parcels, where SO_2 destruction by OH photo-oxidation is in its early stage. Georgii and Meixner (1980) reported on increasing SO_2 mole fractions at high altitudes, above the tropopause level. Their data were obtained with much lower temporal and spatial resolution. To further evaluate these findings it is necessary to determine the location of the tropopause for the relevant ITOP flights. The tropopause was located at about 11 km for FL19, at 12 km for FL22 and at 10 km in case of FL13, determined by the thermal criteria that the derived laps rate (dTpot/dz) drops below 2°C/km [Poulida and R.R.Dickerson, 1996], accompanied by elevated ozone concentrations to more than 100 ppbV. A dynamic definition via the potential vorticity (PVU) is given in [Hoinka et al., 1993]. Tropopause heights, maximum flight altitude and corresponding flight number are listed in **table 4.2**. The derived tropopause heights are consistent with values given by [Gettelman and S.L.Baughcum, 1999] for July and corresponding latitude and compare to values of 2-3 PVU. Only during two flights (FL26 and FL22) the aircraft did not climb to altitudes close or even above the local tropopause level. Thus the vertical SO_2 profiles can be separated into two different categories: (1) Increasing sulfur dioxide abundances above the tropopause (FL13) and slightly below (FL19, FL22) and (2) constantly descending mixing ratios with increasing altitude. For the first case 190 pptv SO_2 (FL13) were measured at about 11 km as well as 80 pptv (FL19 and FL22) between 10 and 11 km. The second case resulted in average mole fractions of 30 pptv (FL 25a, 25b, FL26 and FL31) between 7 and 10 km. On first sight this result surprises, because

considerations of the budget of the stratospheric sulfate layer suggest a decrease in SO_2 mixing ratio just above the tropopause. Elevated SO_2 at altitudes above 10.5 km was accompanied by an increase in ozone of up to 400 ppbv (FL 13), 120 ppbv (FL 19) and 160 ppbV (FL 22) for at least 5 minutes. Water vapor mixing ratios were at about 10 ppmv (FL13), 42 ppmv (FL19) and 130 ppmv (FL22). Typically water vapor mixing ratios above the tropopause layer are below about 50 ppmv. In case of mixing with lowermost stratospheric (LS) air, H_2O mixing ratios strongly decrease to about 5 ppm [Engel, 1996]. In the upper troposphere the air masses showed a strong correlation between SO_2 and NO_y with a correlation coefficient of R = 0.78 (FL13), R = 0.66 (FL19) and R = 0.74 (FL22). No correlation was found for the SO_2/CO ratio. It amounts to 0.0043 (CO = 60 ppbv at 11.5 km) for FL13, 0.009-0.017 (CO = 80 ppbv at 10.6 km) for FL19 and 0.0014 (CO = 45 ppbv at 10.5 km) for FL22. Upper tropospheric CO abundances were generally below 80 ppbv during the ITOP campaign, as can be seen in **appendix B.1**.

A correlation of SO_2 with NO_y in the upper troposphere is more difficult to explain. SO_2 is mainly released from ground level but can also be directly deposited at high altitudes by aircraft emissions [Hofman, 1991], [Forster et al., 2003]. If released from ground, some fraction will be removed by wash out in clouds via the reaction with H_2O_2 to liquid phase H_2SO_4. Also photo-oxidation by OH radicals will decrease its concentration and is the major sink at high altitudes where no clouds are present. Beside ground level emissions of NO_y which are normally related to combustion processes, NO_y is produced by conversion of N_2O in the stratosphere. Thus if mixing of lower stratospheric air occurs, some fraction of the NO_y enhancements might be due to this. Fast uplift of polluted air might be capable to conserve the original correlation between NO_y and SO_2. It was observed that in the case of CO high forest fire activity can lead to cross-tropopause transport [Trentmann et al., 2001] by so-called pyro-clouds. Certain amounts of CO are uplifted to very high altitudes [Andreae et al., 2004]. During the ITOP campaign severe Canadian forest fires existed. If transported over some distance however, the abundance of CO will decrease and could explain observed elevated background CO values. However, no significant correlation of forest fire CO and SO_2 is expected. Apparently these three flights are examples where SO_2-rich air masses became released at high altitudes or transported from underneath quickly enough not to be strongly influenced by cloud processes such that the initial SO_2 mole fraction was not sufficiently reduced. Additionally NO_y was released, primarily from a similar or even the same source such that the emission ratio between the two species was conserved.

4.2.3 Flight 31: Detection of Subtropical Air

The measurements were performed above Northern France with the northernmost position at LAT: 51.05, LON: 2.71 (close to the French city Lille) and the easternmost position at LAT: 49.79, LON: 6.21 (Luxembourg). Backward trajectories indicate that the intercepted air masses stem from the region easterly of the Caribbean and became uplifted from about 4 km to 6.5 km altitude while travelling to Europe. The air mass travelled mainly above the Atlantic region. During the flight average sulfur dioxide abundances of 35 pptv were measured, showing only little variability with altitude between 2.5 - 10.2 km (**figure 4.5**). The boundary layer was clearly marked during ascent (up to 600 pptv) and descent (200 pptv). NO_y and NO abundances varied between 0.2 - 10 ppbv, 0.01 - 0.8 ppbv respectively. The ozone level showed variations between 30 and 90 ppbv. Between 60 and 80 ppbv of CO were detected. Since the air parcel mainly travelled above the ocean and originated from the Caribbean low abundances of all above mentioned trace gases are expected. Emissions by ships are

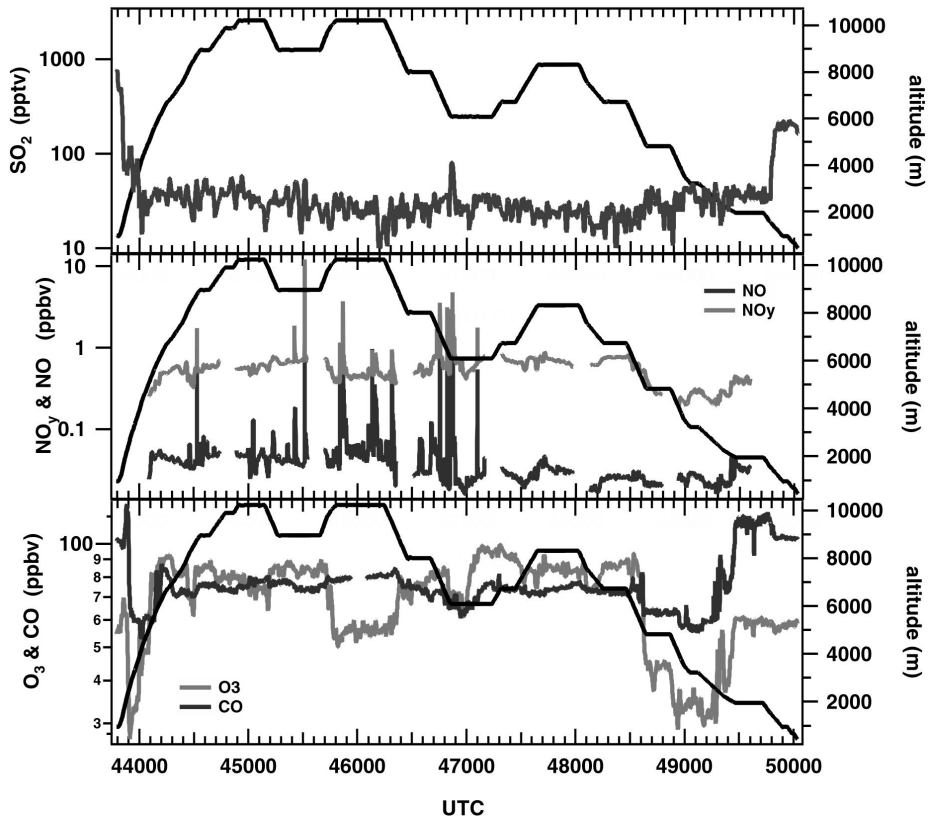

Figure 4.5: Panel of trace gases measured during the flight of 31^{st} of July.

possible pollution sources though. If cloud cover is low, photooxidation by OH radicals will be the dominant SO_2 sink. Considering an initial sulfur dioxide mole fraction of 500 pptv, 20 days of travel derived from trajectory calculations and 10^6 cm^{-3} as 24h average OH concentration, only a fraction of 35 pptv SO_2 would remain.

4.2.4 Flight 26: Detection of an Urban Pollution Plume

The most striking feature of FL26 was the strong SO_2 enhancement up to 2.5 ppbv between at the altitude range 1.4 - 2.2 km at UTC: 62954-63793 (**figure 4.6, 4.7**). The measurements were mainly performed above the English Channel. From trajectory calculations and wind field considerations (**figure 4.6**) it emanates that the measured large sulfur dioxide mole fractions originally stem from the London area.

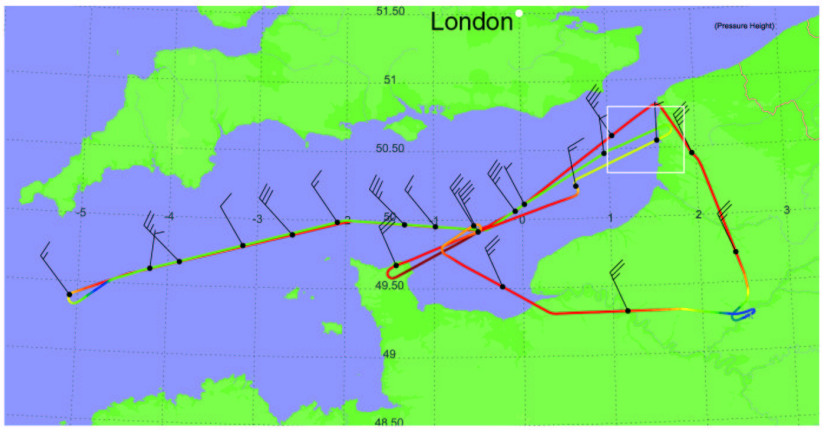

Figure 4.6: Flight pattern: 26^{th} of July, color coded by altitude (red highest; blue lowest flight level). The rectangle marks the area where the urban pollution plume was detected. Wind direction and strength are indicated by arrows.

All trace gases as well as the measured particle number concentrations are summarized in **figure 4.7**. Elevated NO_y (8.5 ppbv) and NO (2.2 ppbv) mole fractions within the plume interception reflect heavy pollution likely to stem from car traffic. These values are by a factor of 10 larger than the measured abundances in clean air, represented by FL31. The ozone level is not significantly enhanced, 46 ppbv are measured during plume crossing. Total particle number concentrations are enhanced within the plume interval. A slightly increased number concentration of N_{13} (D > 13 nm) is observed. But nucleation of fresh particles indicated by an elevated N_4/N_{13} ratio does not appear

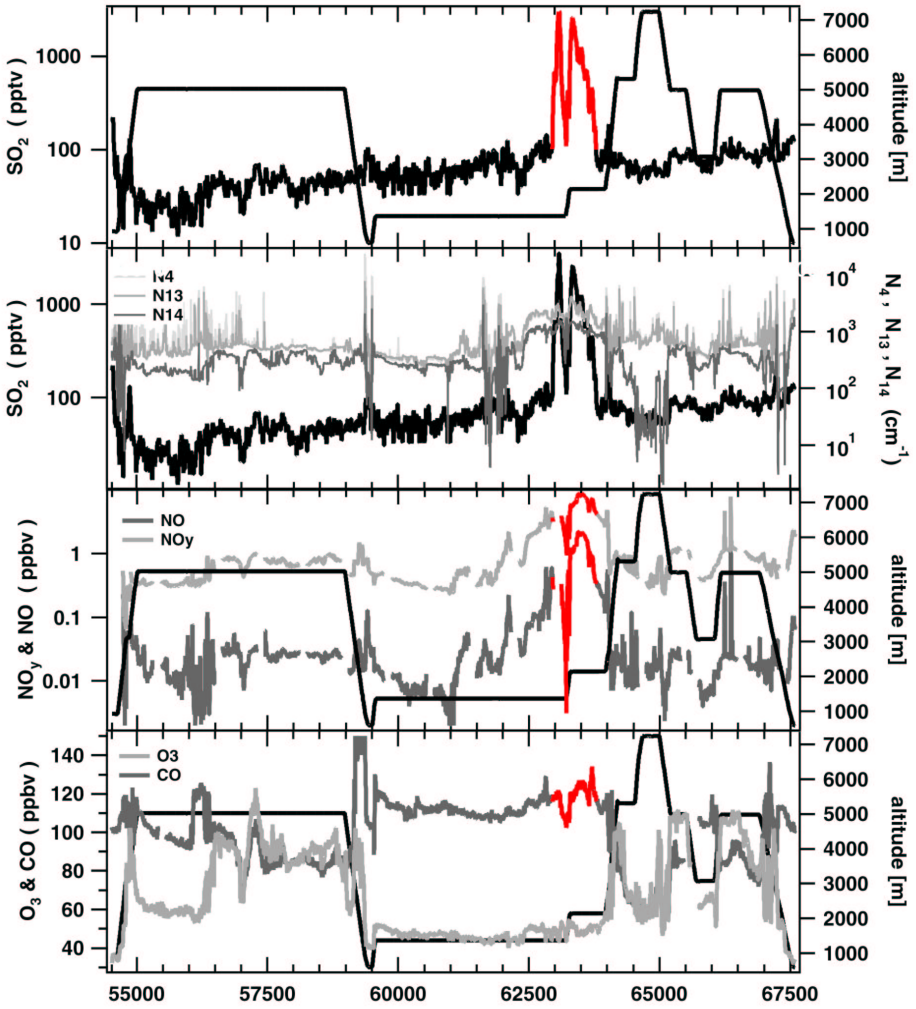

Figure 4.7: Trace gases as well as particle number concentrations measured during flight of the 26^{th}.

[1]. [Weber et al., 2003] reported on high concentrations of 3 to 4 nm diameter particles in anthropogenically polluted plumes that were identified by enhanced CO and fine-particulate sulfate concentrations. In contrast to these anthropogenic plumes, few 3 to 4 nm particles were found in clean background and few were detected within a

[1]Particle Counters TSI 3760A, TSI 3010, nonvolatile particles pre-heated to T = 250°C. N_4 cm^3: number concentration of particles with size D > 4 nm (N4) in $1/cm^3$ ambient. N_{13} cm^{-3}: number concentration of particles with size D > 13 nm (N13) in 1/cm3 ambient. N_{14} cm^{-3}: number concentration of nonvolatile particles of size D > 14 nm (N14)in $1/cm^{-3}$ ambient.

volcanic plume where the highest H_2SO_4 concentrations were recorded. CO increases up to about 125 ppbv inside the plume and is not significantly high compared to values of urban pollution plumes given by [Parrish et al., 1991]. The ratio of CO to NO_y in a polluted air parcel must depend on three factors: (1) the level of CO and NO_y in the background air that initially receives the pollution and dilutes the air parcel during transport; (2) the ratio of emissions of CO and NO_y; and (3) the photochemical transformation of the air parcel, which removes a different fraction of each pollutant in the time between emission and measurement. NO_y background concentrations in the troposphere in regions free of significant anthropogenic input are of the order of a tenth of a part per billion by volume [Parrish et al., 1982]. In contrast the here measured CO background levels are a significant fraction of the total levels that were observed. The CO background mixing ratio was referred to the zero crossing of the plotted CO to NO_y ratio and amounts to 100 ppbv. The derived CO/NO_y emission ratio of 2.9 shown in **figure 4.8** corresponds well to the one found by [Kok et al., 1997] for plumes emitted from urban Hong Kong where the ratio was ~ 3 ppbv. They attributed the low CO/NO_y ratio to a large fleet of diesel vehicles. However, taking the work of [Parrish et al., 1991] into account these low ratios could equally be related to power plant emissions. Also one has to consider that the measurements were performed during midday in July and probably photooxidation reduced the amount of CO that eventually was transformed to HO_2 and CO_2.

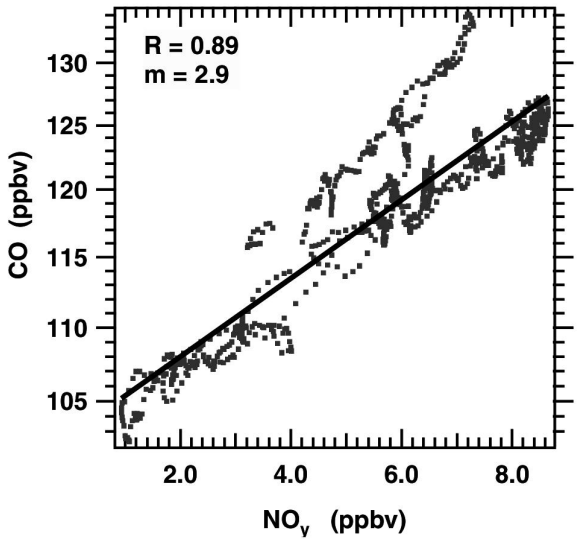

Figure 4.8: Ratio of CO/NO_y measured within the urban plume. The correlation coefficient is R = 0.42. The emission ratio CO / NO_y is derived to 2.9 ppbv/ppbv.

The SO_2 to NO_y ratio provides a key to distinguish between air parcels dominated by point sources (primarily power plants) and those dominated by mobile sources (vehicles). If the SO_2/NO_y emission is high (> 1 ppbv/ppbv), power plant generation dominates the source of NO_y. If low (< 1 ppbv/ppbv) it is more attributed to urban vehicle emissions [Parrish et al., 1991], [Wang et al., 2002]. This criterion assumes that the ratio of SO_2 to NO_y is conserved in the atmosphere, which would be true if no significant removal has occurred or if SO_2 and NO_y are removed at approximately the same rate. The derived SO_2/NO_y ratio for FL26 is shown in **figure 4.9**.

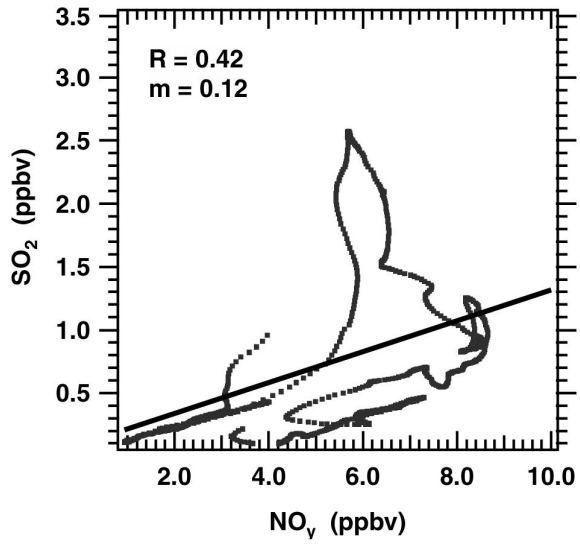

Figure 4.9: Ratio of SO_2/NO_y measured within the urban plume. The correlation is well with R = 0.42. The emission ratio SO_2 / NO_y is determined to be 0.12.

The correlation coefficient is R = 0.42 and the SO_2 to NO_y emission ratio amounts to 0.12 ppbv/ppbv. Thus considering the above-stated partition of SO_2 to NO_y one would refer the measured plume to contain large input from mobile emission sources (car traffic) as expected. In case power plant input would be dominating, more SO_2 compared to NO_y would be present. However, efficient effluent scrubbing present in modern power plants also leads to low SO_2/NO_y emission ratios.
Thus presumably both sources, mobile as well as point sources, have contributed in different amounts to the observed plume with some emphasis on vehicle emissions. To finally characterize different plume sources, the time discrepancy between pollution uptake and plume detection would it make necessary to estimate the effects of photooxidation. The increased number of large particles (D > 14 nm) may result from

an older air mass where small and freshly nucleated particles are scavenged by larger particles.

4.2.5 Conclusions

The SO_2 data gained by use of the IT-CIMS instrument during the ITOP campaign is accurate, reliable and of high temporal resolution. No background problems appear as can be seen by detection of clean subtropical air. Interesting implications concerning new particle formation as well as condensational growth might be given by the detected high sulfur dioxide abundances in the lowermost stratosphere / upper tropopause. Further evaluation of the data could include a comparison of the PBL layer above Paris with the pollution plume from the London area. Therefore the for the London plume already prepared SO_2, NO_y and CO data correlations can be used.

Chapter 5

ATMOSPHERIC SULFUR DIOXIDE TRANSPORT

5.1 Introduction

The origin of stratospheric SO_2 is still uncertain at least for periods unaffected by SO_2 injection from rarely occurring major volcanic eruptions. Little is known about the steady background contribution from OCS to the total amount of stratospheric aerosol by binary homogenous nucleation via sulfuric acid [P.J.Crutzen, 1976] and [Logan et al., 1979]. Until present one experimental data set exists proposing that during periods of low volcanic activity stratospheric SO_2 may be mostly due to convective injection of SO_2 containing ground level air [Thornton et al., 1997]. However, important details of convective SO_2 injection are only poorly understood. The following will report on aircraft-based investigations of convective SO_2 injection into the lower stratosphere (LS). A mesoscale SO_2-rich pollution plume was detected above Central Europe, which formed 9 days prior to our interception. The plume rose in the Eastern United States by convective injection of anthropogenically polluted lower tropospheric SO_2-rich air.

5.2 Convective Transport

Transport of deep convective clouds (cumulonimbus clouds) greatly changes the distribution of chemical species in the troposphere. However convective transport is very localized. In a region typically covering the area of a grid cell in a global model (e.g. 100 km $\times$ 100 km), perhaps 99% of the area is not affected by convective updraft whereas on the remaining 1% the vertical exchange between planetary boundary layer

air (PBL) and upper tropospheric air (UTS) occurs on a timescale of about one hour [Brasseur et al., 1999]. A mesoscale convective complex (MCC), considerably larger than an individual thunderstorm, produces the same result but on a much larger scale. The size of an MCC cold-cloud shield exceeds that of an individual thunderstorm by more than two orders of magnitude [Maddox, 1980].

The force causing the uplift of a certain air mass, results from the density difference between air parcel and environment. The air parcel rises until its actual temperature decrease rate with altitude becomes slower than the moist adiabatic temperature gradient. It then reaches its level of free convection. During adiabatic ascent, the thermal energy is converted into potential energy, which consequently cools the air parcel [1]. The differential temperature decrease of the rising air mass becomes reduced, when temperature falls below the condensation level and latent heat is released. The energy released in this process is called convective available potential energy (CAPE). The larger CAPE, the more buoyant the air, hence stronger convection. CAPE is calculated by integrating over height the (virtual-potential) temperature[2] difference the lifted air parcel and the environment. The integration normally is started from the level of free convection, which is the level above which the lifted parcel is warmer than its environment. The upper limit for the integration is the level of neutral buoyancy in which the parcel and environment temperature meet again.

Consequently convection is capable of transporting air of lower tropospheric origin into higher altitudes. The question arises how far up this transport may occur? Obviously the density of an air parcel is the driving force in terms of convection. The moist adiabatic temperature gradient and the inherent temperature change of a rising air parcel define its level of neutral buoyancy.

The tropopause marks an altitude level where the ambient temperature gradient changes. By definition of the World Meteorological Organization (WMO), the tropopause is defined as the lowest level at which the rate of decrease of temperature with height (the temperature lapse rate) decreases to 2 K km^{-1} or less and the lapse rate averaged between this level and any level within the next 2 km does not exceed 2 K km^{-1} [Holton et al., 1995]. The tropopause is at a maximum height in the tropics and sloping down towards the poles [Seinfeld and Pandis, 1998] leading to the stratosphere-troposphere exchange. The tropopause can be considered as a natural lid of the troposphere. It limits the exchange between LS und upper troposphere. Rising air parcels normally not have enough energy to overcome that barrier.

[1] For an adiabatic process the sum out of thermal and potential energy remains constant.

[2] Virtual potential temperature means: temperature when the air parcel is moved dry adiabatically to standard pressure (1013 mbar) plus the temperature contribution related to latent heat release.

During severe storms (high CAPE) however, this lid can be displaced allowing not only the main stream of the overshooting tops of a cumulonimbus cloud to penetrate through but also the anvil to extend into an area that used to be dominated by air of stratospheric character [Poulida and R.R.Dickerson, 1996],[Fischer et al., 2003]. This context is illustrated in **figure 5.1**. It shows how the tropopause is deformed and lower tropospheric air mixes out of the anvil into the lower stratosphere.

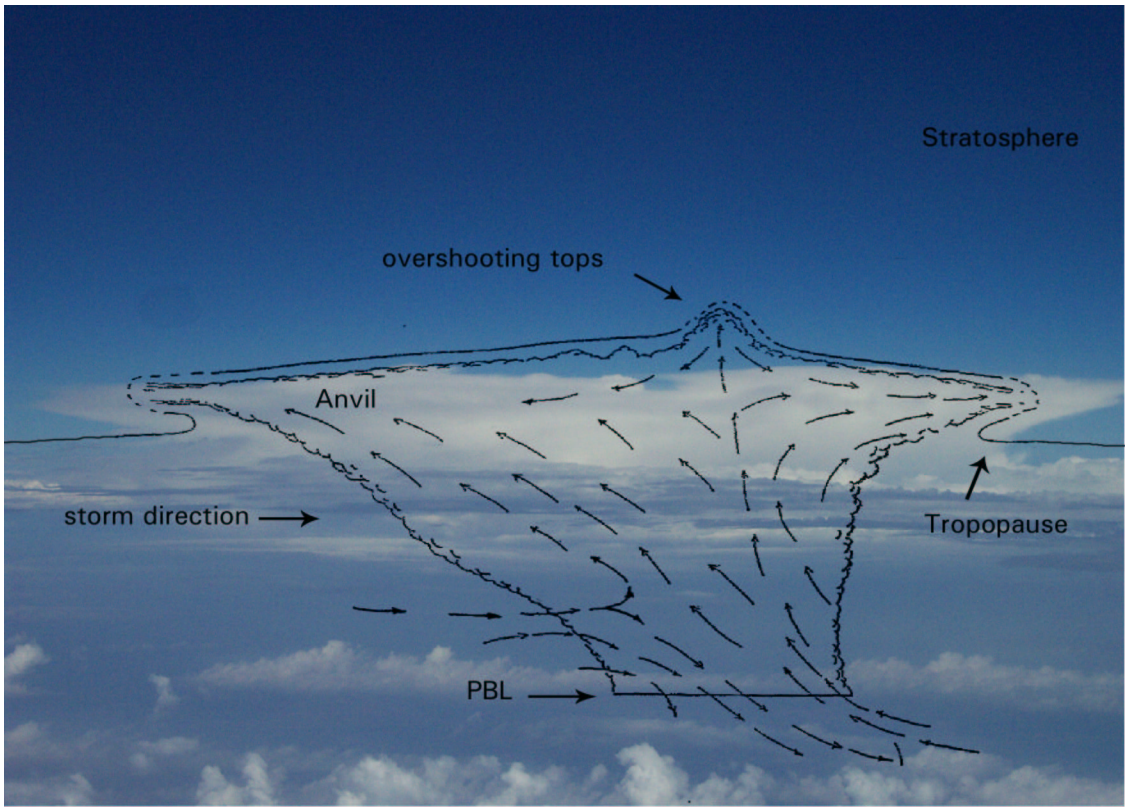

Figure 5.1: Convective system. Arrows represent the updraft and downdrafts with respect to the motion of the storm, scheme from [Poulida and R.R.Dickerson, 1996].

The anvil resides well below the tropopause and is composed of air with modified tropospheric characteristics. Entrainment of ambient air into the downdrafts of the anvil modifies the thermal and chemical properties of the draft. Consequently the vertical profile of the anvil shows upper tropospheric air below the anvil and modified lower tropospheric air inside the anvil.
If entrainment into an updraft is inversely proportional to the diameter of the cloud [E.Palmen and C.W.Newton, 1969], then in a large convective system, the air of the core updraft should shoot through the troposphere with only little entrainment of

middle-tropospheric air.
However, only little is known about convective SO_2 injection into the LS. Frequency and strength of convection events overshooting the tropopause as well as SO_2 removal by clouds usually associated with vertical transport are uncertain (c.f. Wang and Crutzen,1995; Andromache et al, 1999; Crutzen and Lawrence, 2000). Removal of SO_2 by clouds is a complex process as it depends critically on the pH of the cloud droplets and on the presence of liquid-phase oxidants particularly H_2O_2. In turn the pH depends critically on the presence of other atmospheric trace substances particularly HNO_3, NH_3 and alkaline mineral dust.
Stratospheric binary nucleation is particularly efficient in the lower stratosphere (LS) where temperatures are low and water vapor is sufficiently abundant (Turco). Stratospheric aerosol particles have a potential influence on climate for at least three reasons: (1) They scatter incoming sunlight back to space and thereby contribute to the planetary albedo, (2) they catalyze stratospheric ozone destruction and after their ultimate return to the troposphere they may act as cloud condensation nuclei (CCN)(3).
The major source of stratospheric SO_2 during periods unaffected by rarely occurring major volcanic eruptions seems to be convective injection into the LS of tropospheric SO_2, [Chin and D.D.Davis, 1995] and [Kjellstroem, 1997]. In the tropics the SO_2 convectively injected into the LS becomes lifted higher into the middle and upper stratosphere by the residual circulation while at middle latitudes it is preferably returned to the troposphere after an average LS residence time of only about 23 days [Forster et al., 2003]. However, despite its relative shortness this LS residence time of 23 days is mostly sufficient for nearly complete OH-induced SO_2 conversion to sulfuric acid followed by rapid sulfuric acid condensation and nucleation. In a model simulation these freshly nucleated particles grew to different sizes with the largest being 50 nm at a number concentration of 70 cm^{-3}. Conclusively they might get transported into the upper troposphere via the tropopause. Followed by further coagulation and condensation they could possibly terminate as high-altitude cloud condensation nuclei.

5.3 Detection of a Lower Stratospheric SO_2 Plume

The aircraft-based measurements took place on the 13^{th} of July 2004 during a flight of the research aircraft FALCON from Southern Germany to Northern Italy when a LS pollution plume was intercepted at altitudes around 11 km above Northern Italy. Beside SO_2 additionally O_3, H_2O, NO, and NO_y were detected by DLR. **Figure 5.2** illustrates geography and the corresponding flight track with the period of plume interception marked in grey.

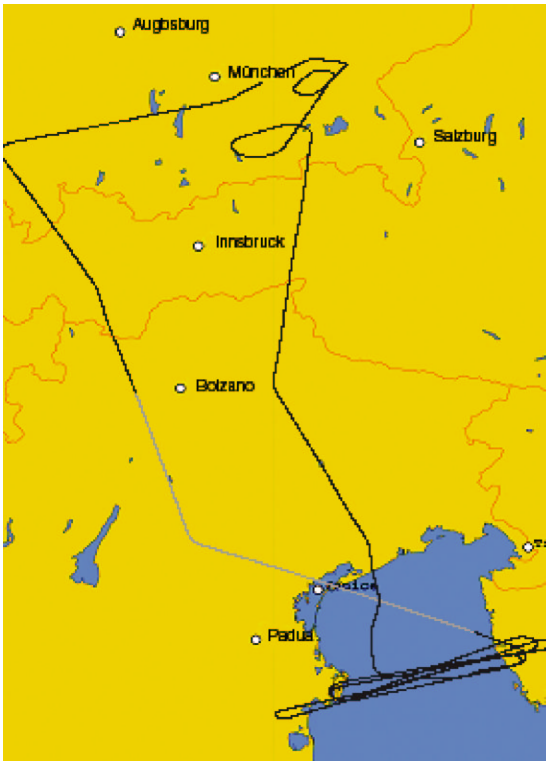

Figure 5.2: Flight track of the FALCON aircraft. The period of interception with the SO_2 plume is marked in grey.

Figure 5.3 shows the flight track of the FALCON along with a FLEXPART model simulation of the SO_2 pollution plume. Plotted is a horizontal cross section at 11000 m altitude of the calculated SO_2 mole fraction. FLEXPART treats SO_2 as a passive pollution tracer and therefore tends to overestimate SO_2. In real sulfur dioxide gas is not passive in fact it may be lost by dry deposition, cloud processes, and OH-induced conversion to sulfuric acid. Some details concerning the FLEXPART model will be presented in a later section of this chapter. **Figure 5.3** reveals that the SO_2 rich plume has the form of a tongue extending from Iceland to Southern Italy. The center of the sulfur dioxide pollution plume lies further north, above Northern Germany.
Figure5.4 depicts vertical profiles of SO_2, O_3, H_2O, and temperature measured above Northern Italy during the flight of 13^{th} of July 2004. The temperature decreases with altitude up to about 10 km indicating that the tropopause was located at around 10 km altitude. This is also supported by the ozone profile. O_3 increases noticeably above 10500 m reaching up to 400 ppmv and markedly exceeds typical tropospheric ozone

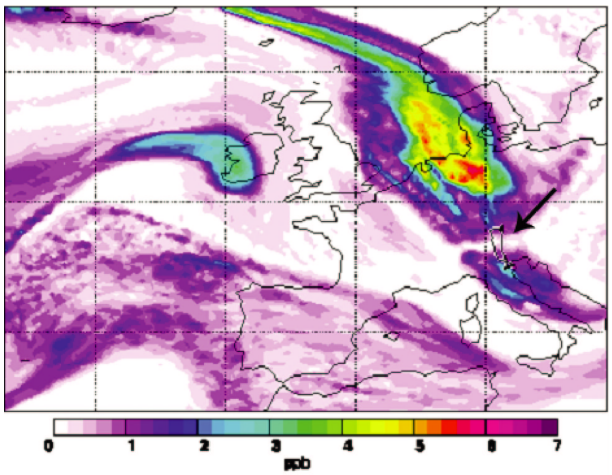

Figure 5.3: FLEXPART model simulation of the SO_2 pollution plume of the 13_{th} of July. Plotted is the horizontal distribution of the SO_2 mole fraction for an altitude of 11 km. Note that the model treats SO_2 as an inert tracer and therefore overestimates the SO_2 concentration. The FALCON flight-path is indicated by an arrow.

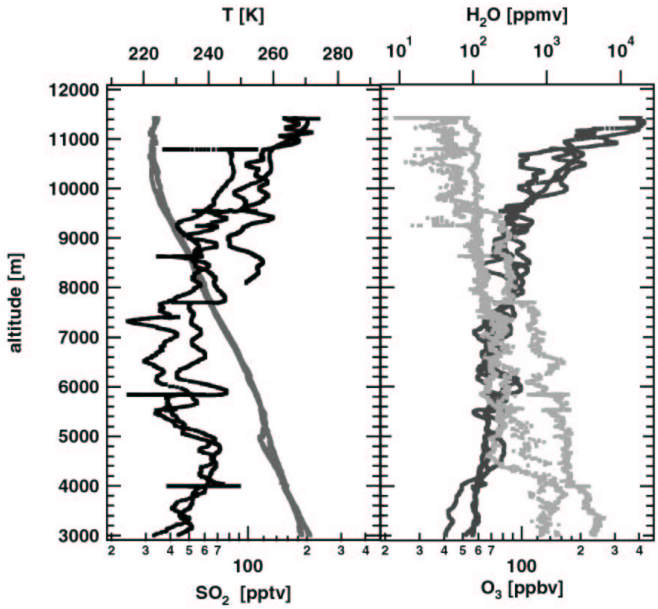

Figure 5.4: Altitude profiles measured during the flight of the 13^{th} of July 2004, above Northern Italy. Given are the atmospheric mole fractions of SO_2, O_3, H_2O and temperature T.

fractions of about 150 pptv. Water vapor mole fractions[3] decline with altitude to values as low as 3-75 ppmv at 11500 m. Values below 10 ppmv are considered to be of typical LS character while mole fractions larger than 100 ppmv rather correspond to upper tropospheric (UT) air.
The following **figure 5.5** shows time-series of flight altitude, atmospheric mole fractions of O_3 and water vapor measured just before, during , and just after interception of the LS pollution plume. In the LS flight segment marked by $O_3 > 150$ ppbv (30450 - 31400 UTC) H_2O ranges mostly between 3 and 50 ppmv. Also shown in **figure 5.5** are the SO_2, NO_y and NO abundances during plume interception.

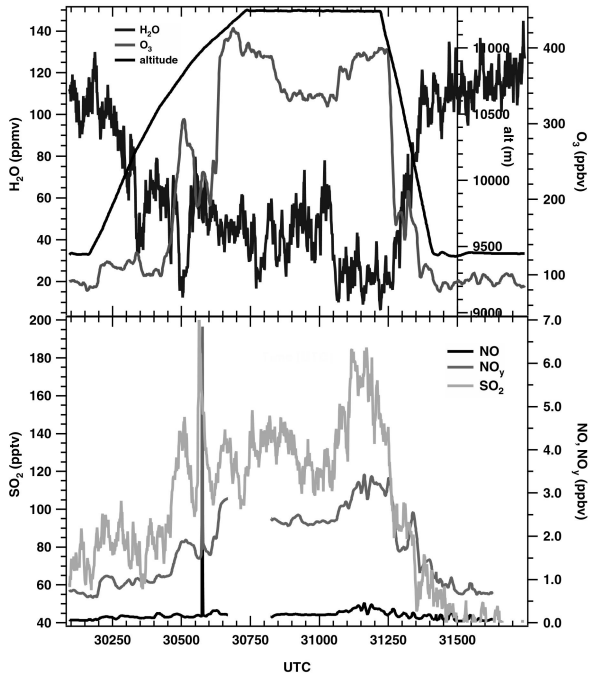

Figure 5.5: Time series of atmospheric data measured during the flight of the 13^{th} of July 2004 along with flight altitude. Given are O_3, H_2O, SO_2, NO_y and NO mole fractions.

In the time interval UTC: 30450 - 31400 s, SO_2, NO and NOy are markedly elevated and significantly correlated with a correlation coefficient of $R(SO_2,NO_y) = 0.88$ (77%). The highest SO_2 (180 pptv) and NOy (3300 ppt) mole fractions were observed mostly

[3]The water vapor mole fractions are obtained by the method presented in appendix A.1.5. The lyman-α instrument operated on board of the FALCON did not produce reliable data for the LS. Thus the mass spectrometric method was developed.

in the segment ranging from UTC: 31000-31400 s. The close correlation suggests that SO_2 and NO from which the NO_y gases are formed originated from a common source. Another striking feature noticeable in **figure 5.5** is the large NO, NO_y spike at around UTC: 30574 s, accompanied by a large SO_2 spike. This small-scale pollution plume is likely to be formed by an aircraft passing some time before the FALCON aircraft the same area. The period of interception is about 1 s, corresponding to a horizontal, aged plume extension of 180 m. The ratio of excess SO_2/NO_y equals 0.025. Typical aircraft SO_2/NO_y emission rates are of about 0.029 considering emission factors of 15 g NO_x (as NO_2) / kg fuel burnt and a mean fuel sulfur content of 300 ppm. The similarity supports an aircraft origin of the plume.

5.4 Meterological Situation

Since the following graphs were obtained by the FLEXPART model the next chapter first introduces briefly the model principle and explains some terminology.

5.4.1 The FLEXPART Model

FLEXPART is a newly developed Lagrangian particle dispersion model designed for emergency response and research applications. It simulates the long-range transport, diffusion, dry and wet deposition, and radioactive decay of air pollutants released from point, line, area or volume sources. The model is based on data from the European Center for Medium-Range Weather Forecasts (ECMWF). A detailed description of the model can be found in " The FLEXPART Particle Dispersion Model Version 3.0 User Guide ", by Dr. A. Stohl.
The here used and shown meteorological FLEXPART forecasts are based on considerations which were developed and tested especially for the framework of the international ITOP campaign. The following lines are taken from the web page which explains the forecast products (by Dr. A. Stohl): "Backward simulations are done from along the flight tracks and the ship cruise, and from the locations of the measurement stations. Whenever an aircraft changes its position by more than 0.2 degrees, a backward simulation is initiated. Also, whenever it changes its altitude by 50 m below 300 m, 150 m below 1000 m, 200 m below 3000 m, or 400 m above, a new backward simulation is initiated. Per box 40000 particles are released. The model comprises full turbulence and convection parameterization."
The shown plots are named **column residence time** and **source contributions** and explained in the following (by Dr. A. Stohl):

"**Column residence time** shows the vertically integrated residence time of the particles without an altitude information. Strictly, this is not a residence time, but the response an emission release of unit source strength would have at the receptor (i.e., at the measurement point) assuming no chemical transformations, deposition, etc. The unit shown is nanoseconds times meters divided by kilograms. The numbers superimposed on the shading are the days back in time and give an approximate indication of where the plume was at what time..."
"The SO_2 **source contribution** is the product between "residence time" (or response function, or source-receptor-relationship; there are different names in the literature) and anthropogenic emission flux (in kilograms per square meter and second) taken from the inventories. The result is an emission contribution in ppb per square meter. If the emission contribution is integrated over the Earth's surface, a "tracer" mixing ratio at the sampling location is obtained. It is also reported on the plot and, furthermore, Asian, American and European contributions are listed separately. These mixing ratios are quantitatively comparable to the measurements under the assumption that the species is conserved (no chemistry, no deposition)."

5.4.2 Model Results

The FLEXPART model results serve to identify the source region of the detected LS sulfur dioxide pollution plume, the time of travel and its altitude range during its travel. **Figure 5.6** shows the column-integrated source receptor relationship. That is response an emission release of unit soruce strength would have at the measurement site. No altitude information is contained in the plot. The plume spreads tongue-like from Norway via Northern Germany to the Po valley where it was detected. No altitude information is contained in the plot but it appears that after two slopes above Greenland, the plume stretches to the North East coast of the United States from where it travelled towards the Great Plains. This is a region of heavy industry (coal mining, steel production and oil refinery) with strong urban traffic contributions. Several large cities such as Detroit, Chicago and Pittsburgh with a lot of industry are present. The plume terminated in that area after about 9 days of travel. **Figure 5.7** gives the sulfur dioxide emission contribution averaged over the Earth's surface. The obtained SO_2 tracer mixing ratio is largest for the North American region, 75% of the total mixing ratio, with a 25% contribution from Asia and no contribution from Europe. The main contribution seen on **figure 5.7** could be related to the region around Pittsburgh and Kansas City. Both cities comprise about one million inhabitants.
[Smith and J.H.E.Clark, 2004] report about a case study on May 21^{st} 2004 where cold-

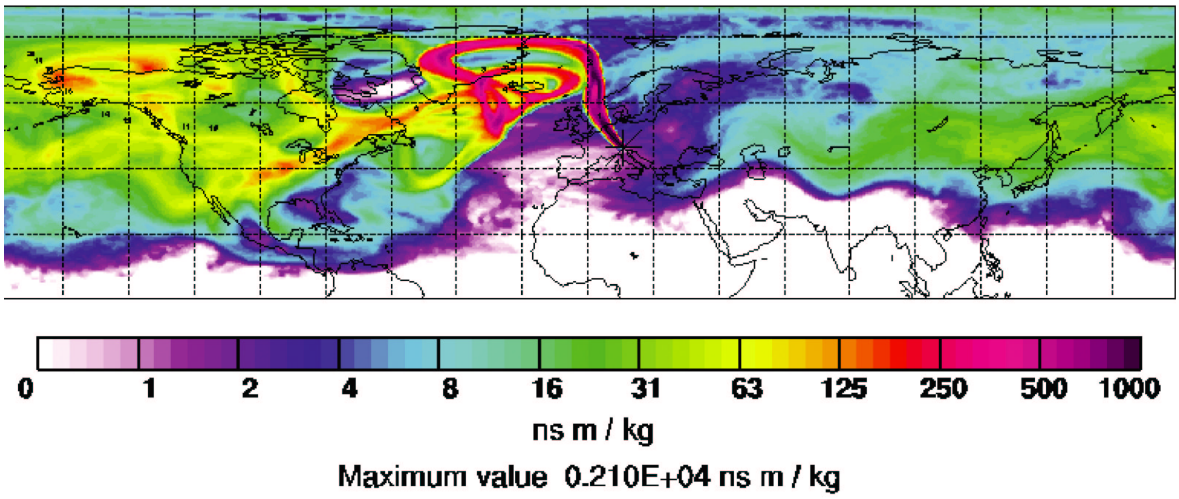

Figure 5.6: Column-integrated source receptor relationship. Start-end time of sampling UTC: 8:25:40-8:27:32. Meteorological data used is 1 × 1 deg ECMWF analysis.

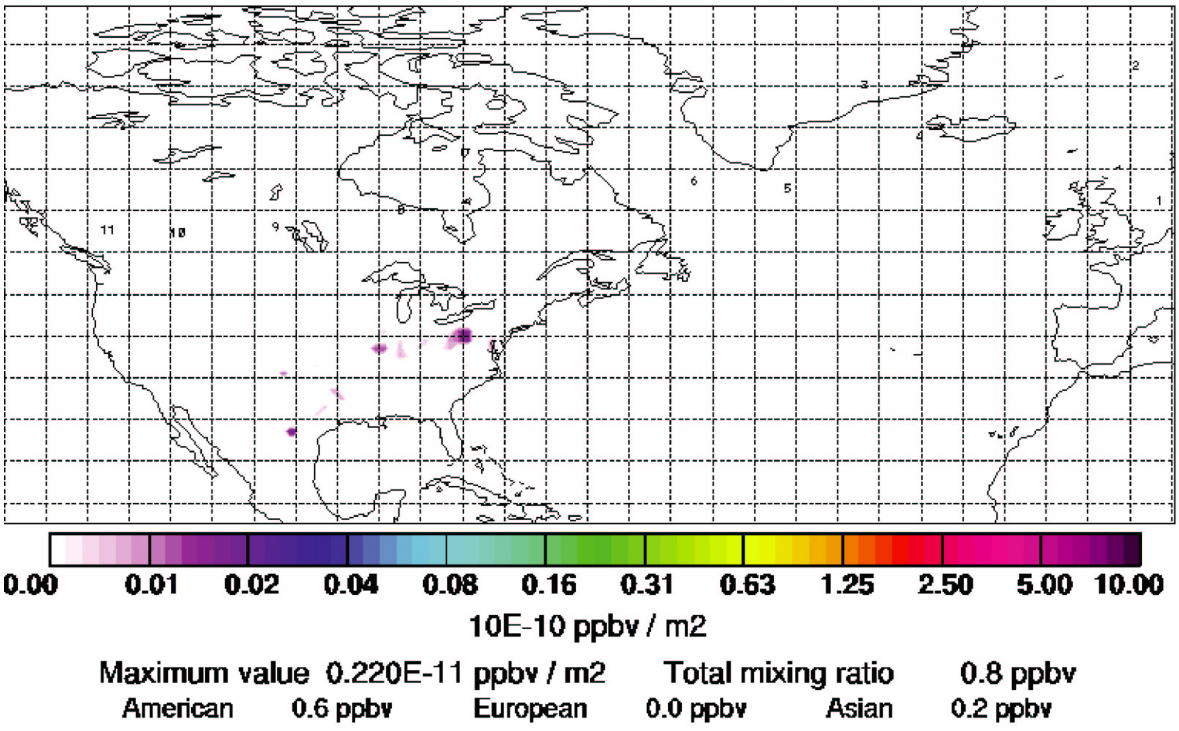

Figure 5.7: SO_2 source contribution. Start-end time of sampling UTC: 8:25:40-8:27:32. Meteorological data used is 1 × 1 deg ECMWF analysis.

front-dominated weather conditions at the surface in the northeastern United States with the front extending from eastern Canada, southward to Ohio and Pennsylvania, led to large scale warm convection above that region with significant moist air being fed from the area into the formed MCC. [Smith and J.H.E.Clark, 2004] claim that MCCs primarily form in the Great Plains of the United States and that they are significant producers of their warm-season rainfall.

5.4.3 Satellite Observations

Figure 5.8 shows the cloud top temperatures obtained by combined analysis of the GEOS/ENVISAT data. It displays the cold cloud top temperatures that were generated by cirrus clouds from the deep convection. A mesoscale vortex with several convective cells embedded appears, which spread over a wide area ranging from Tennessee up to Ontario with cloud top temperatures below -52°C (as it is defined by

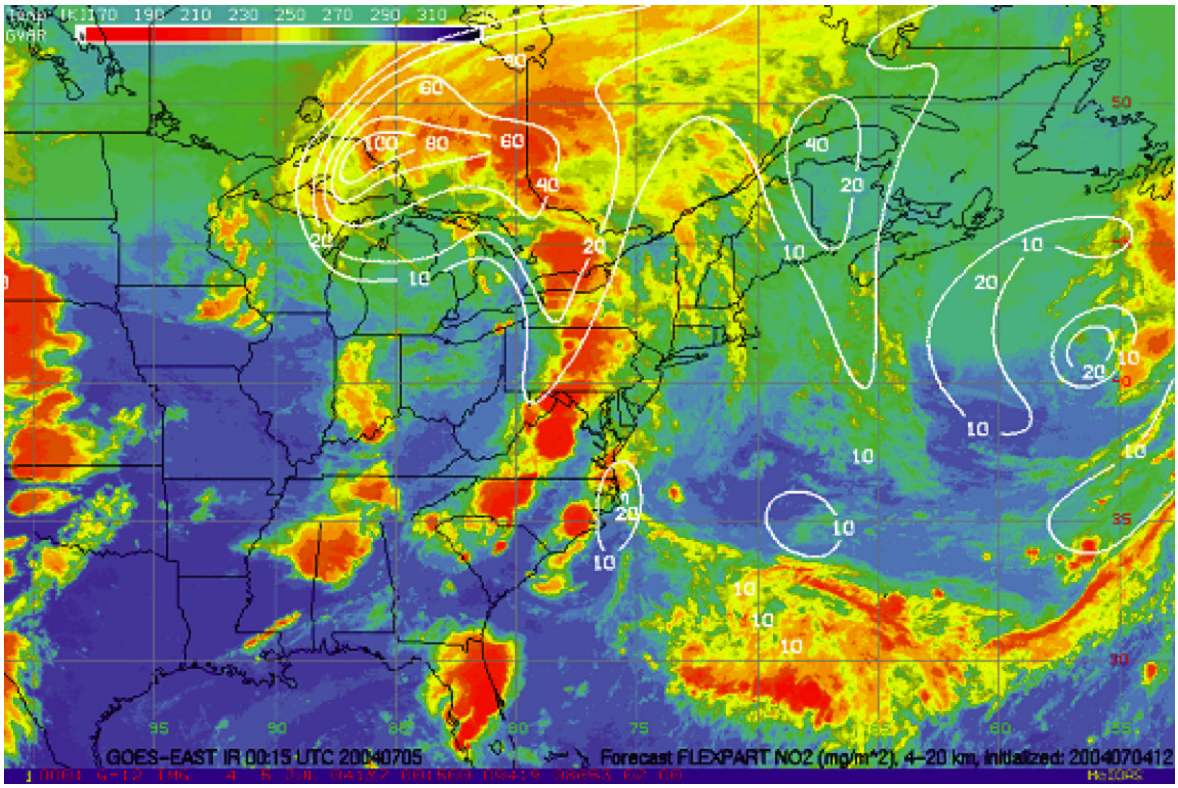

Figure 5.8: Cloud top temperatures during 5^{th} of July above the United States and the Atlantic region. Combined GEOS/ENVISAT analysis, with overlaid FLEXPART NO_2 model prediction.

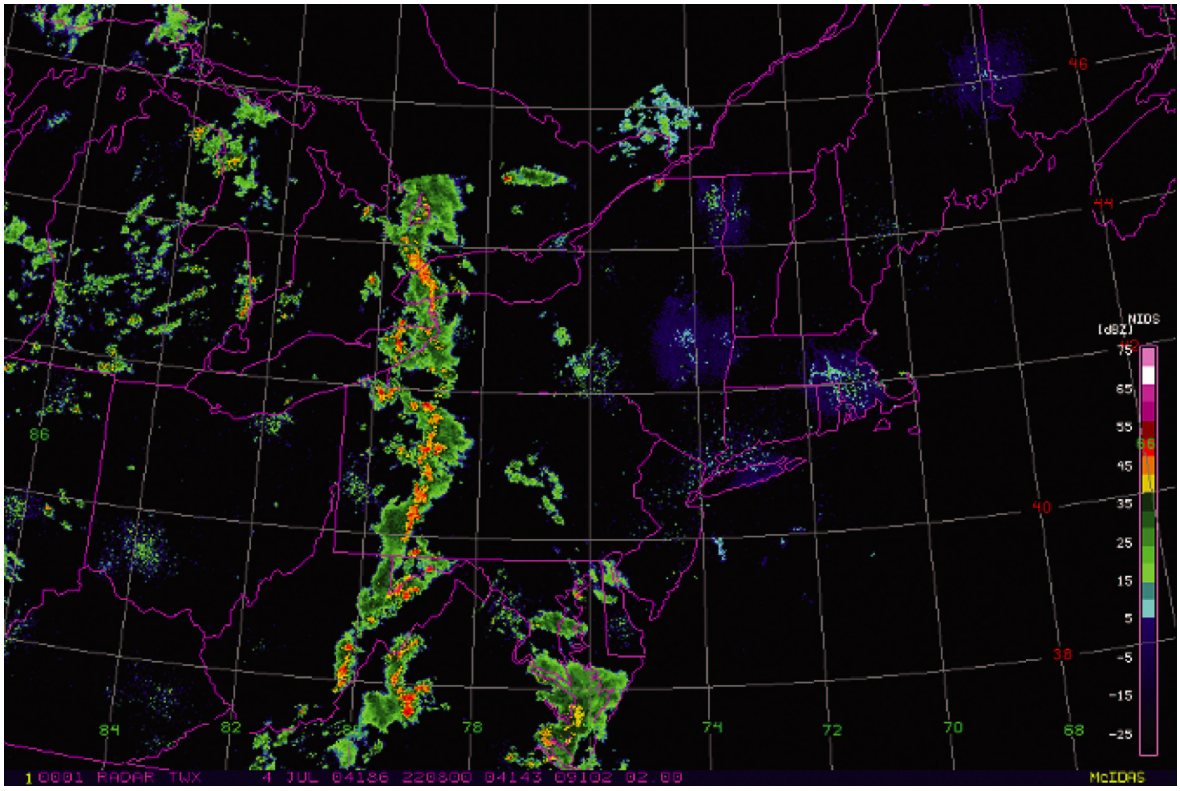

Figure 5.9: Radar image 4^{th} of July. It shows regions of increased radar reflectivity (orange colored) which result from high altitude Cirrus clouds formed by moist air convection above the United States.

[Maddox, 1980]). After an MCC develops, its average life is about 16 hours [Maddox, 1980].

For many MCCs the thunderstorms are located at the leading edge of the MCC while it propagates. A stratiform cloud layer and the vortex are located behind the leading thunderstorms [Smith and J.H.E.Clark, 2004]. **Figure 5.9** shows the radar satellite image. It indicates increased convection due to continuous feed of moist air into the area where convection is formed (convective thunderstorm cells). That is because radar scattering is increased due to a larger amount of water vapor at higher altitudes, caused by the strong vertical motion of the warm, moist air.

5.4.4 Predicted SO_2 and NO_y Mole Fractions

The measured NO_y mole fractions show a pronounced maxima close to the positions of the model predicted NO_y and SO_2 maxima, as can be seen from **figure 5.10**. The

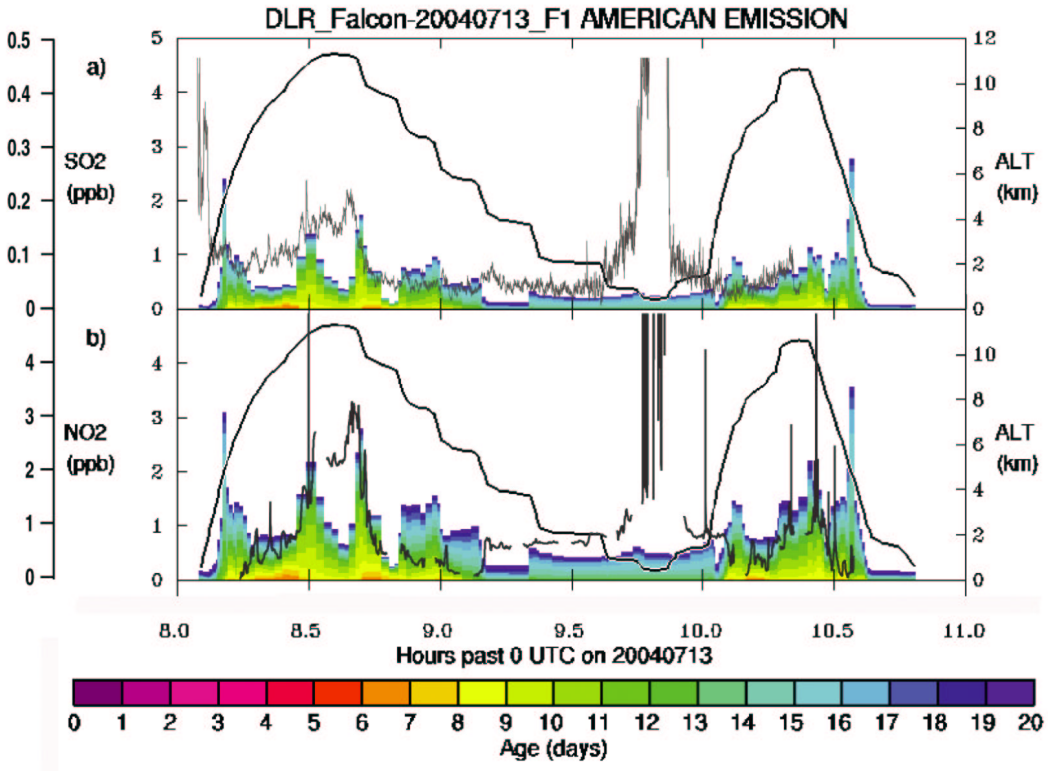

Figure 5.10: FLEXPART model prediction of the North American contributions to the above Northern Italy detected SO_2 and NO_y mole fractions during the flight of the 13^{th} of July. The age of the corresponding air masses is included by color code. Paper in preparation: [Arnold et al., 2005b].

measured absolute NO_y mole fractions are close to the predicted NO_y mole fractions. By contrast the measured SO_2 is only about 14 % of the predicted SO_2 indicating that substantial SO_2 losses must have occurred between SO_2 release by ground level sources and SO_2 detection on 13^{th} of July.

5.5 Conclusions from Meteorology and Trace Gas Measurements

From our aircraft measurements and FLEXPART model simulations the following picture of the formation and evolution of the observed LS mesoscale convective pollution plume emerges: On 5^{th} July 2004 above the Eastern USA a cold frontal system with

embedded deep convective cells, identified by use of cloud top temperatures, injected polluted planetary boundary layer air, rich in man-made SO_2 and NO_y, into the lower stratosphere. A warm conveyor belt then transported the injected air mass at high altitudes to central Europe. After injection into the LS the plume of initially high SO_2, NO_y, and H_2O mole fractions experienced dilution by very substantial entrainment of stratospheric air. The latter had very high O_3, relatively high NO_y (expected stratospheric ratio of $NO_y/O_3 = 0.0025$), and low water vapor mole fractions. During its 9 days of LS travel to Central Europe the plume experienced additional entrainment and also experienced some photochemical processing. The latter led to loss of about 30 % of the injected SO_2 by conversion to sulfuric acid as well as NO_x loss due to conversion to nitric acid and PAN (peroxy acetyl nitrate). This resulted in a mixed plume rich in O_3 (up to 400 ppbv), NO_y (up to 3300 pptv), H_2O (up to 75 ppmv) and surprisingly high SO_2 (up to 180 pptv). Of the NO_y (3300 pptv) observed in the period from UTC: 31047 - 31262 s on 13^{th} of July about 1000 ppt must be of stratospheric origin as indicated by the above-mentioned, expected stratospheric NO_y/O_3 ratio. Hence the ratio of LS-injected SO_2 to NO_y was about 343pptv/2300pptv = 0.15, which is four times smaller than the FLEXPART, predicted SO_2/NO_y ratio of 0.6. The typical SO_2/NO_y ratio of polluted PBL of the Eastern USA is around 0.2 (REF). Thus one could conclude that during convection of the air mass into the LS about 40% of the initial SO_2 mole fraction became washed out.

5.6 Particle Number Concentrations

5.6.1 Introduction

Stratospheric SO_2 experiences photochemical conversion to gaseous sulfuric acid which condenses on preexisting aerosol particles and eventually may even induce new particle formation by binary H_2SO_4 nucleation. This contrasts the situation in the troposphere where SO_2 removal by dry deposition and clouds is usually faster than SO_2 conversion to H_2SO_4.

The pre-existing stratospheric particles which serve as nuclei for H_2SO_4 condensation may enter the stratosphere either from above (meteor smoke particles) or from below (particles of tropospheric origin). In addition it is at least conceivable that new aerosol particles may also be formed in the stratosphere by binary nucleation of H_2SO_4 and H_2O. This process is promoted by the low temperatures and large photochemical activity (no blocking of solar radiation by clouds and haze) which are typical of the lower stratosphere.

Important open questions include: Are the rates of lower stratospheric H_2SO_4-induced particle formation and growth large enough to make such particles important? Is particle growth eventually faster than expected from H_2SO_4 condensation alone? If so this would indicate the presence of additional condensable gases more abundant than H_2SO_4. These questions can be answered by combined measurements of lower stratospheric SO_2 and fresh aerosol particles.

5.6.2 Particle Measurements

Figure 5.11 shows time series of data measured during the flight of the 13^{th} of July just before, during , and just after the interception of the LS plume by the FALCON aircraft. The two bottom graphs show the ratio of N4/N13 number concentrations of aerosol particles with diameters equal to or larger than 4, 13 nm respectively and the total number concentrations.

The temperature T measured inside the plume was around 223 K, and the relative humidity (RH) ranged mostly between about 4 and 35 %, indicating the absence of clouds. In the plume the fraction of small aerosol particles was particularly large as indicated by the large ratio N4/N13, ranging mostly between about 2.5 and 4. Small particles tend to be scavenged by larger particles relatively fast, in a time span ranging from several hours up to a few days. That implies that the observed small particles with diameters between 4 and 12 nm are likely to have been formed while the plume travelled at constant high altitudes from the United States to Central Europe.

Figure 5.12 shows a scatter plot of the ratio N4/N13 versus the measured SO_2 mole fraction. For low SO_2 the N4/N13 is around 1.5 and as the SO_2 fraction reaches beyond about 150 pptv the N4/N13 grow systematically with increasing SO_2 level. This indicates that the formation of measurable particles with diameters larger than 4 nm by nucleation and subsequent growth became efficient above an SO_2 threshold of about 150 pptv. Also given in **figure 5.12** is data obtained by a different plume during the flight of the 22^{nd} of July 2004 at 10644 m altitude. The detected O_3 mole fraction was at about 140 ppbv, temperature between 240 to 250 K, relative humidity at about 10% and the SO_2 mole fraction was determined to 140 pptv. This plume will now be referred to as plume B, whereas the plume of the 13^{th} of July is named plume A.

For plume B the N4/N13 remains small and independent of changes in the SO_2 fraction. It indicates that measurable particles were not formed. The number of N4 and N13 particles in plume B is about a factor of 4 larger than those in plume A. Also the NO/NO_y ratio is different. It equals 0.2 for plume B and 0.01 in the case of plume A.

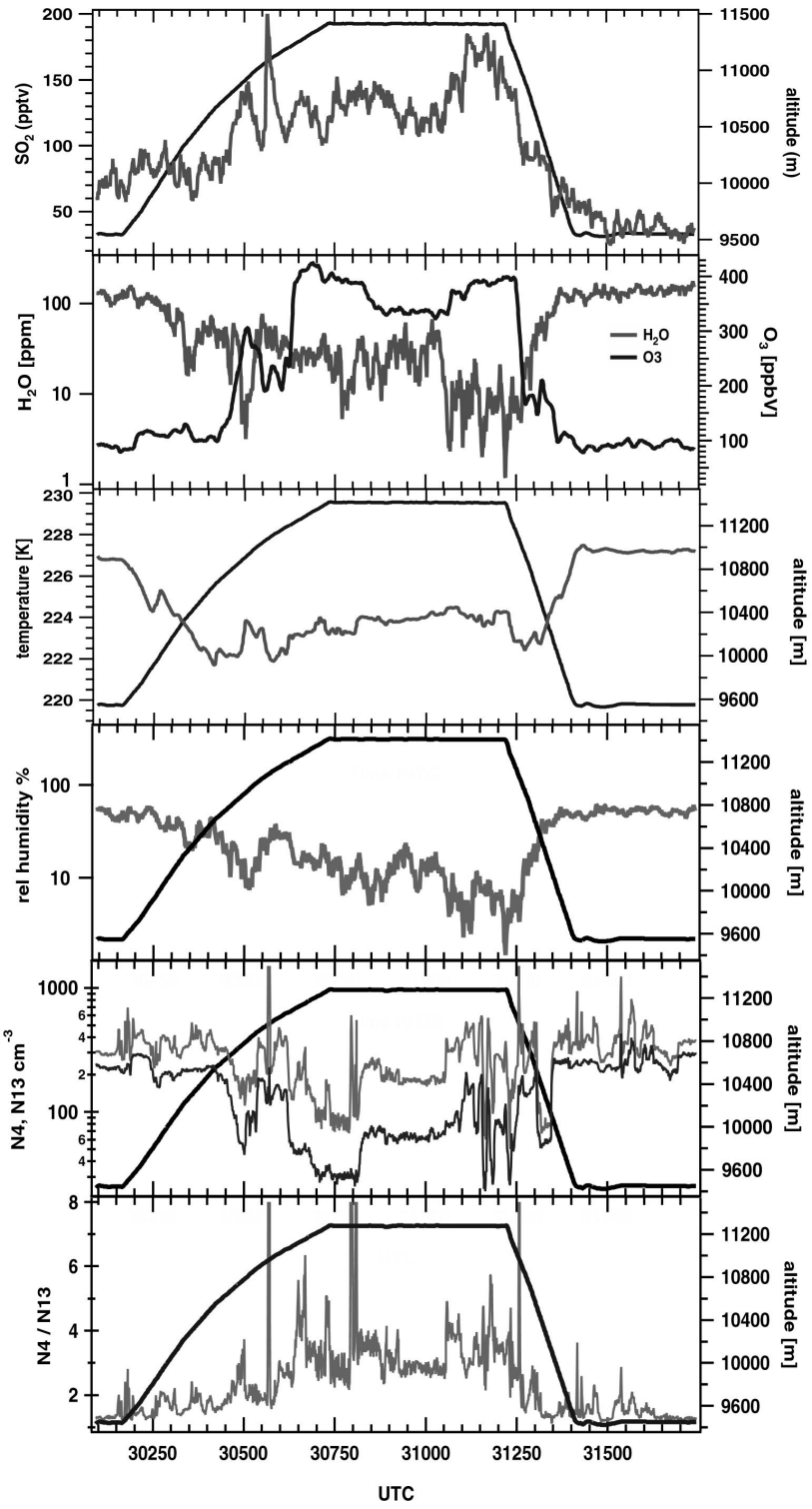

Figure 5.11: Measured trace gases and number concentrations of particles > 4 nm in diameter (N4) and > 13 nm (N13).

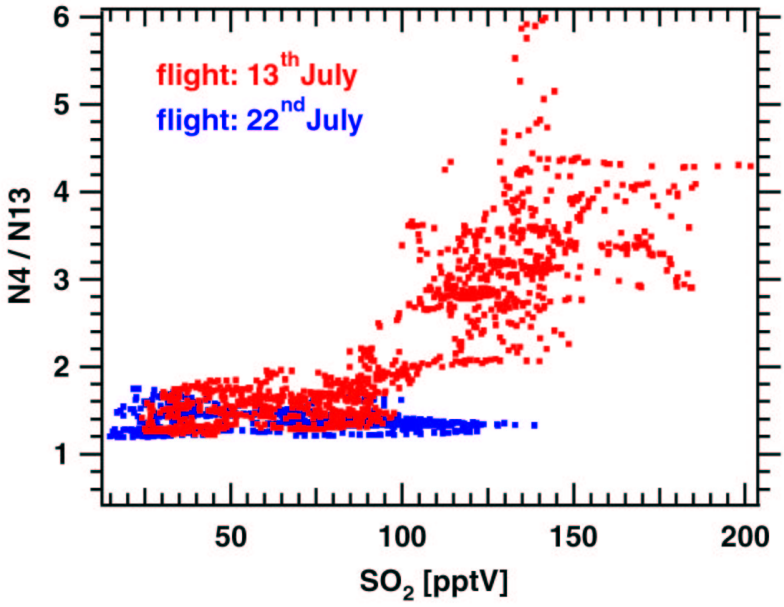

Figure 5.12: Ratio of the determined particle number concentrations N4/N13, plotted against the simultaneously measured sulfur dioxide mole fraction. Compared are two different flights, the 22^{nd} and the 13^{th} of July.

Since the NO_y concentration is related to NO conversion processes resulting in NO_y components, the ratio serves as indicator for the age of an air mass. An old air parcel experienced more chemical conversion of NO to NO_y and thus a lower NO/NO_y ratio. Therefore the air mass B can be seen as relatively young plume, where nucleation is still in its early stage. That could explain the delayed onset of a particle correlation as seen in **figure 5.12**. On the other hand, an enhanced N13 concentration also delivers a larger condensational sink which efficiently reduces the H_2SO_4 fraction. In this case prior to particle nucleation to measurable sizes (e.g. > 4 nm) scavenging to preexisting aerosol occurs. In contrast a possible mechanism by which the observed small particles may have formed in plume A is binary nucleation of SO_2-derived sulfuric acid followed by growth via binary sulfuric acid condensation and new particle coagulation. The critical point as it can be seen from **figure 5.12** seems to be the GSA concentration. If sufficient H_2SO_4 can be formed from SO_2 by OH photooxidation, nucleation and condensation will dominate over scavenging onto preexisting aerosol particles.
In the following aerosol formation and aerosol evolution will be investigated by a model simulation.

5.7 Model Simulations

Formation and growth of new particles in plume A were investigated by model simulations using the AEROFOR model. These model simulations build on the measured SO_2, H_2O, and the temperature and were performed in collaboration with L. Pirjola from the University of Helsinki, who performed the model runs.

5.7.1 The AEROFOR Modell

The model calculates OH-induced SO_2-conversion to H_2SO_4, new particle formation by binary H_2SO_4 nucleation, and particle growth by binary H_2SO_4 condensation and particle coagulation. The model simulation is initialized on day 1, the 5^{th} of July, which is the day of injection and formation of the lower stratospheric mixed air mass. To better understand the model results, let us briefly resume the terms **particle coagulation** and **condensational growth**.
Coagulation basically describes the process when two particles of the same or of different diameter, mass respectively, stick to each other after mutual collision and thereby form a new particle of larger diameter and mass. The coagulation rate, that is the rate of coagulation events per time and unit volume, can be derived as:
$J = 4 \cdot \pi \cdot (R_1 + R_2) \cdot (D_1 + D_2) \cdot N_1 \cdot N_2$
where $R_{i,j}$ refers to the particle radii and $D_{i,j}$ to the diffusion constants [Roedel, 2000]. Apparently J comprises a term which only depends on the particle-inherent properties (R, D) and not on the particle number concentrations. This term is called the coagulation function $K(R_{i,j})$. It is smallest if both particles are of the same size and becomes larger the more different in size the coagulating particles are! That is because the surface ($\sim R^2$) and the diffusion term ($\sim$ R) are dominated by the larger contribution if the two particles are different resulting in the product of two large numbers. The small particles dominate the fast diffusion whereas the large particles act as a big target area. In other words, small particles coagulate with large particles on a much faster timescale then particles of the same size, independent of their concentration.
Condensational growth refers to a rate at which a condensable gas (e.g. H_2SO_4) condenses onto an existing surface. Depending on the surface curvature only a small supersaturation of the gas is necessary to condense. Thus condensation on preexisting aerosol particles is the thermodynamically favored process compared to nucleation. The limiting factor is how fast the condensable molecules can diffuse onto the surface of the preexisting aerosols. Due to the limited diffusion velocity, binary homogenous nucleation can be efficient despite the competing process of heterogenous condensation

if only enough condensable gas is available [Seinfeld and Pandis, 1998],[Roedel, 2000].

5.7.2 Model Results

Figure 5.13 shows the result of the model simulation. The plot depicts a 20-day time series (starting on day 1) of cumulative number concentrations N_{tot}, N4, N6 , N12, N20, N30, N40, and N50 of aerosol particles with diameters equal to or larger than 4, 6, 12, 20, 30, 40, and 50 nm.
On each day with sufficient photochemical H_2SO_4 formation N_{tot} is large and exhibits a pronounced maximum reflecting a diurnal variation of OH and mutual coagulation of fresh particles. The diurnal maximum of N_{tot} varies with photochemical activity, SO_2 abundance, and condensational sink (CS). The condensational sink term basically refers to the number of preexisting aerosol particles and the resulting total aerosol surface area. H_2SO_4 attaches onto the preexisting aerosol and is no longer available for nucleation processes. One can say that the larger the CS of the preexisting aerosol size distribution, the smaller the number of nucleated particles [Pirjola et al., 1999].
Considering the OH concentration two factors have to be taken into account. First, clouds shield the solar intensity and thus reduce the OH production rate. Since the pollution plume stayed during its travel in the LS, the presence of clouds was first ne-

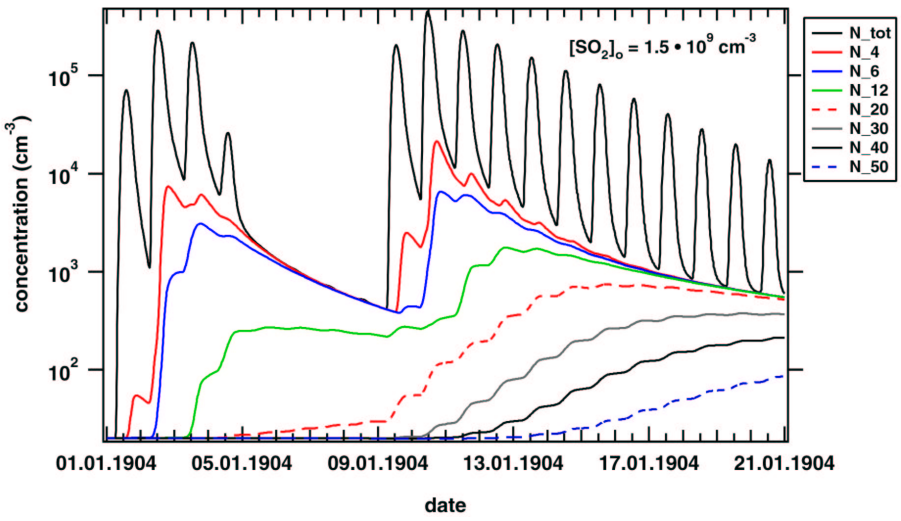

Figure 5.13: Model simulation (20 days) for the lower stratospheric pollution plume A. Shown are aerosol particle number concentrations N4 through N50 (standard case) [Arnold et al., 2005a].

glected. Second, due to the Earth's shape, solar intensity is lower at higher latitudes. The plume travelled via Greenland and thus latitudinal variations had to be considered in the model.
It appears that on day 1 of the simulation only the number concentrations of the very small particles, reflected by N_{tot}, and the N4 particles increased. At night from day 1 to 2 N4 becomes somewhat reduced due to coagulation but remains at a certain level because of its high initial value. Thus during the second day when H_2SO_4 production commences, from these previous N4 particles N6 particles form by condensational growth. Successively N12 particles form as well. This scenario is repeated until day 3, when OH production is reduced (higher latitudes) and at this point the initially mentioned competition between nucleation and heterogenous condensation is shifted towards the condensation on preexisting aerosol particles. Consequently the small particle concentrations are reduced effectively by coagulation. The N20 particle size mode appears after 5 days of LS travel, indicating effective coagulation of the smaller particles to larger ones. At day 9 after initialization, the air mass travelled at lower latitudes again. Sulfuric acid production is reinforced and thus the same scenario as from day 1 to 3 repeats.
The rise of N4 to its maximal daily value at day 9 was after the interception with the FALCON aircraft. Thus the detected particle concentrations on the FALCON correspond to an early stage of the daily nucleation. The interception period was between UTC: 30650 - 31250 which corresponds to a 10 minutes interval.
For the time of interception when the model nucleation commences at day 9 the following particle number concentrations are predicted: N4 = 394, N12 = 234 and thus N4/N12 = 1.7. Before plume interception the average particle concentrations measured on board of the aircraft were N4 = 332 and N13 = 182, which results in a ratio N4/N13 of 1.8. During plume interception the average N4 and N13 changed to N4 = 214, N13 = 65 respectively which equals a ratio of N4/N13 = 3.3. The model predictions are very similar to the measured values.
Therefore it seems that observed small freshly formed particles can in fact be explained by binary sulfuric acid nucleation followed by growth involving binary H_2SO_4 H_2O condensation and mutual particle coagulation.

5.7.3 Conclusions

After day 9 (**figure 5.13**) the model simulation assumes that the plume travelled in the lower stratosphere at latitudes around 45 N. Concurrently the initial SO_2 concentration becomes more and more depleted such that the daily small particle maxima

(N_{tot}) reduce. Consequently condensational growth of the fresh particles to N4 and larger particles becomes less intense and mutual coagulation reduces the overall concentration of the small particles effectively. The big particles still form by coagulation on cost of the smaller ones. After 20 days, the N40 particles reach a level of 200 cm^{-3}. The lifetime ($t_i = N_i \ / \ J_{i,j}$) of i particles according to the coagulation coefficient is independent of their number concentration, since the coefficient itself depends in a linear fashion on the number concentration i,j. The larger the size of the i particles, the slower coagulation will be with bigger j particles. That is because diffusion is reduced. In other words, lifetime increases and hereby the chance of the i particles to be transported into different layers of the atmosphere.
Often cloud condensation nuclei (CCN) are referred to sizes of about 100 nm [Pirjola et al., 1999],[Seinfeld and Pandis, 1998],[Roedel, 2000]. Further coagulation of the observed N40, N50 particles with smaller ones may eventually lead to even larger condensation nuclei with the potential to terminate as a CCN. That could probably happen after their ultimate return into the upper troposphere where water vapor increases and which occurs in average after a LS residence time of about 23 days [Forster et al., 2003].

5.8 Summary

Our investigations suggest that during periods unaffected by rarely occurring major volcanic eruptions convective injection of man-made SO_2 particularly from ground level sources of the USA and eastern Asia represents the dominant source of SO_2 and SO_2-derived new aerosol particles present in the summer LS at northern middle latitudes. Once transported in the LS, SO_2 can contribute significantly to the binary homogenous nucleation. New particles formed are capable of reaching sizes of 50 nm. So far neglected in the model but also of high interest is the effect of charged ions. Present in the LS, they act as nucleation cores and lead to smaller, stable clusters by reducing the critical size [Lee et al., 2003].
In future man-made SO_2 emissions in eastern and south eastern Asia are expected to increase. This may lead to a marked increase of convective injection of man made SO_2 into the stratosphere. Therefore SO_2 measurements of the kind reported here should be extended not only in middle latitudes but should also be extended to the tropics and to the southern hemisphere.

Chapter 6

SUMMARY AND OUTLOOK

6.1 Summary and Outlook

The present thesis reflects the complex interaction and impact of sulfur dioxide on the environment from different points of view. As an acid forming species, SO_2 triggers nucleation and condensational growth of particulate matter but also deforestation and deterioration of material. Its atmospheric abundance is dominantly influenced by human activities.

Two instruments were further developed and characterized for use on airborne platforms. An ion trap mass spectrometer (ITCIMS) served for precise SO_2 measurements by use of an isotopic online calibration method. Its high temporal resolution (1 s) and precision ($\sigma < 15\%$, $SO_2 > 100$ pptv) together with the introduced isotopic calibration, make it a useful tool to reliably detect sulfur dioxide throughout the atmosphere.

A cryogenically pumped quadrupole mass spectrometer (QMS) served to detect natural gaseous ion clusters in the atmosphere. The instrument was fully characterized and optimized for on-flight conditions.

Each instrument was successfully tested in a field experiment. The ITCIMS during the international campaign ITOP, 2004 and the QMS during the campaign CONTRACE, 2003. Objectives and results of these campaigns are described in detail in chapters 3, 4 and 5.

The performed ion cluster measurements showed a significant positive correlation of large sulfuric acid clusters and small particles N4 (> 4nm in diameter). The correlation is referred to coagulation and condensational growth of via SO_2 formed H_2SO_4 molecules. It is likely that the ion-induced nucleation rate exceeds homogenous binary nucleation in the clean, unpolluted free troposphere.

SO_2 vertical profiles determined during the summer ITOP campaign 2004 above central

Europe revealed a free tropospheric SO_2 background of about 50 pptv. Interestingly, three cases indicated increasing SO_2 concentrations slightly below the tropopause layer were observed. The pre-ITOP flight of the 13^{th} of July even resulted in SO_2 mole fractions up to 250 pptv in the lowermost stratosphere (LS), indicated by elevated O_3 and the temperature gradient. This interesting finding is discussed in great detail in chapter 5. It turned out that the detected LS pollution plume originated in the eastern United States (Pennsylvania region, Great Plains). A severe mesoscale convective complex uplifted sufficient SO_2-rich boundary layer (PBL) air to high altitudes. The plume then got transported by a warm conveyor belt to central Europe at high altitude, which efficiently hindered SO_2 wash out by clouds. The result illustrates that apparently a certain fraction of SO_2 survives the moist air convective processes. Once the plume entered the LS, photochemical reactions converted SO_2 to sulfuric acid and particle nucleation commenced. Performed model simulations considering only binary nuclation of sulfuric acid and water, yielded similar particle concentrations as the one measured by DLR. It could be shown that the binary system is capable of sufficiently producing particles within 9 days of LS travel (U.S. to central Europe). After further 20 days these particles grow to sizes as large as 50 nm in diameter. After their ultimate return to the upper troposphere they may act as cloud condensation nuclei.

On the basis of the here given characterization the QMS instrument used for charged cluster measurements can be improved in its operation accuracy. Second, cryogenic pumping with liquid neon is not only expensive but also laborious and an alternative pumping method is needed. Further measurements are important to learn about the role of ion-induced nucleation in the atmosphere.
The ITCIMS instrument setup should be further miniaturized. This is achievable if instead of the after glow discharge source a radioactive source is deployed or a new, smaller-sized and compact discharge source is constructed. To reduce the number of KF 40 tubing used in the setup would be another aim. The main goal of any future instrumental development should be the detection of SO_2, HNO_3 and other trace gases in parallel. In the literature the use of SF_6 as educt ion (SF_6^-) is reported to be suitable for detection of SO_2, HNO_3 and HCl by use of an ion trap [Lovejoy and R.Wilson, 1998]. Certainly the new water vapor detection method developed in this work and presented in appendix A.1.5, needs further improvement. Experiments with a tunable diode laser system (TDL) in addition to the mass spectrometric method may help to finally decode the main ion molecule reaction pathway. It is worthwhile spending more effort into the new detection method, since no comparable method of higher temporal resolution exists and moreover simultaneously operates at H_2O mole fractions below say 50 ppmv.

The described case study of a LS SO_2 pollution plume implies several questions which need to be further investigated. How often occur severe deep convective events in regions of heavy industrialization? What is their contribution compared to aircraft traffic in the LS? How influences ion-induced nucleation the result of fresh particle production in terms of sulfuric acid formed by injected SO_2?

Appendix A

A.1 A New Water Vapor Detection Method

A.1.1 Introduction

Water vapor in the atmosphere varies from values as high as 50000 ppmv above warm water surfaces in the tropics and at sea level to values as low as 4 ppmv [Engel, 1996] in the lower stratosphere. Thus atmospheric vater vapor detectors on aircraft must cover a large dynamic range. Additionally the presence of clouds makes great demands. Also high temporal resolution and finally robust handling must be guaranteed when operating the detector on board of a research aircraft.
Several well established methods exists to detect water vapor in the atmosphere. The techniques used are known as lyman-α fluorescence detection, dew point mirror detection and tunable diode laser detection. Each technique has several drawbacks compared to another. The one covering the most dynamic range comprising high precision at the same time is the lyman-α photofragmentation fluorescence. The technique was developed by Kley and Stone (1978) as well as Bertraux and Delannoy (1978). It is based on the photolysis of H_2O molecules by short-wavelength UV radiation ($\lambda < 137$ nm). The electronically excited OH radicals either decay to the ground state by emission of fluorescence light (λ = 285-330 nm) or radiation free by collision with air molecules. The latter is the dominant process at high pressure (p > 25 hPa). Since the radiation free transition probability is proportional to the molecular number density, one detects a fluorescence signal reciprocal to the amount of excited OH radicals. The instrument is capable of taking a data point each second, with an accuracy of about 5% [Zöger, 1999], [Eicke, 1999].
A dew point mirror also offers a wide dynamic range and can measure very low stratospheric water vapor contents but with a temporal resolution of only 100 s [Ovalez, 1991]. Precision is less than 10%.

Tunable diode lasers are, due to their high precision and high temporal resolution best suited for stratospheric measurements of H_2O vapor although precision decreases with increasing pressure to about 10% at 200 hPa [May, 1998].
The method is based on IR absorption spectroscopy. With temperature fixed, it is the adjustment of current to tune the wavelength of the emitted laser light to sweep it through an absorption peak at a particular wavelength. The resolution of the laser is also fine enough to determine the shape of the peak. The processed signal from the detector analyses the amplitude of the absorption peak and therefore the density of the target gas.
Electronics stabilizes the temperature of the laser (usually 10 to 50 °C) by the use of a small Peltier device, which provides both heating and cooling. The precise wavelength emitted by the laser is swept across the absorption peak of interest by ramping the current in a saw-tooth pattern. A small amplitude sine wave is superimposed on top of the main saw-tooth ramp signal. The sine wave is modulated at a frequency f and the detected signal is de-modulated at 2f improving signal to noise ratios. By monitoring the absorption peak at specific wavelengths, the concentration of the target gas within the sampling volume can be accurately determined. Observed adsorption is related to the density of the target gas by the Beer-Lambert law:

$$\rho \;=\; \frac{-ln(\tau(\nu))}{k(\nu)L} \tag{A.1}$$

where ρ equals the density of the target gas, $\tau(\nu)$ the observed transmission, $k(\nu)$ the adsorption coefficient and L the optical path length.
The here introduced new empirical method is based on the IT-CIMS technique. The amount of water vapor is positively correlated to the count rate of the mass line which appears at 77 amu in the spectrum. Water vapor is transported with ambient air into the flow reactor where it reacts with educt ions. Some fraction will attain the spectrometer and become detected. The temperature of the flow reactor tubing measured at the outer surface of the tube is at least above $25°C$. The sampling line is made of a half-inch PFA tube (chapter C.1) and thus transfers ambient heat well to the sampled atmospheric air. The inlet mounted outside the aircraft is permanently kept at $20°C$ in order to avoid icing. Therefore, condensation of water vapor should not affect the total water vapor content.

A.1.2 Proposed Ion Molecule Reaction Path

The water molecules react with the CO_3^- educt ions produced by the discharge ion source. The ion source also leads to the production of atomic oxygen O, O^1D and ozone

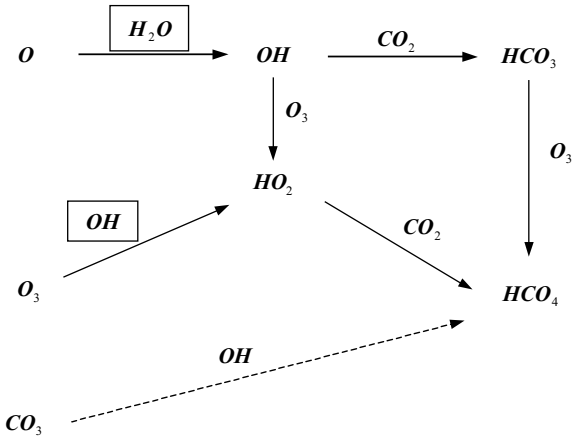

Figure A.1: Reaction pathes which lead to the formation of the HCO_4^- ion with 77 amu. The two boxes mark the reaction steps where water molecules either directly or indirectly via OH alter formation rates.

O_3 (chapter 2.3.3). Discharge ionization experiments done by [Wincel et al., 1995] using a fast flow tube apparatus with a H_2O/He buffer gas mixture led to the formation of $HO_2^-CO_2$ as a major species when adding a small amount of CO_2. Interestingly they found a difference in whether CO_2 was added before or after the discharge ionization source. In the first case $HO_2^-CO_2$ formed as dominant species, whereas introducing CO_2 further downstream (after the discharge) mainly led to the formation of HCO_3^-. **Figure A.1** shows possible reaction pathes which lead to the formation of the HCO_4^- ion at 77 amu. Water vapor concentration directly affects the formation rate of OH^-. It indirectly triggers the formation of HO_2^- by OH via the excited oxygen molecule O^1D. The important reactions in terms of a water vapor dependence are:

$$O(^1D) + H_2O \rightleftharpoons 2\ OH \tag{A.2}$$

$$O^- + H_2O \rightleftharpoons OH^- + OH \tag{A.3}$$

It is important to mention that the above proposed reaction scheme is not yet proven. But the absence of HCO_4^- in drift tube experiments on CO_2-O_2-H_2O mixtures excludes the O_2^- hydrates as precursors [Moruzzi and Phelps, 1966], [Cosby et al., 1976]. Thus free radicals such as OH might be necessary. [McAllister et al., 1978] reported from mass analysis of ions formed in an H_2-N_2-acetone diffusion flame that the detected ions fell into two groups, one at m/e = 60 and 61 (CO_3^- and HCO_3^-) and the other at m/e = 77. The ion at m/e = 77 has be identified as HCO_4^- and clustering, free radical association or ion hydrate decomposition have been suggested as possible formation

mechanisms. The following reactions are proposed by [Moruzzi and Phelps, 1966], [Cosby et al., 1976] and [Bohme et al., 1977] and lead to the formation of HCO_4^-:

$$HO_2^- + CO_2 + M \rightarrow HCO_4^- + M \quad \text{(A.4)}$$

$$CO_3^- + OH + M \rightarrow HCO_4^- + M \quad \text{(A.5)}$$

$$HCO_3^- \cdot H_2O + M \rightarrow HCO_4^- + H_2 + M \quad \text{(A.6)}$$

The clustering reaction (A.4) is reasonable, as its association energy is of the order of 42 kJmol^{-1} [Cosby et al., 1976]. Reaction A.5 is a radical association, exothermic to about 146 kJmol^{-1}, and is quite plausible [Cottrell, 1958]. Reaction A.6 is not so favorable and thus not taken into account in figure A.1,since it does require the breaking of two O-H bonds (849 kJmol^{-1}) to make one H-H and one O-O bond (579 kJmol^{-1}) assuming the HCO_4^- structure given below [Cottrell, 1958]:

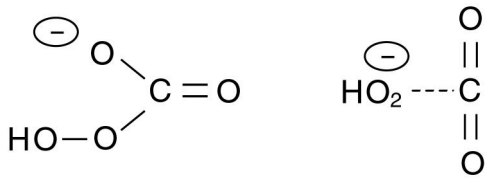

Figure A.2: Structures of HCO_4^-. Either a peroxy compound or a cluster ion.

Figure A.3 shows the to total counts normalized count rates of O_3^-(48 amu), CO_3^-(60 amu), NO_3^- (62 amu), HCO_4^- (77 amu) and $CO_3^-(H_2O)$ (78 amu). Starting with CO_3^- (right scale) its count rate decreases for an increasing water vapor content. The same is observed for e/m = 62 amu (NO_3^-). The correlation between NO_3^- and CO_3^- can be understood when considering CO_3^- as the educt ion for the reaction with NO_2:

$$CO_3^- + NO_2 \rightarrow NO_3^- \quad \text{(A.7)}$$

The rate coefficient for the reaction is 2.0 10^{-10} [Watts, 1992].
The first hydrated state $CO_3^-(H_2O)$ increases as expected with increasing dew point. This leads to the above-mentioned reduced count rate of CO_3^- and NO_3^- while dew point goes up. Finally O_3^- and HCO_4^- are correlated with each other. That is what one would expect if HCO_4^- depends upon O_3^- concentration as proposed in the reaction pathway in **figure A.1**.

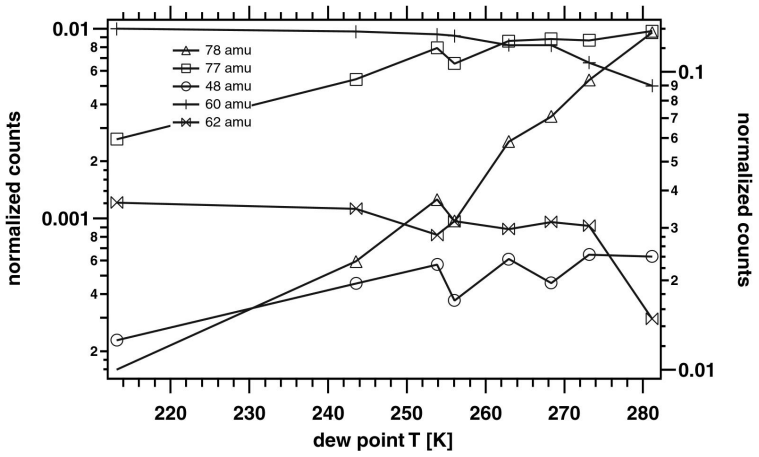

Figure A.3: Count rates of different ions normalized by total counts: O_3^-(48 amu), CO_3^-(60 amu), NO_3^- (62 amu),HCO_4^- (77 amu) and $CO_3^-(H_2O)$ (78 amu). The right-hand scale only holds for the CO_3^- educt ion.

A.1.3 Calibration with a dew point mirror

To derive the water vapor content from the HCO_4^- count rate, calibration with a frost point hygrometer (i.e. a dew point mirror) was performed. Hereby a fit function was searched which describes the relation between measured frost point and the corresponding count rate of the mass spectrometer. The derived function should then be used to obtain all other quantities. Calibration data was taken from the TROCCINOX field campaign, which took place February 2005 in Brazil. Both instruments, the frost point hygrometer and the ion trap mass spectrometer were operated simultaneously during flight.

For further evaluation the dew point temperature was converted to flow reactor pressure. A scatter plot served to define the fit function parameters. Therefore dew point temperature (dew point mirror instrument operated by DLR) versus ion count rate at 77 amu was plotted. The measured dew points of totaly 5 flights were considered. Data recorded in clouds was excluded[1] A sigmoidal function

$$f(countrate) \;=\; C_0 \;+\; \frac{max}{1 \;+\; exp(xhalf - count/rate)} \tag{A.8}$$

turned out to fit best (χ^2-method) to the scattered data, with the defined fit-parameters: $C_0 = 162.35$, max = 109.11, xhalf = 11290 and rate = 13022. **Figure A.4** shows scatter plot (dew point vs count rate) and fit function. The variance for $T_{dewpoint} > 240$

[1]For detecting the presence of clouds a total particle concentration higher than 0.05 particles cm^{-3} proved to be a useful criterion when particles larger than 3μ are considered.

K increases such that a functional dependence of dew point and count rate cannot be derived only from a single data set (one flight) as one might expect for highly correlated data. Instead the average data of several flights has to be taken into account and is shown in **Figure A.4**. For dew points below 240 K a linear relation holds whereas for higher dew points sensitivity increases, i.e. small changes in dew point temperature lead to large differences in the count rate. Thus one can resume that the sensitivity below 240 K is about 500 counts/K and increases for a higher dew point temperature. Why sensitivity changes for higher dew point temperatures is likely to be caused by changes in the ion molecule reaction pathway. Higher dew point temperatures are normally related to lower altitudes. At lower altitudes further trace gases occur what may lead to side reactions which efficiently reduces the OH abundance and thus the HO_2^- concentration.

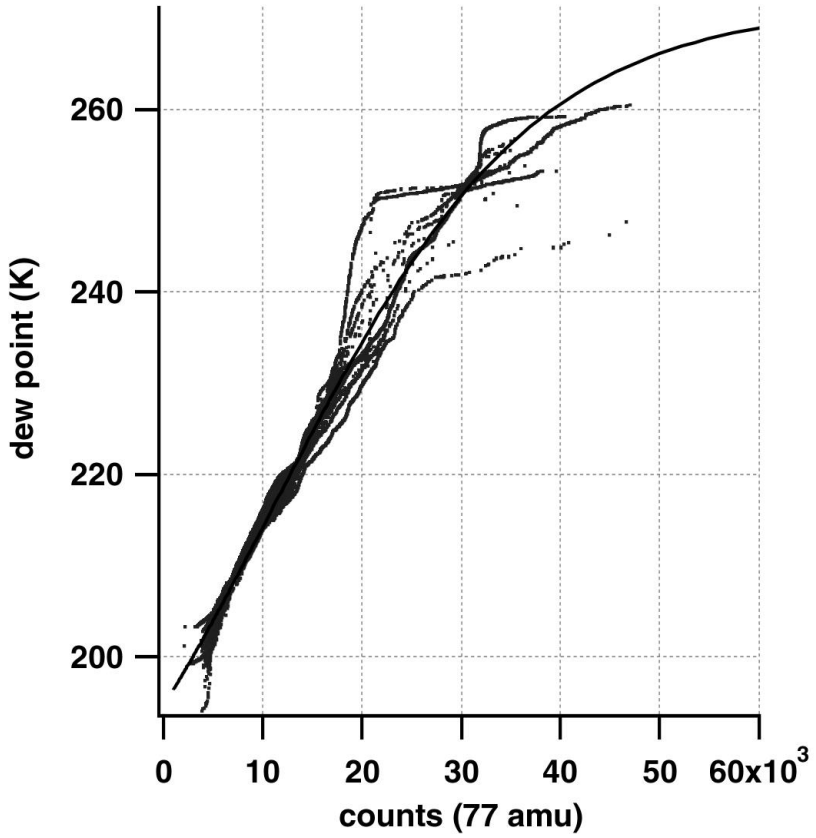

Figure A.4: Scatter plot of dew point temperature and corresponding count rate at mass 77 amu. Data from 5 flights is taken into account and used to obtain an average fit function (black line).

The following data plots show a comparison of relative humidity (%), H_2O mixing ratio (ppmv) and dew point temperature (K). The black lines represent the corresponding quantity obtained by use of the fit function. The gray lines refer to measurements with a frost point hygrometer.

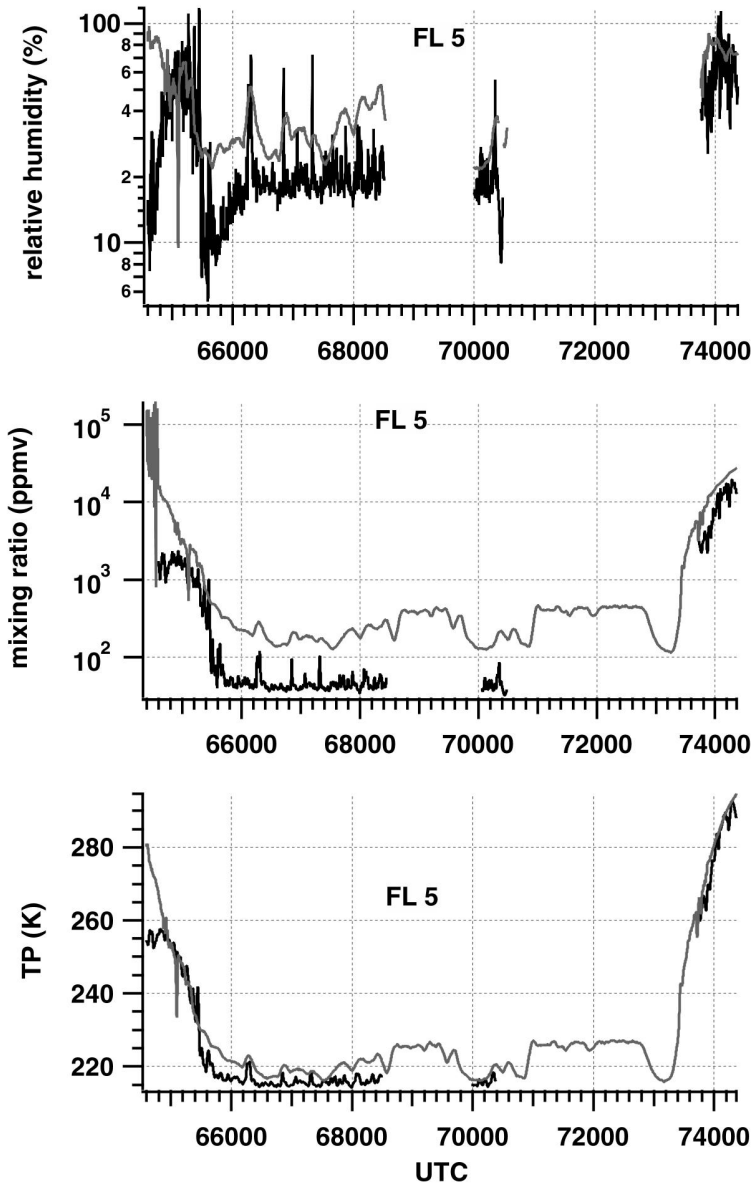

Figure A.5: H_2O mixing ratio, relative humidity and dew point temperature by mass spectrometer (black lines) and frost point mirror (gray lines). Data from the flight of 5^{th} February, TROCCINOX campaign 2005, Brazil.

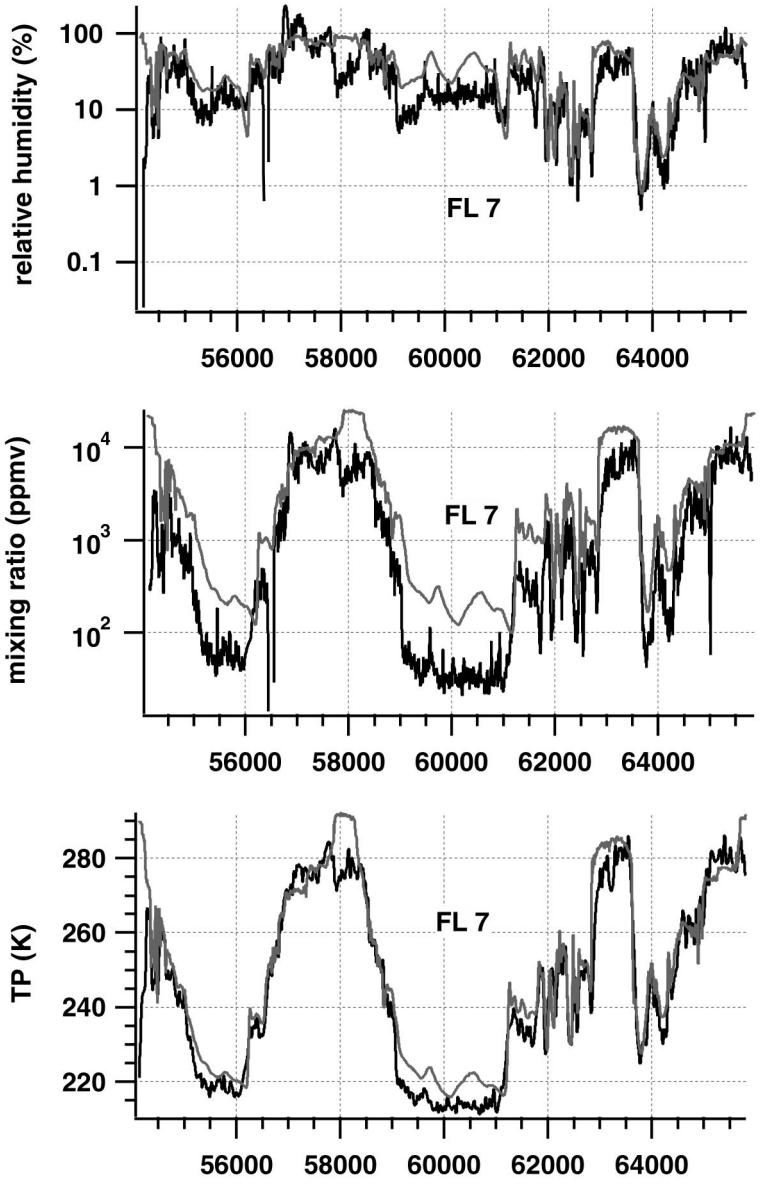

Figure A.6: H_2O mixing ratio, relative humidity and dew point temperature by mass spectrometer (black lines) and frost point mirror (gray lines). Data from the flight of 7^{th} February, TROCCINOX campaign 2005, Brazil.

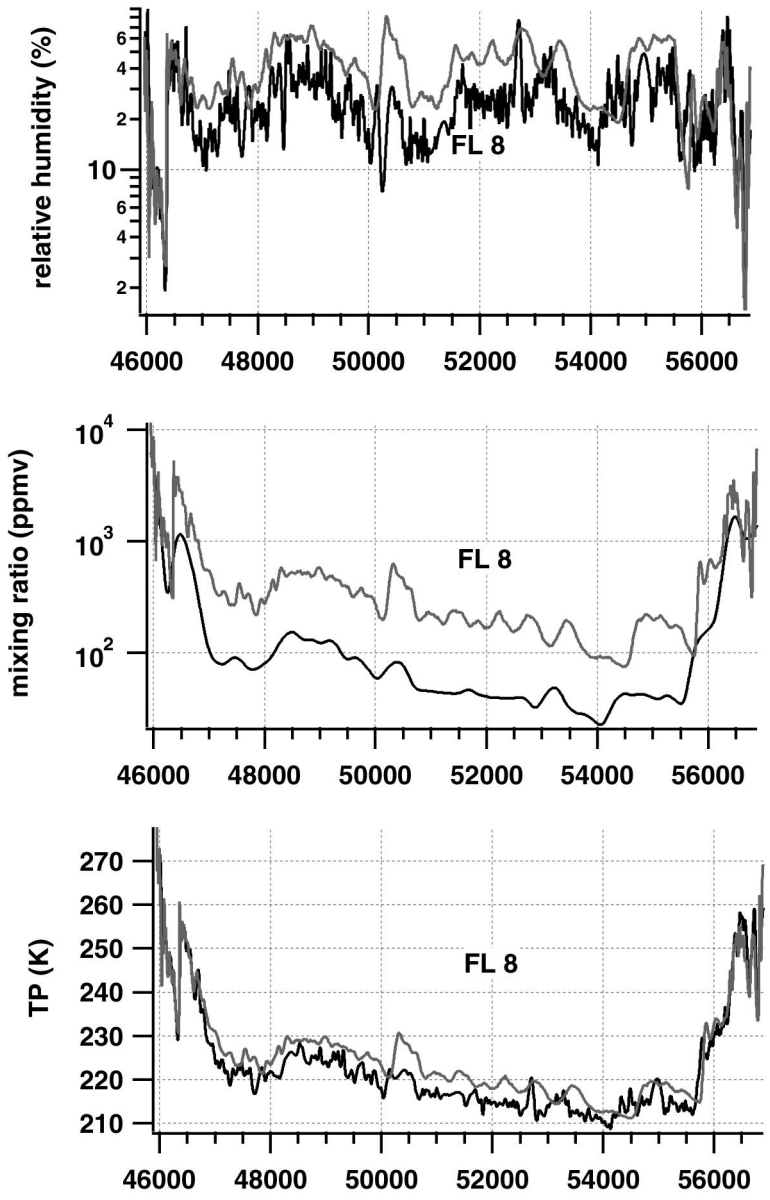

Figure A.7: H_2O mixing ratio, relative humidity and dew point temperature by mass spectrometer (black lines) and frost point mirror (gray lines). Data from the flight of 8^{th} February, TROCCINOX campaign 2005, Brazil.

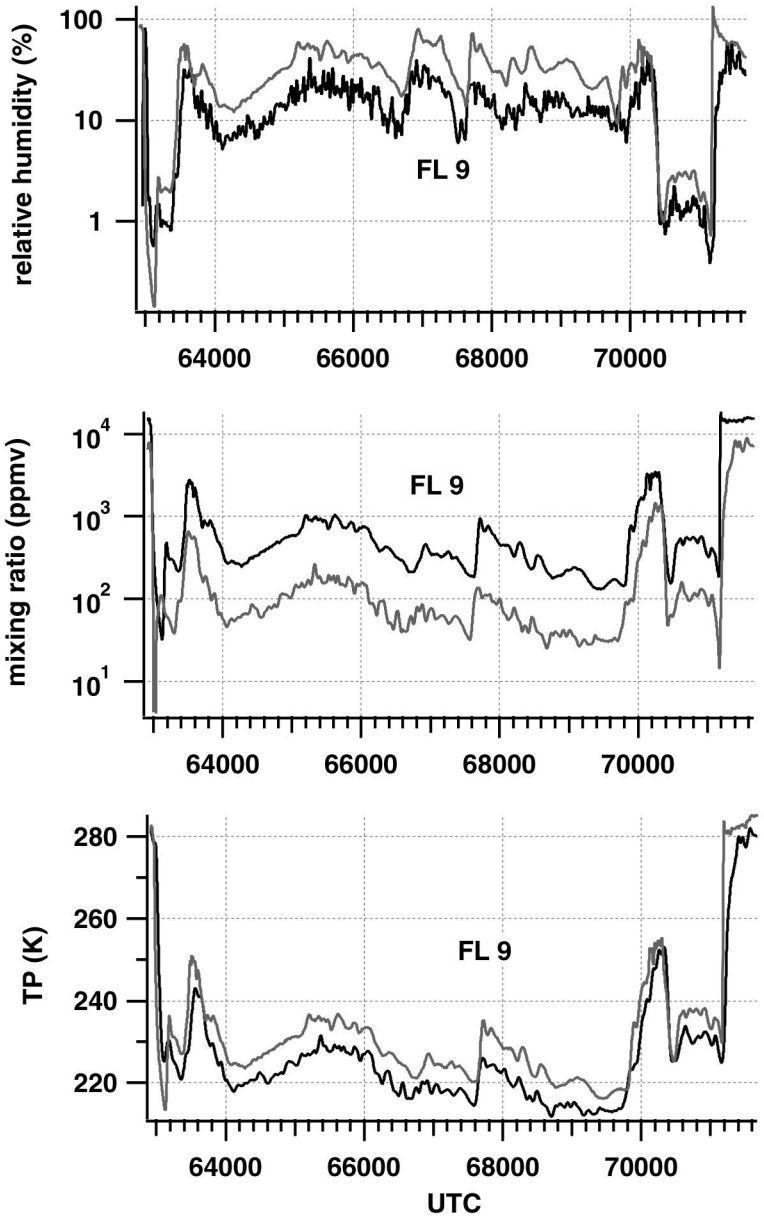

Figure A.8: H_2O mixing ratio, relative humidity and dew point temperature by mass spectrometer (black lines) and frost point mirror (gray lines). Data from the flight of 9^{th} February, TROCCINOX campaign 2005, Brazil.

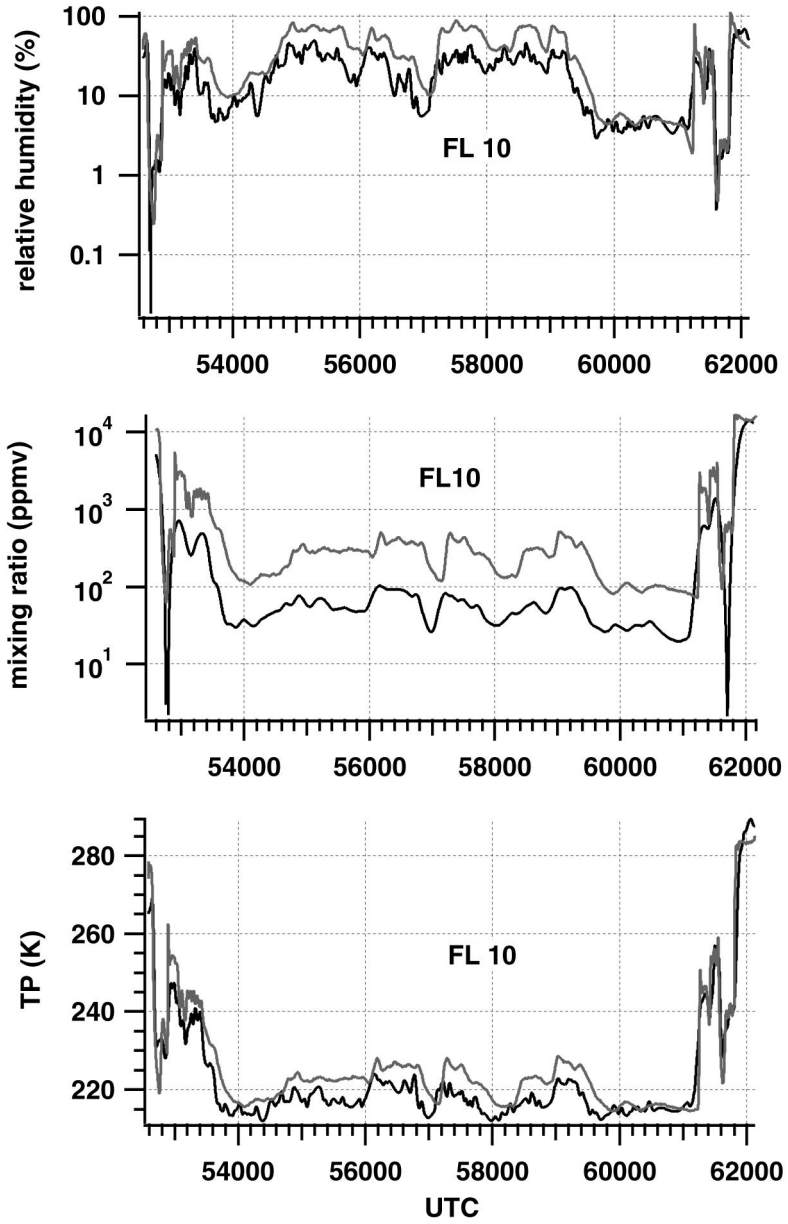

Figure A.9: H_2O mixing ratio, relative humidity and dew point temperature by mass spectrometer (black lines) and frost point mirror (gray lines). Data from the flight of 10^{th} February, TROCCINOX campaign 2005, Brazil.

One can conclude that all three quantities can be well calculated with the derived fit parameters. The correlation between data measured by use of dew point mirror and by use of the ion molecule reaction varies between 86 - 96%. The deviation in dew

point temperature of both techniques is largest for low temperatures where the mass spectrometric method results in lower temperatures than the dew point hygrometer. Concerning high ambient H_2O concentrations both techniques are in good agreement. Relative humidity derived with the fit function normally tends to lower relative humidities than the ones derived with the hygrometer. But here the overall correlation is best. Absolute humidity tends to be low by a factor of 1.5 throughout each flight. This might be since this quantity is most sensitive to wall losses.

A.1.4 Intercomparison with a Lyman-α Detector during the ITOP campaign

The calibrated count rate of the HCO_4^- ion is used to calculate dew point temperature, H_2O mixing ratio and relative humidity for the ITOP campaign data. During this campaign a Lyman-α detector was on board of the aircraft. The frost point hygrometer used during the TROCCINOX field experiment is a more precise instrument than the Lyman-α detector, although sampling frequency is lower. Another disadvantage of the Lyman-α detector is the lower dynamic range and thus its limited capability to measure at high altitudes (lowermost stratosphere) where H_2O mixing ratios are small. This in turn is the reason why some data gaps occur in the plots shown later on when the aircraft cruised at high altitudes. Since during the analysis of the ITOP data set it turned out to be of extreme importance to also have H_2O measurements available at great altitudes like the lowermost stratosphere, the new mass spectrometric method was developed. That was especially the case, since fresh particle nucleation which is related to SO_2 is favored at high altitudes when temperature is low. With the described mass spectrometric method it is possible to derive H_2O abundances later from already recorded mass spectra. However, it is worthwhile comparing both techniques, the Lyman-α and the calibrated ion count rate method.
The **figures A.10-A.13** show examples of four ITOP flights evaluated by the two techniques. The black lines correspond to the ion molecule reaction, the gray lines to the Lyman-α result. The overall curve shapes of all three quantities (dew point (K), relative humidity (%) and water vapor mixing ratio (ppmv)) are well reproduced by the mass spectrometric method. No systematic bias appears when comparing the derived water vapor mixing ratios with those measured by the Lyman-α detector. In the range around 10^4 ppmv the mass-spec-technique tends to exceed the Lyman-α values. Relative humidity sometimes exceeds 100%. It is important to mention that data obtained in clouds still is included in the measurements and might be the reason for that. Especially flight number FL13 shows a huge deviation in relative

humidity. Finally, the dew point is reproduced in good agreement to the Lyman-α detector although for high temperatures the discrepancy is increased whereas at low temperatures the agreement is very good. For the flight of the 22^{nd} of July (FL22) the worst correlation of the two distinct dew point measurement techniques with R = 68% was observed. For FL13 the correlation is best with R = 97%. The other correlations were R = 87% (FL25a), R = 94% (FL 26), respectively. The average dew point correlation of all flights is R = 88%.

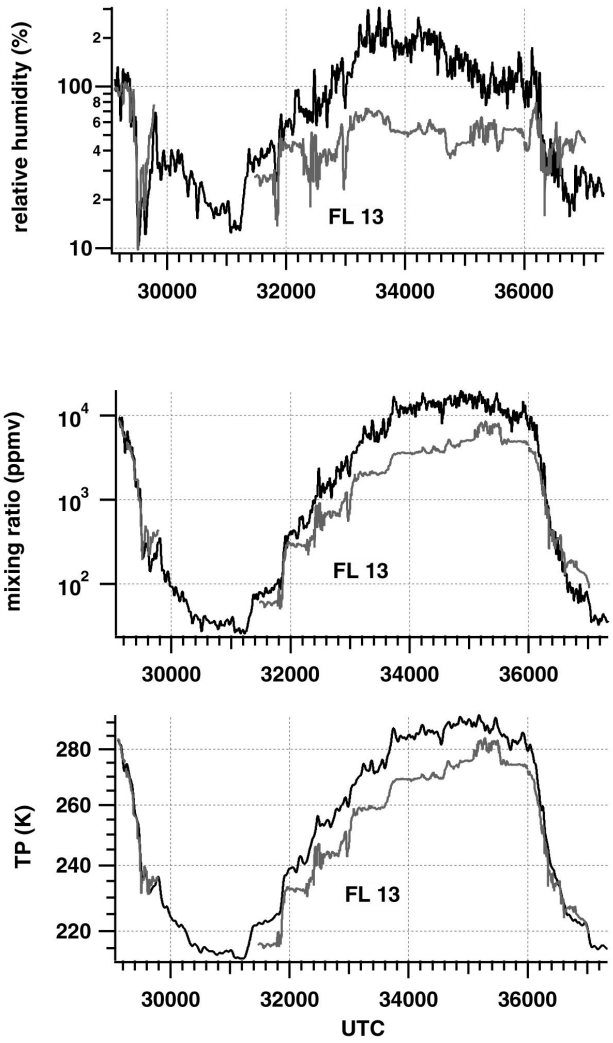

Figure A.10: H_2O mixing ratio, relative humidity and dew point temperature by mass spectrometer (black lines) and Lyman-α detector (gray lines). Data from flight 13^{th} of July, ITOP campaign 2004.

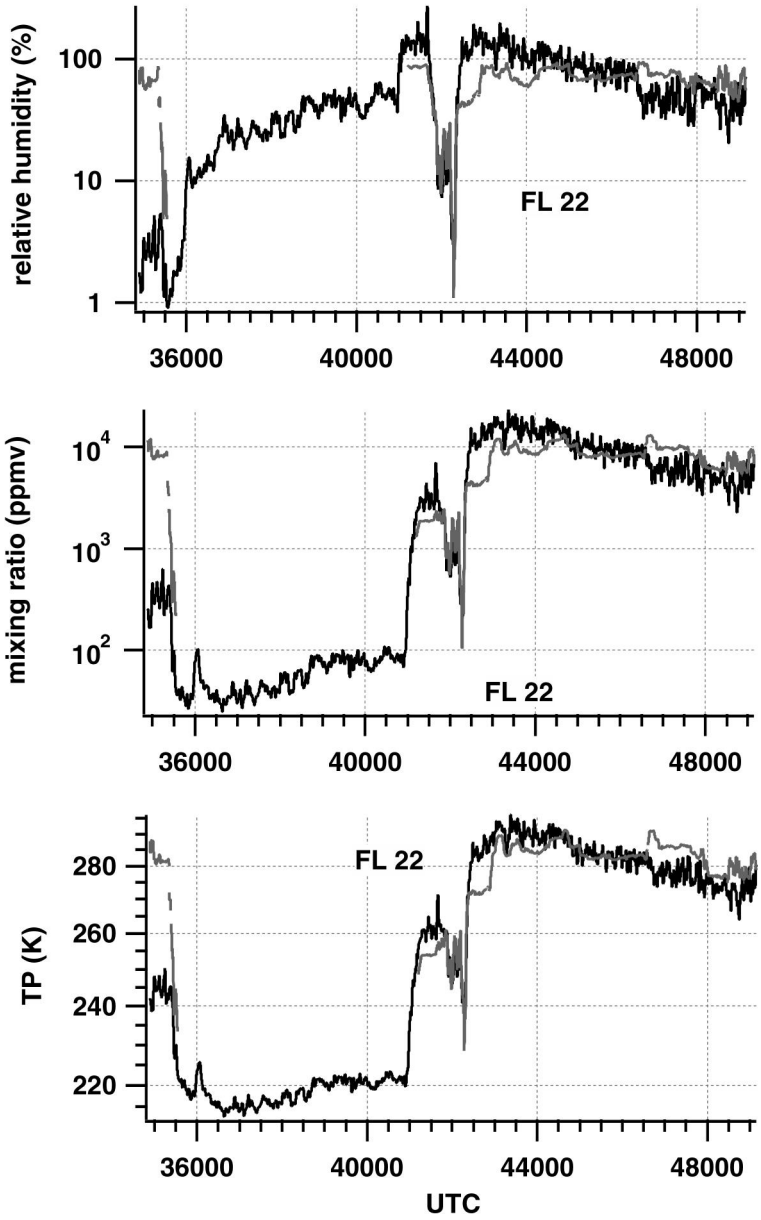

Figure A.11: H_2O mixing ratio, relative humidity and dew point temperature by mass spectrometer (black lines) and Lyman-α detector (gray lines). Data from flight 22^{nd} of July, ITOP campaign 2004.

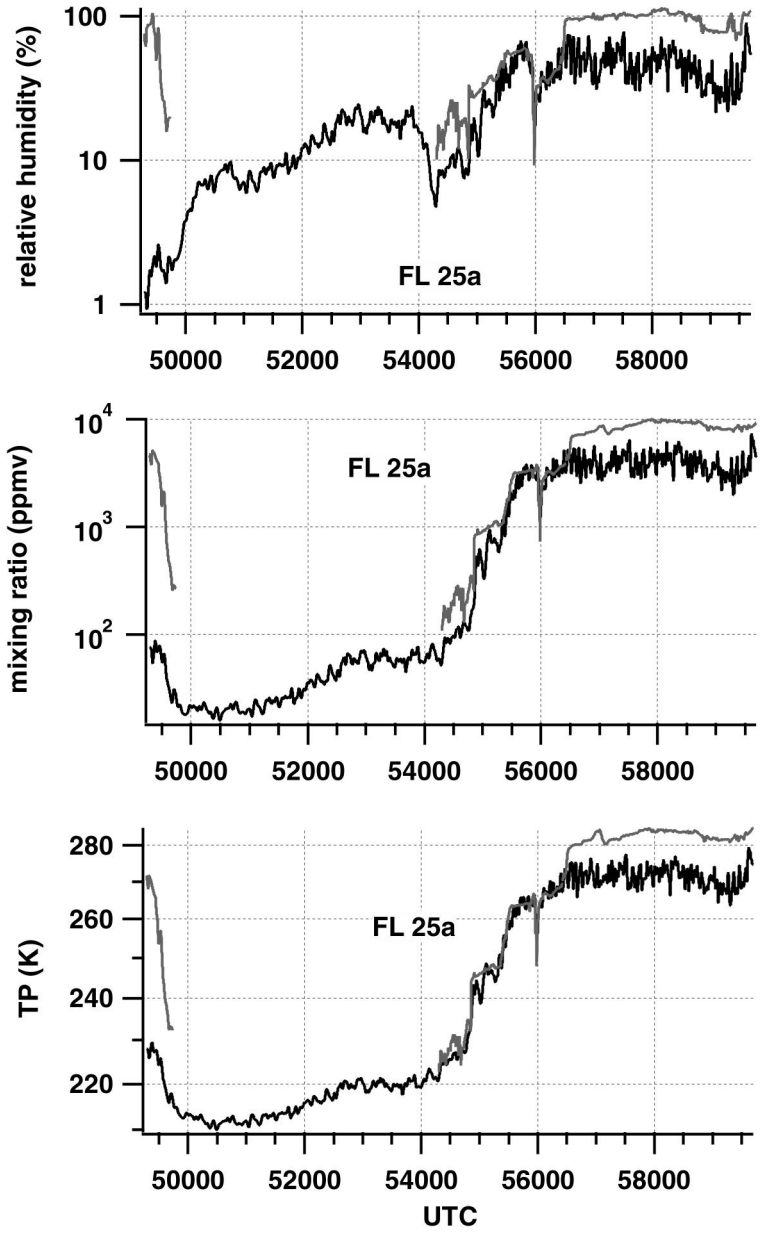

Figure A.12: H_2O mixing ratio, relative humidity and dew point temperature by mass spectrometer (black lines) and Lyman-α detector (gray lines). Data from flight 25^{th} of July, ITOP campaign 2004.

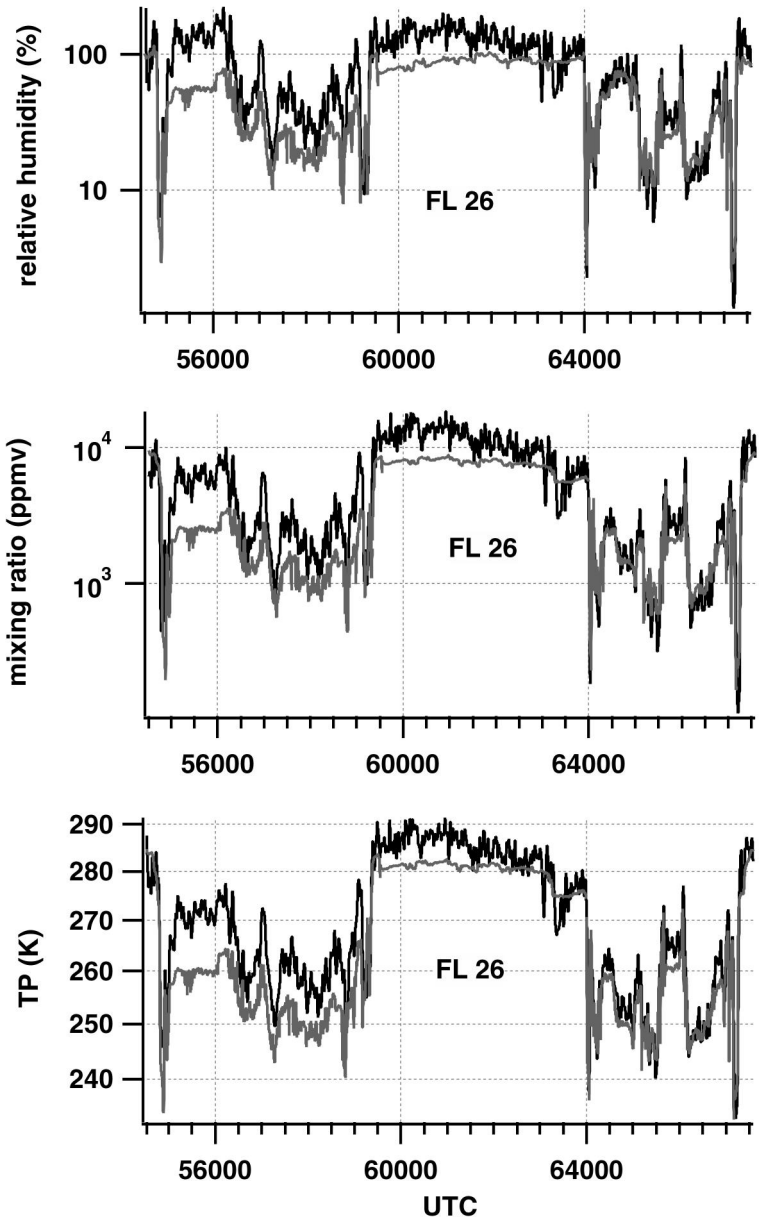

Figure A.13: H_2O mixing ratio, relative humidity and dew point temperature by mass spectrometer (black lines) and Lyman-α detector (gray lines). Data from flight 26^{th} of July, ITOP campaign 2004.

A.1.5 Conclusions

Generally spoken one can conclude that with the found mass spectrometric method the dew point of ambient air can be measured. The method is sensitive over a dynamic range large enough to detect the dew point at all flight levels with a signal strength well above statistical noise. An advantage of the method relies upon the fast sampling time of about 1Hz even at low water vapor mixing ratios. Calibration with a frost point hygrometer yielded a calibration function which can be even used to evaluate data from another campaign without additional modification of the fit parameters. This results from a comparison with a Lyman-α instrument used during the ITOP campaign. Here data is in good agreement although flight FL13 shows large deviations by up to a factor of three in relative humidity. One has to take into account that data obtained while passing through clouds is not excluded. Within clouds the humidity measurement by the Lyman-α detector is affected by evaporation of cloud particles resulting in a relative humidity exceeding 100%. Sensor wetting within clouds can lead to wrong temperature measurements as well. This error can be up to a few Kelvin. Since in the data of the TROCCINOX campaign which was used to derive the fit parameters, cloud segments were excluded, the apparent effect might be due to evaporation of cloud particles or due to sensor wetting of the Lyman-α detector. This especially holds since the calibration data set did not show such strong deviations in relative humidity and especially did not exceed values above 100%. A further advantage of the mass spectrometric method compared to any other currently used technique is the fact that no time is needed for the system to dry down.
Future work should concentrate on the laboratory investigation of the ion molecule reaction as well as on additional laboratory calibrations with a dew point mirror instrument. Certainly the temperature stability of the whole setup could be improved which currently drifts by about 10 K during a flight experiment. To electropolish the inner wall surfaces would additionally reduce water adsorption.
The question raises about the reliability of the method. Usually it is not recommended to completely rely on only one instrument for water vapor detection. Generally one "master" instrument calibrates another one. Calibration with a well established method like a TDL is probably a good idea, also since the sampling rate is at least 1 Hz. In the following the idea of a setup is described which would incorporate a TDL. A TDL instrument basically comprises beside the laser a mirror and a photodiode to detect the transmitted laser light. Depending on sensitivity the light path length is defined. In order to achieve ppm sensitivity (1-1000 ppmv) a light path of several cm would be sufficient for H_2O detection. Generally important to know is the water vapor

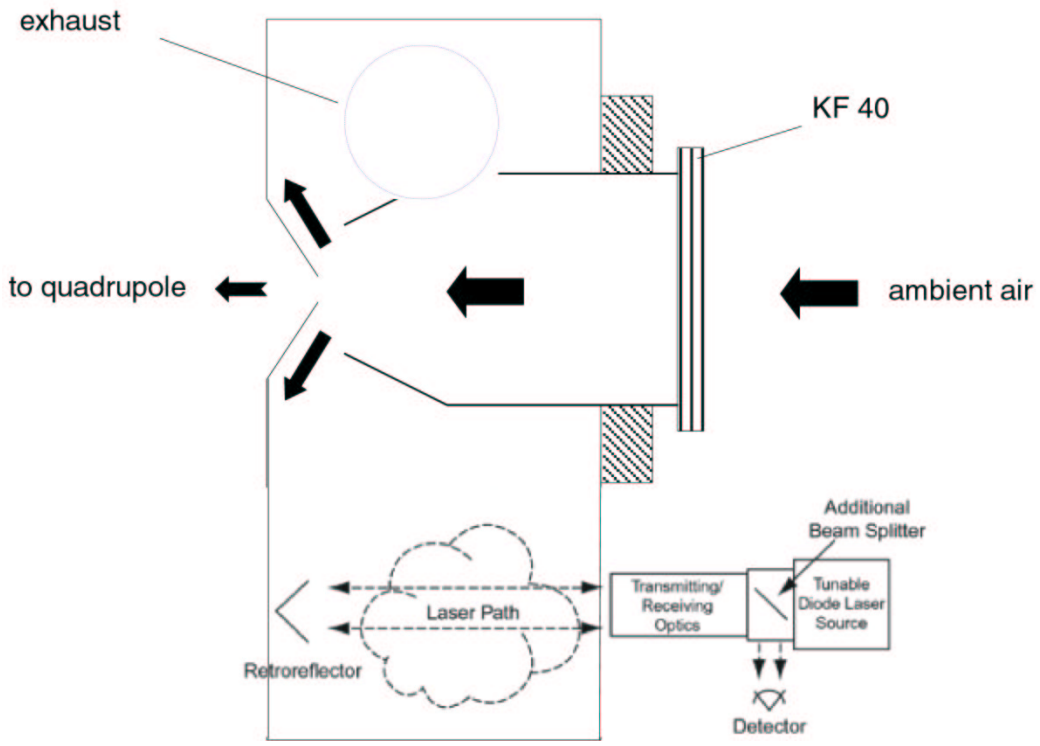

Figure A.14: Proposed setup for an incorporation of a tunable diode laser system which could serve as calibration unit.

concentration directly in the flow reactor where the chemical reactions occur. Since a TDL might change reactions by chemical-vibrational excitation, it has to be incorporated in the region in front of the critical orifice where space is unfortunately limited. **Figure A.14** shows the scheme of such a possible setup, where laser emitted light is reflected onto a mirror and passed onto a photocell. The pressure is sensor controlled by a feedback and kept at 70 mbar, temperature must additionally be stabilized. The TDL is tuned by changing the current and the temperature, controlled by a peltier element. Such a setup would make it possible to detect water vapor with two different techniques and thus to online calibrate the mass spectrometric method.

Appendix B

B.1 Overview Trace Gas Measurements during ITOP

Sulfur dioxide was determined by the Max-Planck-Institute for Nuclear Physics. The other here shown trace gases and the relative humidity data were determined by the DLR-Institue for atmospheric physics.

B.1.1 Flight 19.07.2004

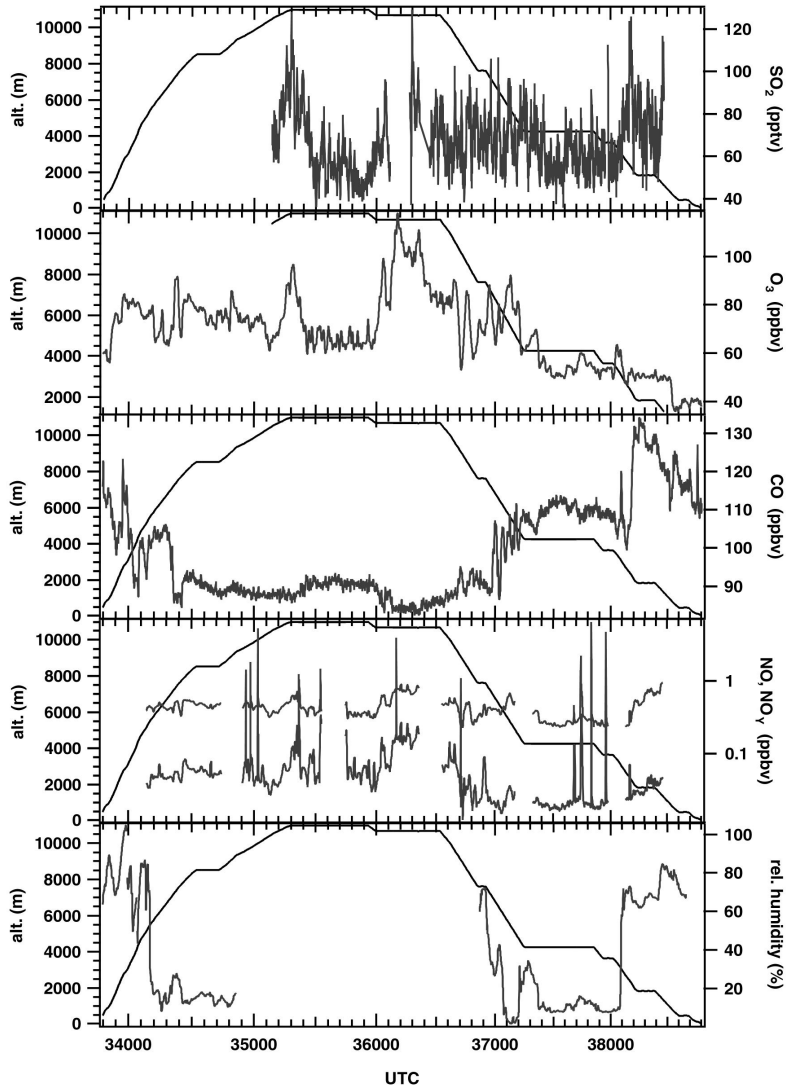

Figure B.1: Time series of flight 19.07.04 of SO_2, O_3, CO, NO, NO_y and relative humidity. Except SO_2 the trace gases were determined by DLR.

B.1.2 Flight 22.07.2004

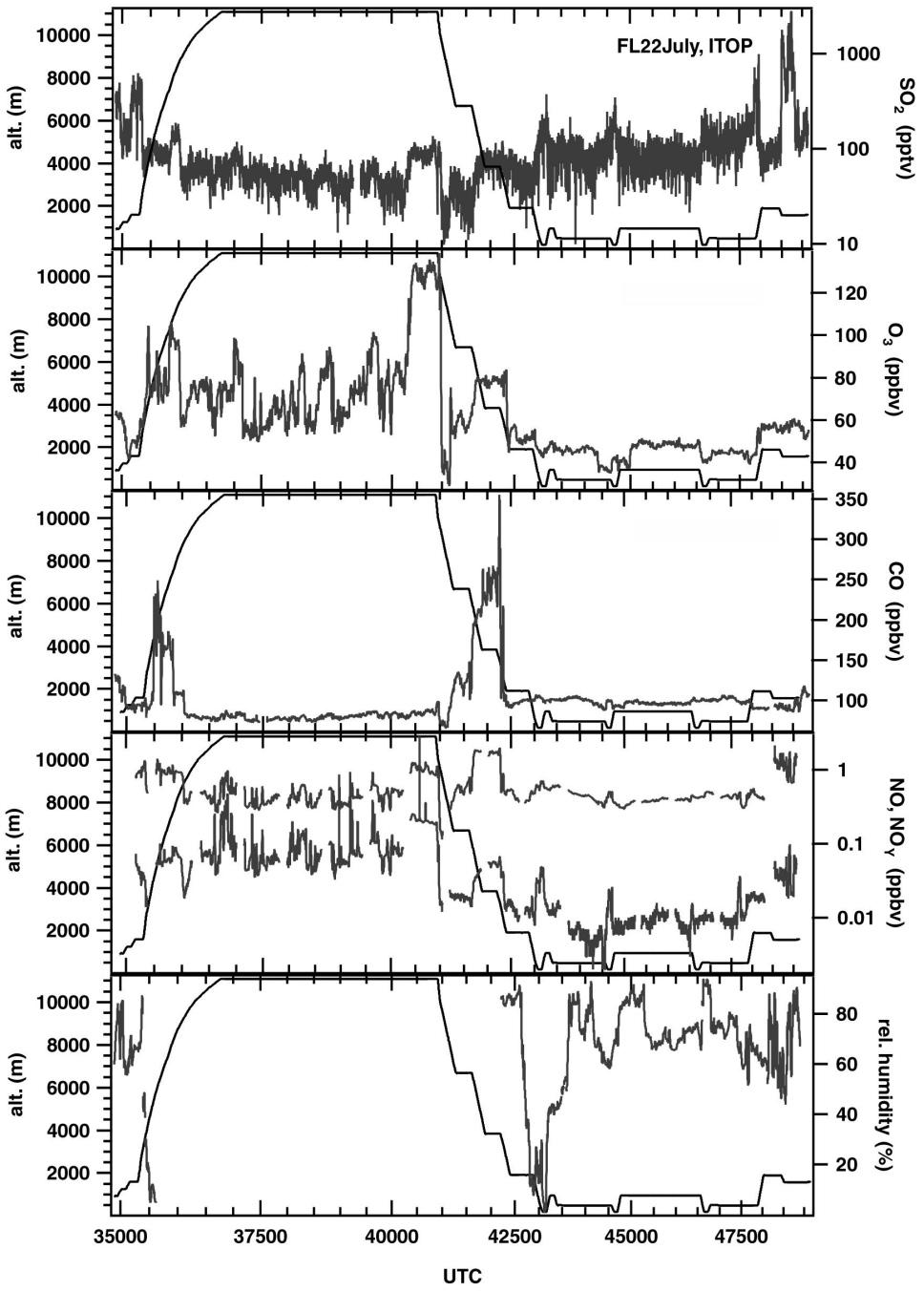

Figure B.2: Time series of flight 22.07.04 of SO_2, O_3, CO, NO, NO_y and relative humidity. Except SO_2 the trace gases were determined by DLR.

B.1.3 Flight 25a.07.2004 and 25b.07.2004

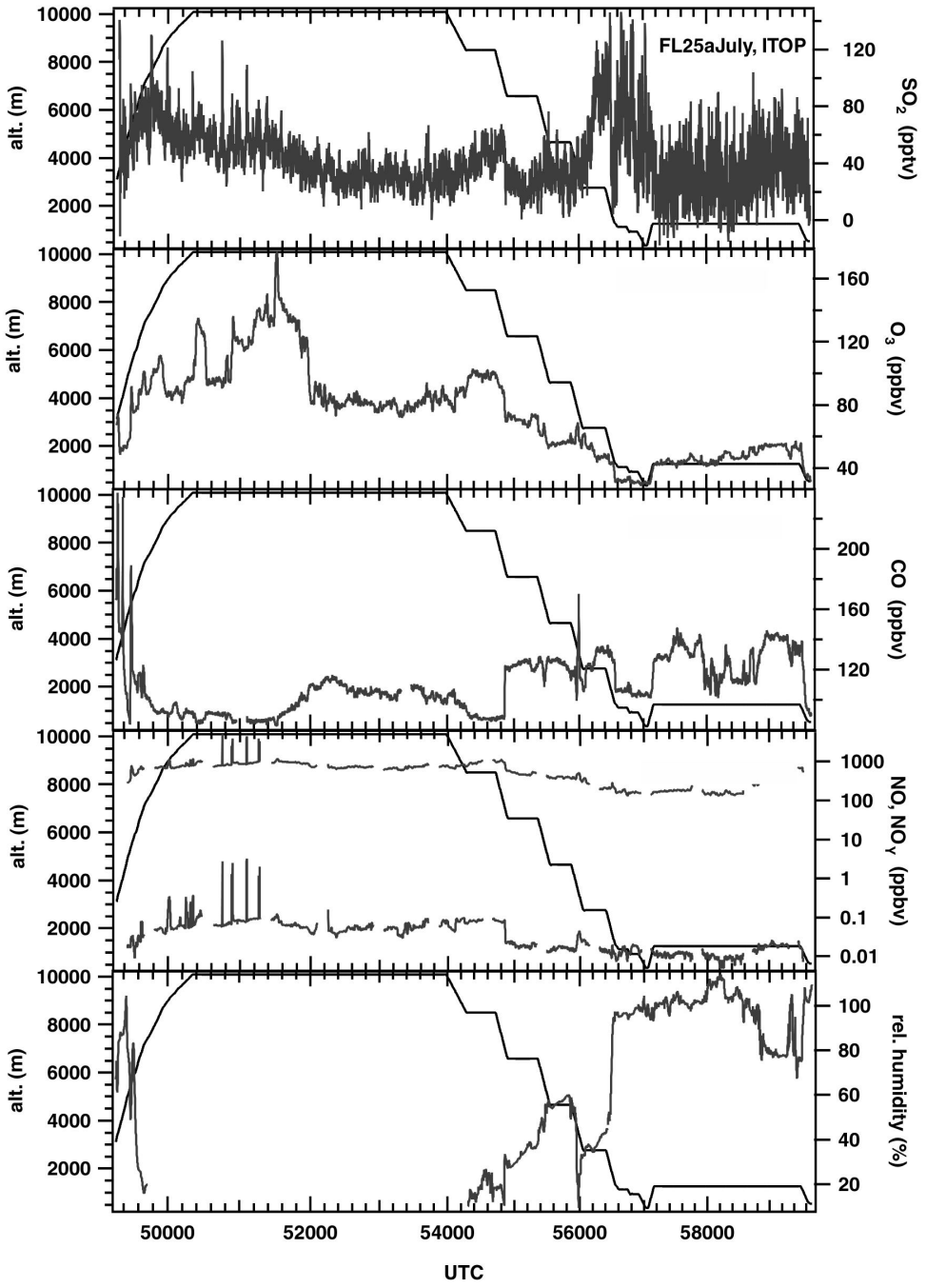

Figure B.3: Time series of flight 25.07.04 (a) of SO_2, O_3, CO, NO, NO_y and relative humidity. Except SO_2 the trace gases were determined by DLR.

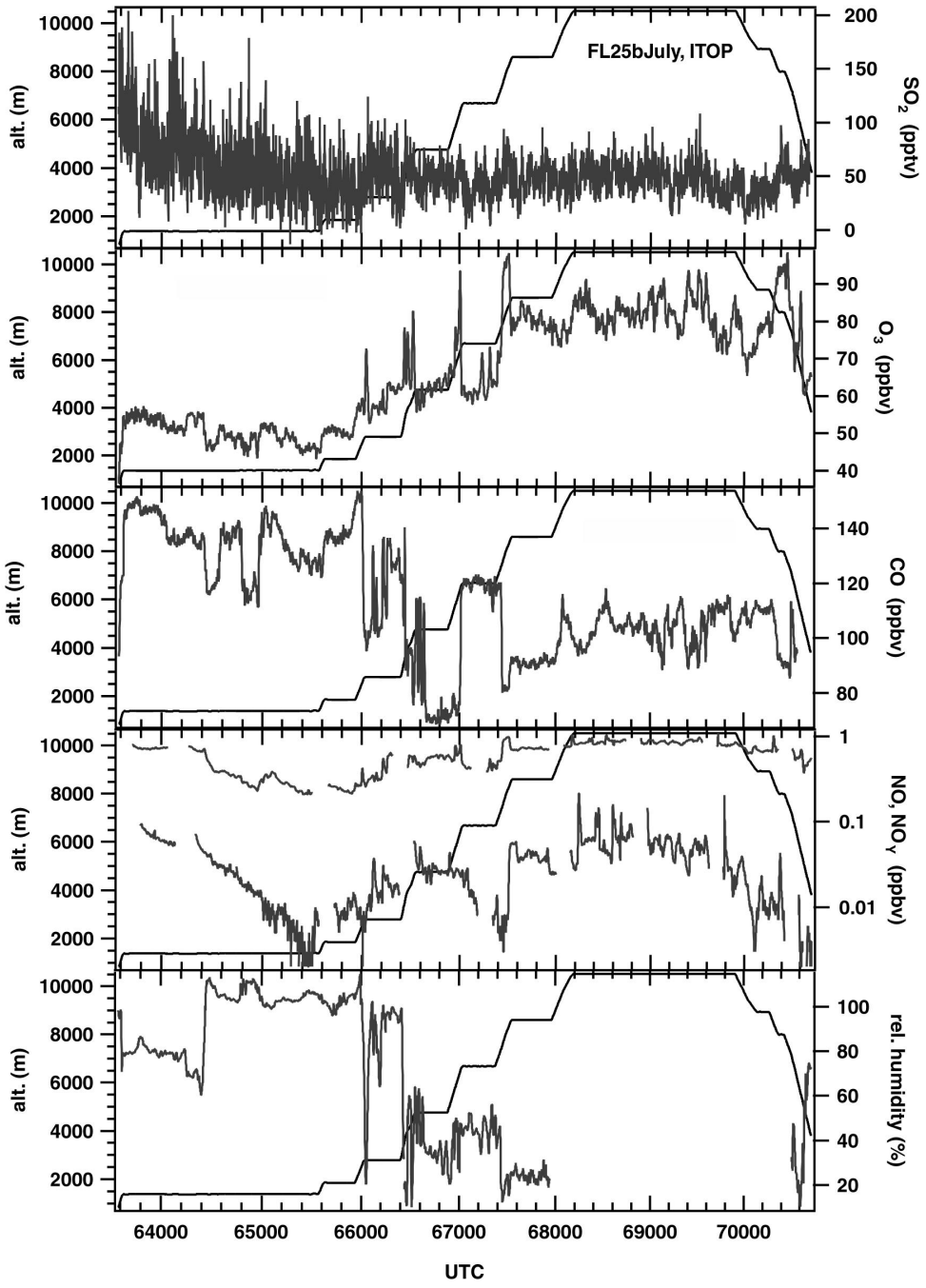

Figure B.4: Time series of flight 25.07.04 (b) of SO_2, O_3, CO, NO, NO_y and relative humidity. Except SO_2 the trace gases were determined by DLR.

B.1.4 Flight 26.07.2004

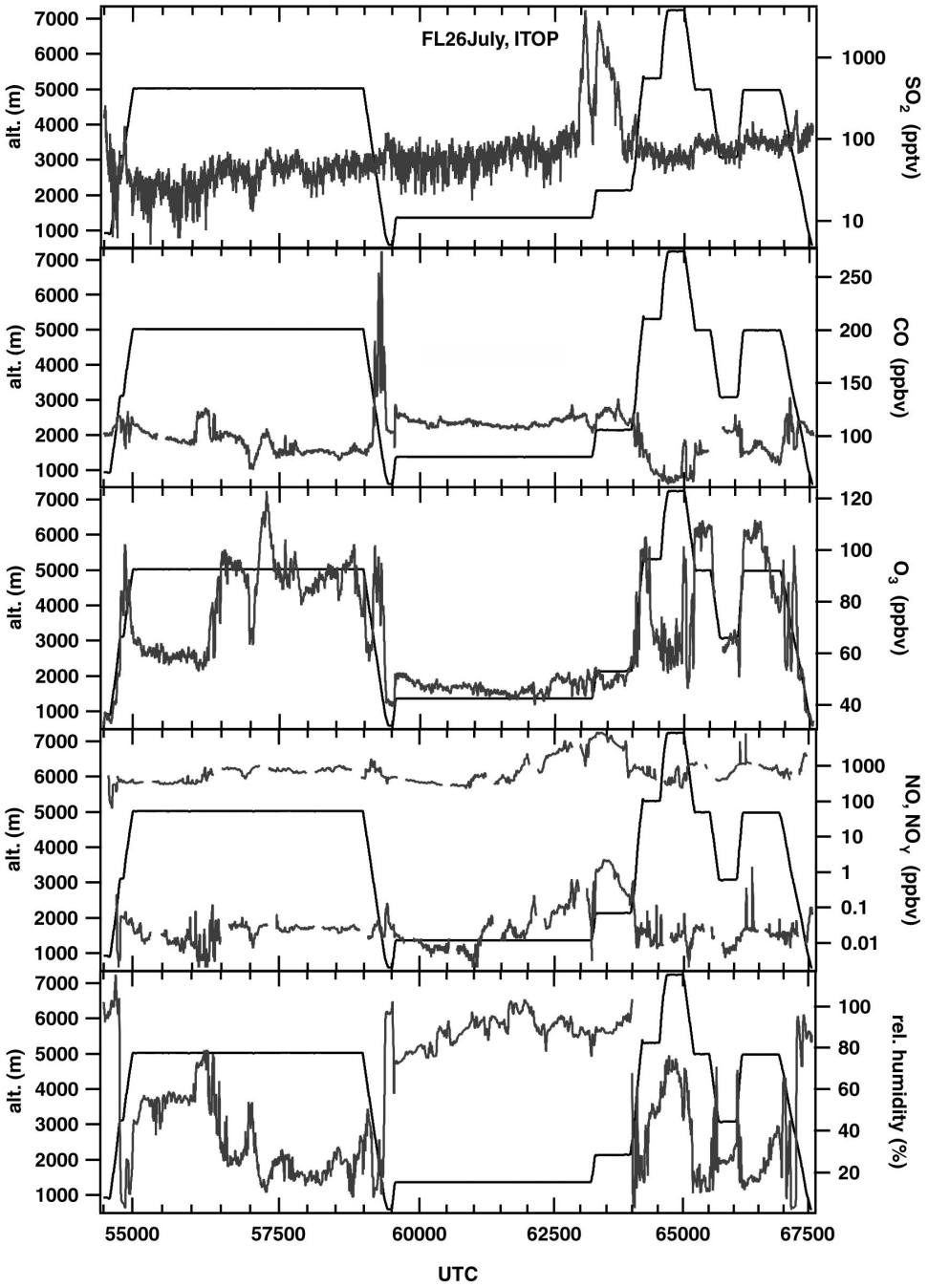

Figure B.5: Time series of flight 26.07.04 of SO_2, O_3, CO, NO, NO_y and relative humidity. Except SO_2 the trace gases were determined by DLR.

B.1.5 Flight 31.07.2004

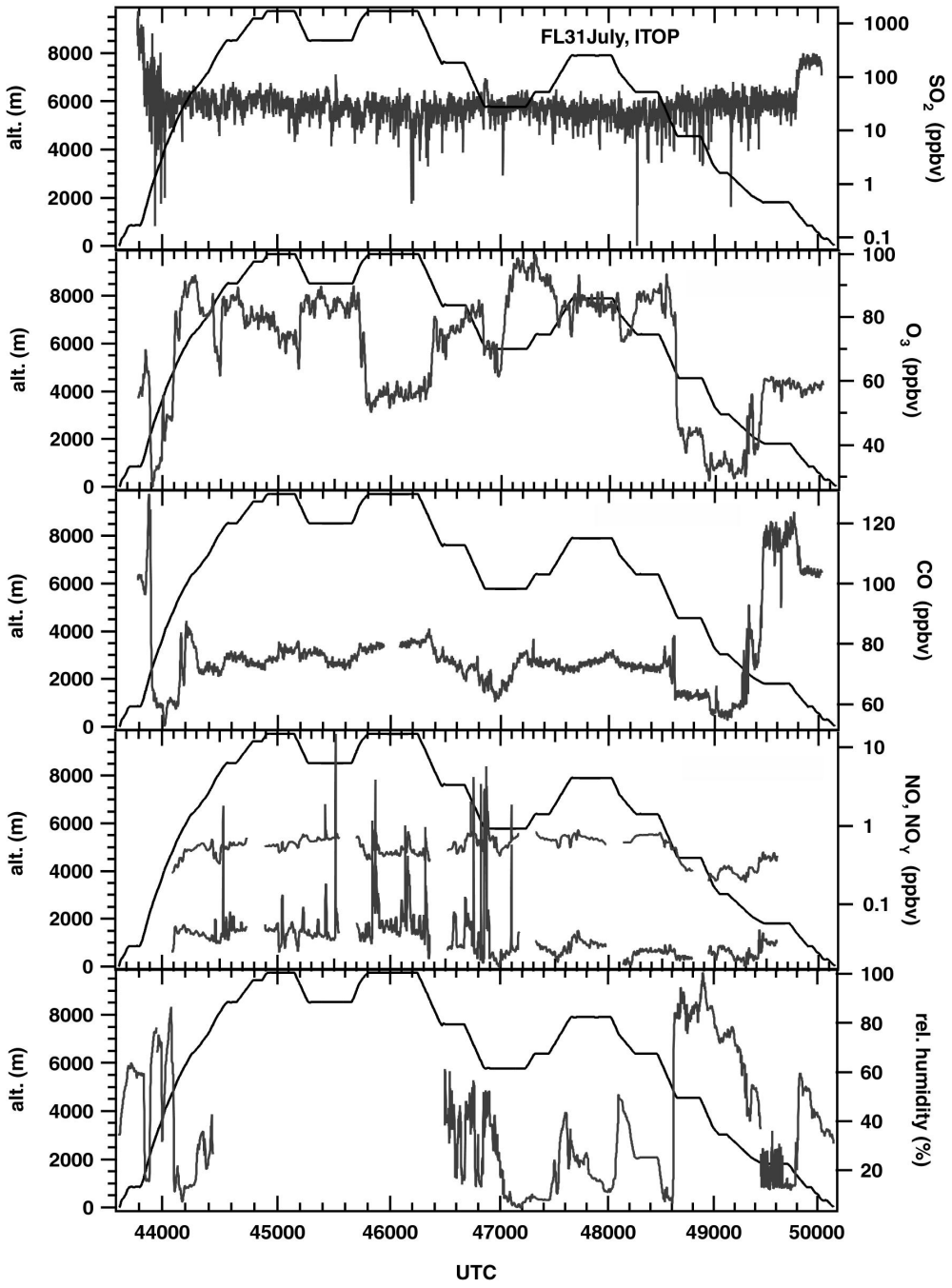

Figure B.6: Time series of flight 31.07.04 of SO_2, O_3, CO, NO, NO_y and relative humidity. Except SO_2 the trace gases were determined by DLR.

B.1.6 Flight 03.08.2004

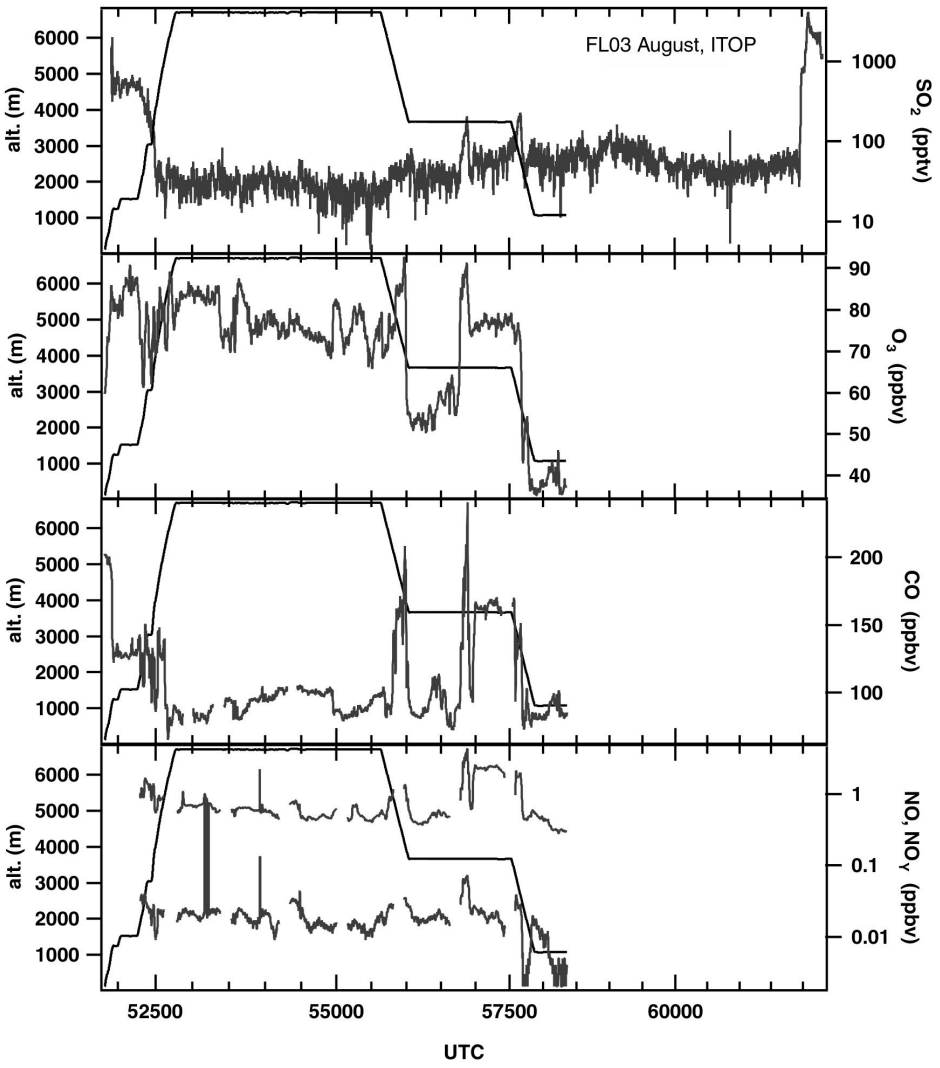

Figure B.7: Time series of flight 03.08.04 of SO_2, O_3, CO, NO and NO_y. Except SO_2 the trace gases were determined by DLR. The flight served as intercomparison with the english aircraft Bae-146. Unfortunately no further sensor data like temperature, relative humidity, etc. is available.

B.1.7 Scatter Plots

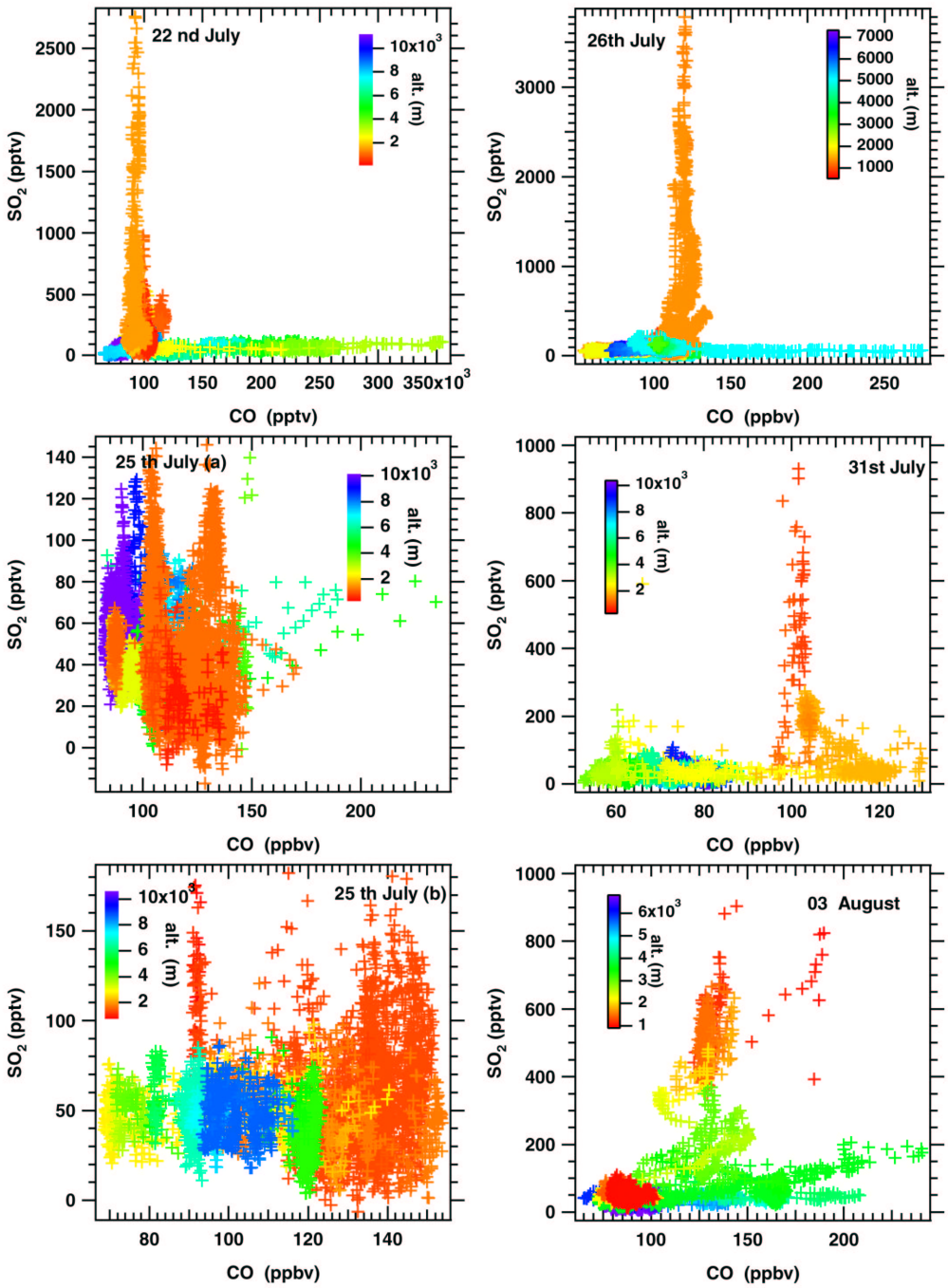

Figure B.8: Overview of CO versus SO_2 scatter plots.

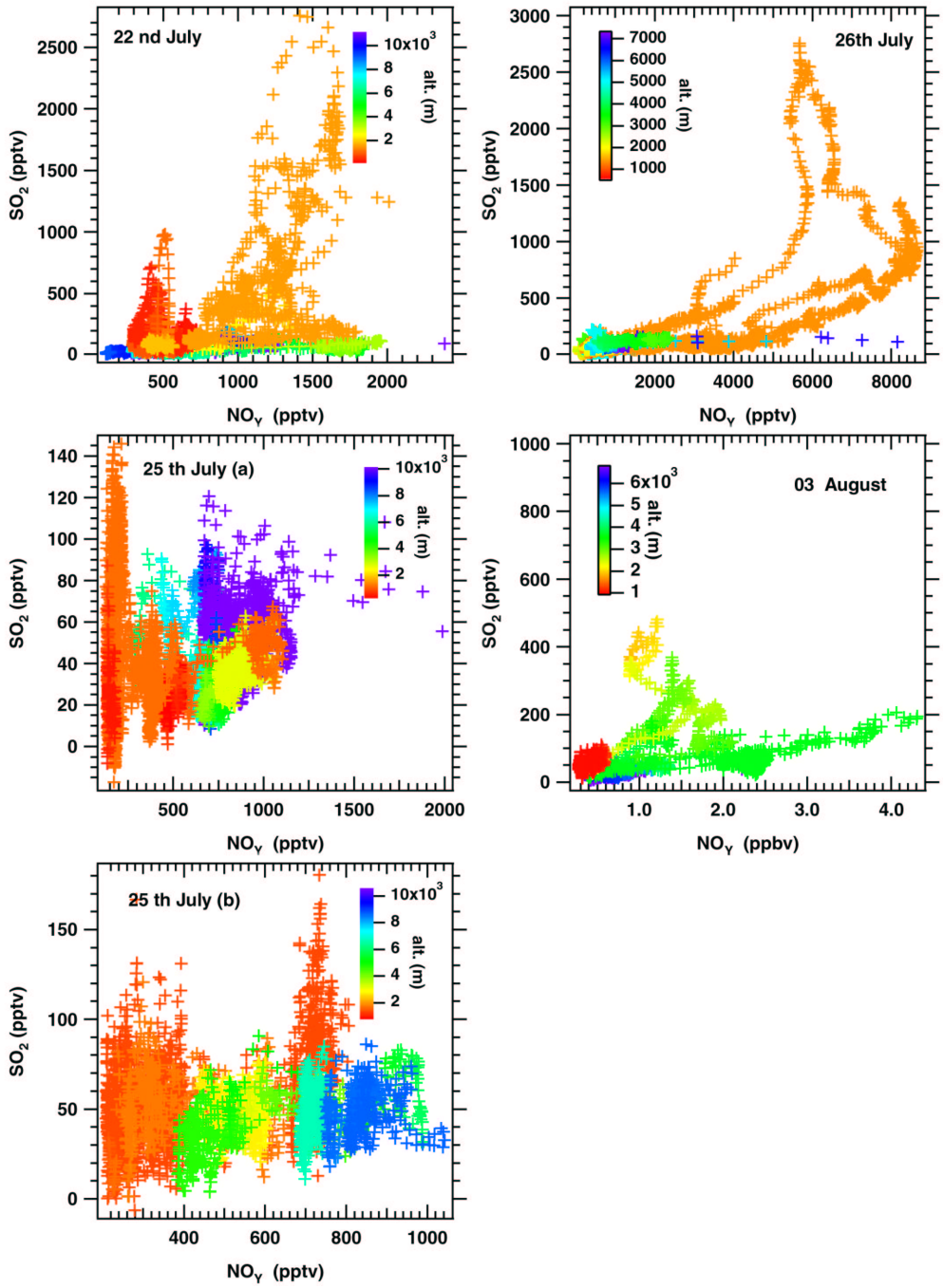

Figure B.9: Overview of NO_y versus SO_2 scatter plots. No data is available for the 31_{st} of July.

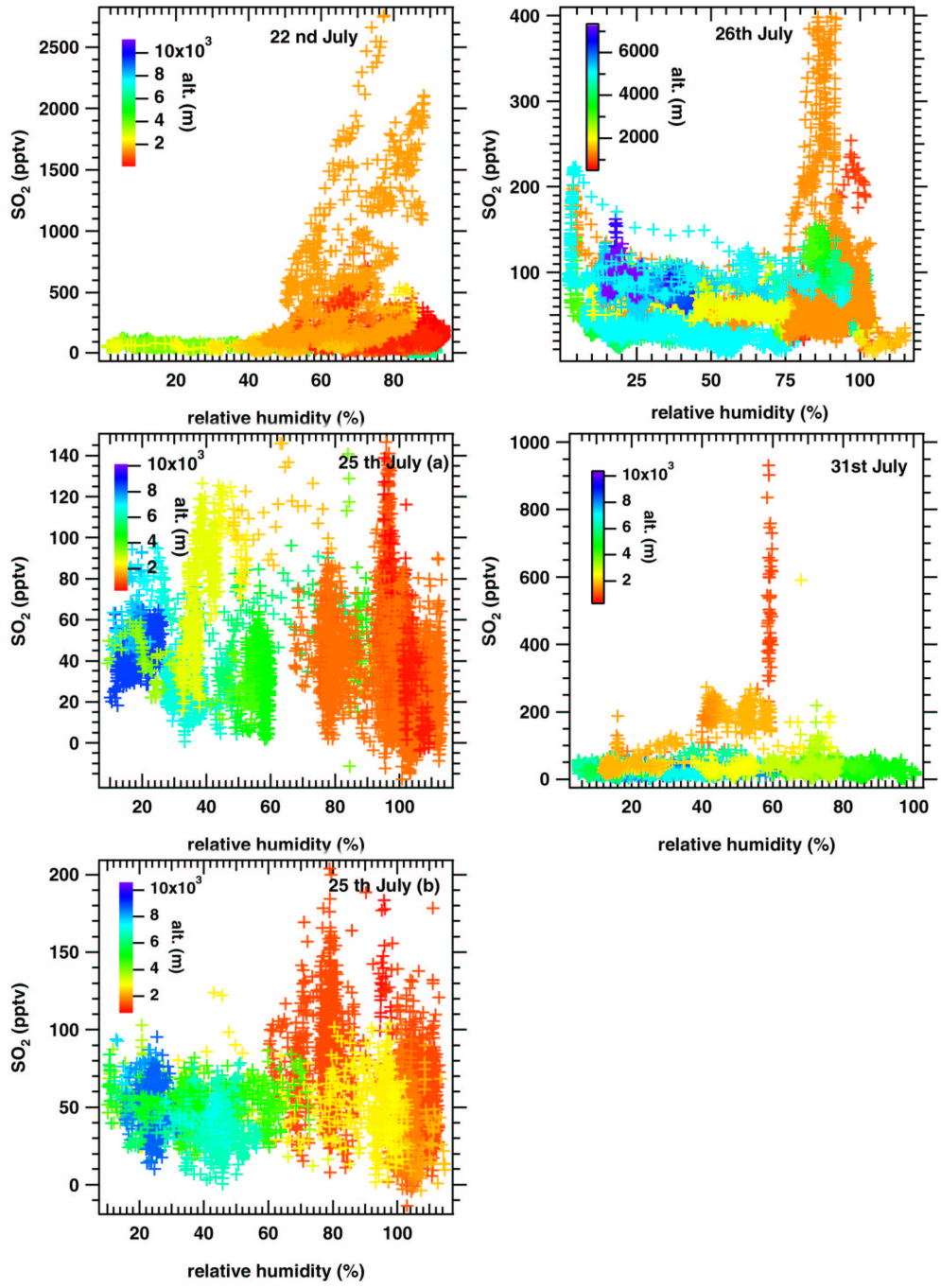

Figure B.10: Overview of relative humidity versus SO_2 scatter plots. No data is available for the 3 of August.

B.2 Overview of SO_2 Measurements during SHIPS

B.2.1 Introduction

Fuels burned by seagoing ships are cheap, low-grade and sulfur-rich residual fuels. The CO_2 emissions from ships constitute 3.8% of the total CO_2 emissions from fossil fuel burning and 23% world transport CO2 emissions (GMES-GATO Strategy Report, 2004). Emissions from seagoing ships are released into the marine boundary layer along the ocean trade routes where ship impact can be significant due to the lack of other pollution. Oxidation of the ship-emitted sulfur dioxide to sulfuric acid followed by condensation leads to an increased concentration of sulfate aerosols, which causes a negative radiative forcing. Aerosols from ships can also cause an increase in droplet number concentration and a decrease in droplet size of marine stratocumulus clouds. Consequently, scattering by clouds and reflectivity increase. Signatures of these effects can be observed in the form of so-called ship tracks. Ship tracks cause a cooling of the atmosphere. The satellite picture shown in **figure B.11** clearly resolves elongated, white cloud patterns, similar to contrails from aviation traffic, which like a net span the area of high ship traffic.

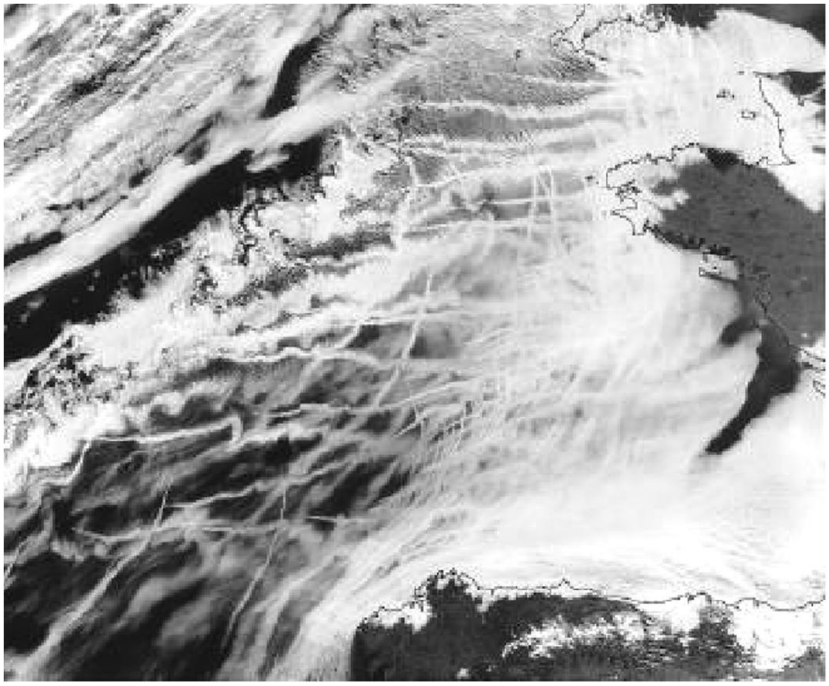

Figure B.11: Satellite image west of the English Channel showing ship tracks.

The international campaign SHIPS (initiated and coordinated by DLR) aimed to observe the effect of marine boundary layer pollution by ships. The MPI-K contribution was mainly sulfur dioxide measurements with our IT-CIMS mass spectrometer on board of the research aircraft Falcon. The measurements took place in the English Channel, a region of heavy ship traffic.

B.2.2 Flight of 23. July 2004

The flight of 23^{th} of July was performed over the English Channel as shown in **figure B.12** within a zone of large ship traffic. Polluted marine boundary layer air was sampled at constant height of 320 m above sea level. SO_2 abundances together with a zoom view of the off-shore period are shown in **figure B.13**. In close proximity to the coast, SO_2 abundances increased to about 100 pptv corresponding to a background mole fraction. Single peaks up to 1.3 ppb and an overall increase to about 300 ppt is apparent when further leaving the coast. The peaks emerge from direct crossings of ship plumes. Since ship traffic was strong in that region, several plumes merge with each other and tend to broadly enhance background SO_2 abundances.

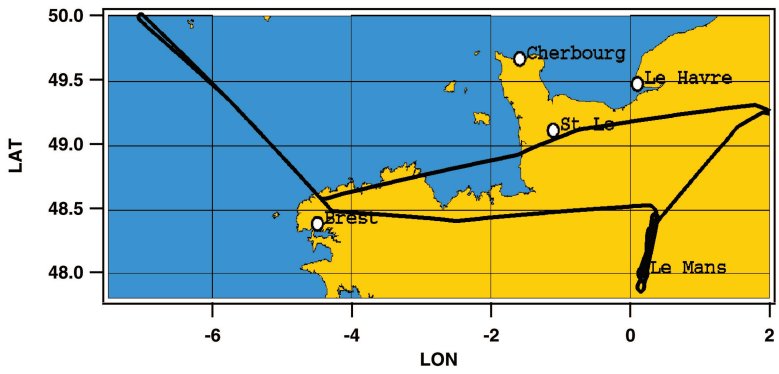

Figure B.12: Map with overlayed flight track. Marine boundary layer air was sampled north west of Brest (France)within a zone of strong ship traffic.

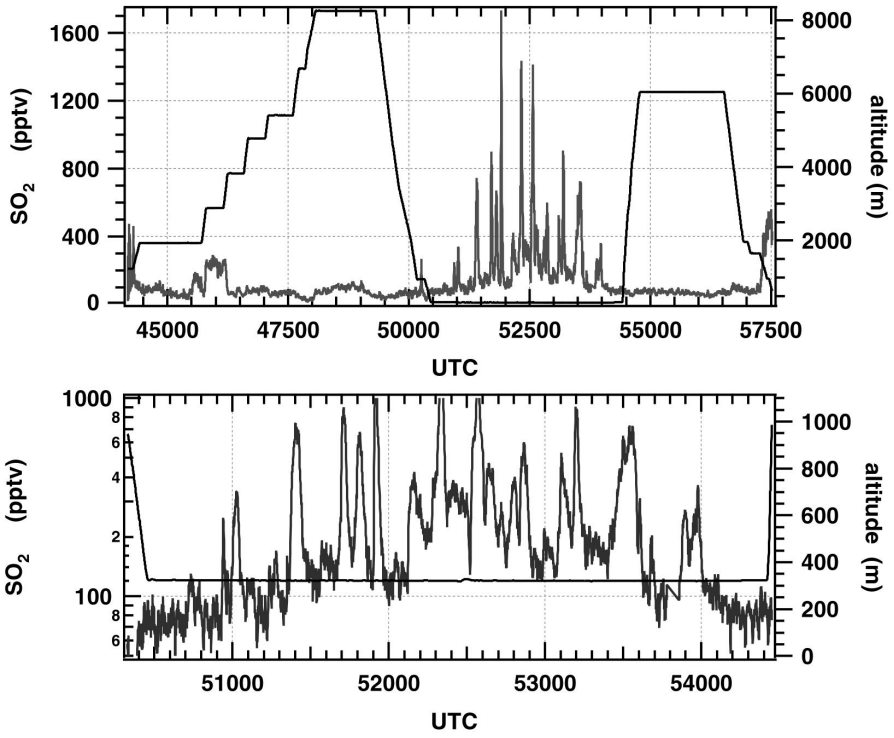

Figure B.13: Total SO_2 time series (upper panel) and zoom of ship corridor passage (bottom plane) of the flight of 23. July.

B.2.3 Flight of 30. July 2004

The flight of 30^{th} of July is an example of a single ship plume chase. The aim was to observe the plume chemistry also in terms of the above mentioned sulfuric acid - particle growth mechanism. Due to the current status of data analysis no aerosol data is available yet and only the analyzed trace gas data can be shown. The flight experiment aimed to sample the pollution plume of a common container ship used for transatlantic traffic. Single plume experiments in that region rise the problem of neighboring ship emissions or contributions of aged plumes released by previous ships. This may lead to mixtures of differently aged plumes. Thus it cannot be excluded that the measured trace gas mixing ratios may contain contributions of ships who earlier used the same passage or a neighbored ship trail. **Figure B.14** shows the container ship whose pollution plume was sampled up to a distance of about 20 km.

Figure B.14: The container ship whose emissions were sampled by the DLR aircraft Falcon. The lower left corner of the picture shows a part of the left wing of the research aircraft.

The corresponding plume age amounts to 33 min considering a ship velocity of 23 knots (11.8 m/s). The experiment was performed about 100 km north of Brest (France) in the north Atlantic region. **Figure B.15** shows flight coordinates with the color code referring to detected NO_y emissions in the ship inertial system. The container ship was twice directly approached by the aircraft. Frontally (bow) to follow the visible, ascending plume and from behind (rare) to stay inside the visible, descending plume. During direct approach from rear side, the aircraft started to descent from about 400 m altitude and followed the looming plume until the ship was crossed in about 25 m altitude. That complete approach period is marked in red in **figure B.16**, where the vertical view of the aircraft track versus ship distance is shown. Significantly higher NO_y concentrations within the plume were detected in both cases (rare side and bow side approach) as seen in **figure B.15**. Three plateaus were performed to horizontally cross the plume and to stay as long as possible inside it. Time periods where NO_y, NO, CO_2 and SO_2 showed highest mixing ratios within these plateaus are marked with circles. The flight trail overlaying dashed red segment indicates the direct ship approach from behind. Also shown in this graph is the calculated altitude versus distance relation obtained by a Gaussian plume model (blue line).
Here the interception at plateau B is shown. Interestingly the plume structure is split

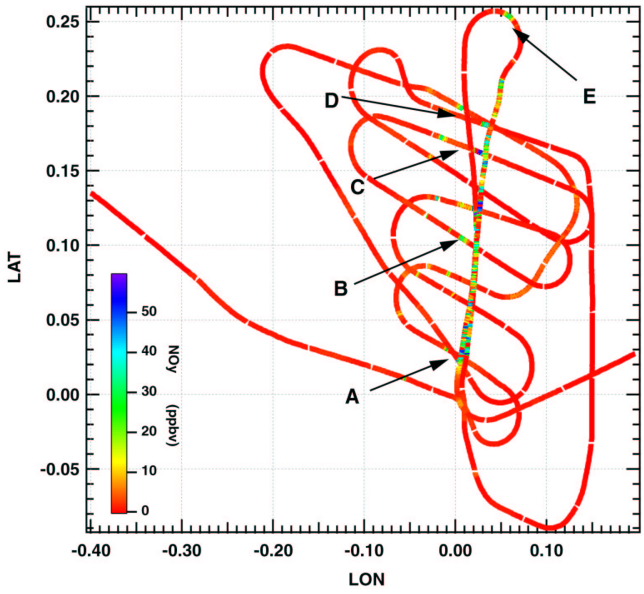

Figure B.15: Flight trail in ship inertial system with the color code referencing to the NO_y trace gas mixing ratio. Altitude levels of vertical plume interception are marked by letters.

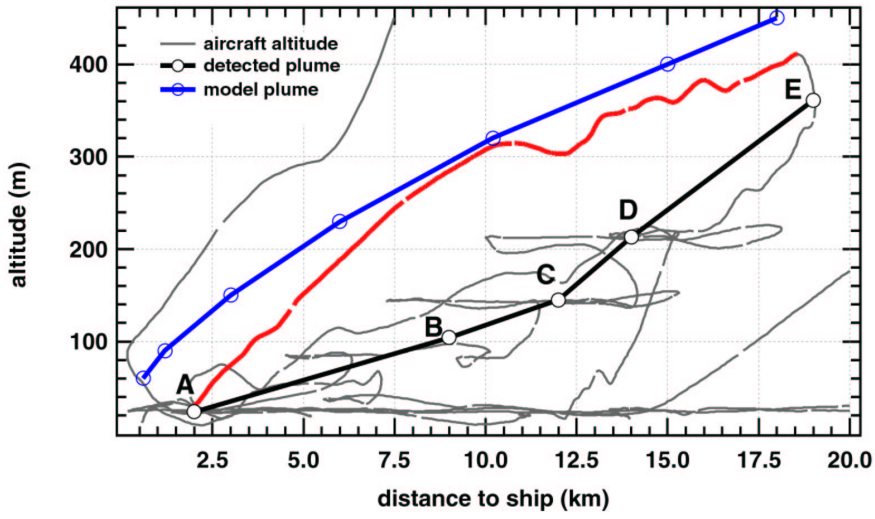

Figure B.16: Vertical view of the flight trail. Altitude levels of vertical plume interception indicated by elevated SO_2, NO, NO_y and CO_2 are marked by letters. The blue line represents the altitude-distance relation obtained by a gaussian plume model.

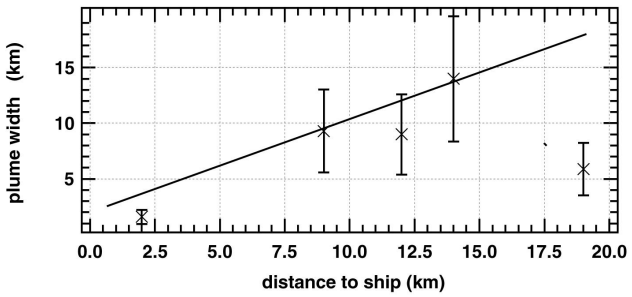

Figure B.17: Plume width derived from SO_2 signal decrease to a background mixing ratio of 700 pptv.

From aircraft speed (about 100 m/s) and plume interception time the width was estimated as shown in **figure B.17**. The interception period was identified by SO_2, NO and NO_y enhancements above a specified background of 700 pptv (SO_2), 0.6 ppbv (NO_y), 0.01 ppbv (NO) and 374 ppmv (CO_2). The plume width then was derived only by taking the temporal extension of the elevated SO_2 signal into account. An error of $\pm$ 40 % for the experimentally derived width was considered. Plotted in **figure B.18** are the trace gas mixing ratios of NO_y, NO, CO_2 and SO_2 measured during a typical plume interception.

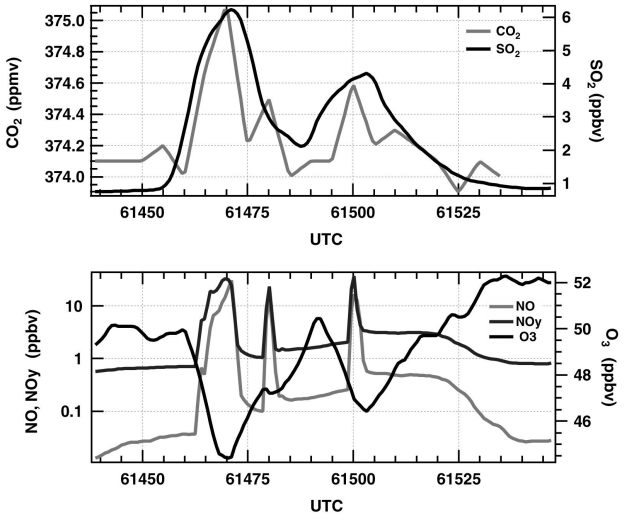

Figure B.18: Trace gas mixing ratios measured during ship plume interception at level B. NO,NO_y and O_3 measured by DLR, CO_2 measured by MPI-Chemistry, Mainz, Germany.

into two main peaks, separated by 30 s (300 m). This effect is not seen in the first crossing (level A) at a distance of 2 km behind the ship and a plume age of 3 minutes. Apparently the plume started to split while it dispersed. The two-peak feature can be also observed during further removal from the ship. SO_2 increases up to 4-6 ppbv, strongly correlated with elevations in CO_2 (376 - 374 ppmv), NO (17 - 30 ppbv), NO_y (32 - 36 ppbv). In contrast, ozone shows a strong anti correlation with the NO, NO_y data. It decreases from a background of about 52 ppbv to 44 - 46 ppbv.
Figure B.19 summarizes the different trace gas abundances as function of plume age. With increasing plume age all trace gases beside ozone experience a loss in concentration whereas ozone increases.

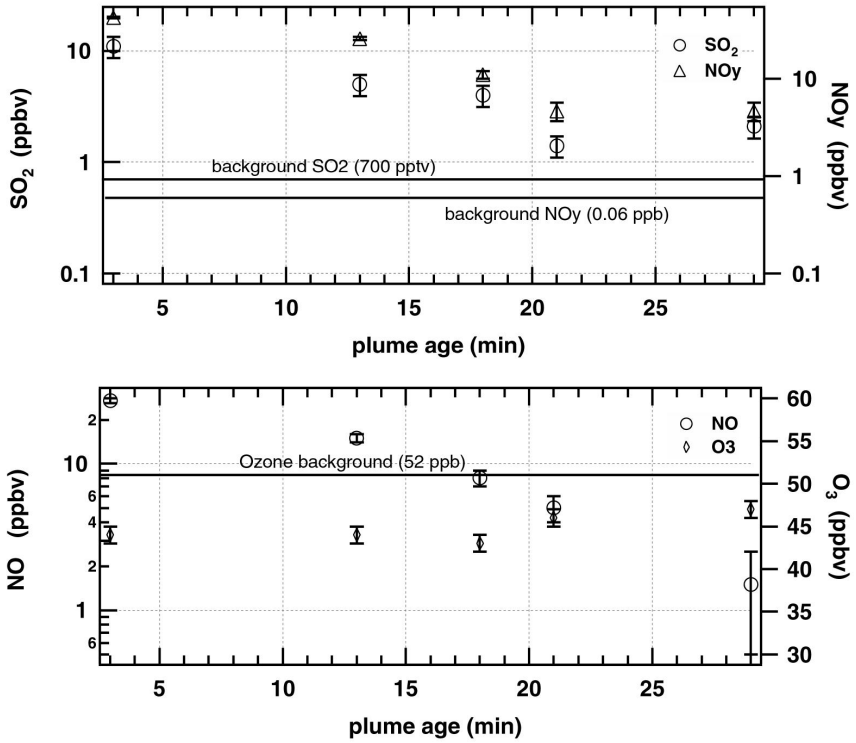

Figure B.19: Evolution of average trace gas mixing ratios as function of plume age, measured while crossing the different altitude levels A,B,C,D and E shown in **figure B.16**.

This behavior is commonly observed in power plant plumes [Gilliani, 1998], [Ryerson, 1998] and ship plume studies [Song, 2003b], [Chen, 2005]. A major difference compared to cases mentioned in the literature is the considerably younger plume age (30 min compared to several hours). Thus the observed behavior of an NO and NO_y re-

duction is more likely to refer to dilution and mixing of the outer plume structure with marine boundary layer air than due to plume chemistry. This becomes more evident when inspecting **figure B.20** which shows trace gas mixing ratios during the direct aircraft approach from about 400 m altitude towards the rare of the ship. The altitude during descent corresponds to the red marked part of the height profile shown in **figure B.16**. NO and NO_y abundances show no significant change during the ship approach. In fact average mixing ratios remain constant at 14 ppbv (NO), 24 ppbv (NO_y) respectively. Ozone reduces from background (52 ppbv) to 18 ppbv and is well correlated with the elevation in NO and NO_y. SO_2 shows some variability with a maximum of 130 ppbv (700 pptv background subtracted) at 5.5 and 6 km distance to the ship. Interestingly the performed altitude profile during descent rather corresponds to the shown Gaussian plume shape in **figure B.16** than to the shape indicated by the altitude levels (A,B,C,D,E). Since trace gas mixing ratios are enlarged compared to the average ratios obtained for the altitude plateaus one may conclude that during direct descent the plume center was hit up to a distance of 9 km to the ship. Because NO and NO_y abundances appear not to significantly change, we deal with an early ship plume evolution. Only the CO_2 mole fraction decreases by about 24 ppmv to a background of 374 ppmv according to the gaussion plume dilution model, although the model underestimated excess CO_2 by at least a factor of 2. In the literature three stages of plume evolution are described [Song, 2003b],[Karamanchanda et al. 2000]: (1) the early plume dispersion when $NO_x < 1$ppm, (2) the mid-range dispersion where NO_x equals several ppb and (3) the long-range dispersion, where $NO_x < 1$ ppb. In the first stage NO_x levels drop below 1 ppm several minutes after a ship puff release. Plume age can also be classified by characteristic ozone concentrations namely ozone depletion (1), O_3 recovery (2) and ozone production (3). Concerning the present case the anti correlation between O_3 and NO proposes that the reduction of ozone by NO via

$$NO + O_3 \longrightarrow NO_2 + O_2 \tag{B.1}$$

was a favored chemical reaction. Literature refers phase 2 to start roughly after 30 - 100 min, when substantial mixing of outside boundary layer air into the plume has restored O_3 to near background level. Thus other chemical reactions become pronounced. It is in this stage that the major HO_x radical formation is reactivated. The rise in OH reflects not only enhancements in

$$O_3 + h\nu \longrightarrow O(^1D) + O_2 \tag{B.2}$$

$$O(^1D) + H_2O \longrightarrow 2\ OH \tag{B.3}$$

but also the strong onset of reaction:

$$NO + HO_2 \longrightarrow NO_2 + OH \tag{B.4}$$

$$NO_2 + h\nu \longrightarrow O(^3P)NO \tag{B.5}$$

$$O(^3P) + O_2 \longrightarrow O_3 \tag{B.6}$$

which leads to the photochemical production of ozone. In the early stage, NO_y mainly comprises contributions from the $NO_x = (NO + NO_2)$ component. This is reflected in the very similar mole fractions detected for both species (**figure B.20**).

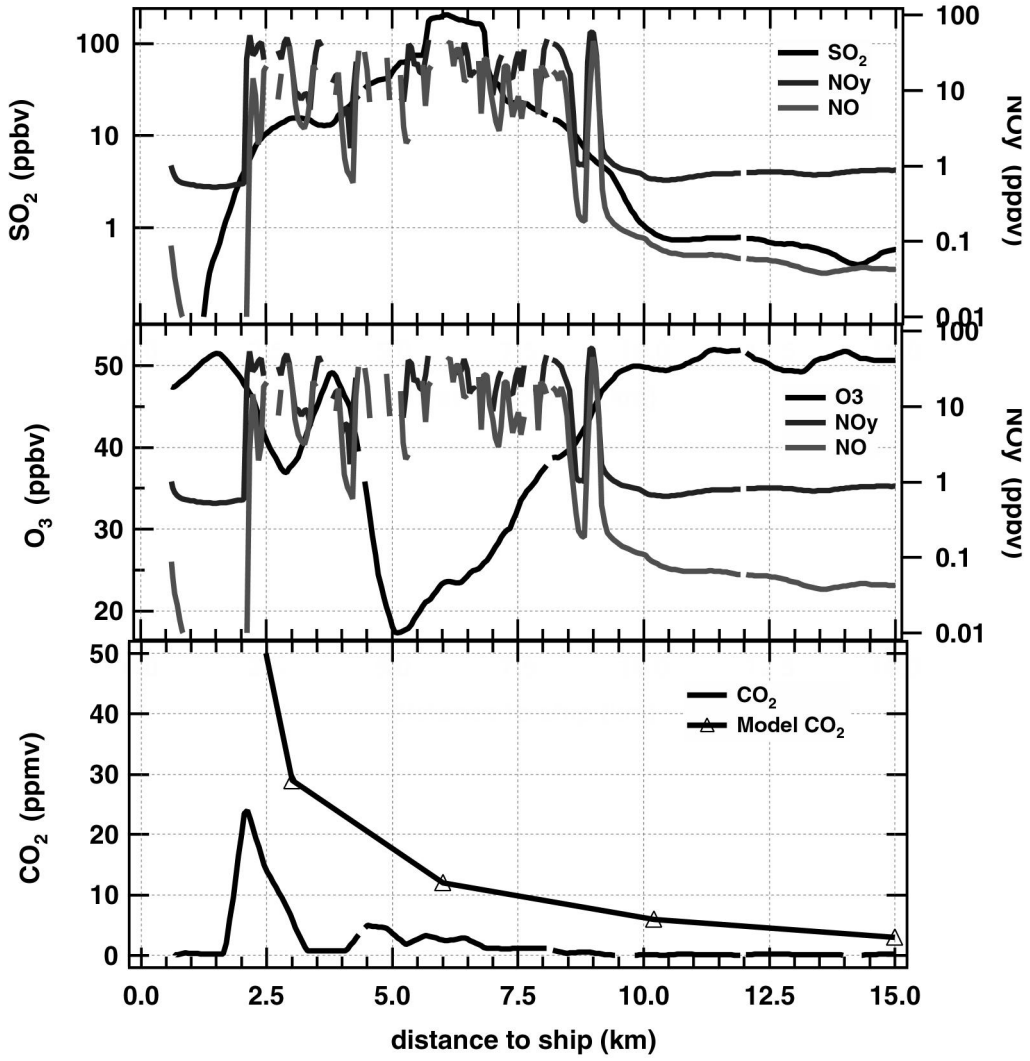

Figure B.20: Trace gas mixing ratios during direct aircraft descent from about 400 m altitude towards the rare of the ship (NO, NO_y,O_3 and CO measured by DLR).

When radical production is enhanced, the formation of HNO_3 results in a further contribution to the NO_y fraction. By contrast the lifetime of SO_2 is primarily controlled by heterogenous processes that are largely independent of plume chemistry. The major loss pathway is via heterogenous loss to sea-salt aerosol and can be strongly influenced by the meteorological stability of the marine boundary layer [Song, 2003a]. Stable conditions lead to the maximum loss rate, whereas the unstable condition gives the minimum value. The production of the oxidation product sulfuric acid (H_2SO_4) depends on both, the level of SO_2 and OH. The maximum in OH is dictated by a combination of solar intensity and NO_x effects. Unlike H_2SO_4 which due to its very low vapor pressure and high mass accommodation coefficient is irreversibly partitioned onto sea-salt aerosols, SO_2 behaves somewhat more complex. First, SO_2 must be transported to the surface of particles or cloud droplets, and then some fraction of this must be scavenged by $SO_2(g) \rightarrow SO_2$ (heterogenous chemistry). Oxidation of SO_2 on sea-salt particles (having high pH values 6.5 - 7.4) occurs predominantly via $O_3(aq)$, whereas reaction in non-sea-salt aerosols (having low pH values 4.5 - 5.0) occurs via H_2O_2.
The observed decrease in SO_2, the constant level of NO and NO_y as well as the recovering ozone level up to a distance of 9 km to the ship propose the following scenario: Reaction of ambient O_3 with NO reduces the ozone level up to a distance of 5.5 km. Further away, this reaction still occurs and keeps the NO, NO_y level constant. Reaction of NO and HO_2 starts due to further entrainment of marine boundary layer air into the plume and OH molecules are produced which in turn lead to a rising O_3 level. SO_2 hereby experiences conversion into sulfuric acid by reaction with OH. Additional loss results from non-visible cloud particles (hazy weather conditions) which oxidize via H_2O_2 a certain amount of SO_2. [Song, 2003a] reports of a very short lifetime of SO_2 (0.35 h) in the presence of clouds. Finally at 9 km distance from the ship all trace gases quickly decrease probably due to the fact, that the aircraft left the plume center.

B.2.4 Conclusions

A gaussian plume model fits the experimentally derived plume center well. Since plume age is low compared to its lifetime, no significant losses in NO and NO_y can be observed. The strong ozone depletion can be explained with known plume chemistry. The interpretation of the SO_2 reduction is more complex but likely due to heterogenous processes such as loss processes at sea-salt and cloud particles. Also the photochemical conversion to sulfuric acid has to be considered as a sink. At the current status of data analysis no aerosol particle data is available for the flights 23^{nd} and 30^{th} of July such that condensational growth of sulfuric acid and the related SO_2 abundances cannot be

discussed. Since within a ship plume, sulfur dioxide from ship emissions is always much larger than any H_2SO_4 produced via DMS and due to the highly elevated SO_2 mixing ratios measured in both flight experiments compared to remote regions, SO_2 from ship emissions can be considered as an important factor concerning marine aerosol growth.

Appendix C

C.1 ITMS implementation in the research aircraft FALCON

The following figures serve to illustrate the implementation of the IT-CIMS setup into the Falcon aircraft. Inlet, exhaust and flow reactor sampling lines are drawn in detail. The used tubes consist of stainless steel, with an inner diameter of 40 mm (KF 40). Connectors from Swagelok (Swagelok company, USA) to 1/2" and 1/4" PFA (ultrahigh-purity perfluoroalkoxy)tubing were used.

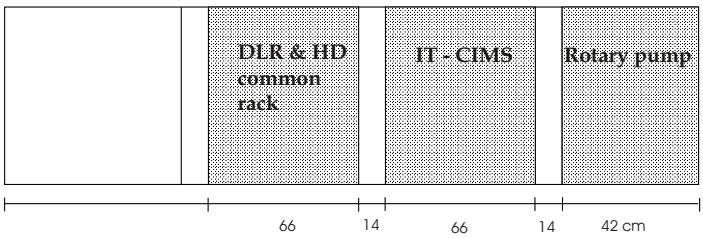

Figure C.1: Installation of IT-CIMS rack, pumping unit and shared rack (HD, DLR).

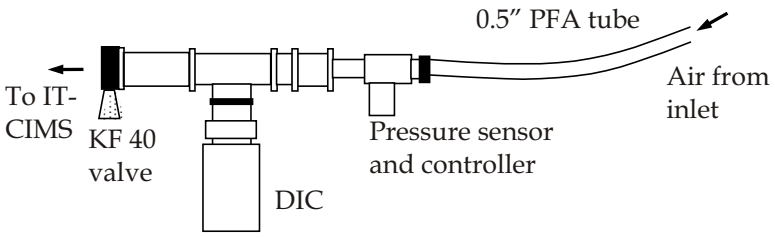

Figure C.2: Flow reactor with DIC and pressure sensor. The about 1 m long PFA tubing directly connects to the inlet.

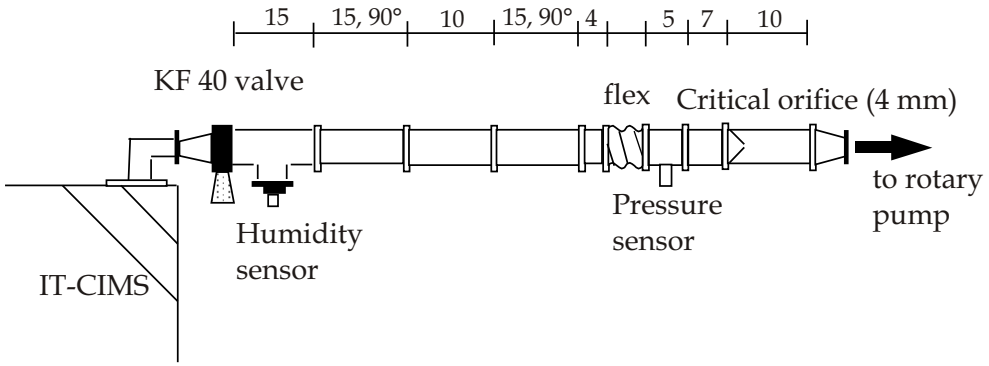

Figure C.3: Exhaust of sampled air (numbers in cm units). Tubing (KF 40) from IT-CIMS to rotary pump. A critical orifice before the pump limits the total flow and keeps it together with the pressure sensor at the flow reactor constant.

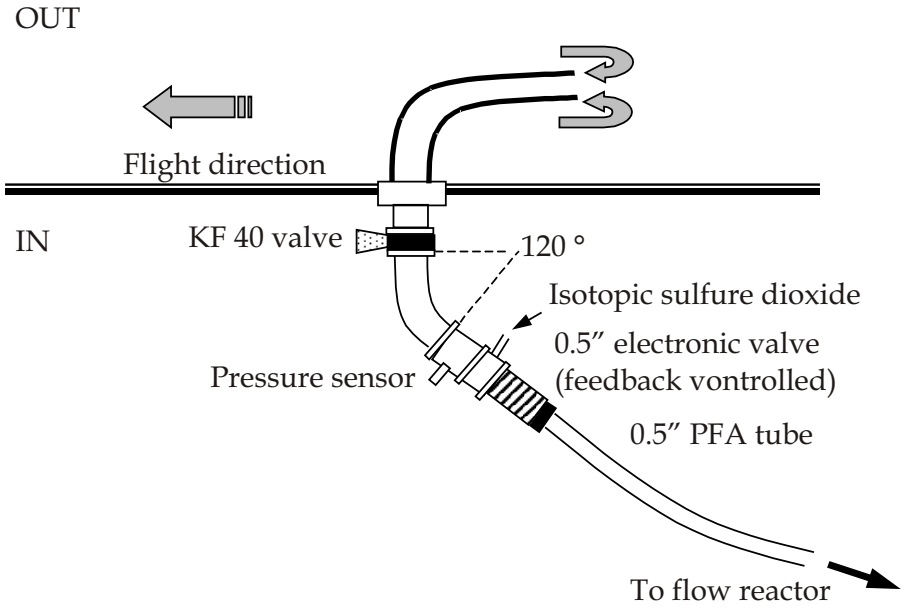

Figure C.4: Inlet for ambient air and isotopic calibration gas.

List of Figures

List of Tables

Bibliography

Andreae, M., D.Rosenfeld, P.Artaxo, Costa, A., G.P.Frank, Longo, K., and Silva-Dias, M. (2004). Smoking rain clouds over the amazon. *Science*, 303:1337–1342.

Arnold, F. (1980). Multi-ion complexes in the stratosphere. implications for trace gases and aerosol. *Nature*, 284:610–611.

Arnold, F. (1981). Mass-spectrometric measurements of fractional ion abundances in the stratosphere-positive ions. *Planetary and Space Science*, 29(2):185–193.

Arnold, F. (1982). Implications for trace gases and aerosols of large neative-ion clusters in the stratosphere. *Nature*, 297:371–376.

Arnold, F., D.Krankowsky, and K.Marien (1977). First mass spectrometric measurements of positive ions in the stratosphere. *Nature*, 267:30.

Arnold, F. and Henschen, G. (1978). First mass analysis of stratospheric negative ions. *Nature*, 257:521.

Arnold, F., M.Speidel, L.Pirjola, R.Nau, H.Schlager, A.Petzold, and A.Minikin (2005a). Stratospheric Anthropogenic SO_2 Pollution and Aerosol Formation: Aircraft Measurements and Model Simulations. *Paper in preparation.*

Arnold, F., M.Speidel, R.Nau, H.Schlager, A.Roiger, M.Lichtenstern, H.Huntrieser, and A.Stohl (2005b). Detection of Lower Stratospheric SO_2 Pollution induced by Injection from the Polluted Planetary Boundary Layer followed by Intercontinental Transport. *Paper in preparation.*

Ashkenas, H. and F.Sherman (1966). *Structure and utilization of supersonic free jets in a low density wind tunnel, in Rarefied Gas Dynamics.* H.Deleuv (ed), pp 84., Academic Press.

Aufmhoff, H. (2004). Atmosphärische gasförmige Vorläufer von Aerosol und Ozon: Messung mit CIMS-Methoden auf einem Flugzeug und am Boden. Dissertation, Universität Heidelberg.

Bandy, A., D.C.Thornton, and A.R.Driedger (1993). Airborne Measurements of Sulfure Dioxide, Dimethyl Sulfide, Carbon Disulfide, and Carbonyl Sulfide by Isotope Dilution Gas Chromatography/Mass Spectrometry. *Geophys. Res.*, 98:23,423–23,433.

Becker, R. (1975). *Theorie der Wärme*. Springer, Berlin.

Bohme, D., Goodings, J., and Chun-Wai, N. (1977). In situ chemical ionization as a probe for neutral constituents upstream in methane-oxygen flame. *International Journal of Mass Spectrometry and Ion Physics.*, 24:335–354.

Brasseur, G., Orlando, J., and Tyndall, G. (1999). *Atmospheric Chemistry and Global Change*. Oxford University Press, New York.

Chen, G. (2005). An investigation of the chemistry of ship emission plumes during itct 2002. *Jounral of Geophysical Research*, 110.

Chin, M. and D.D.Davis (1995). A reanalysis of carbonyl sulfide as a source of stratospheric background sulfur aerosol. *Journal of Geophysical Research*, 100:8993–9005.

Coffman, D. and Hegg, D. (1995). A preliminary study of the effect of ammonia on particle nucleation in the marine boundary layer. *Journal of Geophysical Research*, 100:7147–7160.

Cosby, P., Ling, J., Peterson, J., and Moseley, J. (1976). Photodissociation and photodetachment of molecular negative ions. Ions formed in $CO_2/O_2/H_2O$ mixtures. *J.Chem.Phys.*, 65:5267.

Cottrell, T. (1958). *The Strengths of Chemical Bonds, 2nd edn.* Butterworths, London.

Eichkorn, S., Wilhelm, S., Aufmhoff, H., Wohlfrom, K., and Arnold, F. (2002). Cosmic Ray Induced Aerosol Formation: First observational evidence from aircraft based ion mass spectrometer measurements in the upper troposphere. *Journal of Geophysical Research*, 29.

Eicke, N. (1999). In-situ measurements of water vapor in the lower stratosphere and in the tropopause region. Masterthesis, University of Bonn.

Eisele, F. and Hansen, D. (2000). First Measurements of Prenucleation Molecular Clusters. *Journal of Physical Chemistry*, 104:830–836.

Engel, A. (1996). The total hydrogen budget in the arctic winter stratosphere during the european arctic stratospheric ozone experiment. *Jounral of Geophysical Research*, 23:1653–1656.

E.Palmen and C.W.Newton (1969). *Atmospheric Circulation Systems*. Academic Press, San Diego, Calif.

Fangqun, Y. (2002). Altitude variations of cosmic ray induced production of aerosols: Implications for global cloudiness and climate. *Journal of Geophysical Research*, 107.

Fangqun, Y. and Turco, R. (2001). From molecular clusters to nanoparticles: Role of ambient ionization in tropospheric aerosol formation. *Journal of Geophysical Research*, 106:4797–4814.

Fischer, H., Reus, M., M.Traub, J.Williams, J.Lelieveld, Gouw, J., C.Warneke, H.Schlager, A.Minikin, R.Scheele, and P.Siegmund (2003). Deep convective injection of boundary layer air into the lowermost stratosphere at midlatitudes. *Atmospheric Chemistry and Physics*, 3:739–745.

Forster, C., A.Stohl, P.James, and V.Thouret (2003). The residence times of aircraft emissions in the stratosphere using a mean emission inventory and emissions along actual flight tracks. *Journal of Geophysical Research*, 108.

Georgii, H. and Meixner, F. (1980). Measurement of the tropospheric and stratospheric SO_2 distribution. *Jounral of Geophysical Research*, 85:7433–7438.

Gettelman, A. and S.L.Baughcum (1999). Direct deposition of subsonic aircraft emissions into the stratosphere. *Journal of Geophysical Research*, 104:8317–8327.

Ghosh, P. (1995). *Ion Traps*. Clarendon Press Oxford.

Gilliani, N. (1998). Relatice production of ozone and nitrates in urban and rural power plant plumes. 1. composite results based on data from 10 field measurement days. *Jounral of Geophysical Research*, 103:22,593–22,615.

Glebe, W. (1994). Laboruntersuchungen atmospärischer negativer clusterionen. Masterthesis, University of Heidelberg.

Gollinger, K. (1993). Massenspektrometrische Flugzeugmessungen von Spurengasen in der arktischen Stratosphäre. Diploma thesis, University of Heidelberg.

Gregory, G., D.D.Davis, N.Beltz, A.R.Bandy, R.J.Ferek, and D.C.Thornton (1993). An intercomparison of aircraft instrumentation for tropospheric measurements of sulfur dioxide. *Journal of Geophysical Research*, 98:23,325–23,352.

Hanke, M. (1999). *Development of a Novel Method for Measuring Atmospheric Peroxy Radicals: Calibration, Aircraft-Borne Measurements and Selective Measurements of HO_2 and RO_2.* Dissertation, Universität Heidelberg.

Hartmann, D. (1993). *Aerosol Cloud Climate Interactions.* Academic, San Diego.

Heitmann, H. and Arnold, F. (1983). Composition measurements of tropospheric ions. *Nature*, 306:747–751.

Hofman, D. (1991). Aircraft sulphur emissions. *Nature*, 349:659.

Hoinka, K., Reinhardt, M., and Metz, W. (1993). North atlnatic air traffic within the lower stratosphere: Crusing times and corresponding emissions. *Journal of Geophysical Research*, 98:23.113–23.131.

Holton, J., Haynes, P., McIntyre, M., Douglass, A., Rood, R., and Pfister, L. (1995). Stratosphere-troposphere exchange. *Reviews of Geophysics*, 33:403–439.

Huntrieser, H., F.Arnold, C.Forster, W.Junkermann, A.Stohl, H.Aufmhoff, J.Heland, R.Meier, B.Rappenglück, H.Schlager, M.Speidel, S.Wilhelm, and S.Wimmer (2003). Contrace - convective transport of trace gases into the middle and upper troposphere over europe: Budget and impact on chemistry. *Contrace Final Report.*

Imai, M., K.Yoshida, and M.Kitabatake (1986). Mortality from asthma and chronic bronchitis associated with changes in sulfur oxides air pollution. *Arch.Environ.Health*, 41(1):29–35.

Jaecker-Voirol, A. and Mirabel, P. (1989). Heteromolecular nucleation in the sulfuric acid-water system. *Atmospheric Environment*, 23:2033–2057.

Jaeschke, W. (1978). New methods for the analysis of SO_2 and H_2S in remote areas and their application to the atmosphere. *Atmospheric Environment*, 12:715–721.

Jost, C., D.Sprung, T.Kenntner, and T.R.Reiner (2003). Atmospheric pressure chemical ionization mass spectrometry for the detection of tropospheric trace gases: the influence of clustering on sensitivity and precision. *International Journal of Mass Spectrometry*, 223–224:771–782.

Junge, C. (1974). Sulfur budget of the stratospheric aerosol layer. *paper presented at: First Special Assemblies, Int.Assoc. of Atmosp.Phys/Int.Assoc. of Phys.Sci. of the Oceans, Melbourne Australia.*

Keesee, R. and A.W.Castleman (1985). Ions and cluster ions: Experimental studies and atmospheric observations. *Journal of Geophysical Research*, 90:5885–5890.

Keesee, R. and Castleman, A. (1986). Thermodynamic data on gas-phase Ion-molecule association and clustering reactions. *Journal of Physical Chemistry Reference Data*, 15:1011–1071.

Kerminen, V.-M. and Wexler, A. (1994). Post-fog nucleation of h_2so_4-h_2o particle in smog. *Atmospheric Environment*, 28:2399–2406.

Kernthaler, S., Toumi, R., and Haigh, J. (1999). Some doubts concerning a link between cosmic ray fluxes and global cloudiness. *Geophysical Research Letters*, 26:863–865.

Kiendler, A. (1999). *Aufbau und Einsatz einer neuartigen flugzeuggetragenen Ionenfallen- Massenspektrometersonde zur Analyse von Spurengasen und Ionen: Messungen im Labor, im Abgas von Düsentriebwerken und atmosphärische Spurengasmessungen mit Flugzeugen.* Dissertation, Universität Heidelberg.

Kjellstroem, E. (1997). A three dimensional global model study of carbonyl sulfide in the troposphere and the lower stratosphere. *Jounral of Atmospheric Chemistry*, 29:151–177.

Kok, G., J.A.Lind, and M.Fang (1997). An airborne study of air quality around the hong kong territory. *Journal of Geophysical Research*, 102:19,043–19,057.

Krieger, A. (1988). Messungen stratosphärischer Ionen und Spurengase mit ballongetragenen Massenspektrometern. Diploma thesis, University of Heidelberg.

Kulmala, M., A.Laaksonen, and L.Pirjola (1998). Parameterization for sulfuric acid / water nucleation rates. *Journal of Geophysical Research*, 103:8301–8307.

Kulmala, M., Pirjola, L., and Mäkelä, J. (2000). Stable sulphate clusters as a source of new atmospheric particles. *Nature*, 404:66–69.

Kusaka, I., Wang, Z., and Seinfeld, J. (1995). Ion-induced nucleation, 3, of polarizable multipolar molecules. *Journal of Chemical Physics*, 193:8993–9009.

Laaksonen, A., L.Pirjola, M.Kulmala, K.-H.Wohlfrom, F.Arnold, and F.Raes (2000). Upper tropospheric SO_2 conversion into sulfuric acid aerosols and cloud condensation nuclei. *Journal of Geophysical Research*, 105:1459–1469.

Lawrence, M. and P.J.Crutzen (1999). Influence of nox emissions form ships on tropospheric photochemistry an climate. *Nature*, 402:167–170.

Lee, S.-H., J.M.Reeves, J.C.Wilson, D.E.Hunton, A.A.Viggiano, T.M.Miller, J.O.Ballenthin, and L.R.Lait (2003). Particle Formation by Ion Nucleation in the Upper Troposphere and Lower Stratosphere. *Science*, 301:1886–1889.

Logan, J., M.B.McElroy, S.C.Wofsy, and M.J.Prather (1979). Oxidation of CS_2 and COS: sources for atmospheric SO_2. *Nature*, 281:185–187.

Lovejoy, E., J.Curtius, and K.D.Froyd (2004). Atmospheric ion-induced nucleation of sulfuric acid and water. *Journal of Geophysical Research*, 109.

Lovejoy, E. and R.Wilson (1998). Kinetics Studies of Negative Ion Reactions in a Quadrupole Ion Trap: Absolute Rate Coefficients and Ion Energies. *Journal of Physical Chemistry*, 102:2309–2315.

Maddox, R. (1980). Mesoscale convective complexes. *Bull.Am.Meteorol.Soc.*, 61:1374–1387.

March, R. (1997). An Introduction to Quadrupole Ion Trap Mass Spectrometry. *Journal of Mass Spectrometry*, 32:351–369.

May, R. (1998). Open-path, near infrared tunable diode laser spectrometer for atmospheric measurements of h_2o. *Jounral of Geophysical Research*, 103:19161–19172.

McAllister, T., Nicholson, A., and Swingler, D. (1978). Negative ions in the flame ionization detector and the occurence of hco_4^-. *Internation Jounral of Mass Spectrometry and Ion Physics*, 27:43–48.

Möhler, O. and F.Arnold (1992). Gaseous sulfuric acid and sulfur dioxide measurements in the arctic troposphere and lower stratosphere: Implications for hydroxyl radical abundances. *Journal of Geophysical Research*, 19:1763–1766.

Möhler, O. and Arnold, F. (1991). Flow Reactor and Triple Quadrupole Mass Spectrometer Investigations of Negative Ion Reactions Involving Nitric Acid. *Journal of Atmospheric Chemistry*, 13:33–61.

Möhler, O, T. R. and Arnold, F. (1992). The formation of so_5^- by gas phase ion-molecule reactions. *J. Chem. Phys.*, 97:8233–8239.

Moruzzi, J. and Phelps, A. (1966). Survey of Negative-Ion-Molecule Reactions in O_2, CO_2, H_2O, CO and Mixtures of These Gases at High Pressure. *J.Chem.Phys.*, 45:4617.

Nadykto, A. and F.Yu (2003). Formation of binary ion cluster from polar vapous: Effect of the dipole-charge interaction. *Atmospheric Chemistry and Physics*, 3:4927–4941.

Nau, R. (2004). Das atmospärische Aerosol-Vorläufergas SO_2: Messungen mit einem flugzeuggetragenen Massenspektrometer. Diploma thesis, University of Heidelberg.

Nigel, D. and Svensmark, H. (2000). Low cloud properties influenced by cosmic rays. *Physical Review Letters*, 85(23):5004–5007.

Ovalez, A. (1991). Stratospheric water vapor measurements in the tropical zone by means of a frost point hygrometer on board long duration balloons. *Jounral of Geophysical Research*, 96:15541–15545.

Parrish, D., E.J.Williams, R.B.Norton, and F.C.Fehsenfeld (1982). Measurements of odd-nitrogen species and o_3 at point arena, california. *Journal of Chemical Physics*, 76:5183–5185.

Parrish, D., M.Trainer, M.P.Buhr, B.A.Watkins, and F.C.Fehsenfeld (1991). Carbon monoxide concentrations and their relation to concentrations of total reactive oxidized nitrogen at two rural u.s. sites. *Journal of Geophysical Research*, 96:9309–9320.

Paul, W., H.P.Reinhard, and U.Zahn (1985). Das elektrische massenfilter als massenspektrometer und isotopentrenner. *Zeitschrift für Physik*, 152:143–182.

Pilling, B. and Seakins, P. (1995). *Reaction Kinetics*. Oxford Scientific Press.

Pilling, M. and P.W.Seakins (1995). *Reaction Kinetics*. Offord Science Publication, New York.

Pirjola, L., M.Kulmala, M.Wilck, A.Bischoff, F.Stratmann, and E.Otto (1999). Formation of sulfuric acid aerosols and cloud condesation nuclei: An expression for significant nucleation and model comparison. *Journal Aerosol Science*, 30:1079–1094.

P.J.Crutzen (1976). The possible importance of CSO for the sulfate layer of the stratosphere. *Geophysical Research Letters*, 3:73–76.

Platt, U. (1994). *Differential optical absorption spectroscopy (DOAS), in: Air Monitoring by Spectroscopic Techniques.* John Wiley, New York.

Poulida, O. and R.R.Dickerson (1996). Stratosphere-troposphere exchange in a midlatitude mesoscale convective complex: 1. Observations. *Journal of Geophysical Research*, 101:6823–6836.

Pruppacher, H. and J.P.Klett (1996). *Microphysics of Clouds and Precipitation.* Kluwer Verlag, Springer.

Reiner, T. (1992). Atmosphärische Spurengasmessungen mit einem neuartigen flugzeuggetragenen Tandem-Massenspektrometer. Diplomarbeit, Universität Heidelberg.

Reiner, T. and Arnold, F. (1994). Laboratory investigations of gaseous sulfuric acid formation via $SO_3 + H_2O + M \rightarrow H_2SO_4 + M$: Measurements of the rate constant and products identification. *Journal of Chemical Physics*, 101:7399–7407.

Reiter, R. (1992). *Phenomena in Atmospheric and Environmental Electricity.* Elsevier Publishing Company.

Roedel, W. (2000). *Physik unserer Umwelt: Die Atmosphäre, 3. Auflage.* Springer Verlag.

Rosen, J., D.J.Hofmann, and W.Gringel (1985). Measurements of ion mobility to 30 km. *Journal of Geophysical Research*, 90:5876–5884.

Ryerson, T. (1998). Emission lifetimes and ozone formation in power plant plumes. *Jounral of Geophysical Research*, 103:22,569–22,583.

Schlatter, C. (1994). Environmental pollution and human health. *Sci. Total Environ.*, 134(1):93–101.

Seeley, J. V., Morris, R. A., and Viggiano, A. A. (1997). Rate constants for the reaction of $CO_3^-(H_2O)_{n=0-5}$+ SO_2: Implications for CIMS detection of SO_2. *Geophysical Research Letters*, 24:1379–1382.

Seinfeld, J. and Pandis, S. N. (1998). *Atmospheric Chemistry and Physics*. John Wiley & Sons, Inc.

Smith, J. and J.H.E.Clark (2004). Mesoscale Convective Complexes: A May 2004 Pennsylvania Case Study.

Song, H. (2003a). Chemical evolution and dispersion of ship plumes in the remote marine boundary layer: investigation of sulfur chemistry. *Atmospheric environment*, 37:2663–2679.

Song, H. (2003b). Dispersion and chemical evolution of ship plumes in the marine boundary layer: Investigation of $O_3/NO_y/HO_x$ chemistry. *Jounral of Geophysical Research*, 108.

Stjernberg, N., A.Eklund, L.Nystrom, L.Rosenhall, A.Emmelin, and LH.Stromqvist (1985). Prevalence of bronchial asthma and chronic bronchitis in a community in northern Sweden; relation to environmental and occupational exposure to sulphur dioxide. *Eur.J.Respir.Dis.*, 67(1):41–49.

Su, T. and W.J.Chesnawitch (1985). Parameterization of the ion-polar collision rate constant by trajectory calculations. *Eos.Trans.AGU*, 66:820.

Svensmark, H. and Christensen, E. (1996). Variation of cosmic ray flux and global cloud coverage - a missing link in solar-climate relationships. *Journal of Atmospheric and Solar-Terrestrial Physics*, 59:1225–1232.

Tammet., H. (1995). Size and mobility of nanometer particles, clusters and ions. *J. Aerosol Sci.*, 26:459–475.

Thornton, D., A.R.Bandy, and A.R.Driedger (1987). Sulfur dioxide over the Western Atlantic Ocean. *Glob.Biogeochem.Cycles*, 1:317.

Thornton, D., A.R.Bandy, and B.W.Blomquist (1997). Vertical transport of sulfur dioxide and dimethyl sulfide in deep convection and its role in new particle formation. *Journal of Geophysical Research*, 102:28,501–28,509.

Thornton, D., A.R.Bandy, N.Beltz, A.R.Driedger, and R.Ferek (1993). Advection of sulfur dioxide over the western Atlantic ocean during CITE 3. *Journal of Geophysical Research*, 98:23,549–23,467.

Trentmann, J., Graf, H., Hobbs, P., Ottmar, R., and Trautmann, T. (2001). Simulation of a biomass-burning plume: Comparison of model results with observations. *Journal of Geophysical Research*, 107.

Viggiano, A. u. F. A. (1995). *Ion chemistry and composition of the atmosphere, H. Volland, Hg., Atmospheric Electrodynamics*. CRC Press.

Wagner, G., D.M.Livingstone, J.Masarik, R.Muscheler, and J.Beer (1999). Some doubts concerning a link between cosmic ray fluxes and global cloudiness. *Geophysical Research Letters*, 26:863–865.

Wang, T., F.Cheung, and Y.S.Li (2002). Emission characteristics of CO, NO_x, SO_2 and indications of biomass burning observed at a rural site in eastern China. *Journal of Geophysical Research*, 107.

Wang, W., A.Richter, M.Bruns, J.P.Burrows, W.Junkermann, K.-P.Heue, T.Wagner, U.Platt, and I.Pundt (2005). Airborne multi-axis DOAS measurements of tropospheric SO_2 plumes in the Po-valley, Italy. *Atmospheric Chemistry and Physics Discussion*, 5:2017–2045.

Watts, P. (1992). Studies on gas-phase negative ion molecule reactions of relevance to ion mobility spectrometry: kinetic modelling of the reactions occuring in "celan air". *International Journal of Mass Spectrometry and Ion Processes.*, 121:141–158.

Weber, R., McMurry, P., Eisele, F., and Tanner, D. (1995). Measurement of expected nucleation precursor species and 3-500 nm diameter particles at Mauna Loa Observatory, Hawaii. *Journal of Atmospheric Science*, 52:2242–2257.

Weber, R., S.Lee, G.Chen, B.Wang, V.Kapustin, K.Moore, Clarke, A., L.Mauldin, E.Kosciuch, C.Cantrell, F.Eisele, D.C.Thornton, A.R.Bandy, G.W.Sachse, and H.E.Fuelberg (2003). New particel formation in anthropogenic plumes advecting from asia observed during trace-p. *Journal of Geophysical Research*, 108.

Wilhelm, S. (2003). Untersuchungen zur ioneninduzierten Aerosolbildung in der freien Atmoshpäre: Flugzeug- und Labormessungen. Phd-thesis, University of Heidelberg.

Wincel, H., Mereand, E., and Castleman, A. (1995). Gas phase reactions of $HO_2^- CO_2$ with molecular species of possible atmospheric interest. *J.Phys.Chem.*, 99:6601–6607.

Wollny, A. (1998). Flugzeugmessungen atmosphärischer Spurengase mittels Ionen-Molekül-Reaktions-Massenspektrometrie: Methodische Untersuchungen zur Reaktionskinetik. Diplomarbeit, Universität Heidelberg.

Zöger, M. (1999). Fast in situ stratospheric hygrometers: A new family of balloon-borne and airborne lyman-α photophragment fluorescence hygrometers. *Journal of Geophysical Research*, 104:1807–1999.

Abbreviations

AEROFOR	Model for Aerosol Formation and dynamics
amu	Atomic Mass Unit $\approx 1.67\ 10^{-27}$ kg
CAPE	Convective Available Potential Energy
CCN	Cloud Condensation Nucleus
CG	Condensable Gas
CIMS	Cemical Ionisation Mass Spectrometry
CS	Condensational Sink
DIC	Capillary high frequency glow Discharge Source
DLR	Deutsches Zentrum für Luft und Raumfahrt
DOAS	Differential Optical Absorption Spectrometry
ECMWF	European Centre for Medium range Weather Forecast
EDGAR	Emission Database for Global Atmospheric Research
FLEXPART	Lagrangian Particle Dispersion Model
ITCIMS	Ion Trap Chemical Ionisation Mass Spectrometer
ITMS	Ion Trap Mass Spectrometer
KF 40	Stainless steel tubing, 40 mm in diameter and generally used for air flow reactors experiments by our group.
LCL	Lower Confidence Level
LS	Lower Stratosphere
MFC	Mass Flow Controler
MSC	Mesoscale Convective Complex
PBL	Planetary Boundary Layer
ppbv	Parts Per Billion by Volume $\simeq 10^{-9}$
ppmv	Parts Per Million by Volume $\simeq 10^{-6}$
pptv	Parts Per Tillion by Volume $\simeq 10^{-12}$
QMS	Quadrupole Mass Spectrometer
slpm	Standard Liter Per Minute
smlpm	Standard Mililiter Per Minute

TST ..... Transition State Theory
UCL ..... Upper Confidence Level
UT ..... Upper Troposphere
UTC ..... Universal Time Code

ACKNOWLEDGEMENTS

At this point i would like to thank all who contributed to the success of this work.

- The directors board of the Max Planck Institute for Nuclear Physics, Heidelberg.
- Prof.Dr. F.Arnold who made it possible for me to perform my PhD in his research group. Also for his interests and discussions in the research field.
- Prof.Dr. K.Roth who prepared for the survey of this thesis.
- The people from the DLR, especially H.Huntrieser and H. Schlager.
- C.Gurk and A.Roiger for excellent cooperation during campaigns and meetings and for relaxed evening activities.
- G.Hönes for precious help in writing and correcting proposals, reports and this thesis.
- L.Pirjola from the University of Helsinki
- B.Preissler and especially R.Zilly. Without his help no campaign and most other technical things in our group would simply not work!
- The current and former group members, H.Aufmhoff, T.Schuck, V.Fiedler, A.Kuhlmann, R.Nau, S.Wilhelm, B.Umann, M.Hanke.
- R.Nau for interesting discussions and all sorts of help during my PhD.
- My friends and my family.